Chair of Physics

Doctoral Thesis

Supercritical Hydrogen Adsorption in Nanoporous Carbons: Understanding Confinement Effects Through Neutron Scattering

Dipl.-Ing. Sebastian Manfred Stock, BSc

March 2025

AFFIDAVIT

I declare on oath that I wrote this thesis independently, did not use any sources and aids other than those specified, have fully and truthfully reported the use of generative methods and models of artificial intelligence, and did not otherwise use any other unauthorized aids.

I declare that I have read, understood and complied with the "Preamble on Integrity in Academic Study, Teaching, and Research Operations" of the Montanuniversität Leoben.

Furthermore, I declare that the electronic and printed versions of the submitted thesis are identical in form and content.

Date

(The original signature is kept at the university)

Acknowledgements

"What shoulds"

This rather poor translation of a very Austrian feeling ("Was solls") accompanied and guided me through the past four year. Along with the journey that ended with writing this thesis, I often faced steep hills and challenges, that required a moment of calm reflection to decide which way to go next. Both personal and academic challenges are easier addressed with support from others. So, with this I want to thank all who supported me in the past four years.

First, I would like to thank Prof. Dr. Oskar Paris, who has not only been my *Doktorvater* in the past four years, much more someone who accompanied my academic journey since 2017, when I started as a student assistant at the Chair of Physics. It was through his guidance, the door to his office always being open and him being ready for prolonged scientific discussions that sparked and kept the interest to pursue this academic journey. His strong endorsement of writing yet another abstract for an upcoming conference or beamtime has allowed me to discover many wonderful places around the world and meet yet even more fascinating people in academia. For this I will always be deeply thankful, as those travels and encounters have led to many stories I will forever tell.

On my journey there were many more people to support me throughout the past four years. I remember just too well, even before I started with the PhD in 2021, the first road trip to Grenoble, with my new colleague Malina Seyffertitz back then. Within the 12 hours car ride and the following five days of intense beamtime at D16 at ILL, a friendship began. I want to thank Malina for her everlasting support, for sacrificing her sanity during night shifts and the scientific as well as personal advice that helped me through those years. With this I also want to thank Max Rauscher, Markus Kratzer and Taha Honaramooz, who made the office a place full of joy, excitement and a place where everyone feels welcome. Further, I want to thank Rainer Lechner, Gerhard Popovski for their scientific support and Peter Moharitsch, Bernhard Mürzel and Heinz Pirker for their support in preparation of beamtimes and more.

A special thanks is dedicated to Nadine Aichberger, Heike Knoll and Heide Kirchberger who helped throughout the years with various administrative work and kelp to navigate through the complexity of travel accounting.

I also want to thank all collaborators that have contributed to my work throughout the past years. Especially, Bruno Demé, Viviana Cristiglio, Stephané Rols and Simon Baudoin from the Institut Laue Langevin, have made the many beamtimes a very pleasant experience and through their support making them successful. Further, I want to thank Julian Selinger, Claus Rebholz, Theodore Steriotis and Christian Mitterer for their support of various publications contributing to a better understanding on how bio-waste can be turned into a valuable product. Within the last months of this journey, I had the pleasure of visiting Rutgers University and Alexander Neimark and Nicholas Corrente, who have provided an environment of close collaboration and scientific exchange. Through Nicholas I also had the chance to meet Beth and Ned Both, who opened their home during this time and allowed me with their support to focus on my research and this thesis.

The past four years have been undoubtably the most fun, the most challenging and transformative years in my life. Many people have supported me throughout those years and besides academia it was my friends that made this time, the whole 10 years of my academic journey, the most memorable time. Especially, the everlasting support and friendship with my first ever friend Fabian Kadisch, has shown me what value it is to be able to rely on someone when a storm passes through life. With this I also want to thank my friend and mentor Nikolaos Kostoglou, who has supported me from my first academic steps on and guided me with his advice not only through academic but also personal hardship. It is owed to him, that my interest in hydrogen was sparked and I am very thankful for his support.

As an Austria saying goes: *"Das Beste kommt zum Schluss"*, I want to express my deepest gratitude to my family. It was through their encouragement, their support and guidance that I was able to pursue this wonderful journey called life. Words cannot describe the gratitude I feel for this gift, for their support and for this feeling, that no matter where I am there is always a place I can call home.

- So, I roam those beaches wondering…. Underneath my feet the sand still radiates the past dreams heat, the evening sky turned into darkness. Only the soothing sounds of the waves, about to break loose, seem familiar. So, I wander…-

to all who supported me in the past 4 years

Abstract

The transition to a hydrogen-based energy economy is gaining momentum as industries and governments seek sustainable alternatives to fossil fuels. However, the efficient storage of hydrogen remains a critical challenge, particularly for mobile applications requiring high energy density and compact storage solutions. Among the various hydrogen storage methods, physisorption in nanoporous materials has emerged as a promising approach, offering high storage capacities under cryogenic conditions without the need for extreme pressures. This thesis investigates the potential of nanoporous carbons as hydrogen storage materials, focusing on their structural characteristics, hydrogen adsorption behavior, and the densification of hydrogen in nanopore confinement.

The first part presented explores the synthesis of bio-derived activated carbons from orange peels and used tea leaves, highlighting their potential as sustainable hydrogen storage materials. By employing a simple chemical activation procedure, the resulting nanoporous carbons exhibit surface areas exceeding 2100 m^2/g and pore volumes beyond 1.5 cm^3/g, key factors influencing hydrogen adsorption capacity. The systematic evaluation of pore structure and chemical composition reveals that ultramicropores (< 0.7 nm) dominate hydrogen uptake at low pressures, while supermicropores (0.7–2 nm) and mesopores (>2 nm) enhance adsorption at higher pressures. Statistical correlation analysis confirms that the micropore volume and the total surface area are the strongest predictors of storage performance, whereas the influence of heteroatom concentration on storage performance requires further studies. These insights provide a framework for optimizing activated carbons for hydrogen storage applications.

In the second part, in-situ neutron scattering is utilized to directly probe the spatial distribution of hydrogen in nanoporous carbons. Small-angle neutron scattering (SANS) measurements at cryogenic temperatures reveal a pore-size-dependent densification, where hydrogen confined in the smallest pores approaches or even exceeds its bulk solid density. The study establishes a hierarchical contrast model describing density evolution across different pore classes, confirming that confinement in ultramicropores (< 0.7 nm) leads to extreme densification. The findings underscore the importance of strong confinement effects

on hydrogen adsorption behavior, providing crucial experimental evidence to support the development of next-generation storage materials.

The third part integrates atomistic simulations to complement experimental observations, offering deeper insight into the confinement-dependent adsorption mechanisms. Molecular simulations in realistic atomistic models of nanoporous carbons reveal preferred adsorption sites, showing that highly defective regions enhance local hydrogen density. The comparison between simulated and experimental scattering data suggests that while deuterium (D_2) follows simulated adsorption trends, hydrogen (H_2) shows clustering effects, likely due to specific spin isomer interactions that were not considered in the interaction potentials. These results highlight the complexity of hydrogen adsorption in nanoporous carbons and emphasize the need for refined atomistic models incorporating surface chemistry and spin effects in the interaction potentials.

This thesis advances the understanding of hydrogen adsorption in nanoporous carbons, demonstrating the potential of bio-derived materials for sustainable hydrogen storage applications. The integration of experimental techniques and atomistic modeling provides a comprehensive perspective on the role of pore size, surface area, and chemical composition in optimizing hydrogen uptake. The insights gained contribute to the ongoing development of high-performance hydrogen storage systems, bridging the gap between fundamental adsorption mechanisms and practical applications.

Kurzfassung

Die Transformation zu einer wasserstoffbasierten Energieversorgung gewinnt zunehmend an Bedeutung, da Industrien und Regierungen weltweit nach nachhaltigen Alternativen zu fossilen Brennstoffen suchen. Allerdings bleibt die effiziente Speicherung von Wasserstoff eine große Herausforderung, insbesondere für mobile Anwendungen, die eine hohe Energiedichte und kompakte Speichersysteme erfordern. Unter den verschiedenen Methoden zur Wasserstoffspeicherung hat sich die Physisorption von Gasmolekülen in nanoporösen Materialien als vielversprechender Ansatz erwiesen. Die hohen Speicherkapazitäten unter kryogenen Bedingungen ermöglicht eine effiziente Speicherung, ohne extreme hohe Drücke zu benötigen. Diese Dissertation untersucht das Potenzial von nanoporösen Kohlenstoffen als Wasserstoffspeichermaterialien, wobei der Fokus auf deren strukturellen Eigenschaften, Adsorptionsverhalten und der Verdichtung von Wasserstoff in Nanoporen liegt.

Der erste Teil befasst sich mit der Synthese von biobasierten Aktivkohlen aus Orangenschalen und Teeblättern und hebt deren Potenzial als nachhaltige Wasserstoffspeichermaterialien hervor. Durch ein einfaches chemisches Aktivierungsverfahren entstehen nanoporöse Kohlenstoffe mit Oberflächen größer als 2100 m^2/g und Porenvolumina über 1,5 cm^3/g, die entscheidend für die Wasserstoffspeicherkapazität sind. Die systematische Untersuchung der Einflussfaktoren auf die Wasserstoffspeicherkapazität zeigt, dass Ultramikroporen (< 0,7 nm) die Wasserstoffaufnahme bei niedrigen Drücken dominieren, während höhere Volumenanteile von Supermikroporen (0,7–2 nm) und Mesoporen (> 2 nm) die Adsorption bei höheren Drücken verbessern. Eine statistische Korrelationsanalyse zeigt, dass das Mikroporenvolumen und die gesamte Oberfläche die stärksten Prädiktoren für die Speicherkapazität sind, während der Einfluss der Heteroatom-Konzentration (atomarer Sauerstoff, Stickstoff und Wasserstoff) auf die Speicherleistung weiter untersucht werden muss. Diese Erkenntnisse liefern eine Grundlage für die Optimierung von Aktivkohlen für Wasserstoffspeicheranwendungen.

Im zweiten Teil wird in-situ Neutronenstreuung eingesetzt, um die räumliche Verteilung von Wasserstoff in nanoporösen Kohlenstoffen direkt zu untersuchen. Messungen mittels Kleinwinkel-Neutronenstreuung (SANS) bei kryogenen Temperaturen zeigen eine Abhängigkeit der Wasserstoffdichte von der Porengröße. Mit Hilfe eines hierarchischen

Kontrastmodells konnte die Dichteentwicklung in verschiedenen Porenklassen berechnet werden, und es zeigt sich, dass die Anreicherung von Gasmolekülen in Ultramikroporen (< 0,7 nm) zu extremer Verdichtung führt, welcher jener von festem Wasserstoff entspricht, oder diese gar übersteigt. Die Ergebnisse unterstreichen die Bedeutung der Porengröße auf die Wasserstoffadsorption und liefern experimentelle Erkenntnisse für die weitere Entwicklung der nächsten Generation von Speichermaterialien.

Der dritte Teil kombiniert atomistische Simulationen mit experimentellen Neutronenstreuexperimenten. Molekulare Simulationen in realistischen atomistischen Modellen nanoporöser Kohlenstoffe zeigen bevorzugte Adsorption an hochdefekte Regionen. Der Vergleich zwischen simulierten und experimentellen Streudaten zeigt, dass Deuterium (D_2) den erwarteten Adsorptionstrends folgt, während Wasserstoff (H_2) mögliche Clusterbildung aufweist, was vermutlich auf spezifische Spin-Isomer-Interaktionen zurückzuführen ist, die in den Interaktionspotenzialen der Simulation nicht berücksichtigt wurden. Diese Ergebnisse verdeutlichen die Komplexität der Wasserstoffadsorption in nanoporösen Kohlenstoffen und zeigen die Notwendigkeit verfeinerter atomistischer Modelle, die Oberflächenchemie und Spinisomer-Effekte berücksichtigen.

Zusammenfassend erweitert diese Dissertation das Verständnis der Wasserstoffadsorption in nanoporösen Kohlenstoffen und zeigt das Potenzial biobasierter Materialien für nachhaltige Wasserstoffspeicher. Die Kombination aus experimentellen Methoden und atomistischer Modellierungen liefert einen umfassenden Einblick auf den Einfluss von Porengröße, Oberfläche und chemischer Zusammensetzung auf die Wasserstoffaufnahme. Die gewonnenen Erkenntnisse tragen zur Weiterentwicklung zukünftiger Wasserstoffspeichersysteme bei und verbinden fundamentalen Adsorptionsmechanismen und praktischen Anwendungen.

Abbreviations

AC	activated carbon
ACC	Activated carbon cloth
BET	Brunauer-Emmett-Teller
CNT	Carbon nanotube
DAB	Debye-Anderson-Brumberger
DoC	Degree of Confinement
DoE	Department of Energy
fcc	Face centered cubic
FCEV	Fuell Cell Electric Vehicle
FWHM	full width at half maximum
GCMC	Grand Canonical Monte Carlo
GSA	gas (ad)sorption analysis
hcp	Hexagonally closed pack
ILL	Institut Laue-Langevin
INS	Inelastic neutron scattering
IUPAC	International Union of Pure and Applied Chemistry
LJ	Lennard-Jones
LOHC	Liquid organic hydrogen carriers
MD	Molecular dynamics
MOFs	metal organic frameworks
NLDFT	Non-local Density Functional Theory
NPC	Nanoporous carbon
NZ	Net Zero Emission
OP	Orange peels
PSD	pore size distribution

PV	photovoltaic
QENS	Quasi-elastic neutron scattering
QSDFT	Quenched Solid Density Functional Theory
RDF	Radial distribution function
RT	Room temperature
SANS	Small-angle neutron scattering
SAXS	Small-angle X-ray scattering
SLD	Scattering length density
SPV	Specific pore volume
SSA	Specific surface area
TPV	total pore volume
UTL	Used tea leaves
vdW	Van der Waals
WAXS	wide angle X-ray scattering
XRD	X-ray diffraction
ZPE	Zero-point energy

Table of content

1 Introduction

"I believe that water will one day be employed as fuel, that hydrogen and oxygen, which constitute it, used singly or together, will furnish an inexhaustible source of heat and light" The Mysterious Island, Jules Verne, 1875

As the world seeks alternatives to fossil fuels, hydrogen has emerged as a compelling energy carrier with the potential to drive a sustainable energy transition. Unlike conventional hydrocarbons, hydrogen releases only water when used in a fuel cell, making it an attractive option for reducing carbon emissions in transportation and industry [1]. However, despite its promise, one of the most pressing challenges in realizing a hydrogen-based economy is storage. Hydrogen, in its molecular state, has an extremely low density, requiring innovative approaches to achieve practical and efficient storage solutions.

Governments and industries worldwide have recognized this challenge, prompting significant investments in hydrogen research and infrastructure. The European Union, for example, has outlined ambitious hydrogen strategies aiming to scale up production to 10 million tons of renewable hydrogen annually by 2030, with a long-term goal of achieving hydrogen-based climate neutrality by 2050 [2]. Globally, hydrogen demand reached 97 million tons in 2023, a 2.5% increase from the previous year, and is projected to surpass 150 million tons by 2030 as more sectors transition to hydrogen-based energy solutions. However, producing hydrogen at a competitive cost remains a key barrier to widespread adoption. In the Net Zero Emissions by 2050 (NZE) Scenario, hydrogen production costs could fall to around or below USD 2/kg H_2 by 2030 in regions with abundant renewable resources, such as Argentinian and Chilean Patagonia, and certain parts of central China (see Figure 1.1) [1]. Achieving these cost reductions requires significant expansion of renewable energy capacity, particularly through the coupling of solar and wind parks with electrolyzers. Large-scale hydrogen production from hybrid solar photovoltaic (PV) and onshore wind, as well as offshore wind farms, is expected to play a crucial role in providing a stable and low-cost supply of hydrogen. Once produced, hydrogen must be stored efficiently to ensure a continuous energy supply.

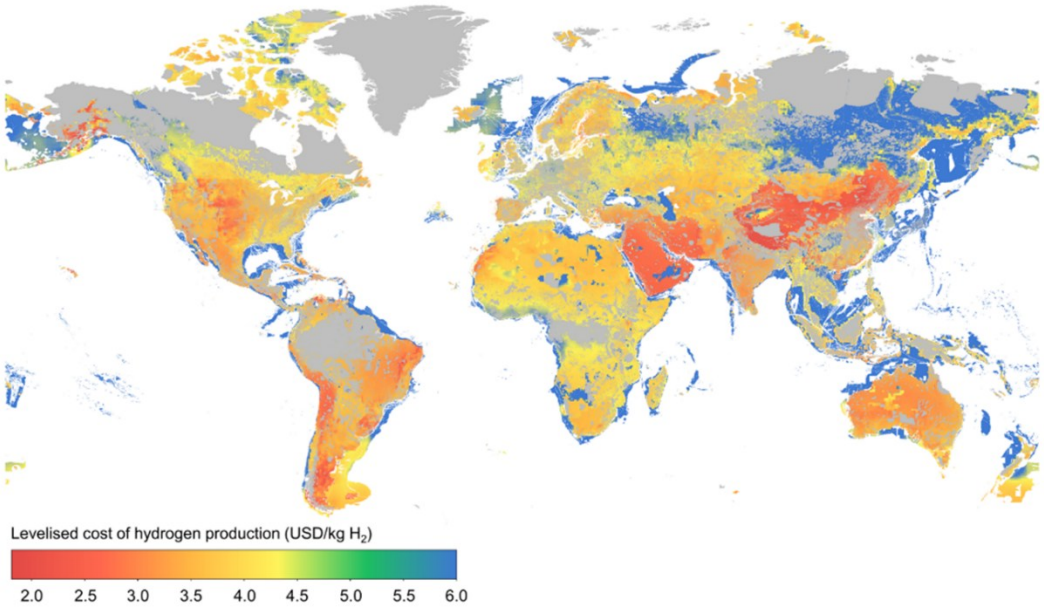

Figure 1.1: Hydrogen production cost from hybrid solar PV and onshore wind, and from offshore wind in the Net Zero Emissions by 2050 Scenario, projected for the year 2030. Reprinted from Ref. [1] published under creative common license CC BY 4.0.

Large-scale hydrogen storage will primarily rely on underground salt caverns, depleted gas fields, and other geological formations that can accommodate vast quantities of hydrogen. These storage solutions will act as buffers, mitigating fluctuations in renewable energy generation and enabling hydrogen distribution to key demand sectors, including industry and transportation (the circular hydrogen economy is depicted in Figure 1.2). In mobility applications, fuel cell electric vehicles (FCEVs) are a promising alternative to conventional combustion engines, particularly in heavy-duty transport, aviation, and maritime shipping, where battery-electric solutions face challenges in energy density and range.

Among the various methods for onboard hydrogen storage, physisorption in nanoporous materials has gained increasing attention as a promising solution. By confining hydrogen within nanometer-sized pores, these materials can significantly increase the volumetric density without the need for extreme pressures. Hydrogen physisorption at cryogenic temperatures is governed by weak van der Waals interactions between hydrogen molecules and the surface of the storage material. Thus, activated carbons, which possess high surface areas and large pore volumes, are well-suited for this purpose. A key advantage of nanoporous

carbons is their ease of synthesis from a wide variety of precursors, including biowaste materials [3–11].

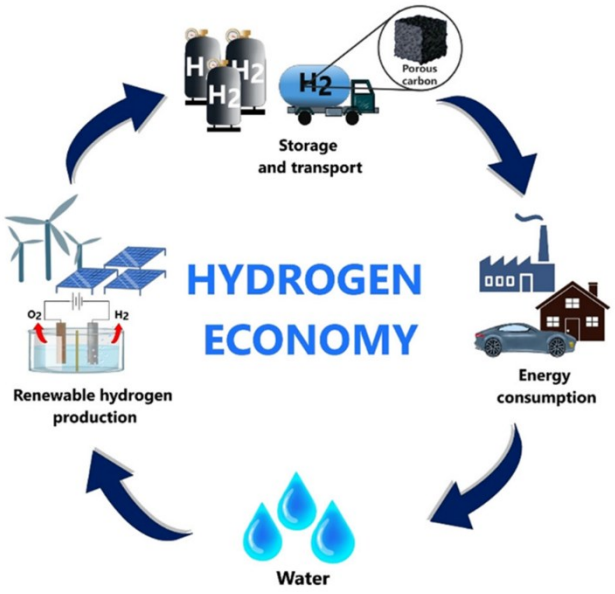

Figure 1.2: Schematic of the hydrogen circular economy: From water to hydrogen production utilizing renewable energy, to hydrogen storage and consumption. Reprinted from Ref. [12] with permission from Royal Society of Chemistry.

This thesis explores how bio-derived carbons, specifically activated carbons synthesized from orange peels and used tea leaves, can serve as sustainable and efficient hydrogen storage materials. Through a carefully designed experimental approach, the study systematically investigates the relationship between pore structure, chemical composition, and hydrogen storage performance. This work aims to demonstrate how chemical activation techniques influence pore size distribution and heteroatom content, ultimately determining hydrogen uptake capacity. The findings, obtained through gas adsorption measurements, small-angle X-ray scattering (SAXS), and other complementary characterization techniques, are expected to offer a comprehensive picture of how nanoporous carbons can be optimized for hydrogen storage.

While gas sorption measurements provide valuable insights into hydrogen storage capacity and adsorption behavior, they offer only indirect information about the spatial arrangement of hydrogen within the pores. To gain a more comprehensive understanding of hydrogen densification and distribution in confinement, a direct observation method is required. This

thesis employs neutron scattering as a powerful technique to directly probe the structural arrangement of hydrogen within nanopores. Due to the strong contrast between hydrogen and its heavier isotope deuterium (D_2) in neutron scattering, this method allows us to extract spatially resolved information on hydrogen adsorption with high precision.

Despite the increasing interest in porous carbons for hydrogen storage, neutron scattering studies in this context remain limited. In 2000, only four studies employed neutron scattering to investigate hydrogen adsorption, rising to 44 in 2024, a tenfold increase that still represents only a small fraction of the total research output, as depicted in Figure 1.3. Some previous studies have focused on the dynamics of hydrogen in confinement, yet none have systematically investigated the spatial arrangement of hydrogen in nanopore confinement at low pressures (< 1 bar) and supercritical conditions.

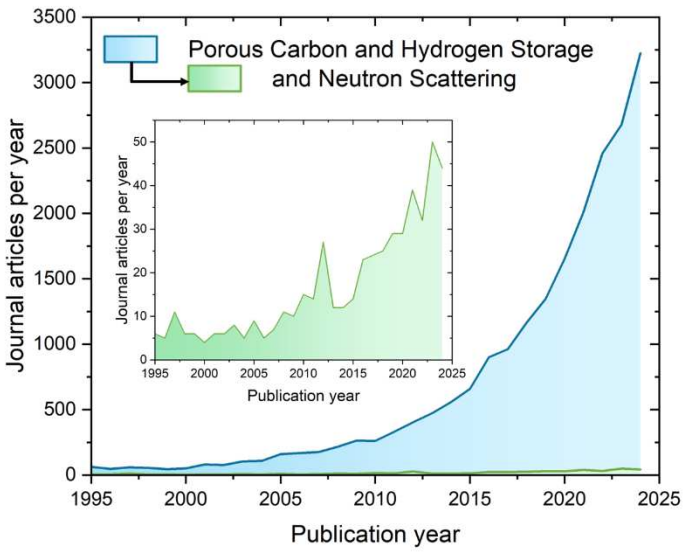

Figure 1.3: Number of journal articles per year published from 1995-2024: studies including porous carbons and hydrogen storage (blue) and studies especially leveraging neutron scattering techniques in this respect. The data was sourced using Lens.org and the search terms as depicted in the figure legend.

To address this gap, this thesis aims at the development of advanced models for the analysis of small-angle neutron scattering (SANS) patterns, to better approach pore-size-dependent hydrogen densification in nanopore confinement. By leveraging experimental neutron

scattering data, such models are expected to offer new perspectives on how hydrogen molecules densify within nanopores.

The thesis further aims at incorporating for the first time atomistic simulations, using realistic nanoporous carbon structures to explore theoretical hydrogen adsorption behavior. By comparing simulated results with experimental neutron scattering data, this approach is expected to provide an in-depth view of confinement effects on hydrogen densification at the molecular level. The synergy between experimental observation and computational modeling will thus strengthen our understanding of how nanoconfinement impacts hydrogen adsorption.

Thus, this thesis presents a comprehensive investigation into hydrogen adsorption in nanoporous carbons, covering three key areas: (i) the synthesis and characterization of bio-derived activated carbons and influences of structural characteristics and chemical composition on the hydrogen storage performance, (ii) the direct observation of hydrogen densification via neutron scattering, and (iii) the comparison of experimental findings with atomistic models to gain further insight into the confinement effects on hydrogen adsorption. While several open questions remain, this research contributes to a better fundamental understanding of supercritical hydrogen adsorption, helping to guide future developments of high-performance hydrogen storage materials for a sustainable energy economy.

2 Fundamentals

In the following chapter the basis to understand the experiments performed within the framework of this thesis and how to interpret the complex interplay of hydrogen adsorption in carbon materials considering gas sorption analysis and neutron scattering will be discussed. The first part introduces the terminology of porous materials, their characterization using gas sorption analysis and the respective pore characteristics. The second part introduces the different forms of carbon and the synthesis of nanoporous carbons and their characteristics. Further, the hydrogen molecule, its properties and technological aspects of H_2 storage are discussed. A general introduction to different neutron scattering techniques will be given and the insights in respect to the adsorption of hydrogen within nanoporous carbons found in literature are discussed.

2.1 Characterization of nanoporous carbons

A porous medium refers to a solid material that contains voids or channels (pores) on its surface, where the depth of these pores exceeds their width. Several physical properties of the material, including density, thermal conductivity, and mechanical strength, are influenced by its pore structure. Porosity (φ) refers to the volume fraction of the material that is made up of pore spaces and is defined as the ratio of the total pore volume (TPV) to the apparent volume (V) of the material. In contrast, macroscopic roughness describes the external non-porous surface of the material. The total specific surface area (SSA) is a measure of the accessible surface area per unit mass of the material, expressed in m^2/g, and includes both external and internal pore surface areas. According to IUPAC [13], pores can be classified based on their size, shape, and interaction with external fluids. In terms of size, there are three main categories: (a) micropores, with widths less than 2 nm, (b) mesopores, with widths ranging from 2 to 50 nm, and (c) macropores, which have widths greater than 50 nm. Micropores can be further divided into super-micropores (0.7 to 2 nm) and ultra-micropores (less than 0.7 nm). Pores with widths smaller than 100 nm are generally referred to as nanopores.

Pores can also vary in shape, including cylindrical (as shown in Figure 2.1 (c) and (f)), ink-bottle shaped (Figure 2.1 (b)), funnel-shaped (Figure 2.1 (d)), or slit-shaped. Pore size is typically measured as the distance between two opposite walls, which is referred to as the width for slit-shaped pores and the diameter for cylindrical pores. The external non-porous surface is illustrated in Figure 2.1 (g). Pores may also be classified based on their accessibility to external fluids, with some being closed (Figure 2.1 (a)) and others open (Figure 2.1 (b-f)). Characterization techniques that use fluids, such as nitrogen adsorption at 77 K, can only assess the open porosity of a material, not the closed porosity. Other complementary techniques, such as small-angle X-ray scattering, can help to identify the presence of closed porosity, as will be discussed in section 4.3.

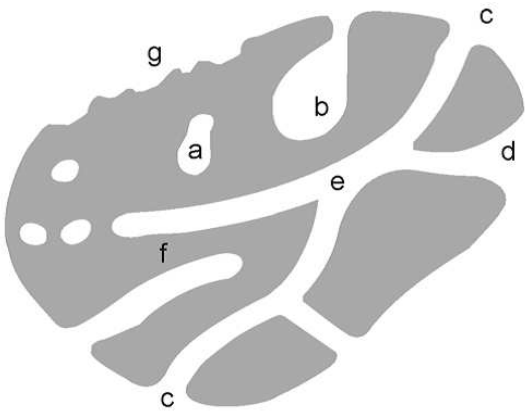

Figure 2.1: Schematic representation of different pore geometries of a porous solid. (a) closed pore, (b) ink-bottle shape, (c) open cylindrical, (d) funnel-shaped, (e) connection point of different pores to the external surface, (f) closed end cylindrical and (g) external rough surface.

2.1.1 Interaction of gases with porous materials

According to the International Union of Pure and Applied Chemistry (IUPAC) [13], adsorption refers to the accumulation of one or more substances on an interfacial layer. In a more specific sense, adsorption occurs when molecules are drawn towards or accumulate near the surface of a solid material, resulting in an increase in the density of the fluid near that surface. The reverse process, where molecules are removed from the solid surface and the gas density decreases, is known as desorption. The substance that is adsorbed is called the adsorbate, the material that attracts the adsorbate is the adsorbent, and the free gas that can be adsorbed

is termed the adsorptive. The term sorption can be used to describe either adsorption on a surface or absorption into the internal structure of a material.

There are two main types of adsorption: (a) physical adsorption or physisorption, which involves weak Van der Waals interactions between the gas molecules and the solid surface, and (b) chemical adsorption or chemisorption, which involves the formation of chemical bonds, as shown in Figure 2.2. Physisorption typically occurs in porous materials, where gas molecules weakly adhere to the external surface and accumulate in pores. In contrast, chemisorption involves stronger interactions, often seen in materials where the gas molecules dissociate and form bonds with the solid surface.

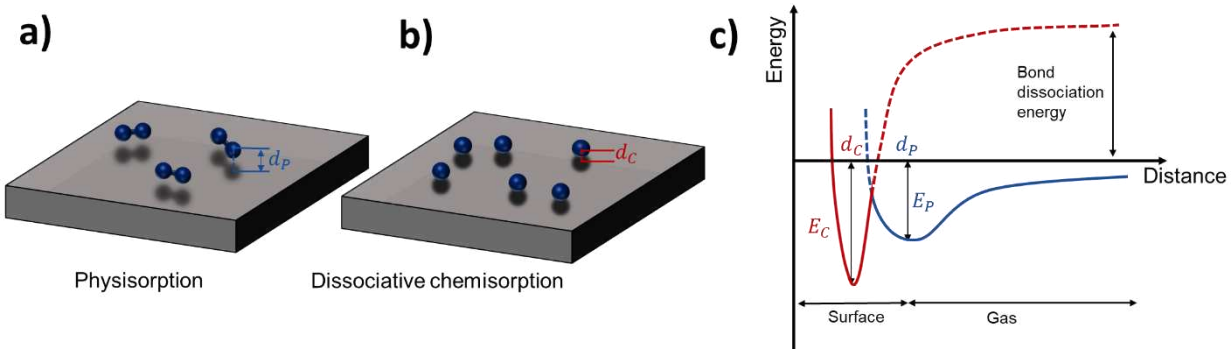

Figure 2.2: schematic representation of: a) physisorption of molecules on a surface and b) dissociative chemisorption on a surface. c) Energy curves for a physiosorbed and dissociative chemisorbed molecule in distance d from a surface, respectively.

From a thermodynamic perspective, adsorption is an exothermic process involving an interaction potential between the adsorbate and adsorbent, whereas desorption is endothermic. The heat of adsorption, or enthalpy, represents the strength of interaction between the gas molecules and the solid surface. Physisorption is enhanced at low temperatures (< 100 K) due to weaker intermolecular interactions and shows an adsorption enthalpy of 1-10 kJ/mol, while chemisorption happens at higher temperatures, exhibiting stronger interactions and an enthalpy of 50-100 kJ/mol [14]. The ideal interaction energy for effective gas storage at room temperature falls between these two ranges (10-50 kJ/mol), balancing the ease of reversibility and storage capacity [14].

2.1.2 Isotherm shapes and gas sorption analysis

Physisorption below the critical point of a gas occurs in distinct stages as pressure increases, with adsorption behavior varying depending on pore size, as illustrated in Figure 2.3. At very low pressures (~10^{-6} mbar, typical for gas sorption experiments), micropores (pore widths <2 nm) fill spontaneously with gas molecules, a process known as micropore filling. This differs from adsorption in wider pores, where molecules first form a dense monolayer on the internal surfaces of meso- and macropores, as well as on the external surface (monolayer adsorption). As pressure increases further, interactions between adsorbed molecules become more significant, leading to the formation of multiple layers of adsorbate (multilayer adsorption). In mesopores, at pressures below the bulk condensation point ($P/P_o < 1$), gas molecules can undergo a gas-liquid phase transition, filling the pores in a liquid-like state, a process known as capillary condensation

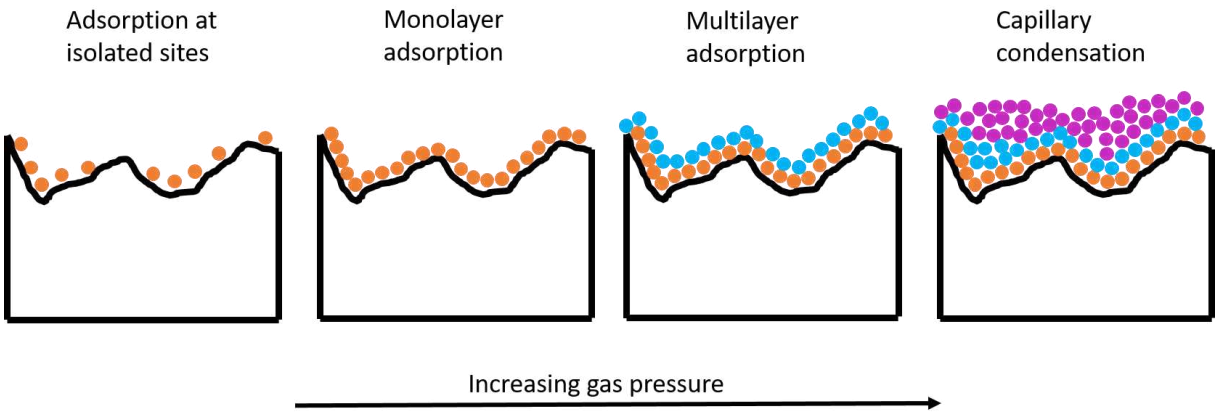

Figure 2.3: Stages of physisorption in different pore structures: At very low pressures, gas molecules spontaneously fill micropores. With increasing pressure, monolayer adsorption occurs on meso- and macropore surfaces (orange dots), followed by multilayer adsorption (blue dots). At higher pressures, mesopores undergo capillary condensation, forming a liquid-like phase (purple dots). Reprinted from Ref. [15]

According to IUPAC [13], adsorption and desorption isotherms can be divided into six primary categories (I-VI), as illustrated in Figure 2.4. These types of curves offer valuable insights into the adsorption mechanisms and the porosity characteristics of the material. The most frequently encountered isotherms are Type I, II, and IV, whereas Type III, V, and VI are seldomly observed. Type I isotherms, also known as Langmuir isotherms, are reversible and typical of microporous materials (pore widths < 2 nm) with minimal external surface area. The

adsorption rapidly increases at low relative pressures, indicating a micropore filling mechanism due to the enhanced gas-solid interactions in narrow micropores (i.e., pores with molecular-scale dimensions). As relative pressure rises, the isotherm reaches a saturation point (plateau), reflecting the amount of gas adsorbed in relation to the accessible micropore volume rather than the internal surface area. Type I isotherms can be further divided into Type I(a), representing materials with very narrow micropores (< 1 nm), and Type I(b), associated with materials that have a broader pore size distribution, encompassing both micropores and small mesopores (pore widths < 2.5 nm).

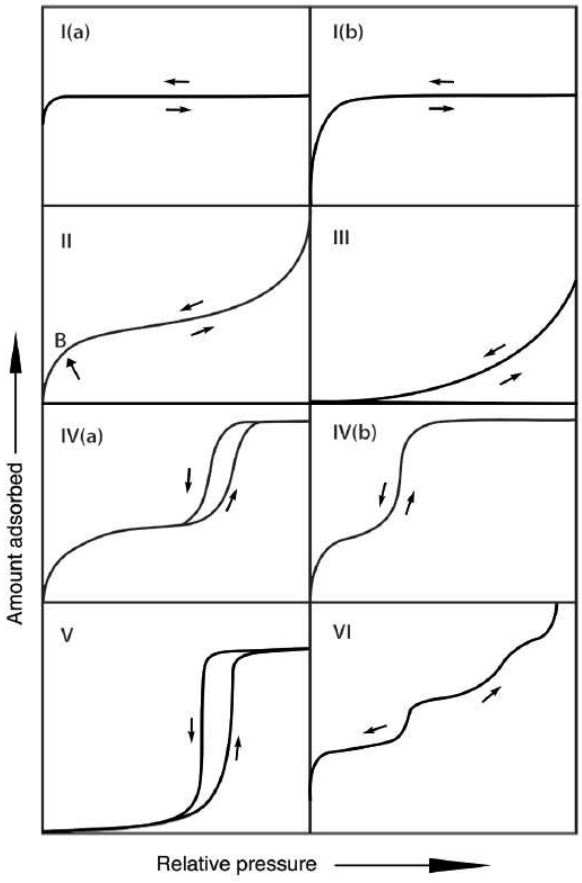

Figure 2.4: Classification of physisorption isotherms I – VI according to IUPAC. Reprinted from Ref. [13] and with permission from International Union of Pure and Applied Chemistry.

Type II isotherms are reversible and typically represent non-porous or macroporous materials. The isotherm shape results from unimpeded monolayer to multilayer adsorption at high relative pressures due to macropores (> 50 nm) and/or external surface area. The adsorption point B, shown in Figure 2.4 II, marks the completion of monolayer coverage and the start of multilayer formation.

Type IV isotherms are characteristic of mesoporous materials (pore widths between 2-50 nm). The initial part of the adsorption curve mirrors that of Type II, corresponding to monolayer and multilayer adsorption, but at higher relative pressures, pore condensation occurs; gas condenses in the pores in a liquid-like state at $P/P_0 < 1$. Type IV isotherms can be subdivided into Type IV(a), which features a hysteresis loop due to capillary condensation in pores exceeding a critical width (e.g., for N_2 adsorption at 77 K, hysteresis may occur in cylindrical pores wider than 4 nm), and reversible Type IV(b), representing materials with smaller mesopores.

Figure 2.4 illustrates the types of adsorption/desorption isotherms based on IUPAC classification [13]. Additionally, hysteresis loop types provide key insights into pore structure and shape in mesoporous materials. According to IUPAC [13], hysteresis loops are classified into five types (H1-H5), as seen in Figure 2.5. Type H1 loops are linked to materials with uniform mesopore sizes, such as ordered mesoporous carbons or silicas, and are characterized by steep and narrow loops indicating delayed condensation during adsorption. Type H2 loops appear in materials with complex pore structures, often due to pore-blocking effects. These can be divided into Type H2(a), common in silica gels, porous glasses, and other ordered mesoporous materials, and Type H2(b), seen in silica foams or hydrothermally treated ordered mesoporous silica.

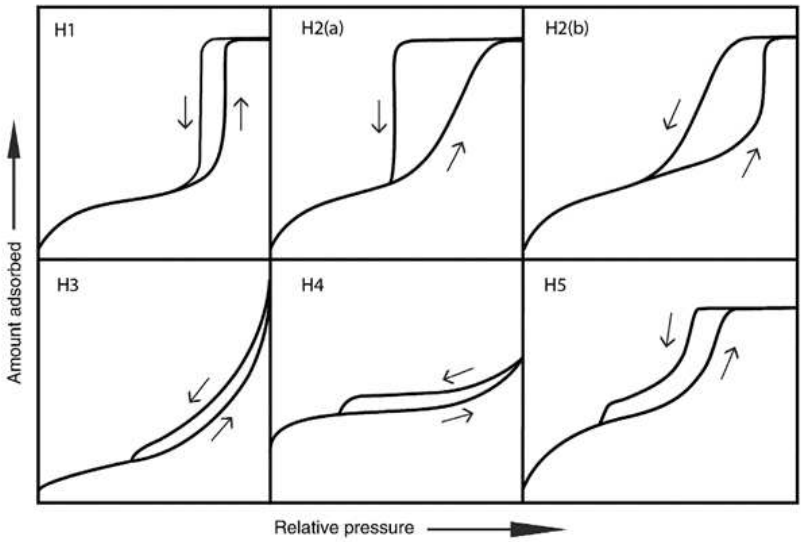

Figure 2.5: Types of hysteresis loops based on the IUPAC classification. Reprinted from Ref. [13] and with permission from International Union of Pure and Applied Chemistry.

Type H3 loops correspond to materials with non-rigid plate-like particles (aggregates) and/or macroporous networks that are not fully filled with condensate. The characteristic step at the desorption curve's closure is attributed to cavitation-induced evaporation, where gas bubbles form spontaneously in the condensed fluid within the mesopores [16]. As the liquid nitrogen evaporates, the bulk of the mesopores empties while their necks remain filled. Type H4 loops occur in materials containing both micropores and mesopores, such as zeolites or carbon materials with combined micro- and mesopores, where enhanced adsorption at low pressures is due to micropore filling. Lastly, the rare Type H5 loop is associated with materials featuring both open and partially blocked mesopores.

2.1.3 Hydrogen sorption measurements

The quantity measured by a manometric gas sorption apparatus, which measures the pressure difference before and after dosing a certain gas volume, delivers the Gibbs surface excess amount. The total gas amount n in the system can be divided into the adsorbed amount n_a and the amount remaining in the gas phase n_g, as described by equation (2.1).

$$n = n_a + n_g = n_a + \rho_g \cdot V_g, \tag{2.1}$$

Here ρ_g is the bulk gas density and V_g is the volume occupied by the gas phase. Gibbs (1887) introduced the concept of the surface excess amount n_σ to represent the deviation from the bulk gas phase behavior due to adsorption. The Gibbs dividing surface is an imaginary surface parallel to the adsorbent that separates the adsorbed and bulk phases, defining a reference volume $V_{g,0}$ where the gas density matches the bulk value ρ_g. The surface excess $n_\sigma = n - \rho_g \cdot V_{g,0}$ captures the adsorption's contribution relative to the bulk gas phase. The relationship between excess and absolute amounts is critical in adsorption studies. The absolute adsorbed amount n_a accounts for the total adsorption, including the excess n_σ and the gas-like contribution within the volume V_a, leading to $n_a = n - \rho_g \cdot V_a$.

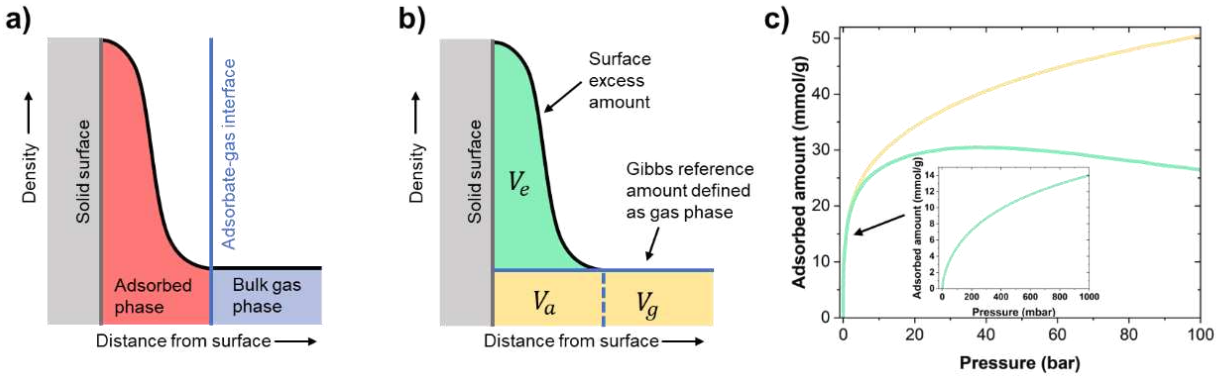

Figure 2.6: Representation of the Gibbs surface excess amount: a) the adsorbed layer and the gas phase are equal at am imaginary surface parallel to the adsorbent surface (blue line), b) the Gibbs excess surface corresponds to the adsorbed molecules in addition to the number of molecules that contribute to gas density in absence of any interaction with the absorbent and c) difference between the measured surface excess amount and the calculated absolute adsorbed amount. The inset shows a low-pressure adsorption isotherm up to 1 bar. Adapted from Ref. [17]

For low bulk gas densities ($\rho_g \ll 1$), the excess and absolute amounts become approximately equal (see Figure 2.6 (c)). However, at higher pressures, the difference between these quantities becomes significant due to the contribution of $\rho_g \cdot V_a$. The total adsorption n_{tot} can also be expressed as $n_{tot} = n_\sigma \cdot \left(1 + \frac{\rho_g}{\rho_{liq}}\right)$, assuming that the density of the adsorbed phase equals the liquid density (see Figure 2.6 (c)). As H_2 is in a supercritical state at 77 K, the sorption mechanisms proposed in section 2.1.1 for a fluid at its boiling point cannot be directly applied to explain the isotherm shape at certain pressure steps. Due to strong overlap of interaction potentials of opposing pore walls, H_2 will first accumulate in ultramicropores and with increasing the pressure densify within larger pores, yet never condense to a liquid phase.

2.1.4 Specific surface area – multi-point BET method

The experimentally obtained isotherms provide valuable information for calculating various pore structure properties of the material. One of the most commonly used methods for determining the specific surface area (SSA) is the BET method, developed by Brunauer, Emmett, and Teller [18,19]. This method is based on several assumptions about the adsorption process: 1) adsorption occurs on a homogeneous surface, 2) the heat of adsorption applies to the first layer, while the heat of condensation applies to the subsequent layers, 3) interactions between molecules in different layers are ignored, 4) the topmost layer is in equilibrium with the gas phase, and 5) the number of layers becomes infinite at the saturation pressure. The linear form of the BET equation is as follows:

$$\frac{1}{W \cdot \left[\left(\frac{P_0}{P}\right) - 1\right]} = \frac{1}{W_m \cdot C} + \frac{(C-1)}{W_m \cdot C} \cdot \left(\frac{P}{P_0}\right) \tag{2.2}$$

In this equation, W represents the amount of adsorbed gas at relative pressure P/P_0, W_m is the amount of adsorbate forming a monolayer, and C is a constant that accounts for adsorbent-adsorbate interactions in the first layer. By plotting the left-hand side of equation (2.2) against the relative pressure (within the range of $0.05 < P/P_o < 0.35$ for meso- and macroporous materials, and $P/P_o < 0.01$ for microporous materials), one can obtain the slope

(s) and intercept (i) from linear fitting. These values can then be used to determine W_m and calculate the BET surface area (S_{BET}) using the following equation:

$$S_{BET} = \frac{N_A \cdot A_{CS}}{M \cdot W} \cdot \frac{1}{s+i} = \frac{N_A \cdot A_{CS} \cdot W_m}{M \cdot W} \tag{2.3}$$

Here, N_A is Avogadro's number, A_{CS} is the cross-sectional area of the adsorbate molecule, and M is the molecular weight.

2.1.5 Total pore volume – single-point Gurvich rule

The total pore volume can be estimated using the single-point Gurvich rule [19] applied to the adsorption isotherm. This method relies on the volume of N_2 adsorbed at a relative pressure near the saturation pressure of N_2 ($P/P_o \approx 0.99$), assuming the pores are completely filled with liquid nitrogen. The final adsorption point, where adsorption ceases and desorption begins, is selected for this calculation. The adsorbed nitrogen volume (V_{ads}) is converted into the corresponding liquid nitrogen volume (V_{liq}) using the equation:

Here, P_a is the ambient pressure, V_m is the molar volume of the liquid adsorbate (34.7

$$V_{liq} = \frac{P_a \cdot V_{ads} \cdot V_m}{RT} \tag{2.4}$$

cm^3/mol for N_2), R is the universal gas constant (8.314 J mol^{-1} K^{-1}), and T is the ambient temperature. If the material lacks macropores or an external surface, the adsorption isotherm levels off at high relative pressures, allowing the total SPV to be determined. However, if macropores or an external surface are present, the isotherm continues to rise steeply at $P/P_o \approx 0.99$, preventing the extraction of the total SPV via the Gurvich rule.

2.1.6 Micropore specific surface area and volume

The specific surface area and micropore volume were determined using the Carbon Black statistical thickness equation applied to the total adsorption isotherm [19]. This approach is similar to the BET method but extends to higher relative pressures (P/P_o) and accounts for micropores smaller than 2 nm. The t-plot technique involves plotting the adsorbed N_2 volume (V) against the statistical thickness (t) of the adsorbed film. The statistical thickness is calculated by comparing the adsorption behavior to that of a non-porous solid, using the equation:

$$t[\text{Å}] = 0.88 \cdot (P/P_0)^2 + 6.45 \cdot (P/P_0) + 2.98 \tag{2.5}$$

The micropore volume (V_μ) is obtained by converting the t-plot intercept (i) into the corresponding liquid N_2 volume:

$$V_\mu = 0.001547 \cdot i \tag{2.6}$$

Similarly, the micropore-specific surface area (S_{mp}) is determined as a fraction of the total BET surface area, based on the slope (s) of the t-plot:

$$S_m = S_{BET} - 15.47 \cdot s \tag{2.7}$$

2.1.7 Pore size distribution

The BJH method (developed by Barrett, Joyner and Halenda) is typically applied to the desorption branch of the adsorption isotherm and relies on two key assumptions: (a) the pores have a cylindrical geometry and (b) they are filled with liquid N_2 near its vapor pressure ($P/P_o \approx 0.99$). A standard BJH pore size distribution (PSD) plot represents the first derivative of the cumulative pore volume with respect to pore diameter (dV/dD) as a function of pore diameter (D).

The BJH analysis is based on the Kelvin equation:

$$r_K = -\frac{2\gamma V_m}{RT} \ln\left(P/P_0\right) \tag{2.8}$$

where r_K is the Kelvin pore radius, γ is the surface tension of N_2 at its boiling point (8.85 ergs/cm² at 77K), V_m is the molar volume of liquid N_2 (34.7 cm³/mol), R is the universal gas constant (8.314 J mol^{-1} K^{-1}), T is the boiling point of N_2 (77K), and P/P_0 is the relative pressure. The actual pore radius (r_p) is determined by adding the thickness of the adsorbed layer (t) to the Kelvin pore radius (r_K):

$$r_p = r_K + t \tag{2.9}$$

Non-Local Density Functional Theory (NLDFT) and Quenched Solid Density Functional Theory (QSDFT) are advanced atomistic approaches used to characterize porous materials, particularly by analyzing adsorption isotherms and calculating pore size distributions (PSD) and assessing the surface area and the pore volume [20,21]. While both methods are based on Density Functional Theory, there are key differences in their approach. NLDFT assumes smooth, regular pore geometries and neglects surface roughness, making it ideal for mesoporous and macroporous materials with well-defined structures, such as cylindrical or slit-shaped pores. In contrast, QSDFT extends NLDFT by accounting for surface roughness and heterogeneity, which is crucial for materials with disordered or irregular structures. In QSDFT, the solid adsorbent (the porous material) is treated as a "quenched" system, meaning that it is considered fixed and non-responsive during the adsorption process. This makes QSDFT

particularly suited for microporous carbons, where the complex, often rough surfaces significantly affect adsorption behavior. Microporous carbons have small pore widths (<2 nm), where the interaction between gas molecules and the irregular pore walls plays a major role in adsorption. QSDFT provides a more accurate representation of these interactions, capturing the enhanced physisorption effects in micropores, and yielding a more realistic PSD and surface area analysis than NLDFT, which would otherwise oversimplify the surface effects.

QSDFT models the porous material as a collection of pores of varying sizes and shapes (e.g. slit-like, cylindrical or spherical). The adsorption isotherm is assumed to be the sum of contributions from all these pores (see equation (2.10)). Each pore size has its adsorption behavior, and QSDFT fits the measured isotherm data to theoretical models of adsorption in pores of different sizes. By fitting the experimental data to the generalized adsorption isotherm, QSDFT can generate a pore size distribution (PSD), which indicates the proportion of pores of various widths present in the material.

$$N\left(\frac{P}{P_0}\right) = \int_{W_{min}}^{W_{max}} N\left(\frac{P}{P_0}, W\right) f(W) dW \tag{2.10}$$

Here $N\left(\frac{P}{P_0}\right)$ represents the measured adsorption data, W is the pore width and $f(W)$ is the pore size distribution (PSD) function.

As outlined in section 2.2.2, nanoporous carbons mostly exhibit complex pore geometries and are far from the idealistic cases considered in the QSDFT approach. Thus, simulating the adsorption of different fluids, like N_2 or CO_2 within realistic atomistic models of nanoporous carbons adds a new level of complexity to the description of the pore space [22]. Vallejos-Burgos et. al. have used a plethora of different atomistic models, similar to the ones depicted in Figure 2.9, and simulated the N_2 adsorption isotherm using grand canonical Monte Carlo (GCMC) simulations. The resulting isotherms were collected in kernels, which were later fitted to experimental datasets using a non-negative least square algorithm. As depicted in Figure 2.7 (a-d), such fitting routine results in very good agreement between experiment and simulations. With this approach it is possible to generate a more realistic PSD as well as have direct visualization of the main contributing pore systems.

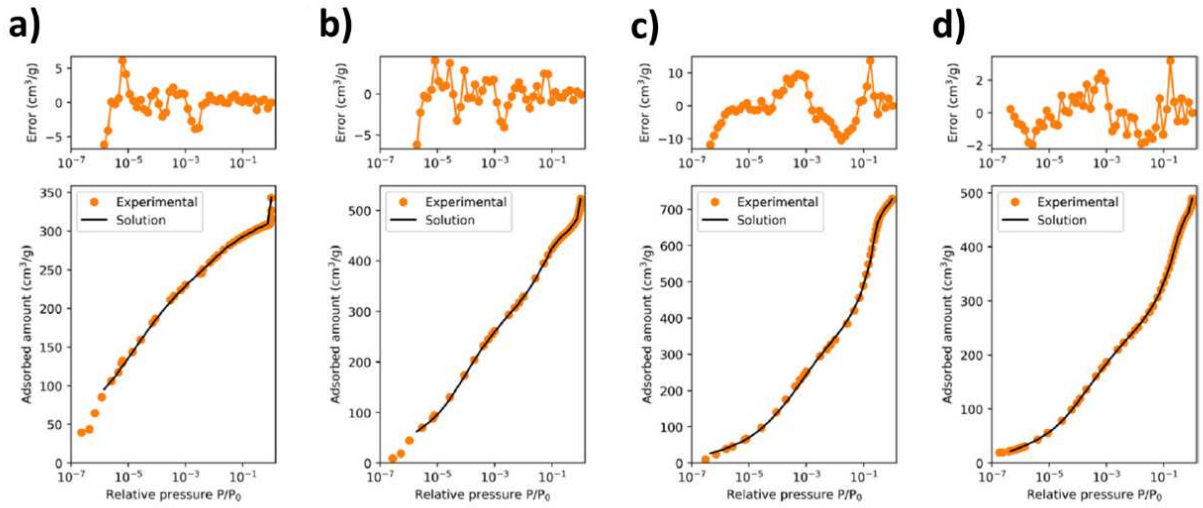

Figure 2.7: Experimental N_2 adsorption isotherms and the fit resulting from the 3D-VIS model: a) CDC-400, b) AC-YP50F, c) ACF-A20 and d) PG-600. Reprinted from Ref. [22] with permission from Elsevier.

2.2 Nanoporous carbon materials – synthesis and properties

Pores are found in various natural systems, like sponges, trees or human skin. The size of these pores is crucial to support certain functionalities, like water transport, ion exchange and mechanical movement. The pores within nanoporous materials range in sizes from 0.5-100 nm, thus from the distance of atoms within a solid (~ 0.3 nm), to the size of a DNA-molecule (2.5 nm) to the size of the SARS-COV-2 virus (50-140 nm). Like in biological systems, differently sized and shaped pores influence chemical and physical processes happening at surface of the pore. Thus, controlling the pore size and shape of materials is important to tailor certain functionalities, like gas storage capability, water diffusion or ion exchange rates. As diverse as the periodic table of elements is, as diverse is the zoo of nanoporous materials. They can be synthesized from biological precursors, metal alloys, various oxides and contain organic linkers, like in metal-organic-frameworks. The possibilities and complexity of such systems seems sheer endless, yet one element in particular has outstanding abilities to form a plethora of nanoporous materials: Carbon.

2.2.1 The carbon allotropes

Carbon- in the early 1800 the widespread use of coal to fuel our growing economy, heating our homes or move us to faraway places, has begun [23]. Ever since, carbon-based fossil fuels are associated all around the globe with wealth and prosperity. Just, now we seem to understand what impact, burning of carbon and thus emitting CO_2 into the atmosphere has on the global climate and health of people [24,25]. The wealth of western society may be displayed by some form of wearing a diamond-ring, a crystalline allotrope of carbon (see Figure 2.8 (f)), often unfortunately mined as a result of child labor and lethal conflicts [26]. Apart from its brightness, beauty value and social-economic impacts, diamonds are a valuable material used in many industrial applications, due its hardness and high thermal conductivity. When we think of the human body, its complexity and its basic building blocks, namely carbon and hydrogen, it isn´t surprising that carbon is found in various forms.

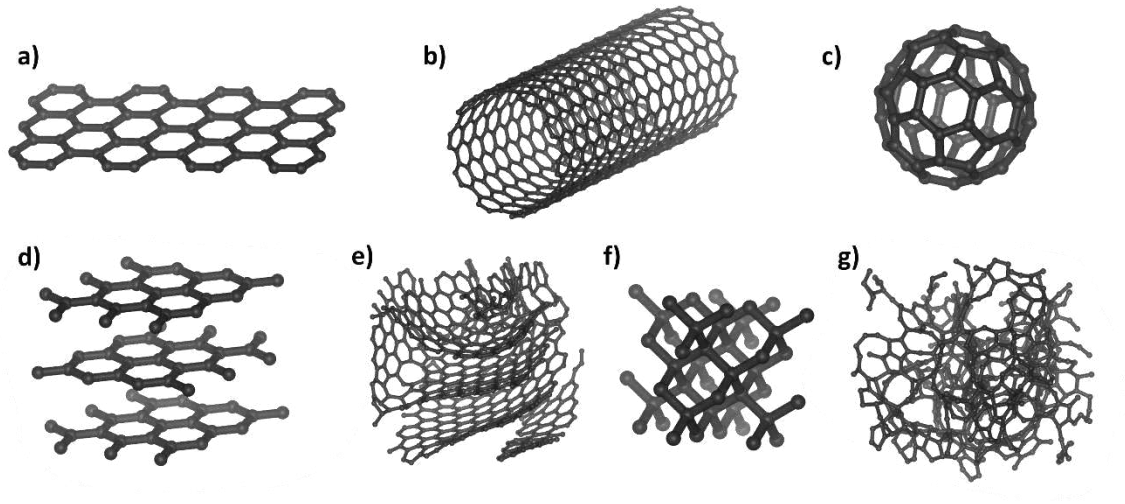

Figure 2.8: Different carbon allotropes and morphologies: sp^2-hybridization: a) graphene, b) carbon nanotube (CNT), fullerene (C_{60}), d) graphite and e) turbostratic carbon. sp^3-hybridization: f) diamond and g) amorphous carbon (shows sp^2- and sp^3-hybridization)

Another form widely known is graphite, which is used in everyday utensils and is crucial for electric steel making. The difference in structure between diamond and graphite (see Figure 2.8 (d and f) is found in the electron hybridization of the carbon atom. In graphite, the carbon atoms are sp^2-hybridzed, leaving a delocalized electron, which is responsible for the good electric conductivity, and a hexagonal arrangement of atoms, whereas in diamond the carbon atoms are sp^3-hybridzed. The layer structure of graphite, held together by weak van der Waals forces, lead to the question about stability of a single sheet of graphite, called graphene (see Figure 2.8). The story behind the "discovery" of graphene, the exfoliation method using sticky tape on graphite, is usually told in introductory lectures to carbon materials. While most children have unknowingly exfoliated graphite to graphene, while ripping sticky tape from pencil drawings, most wouldn't know what special properties graphene possesses. The description of the ballistic charge transport of delocalized electrons and the extraordinary charge carrier mobility, lead to a Nobel Prize in 2010 [27]. Long before graphene was first produced, the existence of tube- and ball shaped structures, called carbon nanotubes (CNT) and fullerenes, was known. The shape of those structures is quite more thermodynamically favorable compared to a single graphene sheet, thus it was for long suspected that graphene could not exists. CNT´s, based on their configuration, can possess a metallic or semiconducting property, thus opening many ideas for future electronics [28]. Fullerenes are symmetric

structures consisting of up to 540 carbon atoms and they were even found to form in young planetary nebula [29]. An interesting study, proving the wave-particle duality of matter, was performed by Arndt et. al. using a C60 fullerene (see Figure 2.8 (c)) in a double-slit experiment [30]. Carbon can also form in a non-regular manner and exhibit an amorphous structure of sp^3-hybridized atoms as shown in Figure 2.8 (g). Introducing Stone-Wales defects into the graphene lattice changes the connectivity of two sp^2-hybridized carbon atom, leading to a rotation by 90°, which can be achieved by exchanging two hexagons with a penta- and a heptagon. Such defects may cause bending of the graphene sheets, that may still exhibit of layering of graphene sheets, like in graphite, yet have a higher degree of disorder, which is known as turbostratic carbon. Such kind of structure, also seen in Figure 2.8 (e), exhibits nanopores and is likely to be found in activated carbon, which will be the subject in the following.

2.2.2 Nanoporous carbon

Nanoporous carbon are characterized by large surface areas, high pore volumes and different pore sizes, ranging from 0.5 – 50 nm. They can be synthesized by a plethora of different precursors, basically everything containing carbon. For example, carbides can be used, where the metal is dissolved to leave a porous carbon backbone. Any natural or synthetic polymer, may be facilitated as a precursor as well. For example biological materials like coconut shells, banana and orange peels, coffee waste or even washed ashore jellyfish have been used to synthesize nanoporous carbon [3–11,31,32]. The synthesis of nanoporous carbon from organic precursors typically includes a pyrolysis/calcination step, which breaks the polymer bonds at elevated temperatures and under inert gas atmosphere. During this process the carbon atoms rearrange and form a turbostratic like structure, in the best case containing no other heteroatoms, like hydrogen, oxygen and nitrogen. After the pyrolysis, an activation step at elevated temperature and with the presence of an activation agent is performed. The chosen parameters influence the resulting pore structure and atomistic structure of the nanoporous carbon [33,34]. The idea of the activation step is to provoke a chemical reaction of carbon with another chemical component like carbon dioxide (CO_2), water vapor (H_2O), zinc

chloride ($ZnCl_2$) or potassium hydroxide (KOH), leading to a net loss of carbon mass and increased porosity.

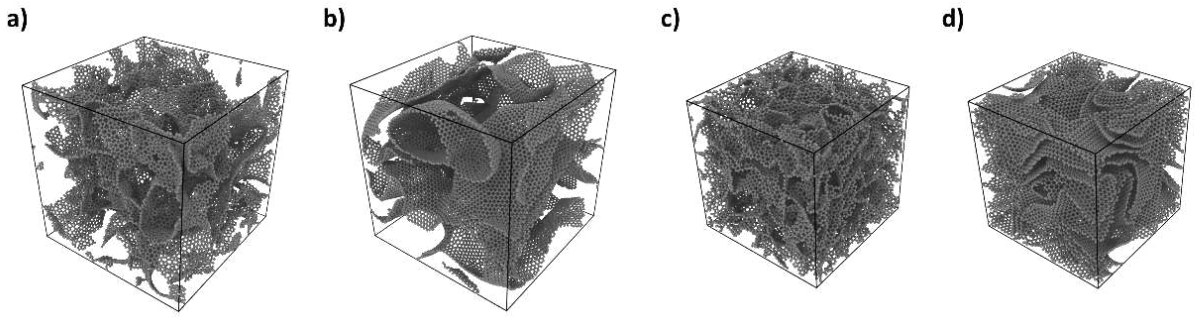

Figure 2.9: atomistic models of disordered carbon of different density generated using Molecular Dynamics simulations (MD) and different annealing temperatures: a) and b) 0.5 g/cm³ and c) and d) 1.0 g/cm³. Structures a) and c) and b) and d) were annealed at 2000 and 4000 K, respectively. Reproduced with data from Ref. [35].

For analyzing the pore structure of nanoporous carbons, gas adsorption methods are commonly employed, as discussed in section 2.1. These techniques often rely on idealized pore geometries, such as slit-shaped, cylindrical, or spherical pores, to calculate pore size distributions. However, the intricate and heterogeneous nature of nanoporous carbons may not be fully represented by these simplified models. The development of atomistic models capturing the complexity of nanoporous carbons on different length scales has made substantial progress throughout the years. Traditional models, such as slit-shaped or cylindrical pores, failed to accurately represent the disordered nature of real nanoporous carbons, leading to the adoption of more advanced computational techniques. The choice of interatomic potential, annealing temperature, and target density parameters plays a crucial role in shaping the resulting carbon structures. Certain potentials promote a higher degree of sp^3-hybridization, leading to amorphous structures, while others favor sp^2-hybridization, resulting in curved graphene sheets with defects. These models, shaped by density constraints during annealing, display diverse pore structures and atomic characteristics. Notably, the impact of annealing temperature is striking, even when targeting similar densities. Lower temperatures produce more fragmented surfaces with a higher concentration of local defects, whereas higher temperatures result in smoother structures with fewer defects. To generate realistic carbon models, various computational approaches have been employed, including Hybrid Reverse Monte Carlo simulations, which reconstruct carbon structures based on

experimental radial distribution functions, and Molecular Dynamics simulations, such as Quench Molecular Dynamics and Annealed Molecular Dynamics (AMD), which create amorphous carbon models from high-temperature liquid carbon precursors followed by controlled cooling. The AMD approach, combined with an extended Environment-Dependent Interaction Potential (EDIP) forcefield, has successfully yielded models exhibiting graphitization and layered defected graphene structures. The impact of annealing temperature, even when targeting similar densities, is strikingly evident, as illustrated in Figure 2.9 (a-d). Lower annealing temperatures produce more fragmented surfaces with a higher concentration of local defects (Figure 2.9 a and c), whereas higher temperatures result in smoother structures with fewer defects (Figure 2.9 (b and d)).

2.3 The hydrogen molecule

Hydrogen is the lightest, simplest and most abundant atom found in the universe. On earth, it is mostly found in chemical bonds with oxygen as H_2O. In its molecular form it is stable as a diatomic gas H_2 at room temperature (RT), with two protons tightly bound by strong covalent bonds of the two shared electrons. The heavier isotope deuterium (D_2) additionally accommodates a neutron within the atomic nucleus, which changes the molecular properties. The binding energy of H_2 is 4.746 eV and 4.747 eV of D_2, whereas the dissociation energies are 4.4775 and 4.5557 eV, respectively [36]. The critical point, the thermodynamic state where gas and liquid cannot be distinguished, is at 33.15 and 38.34 K for H_2 and D_2, respectively, whereas the boiling points are at 20.37 and 23.66 K. The density of the respective liquid phases is 0.07085 g/cm³ and 0.162 g/cm³. The triple point, where gas, liquid and a solid phase coexists, is at 13.96 and 18.72 K, for H_2 and D_2, respectively. The solid phase of H_2 exhibits a density of 0.086 g/cm³ and 0.1967 g/cm³ for D_2.

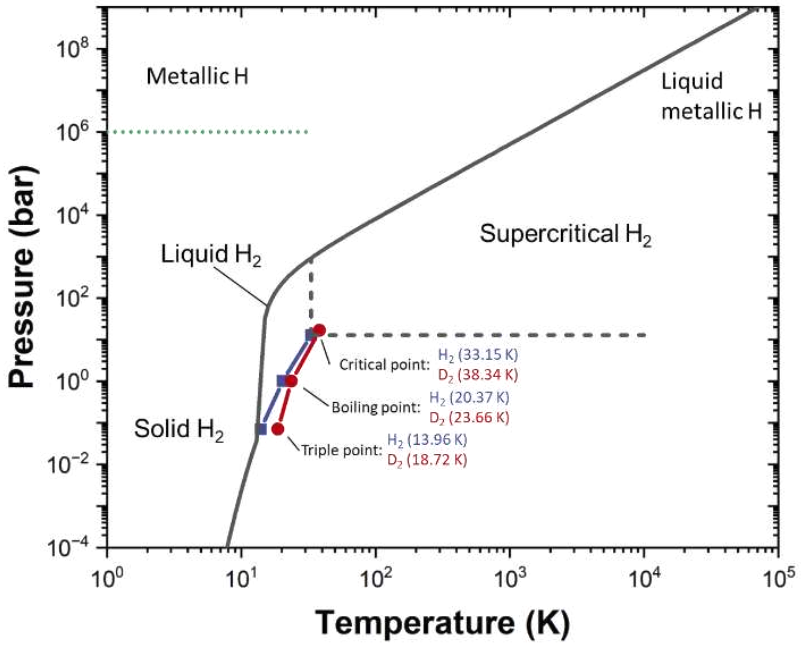

Figure 2.10: Pressure and temperature phase diagram of H_2 (blue) and D_2. (red): triple, boiling and critical points are indicated by squares and circles at the respective temperatures. The phase diagram was constructed using the REFPROP software and adapted from Ref. [17].

Hydrogen exists in two spin-isomeric forms: ortho, where the nuclear spins are aligned in a triplet state (parallel, ↑↑), and para, where the nuclear spins form a singlet state (anti-parallel, ↑↓). As a result of the symmetry of the wave function the ortho-state has even (J=0, 2, 4…) and the para-state odd rotational numbers (J=1, 3, 5…) [37,38]. Although spin-spin interactions are small, symmetry requirements impose constraints on the rotational states. For instance, para-H_2 and ortho-D_2 in the spherically symmetric J = 0 state experience no anisotropic interactions, whereas ortho-H_2 and para-D_2, in non-spherically symmetric J = 1 states, exhibit strong anisotropic interactions, which results in a quadrupole moment and thus to stronger physisorption interactions [36]. The energies of the rotational states are given by equation (2.11), where B_J is the rotational constant and J the rotational number. The rotational constant B_J can be calculated using equation (2.12), where h is the Planck´s constant, c the speed of light, the moment of inertia is given by $I_{HH} = \mu_r \cdot r_{HH}^2$, with μ_r being the reduced mass of the quantum rotor and r_{HH} being the proton-proton distance of 0.74 Å.

$$E_J = B_J \cdot J(J+1) \tag{2.11}$$

$$B_J = \frac{\hbar^2}{2I_{HH}e}\ [eV] \tag{2.12}$$

The theoretical value of the first rotational transition (J 1→0) from the ortho- to para-H_2 has an energy of 15.2 meV, whereas measured values of 14.7 meV where reported (see Figure 2.11 b). The para- to ortho-D_2 transitions has a theoretical energy of 7.6 meV and was measured at 7.4 meV.

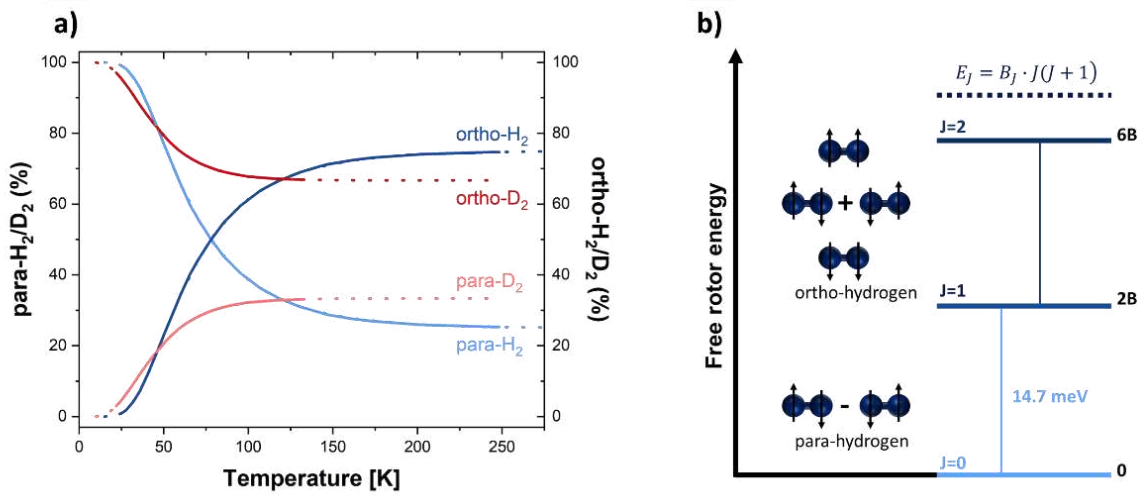

Figure 2.11: Para- and ortho-H_2 and D_2 compositions as a function of temperature, reconstructed with data from Ref [39]. b) Free rotor energy transition scheme, where the rotational translation from J=1→ 0 corresponds 14.6 meV. The transition from para- (J=0) to ortho- (J=1) spin states is observed, as a result of the symmetric wavefunction.

The boiling and melting points of hydrogen are only weakly affected by the ortho/para ratio. At room temperature, thermodynamic equilibrium hydrogen consists of 25% para and 75% ortho forms, known as "normal hydrogen." At 20.4 K, the para concentration reaches 99.8%, and at 0 K, it becomes entirely para. However, the conversion between these forms is slow, occurring at a rate of about 2% per hour in the solid state. Rapidly cooled and condensed hydrogen gas can take days to reach equilibrium [36]. Understanding the ortho/para composition and conversion is crucial for interpreting certain phenomena, especially at low pressures and temperatures. The ratio of para/ortho hydrogen is dependent on the temperature and was experimentally assets by Frauenfelder et. al., as shown in Figure 2.11 (a) [39] and can be theoretically calculated using equation (2.13).

$$\frac{N_{ortho}(T)}{N_{para}(T)} = \frac{3\sum_{J=1,3\ldots}(2J+1)\cdot\exp\left(\frac{-J(J+1)\Theta_r}{T}\right)}{1\sum_{J=0,2\ldots}(2J+1)\cdot\exp\left(\frac{-J(J+1)\Theta_r}{T}\right)} \; with\; \Theta_r = \frac{hcB_J}{k_b} \qquad (2.13)$$

The thermodynamic conversion of ortho- to para-states can be influenced by be the presences of paramagnetic metal centers and or hindered by strong confinement effects [36,38].

2.3.1 Methods of storing hydrogen – technical aspects

With the basic understanding of the H_2 molecule and nanoporous carbon materials developed in the previous chapters, the focus will shift on some technical aspects of H_2 storage. Generally, there are two methods of H_2 storage to be categorized [40]. The first one involves storing the gas in tank systems and increasing the mass density by means of compression, cooling or both combined. In onboard storage systems for light duty vehicles, like fuel cell operated cars, the compression of H_2 up to 200 bar is utilized [40,41]. For stationary storage solutions, a compression up to 700 bar is favored, as risks, regarding damages due to accidents are much less. The liquefication of H_2 (LH_2) at the respective boiling point at 20.3 K roughly requires an energy input of one third of the energy content contained in H_2 (e.g. 2.8 kWh/L or 10 MJ/L). In comparison to storing compressed H_2 at 700 bar, the energy density of LH_2 is 2.6 times higher [41,42]. The second category involves the interaction and storage of H_2 within another host materials, hence the term materials-based hydrogen storage. Based on the nature of interaction three sub groups were established, namely chemical storage involving chemical bonds of H to another species, metal hydrides, which incorporate H within a crystal lattice and physically adsorbed H_2 within a porous structure (see Figure 2.12). Those three materials groups offer a plethora of different processes and research questions, to find the optimal H_2 storage material for a certain application. In a broader economical aspect, all three methods have their pros and cons and it is up to industrial requirements and governmental regulations to decide which way to go [43]. For example, liquid-organic hydrogen carriers (LOHC), store hydrogen within a molecule which is liquid at ambient conditions, offering the possibility to transfer it within existing pipeline infrastructure [44]. Metal hydrides achieve a high storage capacity [45], yet heating is required to extract hydrogen from the structure, posing additional difficulties regarding utilization. Due to the fast kinetics of H_2 at ambient conditions and therefor weak interaction with a host material, physical adsorption only yields reasonable storage capacities at cryogenic temperatures, which in return requires additional cooling of a respective tank system [41,46].

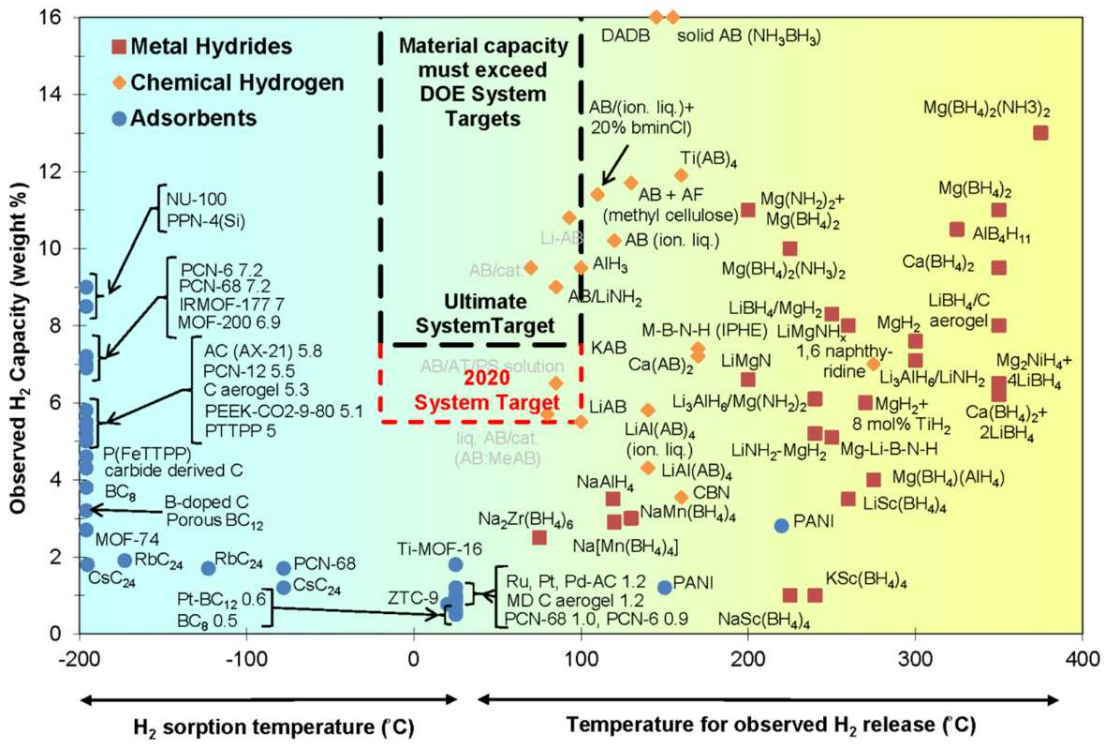

Figure 2.12: Observed H_2 storage capacities of different materials and their respective sorption or H_2 release temperature. The sorption materials operate at cryogenic temperatures (< 0 °C), whereas the metal hydrides and chemical H_2 storage materials accommodate H_2 at room temperature and release the H_2 at elevated temperatures [40].

For a materials-based onboard tank system the US Department of Energy (DoE) has specified certain H_2 storage goals for 2025 and proposed that an optimal storage material shall exceed an gravimetric H_2 uptake of e.g. 5.5 wt.% (e.g. 55 g H_2 per kg of tank system), whereas the ultimate goal is set to 6.5 wt.% [40]. Electric cars fueled by H_2 consume around 0.8 kg of H_2 per 100 km, thus given the DoE target, a practical range of 600 km can be achieved by a tank system of < 100 kg, which is much less compared to up to 700 kg of a batterie within an electric car and roughly double the weight of a full gasoline tank. Nevertheless, a transition from a fossil fuel-based economy and transportation towards a climate friendly one is inevitable. This in return requires sophisticated technical solutions and wise legislative decision, considering not only the benefits to certain group of people, but considering the broader social economic impact, regrading resources for the production/recycling of batteries and clean H_2 production [47–50].

2.3.2 Interaction of hydrogen with nanoporous carbons

Cryogenic H_2 storage based on physisorption of gas molecules within nanopore structures poses an environmentally friendly storage solution, given clean H_2 production and the use of activated carbon materials. It was established earlier that the interaction of gas molecules with the pore surface is governed by weak van der Waals forces, thus requiring large surface areas and pore volumes to accommodate large amounts of H_2. Carbon materials due to their easy and safe production and handling, high tunability of pore sizes and large surface areas up to 2500 m^2/g, have gained much interest in the field of H_2 storage [51,52]. An empirical relation of the surface area and the gravimetric H_2 uptake, known as the Chahine's rule, poses that for every 500 m^2/g increase in surface area of a porous material a storage increase of 1 wt.% can be achieved at 350 bar and 77 K [52,53]. Porous materials often exceed expected hydrogen storage capacities due to an additional crucial factor: pore size. While a correlation exists between surface area and hydrogen uptake, it is equally important to consider how surface area and pore volume together influence storage capacity. The size and shape of the pores play a key role in determining hydrogen interactions by affecting both the accessibility of adsorption sites and the strength of hydrogen binding [54,55]. Micropores are particularly effective, as their dimensions allow for overlapping potential fields from opposing pore walls, which enhances the enthalpy of adsorption and enables hydrogen to be stored at densities far exceeding its gaseous state—reaching up to 100 kg/m^3 [56,57]. Studies have shown that the optimal pore diameter for hydrogen uptake at 77 K and elevated pressures falls between 0.6–0.7 nm [58]. Pores smaller than this limit restrict hydrogen mobility, whereas larger pores weaken the interaction between hydrogen molecules and the pore walls, reducing adsorption efficiency. Extensive research has confirmed this trend, demonstrating that the highest hydrogen uptake occurs within a well-defined pore size distribution (PSD) below 1 nm [52]. Consequently, PSD is a critical parameter in the design of porous materials for hydrogen storage. Another key factor influencing hydrogen storage capacity is micropore volume, which quantifies the extent of microporosity in a material. It has been well established that higher micropore volumes correlate directly with increased hydrogen uptake, making the micropore volume optimization an essential aspect of developing efficient hydrogen storage materials.

As the pore size is decreasing and the hydrogen molecules become more confined, quantum effects must be considered as the wave-like nature of hydrogen molecules become significant. These quantum effects become particularly pronounced when the thermal de Broglie wavelength λ of the hydrogen isotopes becomes comparable to the pore dimensions, influencing their interaction with the pore walls. The thermal de Broglie wavelength is given by:

$$\lambda = \frac{\hbar}{\sqrt{mk_bT}} \tag{2.14}$$

where $\hbar$ is the reduced Planck's constant, m is the mass of the molecule, k_b is the Boltzmann constant, and T is the temperature. At 77 K, the thermal de Broglie wavelength of H_2 is 0.176 nm, while for D_2 it is 0.124 nm, highlighting the stronger quantum effects experienced by the lighter isotope. The interaction potential between gas molecules and solid surfaces is typically modeled using the Lennard-Jones (LJ) potential, which describes both repulsive and attractive interactions:

$$\phi(r_{ij}) = 4\varepsilon_{ij}\left[\left(\frac{\sigma_{ij}}{r_{ij}}\right)^{12} - \left(\frac{\sigma_{ij}}{r_{ij}}\right)^{6}\right] \tag{2.15}$$

where ε_{ij} is the depth of the potential well, and σ_{ij} is the collision diameter of the interacting species. However, at low temperatures, quantum effects modify the effective potential experienced by the molecule. This is accounted for by the Feynman-Hibbs (FH) effective potential, which adds a quantum correction term to the classical potential:

$$\phi_{FH}(r_{ij}) = \phi(r_{ij}) + \left(\frac{\hbar^2}{24m_r k_b T}\nabla^2\phi(r_{ij})\right) \tag{2.16}$$

here m_r is the reduced mass of the molecule. The FH effective potential represents an average over the classical potential by integrating the wave-packet representation of the quantum particle, effectively spreading the isotope's center as a Gaussian-like wave function with a distribution of $\lambda^2/12$. The applicability of the FH approximation is ensured when the reduced thermal de Broglie wavelength remains below the typical intermolecular separation given by

$\Lambda = \frac{h}{\sqrt{12 m k_b T \sigma^2}} \leq 0.5$. For H_2 at 77 K, Λ=0.47, confirming that the FH approximation is valid under these conditions. This correction is crucial for accurately describing quantum effects on adsorption potential landscapes and is further visualized in Figure 2.13 (a).

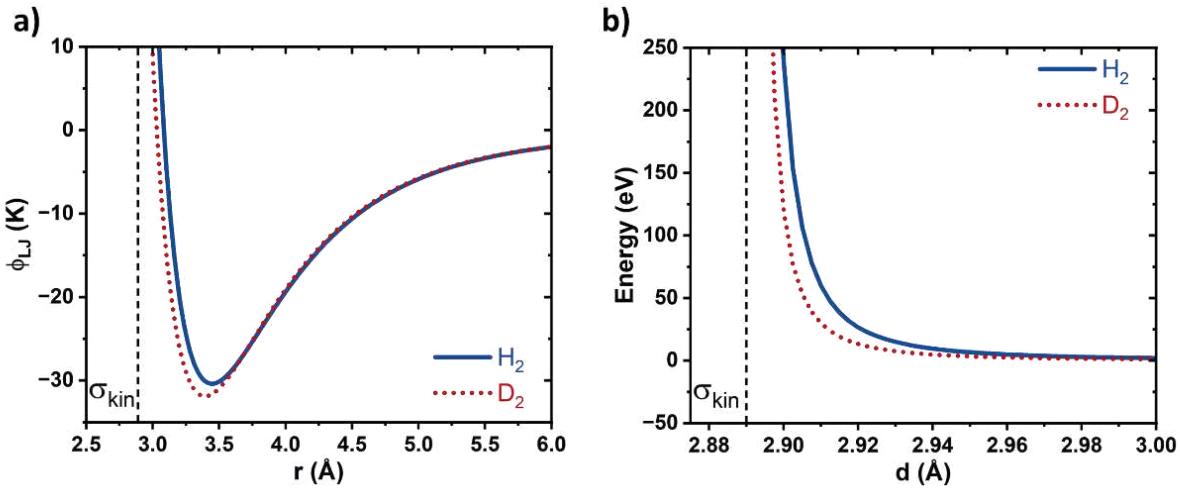

Figure 2.13: a) Lenard-Jones fluid-fluid interaction potential of H_2 (blue) and D_2 (red) at 77 K, considering the classical Feynman-Hibbs-quantum correction. The values for ε_{ij}, σ_{ij} and m_r are summarized in Table 6.7 b) ZPE of H_2 (blue) and D_2 (red) confined in a cylindrical pore with a square well potential, according to equation (2.17).

The quantum effects alter both the adsorption capacity and the diffusion dynamics, which results in difference in adsorption energy between the isotopes and thus leads to isotope separation. First introduced by Beenakker et al. [59], this quantum sieving effect describes how restricted transverse motion of a molecule within a narrow pore leads to an increase in its zero-point energy (ZPE). The magnitude of this effect is highly dependent on the isotope mass. Since lighter isotopes, such as H_2, have a larger de Broglie wavelength than heavier isotopes, such as D_2, they experience stronger quantum confinement, which in turn reduces their adsorption affinity and mobility within nanopores. This effect becomes particularly relevant when the pore diameter d approaches the kinetic diameter σ_{kin} of the gas molecules—which is 2.89 Å for H_2 and 2.97 Å for D_2. According to Bennakker et al. [59], the zero-point energy (ZPE) for an ideal cylindrical pore exhibiting a square well potential is given by equation (2.17):

$$E_0 = \frac{2\gamma_0^2 \cdot \hbar^2}{m \cdot (d - \sigma_{kin})^2} \tag{2.17}$$

with the isotope mass *m*, and γ_0 = 2.4048 being the first zero of the cylindrical Bessel function of the first kind. In this model, the molecule is expected to interact solely with the pore's potential well $\varepsilon(d)$ based on van-der-Waals interactions, assuming a low concentration, thus neglecting molecule-molecule interactions. The ZPE of D_2 is lower than H_2 due to its higher mass (see Figure 2.13 (b)), overcoming the potential barrier of a pore of similar size more easily. Hence, D_2 should be favored for adsorption in smaller pores, resulting in a larger accessible volume and, thus, higher adsorbed amounts. For pore diameters approaching the kinetic diameter of the molecules, the uptake of molecules at temperature *T* is proportional to the Boltzmann factor $e^{\left(\frac{\varepsilon(d)-E_0}{k_bT}\right)}$ [59]. Neglecting temperature-dependent changes in the depth of the potential well and/or changes in the interaction energy, the uptake ratio can be estimated via equation (2.18):

$$\frac{n_{D_2,T_1}}{n_{H_2,T_1}} = e^{\left(\frac{E_{0,H_2}-E_{0,D_2}}{k_bT_1}\right)} \tag{2.18}$$

The above considerations will become of importance in the later discussion of measured and simulated adsorption capacities of H_2 and D_2 within different nanoporous carbons and respective atomistic models of nanoporous carbons.

“Before I came here I was confused about this subject. Having listened to your lecture I am still confused. But on a higher level.”

Enrico Fermi

2.4 Neutron scattering

In February 1932 the New York Times published an interview with Sir James Chadwick titled: *Chadwick calls Neutron a 'difficult catch'*, following his letter in Nature journal proposing the possible existence of the neutron [60]. In this interview Chadwick only smiled, when asked if his discovery had any practical importance. He replied: *"I am afraid neutrons will not be of any use to any one"*. Soon he and the rest of the world would learn of what use neutrons were and still are to this day, saying the least, it is owed to him that this thesis was written. Neutrons are neutral particles found in the atomic core, possessing a spin of 1/2 and a mass of 1.675×10^{-27} kg. They can be produced in high numbers by nuclear fission processes involving the fission of enriched Uranium (^{235}U). When bombarded with high energy neutrons ^{235}U transforms into the unstable ^{236}U, which splits into lighter fission products, while generating 2.7 neutrons on average per fission reaction. The energy of these neutrons is in the order of MeV, thus too high to be used in experiments, for which moderators such as heavy water (D_2O), are used to slow down the neutrons. One neutron originating from the fission process is used to maintain the chain reaction, whereas some neutrons may be absorbed, some can escape the reactor and be used for experiments. It was in 1924 when French PhD-student Louis de Broglie submitted his Dissertation to the committee of Paris Sorbonne University, to which Paul Langevin was a member. In his thesis, following the work of Albert Einstein, he proposed the duality of matter (electrons) acting as particles and waves, which is summarized in equation (2.19), where λ is the wavelength, h the Planck constant and p the linear momentum. This fundamental property of matter allows to make use of this one neutron escaping the reactor for scientific experiments involving the scattering of neutrons on matter.

$$\lambda = \frac{h}{p} = \frac{h}{m|\boldsymbol{v}|} = \frac{2\pi}{|\boldsymbol{k}|} \tag{2.19}$$

$$E = \frac{1}{2}mv^2 = \hbar\omega = \frac{\hbar^2 k^2}{2m} = \frac{h^2}{2m\lambda^2} \approx k_B T \tag{2.20}$$

At the Institut Laue-Langevin (ILL), the neutron source is a high flux reactor with a thermal power of 58.3 MW and a neutron flux of $1.5 \cdot 10^{15}$ neutrons $s^{-1}cm^{-2}$ at the moderator, thus providing the most intense continuous neutron flux in the world [61]. The neutron energy can

be converted to a neutron temperature, according to equation (2.20). The neutron properties as a result of moderation using different moderators are summarized in Table 2.1.

Table 2.1: Neutron temperatures, energies and wavelengths ranges achievable with different moderators at the ILL [61]

	Moderator	Hot	Thermal	Cold
Temperature (K)	graphite	2000	300	25
Energy E (meV)	D_2O	100-500	5-100	0.1-10
Wavelength λ (Å)	D_2	0.4-1.0	1-4	4-30

As neutrons have no charge, they interact with nuclear forces of the atomic core instead of instead of the electron cloud. These forces are of short range compared to the distances between nuclei, thus neutrons can penetrate matter significantly better than electromagnetic radiation, such as X-rays. Hot neutrons with a wavelength of ~0.5 Å allow the study of high-frequency dynamics like molecular vibrations or rotations. The wavelength of thermal neutrons is comparable to the atomic distances in solids, thus making them an ideal probe to study structure solids. Larger macromolecular structures, such as proteins or viruses are usually probed using cold neutrons, as they exhibit the largest wavelength in the order of 4-30 Å.

2.4.1 Interaction of neutrons with matter

“"Do not worry about your difficulties in Mathematics. I can assure you mine are still greater."
-Dear Professor Einstein: Albert Einstein's Letters to and from Children-

With that comforting thought from Albert Einstein, the writing of this chapter began—only to be met with an avalanche of textbooks [62–66]. Many of them enthusiastically start with wave functions and scattering amplitudes, swiftly diving into the intricate interactions of neutrons with atomic cores. In keeping with tradition, this chapter also begins with the wave function of a scattered neutron at the atomic core and the corresponding scattering amplitude Ψ_f. However, rather than dwelling too long in the depths of quantum mechanics, a more structured and digestible approach will soon take over—one that gradually introduces the

necessary equations of neutron scattering without requiring a prerequisite existential crisis in theoretical physics.

The simplest case considers the scattering of an incident neutron described as a plane wave $\Psi_i = e^{i\boldsymbol{kr}}$ at a single and fixed nucleus. The interaction of a neutron with the nucleus is of short range and in the order of a few fm, which is considerably smaller compared to the neutron wavelength (0.4-30·10^5 fm). Consequently, the atomic nucleus is a point-like object for the incoming neutron wave, which results in an isotropic and spherical scattered wave. The amplitude of the scattered wave at point r for elastic scattering is given by equation (2.21), where b is a constant called the scattering length.

$$\Psi_f = -\frac{b}{r} e^{i\boldsymbol{kr}} \tag{2.21}$$

The scattering length describes the strength of the interaction of a neutron with a given nucleus and is not dependent on the atomic number (compared to X-rays) and thus varies across the periodic table in a seemingly random manner, as shown in Figure 2.14. The scattering length is influenced by the spin state of the neutron-nucleus system. Given that the neutron has a spin of *1/2*, the possible spin states for a nucleus with spin *I* are *I ± 1/2*. Each of these spin states corresponds to a distinct value of b. As there is no satisfactory description of the nuclear potentials, this quantity is measured by neutron scattering experiments. Simple considerations involving a square-well potential can qualitatively reproduce the randomness across the periodic table, yet a derivation would go beyond the proposed simplicity of this chapter.

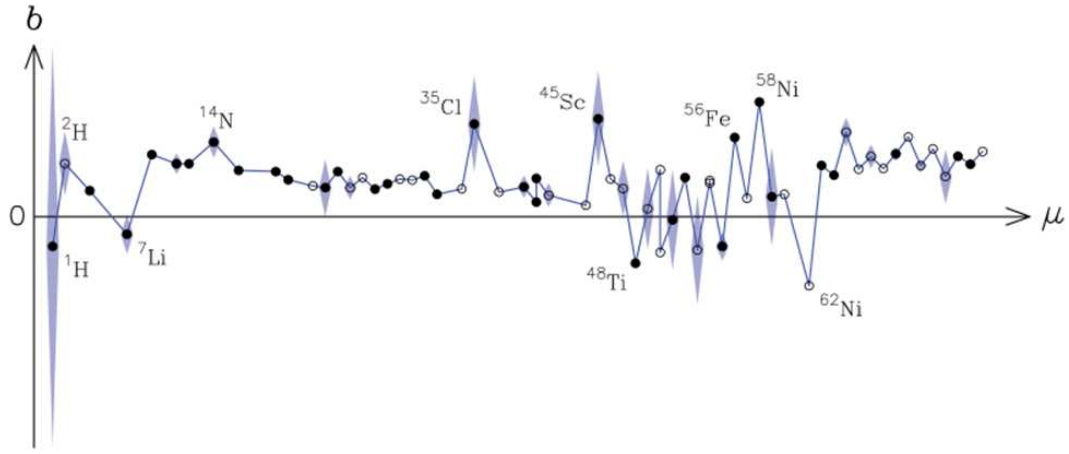

Figure 2.14: Coherent scattering lengths b for neutrons across the elements of the periodic table, with μ.being the atomic mass The average scattering length over different nuclear–neutron spin states, $\langle b \rangle$, is represented by points, while the standard deviation (Δb) is illustrated by the shaded regions. The most abundant isotopes are denoted by filled circles, whereas rare isotopes and strongly absorbing nuclei are excluded. Reproduced from Ref. [63] with permission from Oxford University Press.

The scattering event of a neutron at an atomic nucleus can either be of elastic or of inelastic nature (see Figure 2.15 and Figure 2.16 (a)). The momentum transfer between an incoming (wavevector $\boldsymbol{k_i}$) and scattered (wavevector $\boldsymbol{k_f}$) is defined as $\boldsymbol{q} = \boldsymbol{k_i} - \boldsymbol{k_f}$. The elastic scattering is governed by the exchange of momentum between a neutron and a nucleus, which leads to a change in direction, without an energy transfer. The incoming and the scattered neutron have the same modulus, yet differ in direction. The momentum transfer $\boldsymbol{q}$ is also often referred to as the scattering vector and is related to the scattering angle 2θ and the neutron wavelength with $q = \frac{4\pi}{\lambda} sin\,(\theta)$, for the elastic case. The inelastic scattering process involves the exchange of both, momentum and energy between a neutron and a nucleus, where the difference in energy is given by $\Delta E = E_i - E_f = \frac{\hbar^2}{2m}(k_i^2 - k_f^2)$.

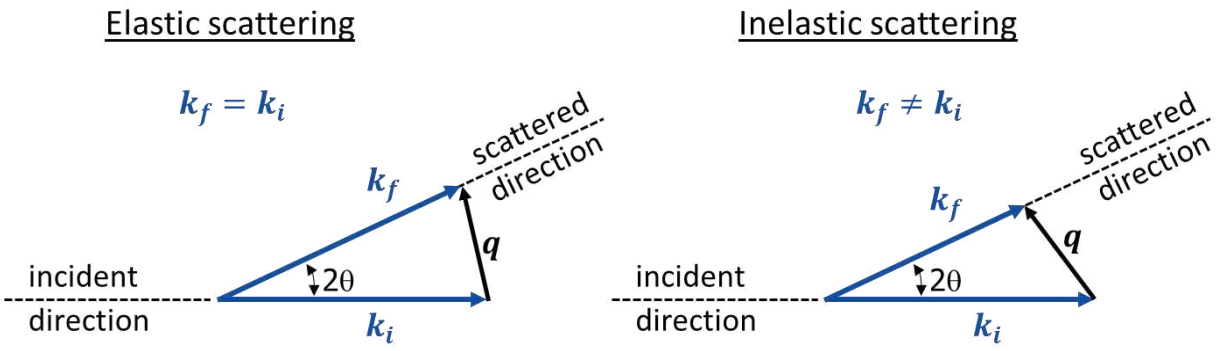

Figure 2.15: The scattering triangle of an incoming and scattered neutron, visualizing the elastic and inelastic scattering process.

Extending the discussion of neutron scattering to an ensemble *monoatomic* of scatterers, the measured quantity of a neutron scattering experiment is defined by the number of neutrons N_f, with a certain energy range dE, that are scattered into a solid angle $d\Omega$ of the detector per unit time. This quantity is called the double differential cross section and is calculated by equation (2.22), where ϕ is the incident neutron flux.

$$\frac{d^2\sigma}{d\Omega dE_f} = \frac{1}{\phi}\frac{dN_f}{d\Omega dE} \tag{2.22}$$

Given an ensemble of scatterers, one can derive the double differential cross section from considering the time depended transition of a system from an initial state to a final state, e.g. from an incident to a scattered neutron. For a detailed derivation of the following equation, one may be referred to the aforementioned textbooks by Squires [62] or Sivia [63]. Using the two quantities measurable by a scattering experiment, the momentum and the energy transfer, the double differential cross section of an monoatomic ensemble as a function of their position $\boldsymbol{r}(t)$ in time is given by [62,63]:

$$\frac{\mathrm{d}^2\sigma}{d\Omega dE_f} = \frac{1}{N}\frac{k_f}{k_i}\frac{1}{2\pi\hbar}\sum_{i,j}\langle b_i b_j\rangle \int_{-\infty}^{\infty}\langle e^{-i\boldsymbol{q}\boldsymbol{r}_i(0)} e^{i\boldsymbol{q}\boldsymbol{r}_j(t)}\rangle \cdot e^{-i\omega t} dt \tag{2.23}$$

In equation (2.23), N is the number of atomic nuclei, $\hbar$ the reduced Planck constant, $b_i$and b_j the scattering length of nucleus i and j (not to be mistaken with the imaginary number in the exponent), respectively and ω the angular frequency, which is related to the energy. At time

zero, nucleus i is at position $\boldsymbol{r_i}(0)$, while nucleus j is at $\boldsymbol{r_j}(t)$ at time t. Equation (2.23) sums over all nuclei positions at time t in the samples, while the angular brackets indicate that the spatial average over all possible ensemble configurations has to be considered. Every nucleus with non-zero spin (like hydrogen) exhibits two values of b, thus average value of $\langle b_i b_j \rangle$ needs to be considered, which can be separated into two sperate cases:

$$\text{For } i = j\text{: } \langle b_i b_i \rangle = \langle b \rangle^2 \text{and for } i \neq j\text{: } \langle b_i b_j \rangle = \langle b_i \rangle \langle b_j \rangle = \langle b^2 \rangle \tag{2.24}$$

With this consideration equation (2.23) is transformed to equation (2.25), separating the differential cross section in a time and spatial correlation contribution between different scatterers and a time and spatial self-correlation contribution.

$$\begin{aligned}\frac{\mathrm{d}^2\sigma}{d\Omega dE_f} = \frac{1}{N}\frac{k_f}{k_i}\frac{1}{2\pi\hbar}\sum_{i\neq j}\langle b\rangle^2 \int_{-\infty}^{\infty}\langle e^{-i\boldsymbol{q}\boldsymbol{r_i}(0)} e^{i\boldsymbol{q}\boldsymbol{r_j}(t)}\rangle \cdot e^{-i\omega t}dt \\ + \frac{1}{N}\frac{k_f}{k_i}\frac{1}{2\pi\hbar}\sum_{i}\langle b^2\rangle \int_{-\infty}^{\infty}\langle e^{-i\boldsymbol{q}\boldsymbol{r_i}(0)} e^{i\boldsymbol{q}\boldsymbol{r_j}(t)}\rangle \cdot e^{-i\omega t}dt\end{aligned} \tag{2.25}$$

We can further introduce the coherent $b_{coh}^2 = \langle b \rangle^2$ and incoherent $b_{inc}^2 = (\langle b^2 \rangle - \langle b \rangle^2)$ scattering length, as well as their respective cross sections [62,66]:

$$\sigma_{\mathrm{coh}} = 4\pi\langle b\rangle^2 = 4\pi b_{coh}^2 \tag{2.26}$$

$$\sigma_{inc} = 4\pi(\langle b^2\rangle - \langle b\rangle^2) = 4\pi b_{inc}^2 \tag{2.27}$$

Combining (2.26) and (2.27) with (2.25), yields:

$$\frac{\mathrm{d}^2\sigma}{d\Omega dE_f} = \frac{1}{4\pi}\frac{k_f}{k_i}(\sigma_{\mathrm{coh}}\, S_{coh}(\boldsymbol{q},\omega) + \sigma_{inc}\, S_{inc}(\boldsymbol{q},\omega)) \tag{2.28}$$

The differential cross section is now comprised of a coherent and incoherent scattering contribution, which are called the coherent $S_{coh}(\boldsymbol{q},\omega)$ and incoherent dynamic structure factor $S_{inc}(\boldsymbol{q},\omega)$, respectively [62,63].

$$S_{coh}(\boldsymbol{q},\omega) = \frac{1}{N}\frac{1}{2\pi\hbar}\sum_{i,j}\int_{-\infty}^{\infty}\langle e^{-i\boldsymbol{q}\boldsymbol{r}_i(0)}e^{i\boldsymbol{q}\boldsymbol{r}_j(t)}\rangle \cdot e^{-i\omega t}dt \tag{2.29}$$

$$S_{inc}(\boldsymbol{q},\omega) = \frac{1}{N}\frac{1}{2\pi\hbar}\sum_{i}\int_{-\infty}^{\infty}\langle e^{-i\boldsymbol{q}\boldsymbol{r}_i(0)}e^{i\boldsymbol{q}\boldsymbol{r}_i(t)}\rangle \cdot e^{-i\omega t}dt \tag{2.30}$$

These contributions in the integral represent correlation functions related to the sample properties. Coherent scattering arises from both the correlation of a nucleus's position over time and the spatial correlation between different nuclei at different times. Since it results from interference effects, it depends on the distances between nuclei, thereby reflecting their positional correlations. As a result, coherent scattering generally describes collective properties such as atomic structure. Figure 2.16 (b) illustrates how its intensity may vary with $\boldsymbol{q}$ due to interference effects. In contrast, incoherent scattering is determined solely by the self-correlation of an individual nucleus's position over time. It occurs due to random variations in atomic scattering lengths, which stem from non-zero nuclear spins or the presence of different isotopes. Unlike coherent scattering, the scattered intensities from individual nuclei sum up independently, making incoherent scattering a signature of diffusion, i.e., atomic motion. As shown in Figure 2.16 (b), its intensity remains independent of $\boldsymbol{q}$.

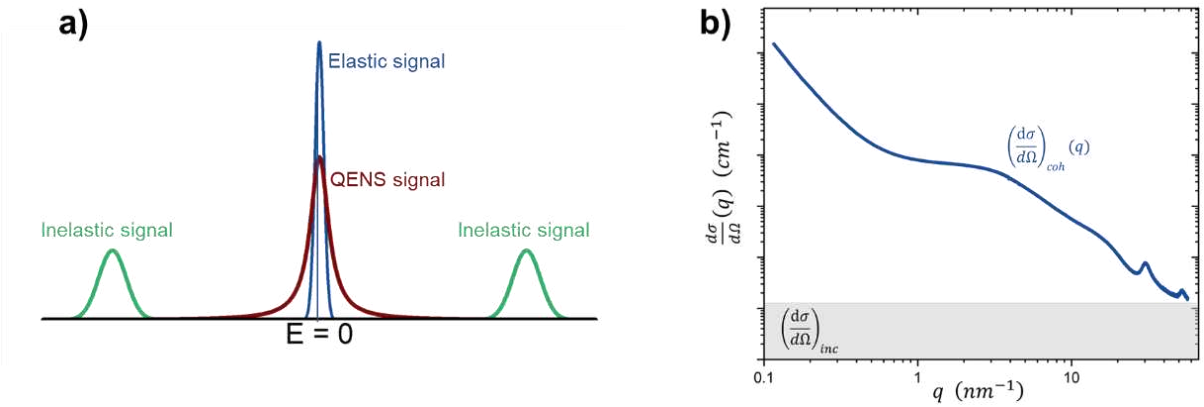

Figure 2.16: a) Schematic representation of a neutron scattering spectrum as a function of neutron energy, showing the elastic peak, a QENS contribution, as well as inelastic peaks. Adapted from Ref. [61] b) representation of the coherent and incoherent scattering cross-section contribution to elastic scattering.

Figure 2.16 (a) presents a schematic example of a neutron scattering spectrum. Theoretically, the elastic peak should be located at $E = 0$. However, due to the finite resolution of all instruments, this peak broadens into a Gaussian shape. The resolution of a given instrument determines the timescales of dynamics that can be investigated. If the diffusion timescale in a material is comparable to the timescale probed by the instrument, a Lorentzian peak emerges, further broadening the elastic line. This effect results from thermally activated processes, such as translational motion or random jumps, which cause transitions between configurations of equal energy. In principle, this corresponds to inelastic scattering centered at $E = 0$, where the transferred energy dissipates rapidly, leaving the system in a final state with the same energy as its initial state. Consequently, this phenomenon is known as quasielastic neutron scattering (QENS).

2.4.2 Elastic scattering

"It is important to point out that the mathematical formulation of the physicist's often crude experience leads in an uncanny number of cases to an amazingly accurate description of a large class of phenomena." Eugene Wigner

In the previous section the derivation of the differential cross section measurable by a neutron scattering experiment was shown. This section is dedicated to a special case of equation (2.28), just considering elastic coherent scattering processes, which contain information of positional correlation of the monoatomic scattering ensemble. For elastic scattering processes double-differential cross section is summed over all possible final neutron energies dE considering the integral:

$$\frac{\mathrm{d}\sigma}{d\Omega} = \int_0^\infty \frac{\mathrm{d}^2\sigma}{d\Omega dE_f}\, dE \tag{2.31}$$

Further, the assumption of thermodynamic equilibrium is introduced, which results in the wavefunction $e^{i\boldsymbol{q}\boldsymbol{r}_j(t)}$ being independent of time (e.g. $\boldsymbol{r}_{\boldsymbol{i,j}} \neq f(t)$) and as well as considering the result of the time-dependent Fourier transform $\int_{-\infty}^{\infty} e^{-i\omega t} dt = 2\pi\delta(\omega)$, where $\delta(\omega)$ is the Dirac-delta-function. Inserting equations (2.29) and (2.30) into equation (2.28) yields:

$$\frac{\mathrm{d}^2\sigma}{d\Omega dE_f} = \frac{1}{4\pi}\frac{k_f}{k_i}(\sigma_{\mathrm{coh}}\, S_{coh}(\boldsymbol{q},\omega) + \sigma_{inc}\, S_{inc}(\boldsymbol{q},\omega))$$

$$= \frac{1}{N}\frac{1}{4\pi}\frac{k_f}{k_i}\frac{1}{\hbar}\left(\sigma_{\mathrm{coh}}\sum_{i,j}\langle e^{-i\boldsymbol{q}\boldsymbol{r}_i}e^{i\boldsymbol{q}\boldsymbol{r}_j}\rangle + \mathrm{N}\sigma_{inc}\right)\delta(\omega) \tag{2.32}$$

Integration over all final neutron energies $dE = \hbar d\omega$ and considering the elastic scattering event, where $k_f = k_i$, gives:

$$\frac{\mathrm{d}\sigma}{d\Omega}(\boldsymbol{q}) = \int_0^\infty \frac{\mathrm{d}^2\sigma}{d\Omega dE_f}\hbar d\omega = \frac{1}{N}\frac{1}{4\pi}\left(\sigma_{\mathrm{coh}}\sum_{i,j}\langle e^{-i\boldsymbol{q}\boldsymbol{r}_i}e^{i\boldsymbol{q}\boldsymbol{r}_j}\rangle + \mathrm{N}\sigma_{inc}\right)\int_0^\infty \delta(\omega)d\omega \tag{2.33}$$

Given the identity of the Dirac-delta-function $\int_0^\infty \delta(\omega)d\omega = 1$ [67], equation (2.33), while also considering equations (2.26) and (2.27), reduces to the microscopic differential cross section:

$$\frac{\mathrm{d}\sigma}{d\Omega}(\boldsymbol{q}) = \frac{1}{N}b_{coh}^2\sum_{i,j}\langle e^{-i\boldsymbol{q}\boldsymbol{r}_i}e^{i\boldsymbol{q}\boldsymbol{r}_j}\rangle + b_{inc}^2 \tag{2.34}$$

It is now more evident that the incoherent scattering contribution in the elastic case does not depend on the scattering vector and thus ads a constant background (see also Figure 2.16 (b)). While the microscopic differential cross section is a measurable quantity, most experiments rely on the comparison to the scattering of a known calibration standard of same volume and scattering conditions, such as H_2O or Vanadium [57,68], which only show a flat incoherent background at small scattering vectors. For this we further introduce the macroscopic differential cross section as:

$$\left(\frac{\mathrm{d}\Sigma}{d\Omega}\right)(\boldsymbol{q}) = \left(\frac{\mathrm{d}\Sigma}{d\Omega}\right)_{coh}(\boldsymbol{q}) + \left(\frac{\mathrm{d}\Sigma}{d\Omega}\right)_{inc} = \frac{N}{V}\left[\left(\frac{\mathrm{d}\sigma}{d\Omega}\right)_{coh}(\boldsymbol{q}) + \left(\frac{\mathrm{d}\sigma}{d\Omega}\right)_{inc}\right] \tag{2.35}$$

$$\left(\frac{\mathrm{d}\Sigma}{d\Omega}\right)_{coh}(\boldsymbol{q}) = \frac{1}{V}b_{coh}^2\sum_i\sum_j\langle e^{-i\boldsymbol{q}(\boldsymbol{r}_i-\boldsymbol{r}_j)}\rangle \tag{2.36}$$

$$\left(\frac{\mathrm{d}\Sigma}{d\Omega}\right)_{inc} = \frac{N}{V} b_{inc}^2 \tag{2.37}$$

The further discussion will be focused on the coherent scattering part only. Thus, in equation (2.36), for the sake of convenience, the subscript indicating the coherent scattering part will be further neglected. While the previous discussion and derivation was evolving around a monoatomic system, in most cases more than one atom is present in a system. Thus, equation (2.36) can be generalized accounting for multiple atoms (i, j) present and reads:

$$\left(\frac{\mathrm{d}\Sigma}{d\Omega}\right)(\boldsymbol{q}) = \frac{N}{V}\left(\frac{\mathrm{d}\sigma}{d\Omega}\right)(\boldsymbol{q}) = \frac{1}{V}\sum_i \sum_j b_i b_j \langle e^{-i\boldsymbol{q}(\boldsymbol{r_i}-\boldsymbol{r_j})}\rangle \tag{2.38}$$

2.4.3 Small angle scattering

"We cannot solve our problems with the same thinking we used when we created them." Albert Einstein

Considering the derivations above, the following section outlines a different approach to the same problem and towards the end comes back to the original equation proposed above. The spatial correlation of the ensemble of monoatomic scatterers as described by equation (2.36), may further consider separating the double summation, where $i = j$, and replacing the second summation by an integral. Additionally, as scattering ultimately arises from deviations in the density, a term proportional to the atomic number density $n_i(\boldsymbol{r_{ij}})$ is introduced. With $\boldsymbol{r_{ij}} = \boldsymbol{r_j} - \boldsymbol{r_i}$ as the distance vector between $\boldsymbol{r_j}$ and the reference atom position $\boldsymbol{r_i}$, equation (2.36) is transformed to [64]:

$$\begin{aligned}\left(\frac{\mathrm{d}\Sigma}{d\Omega}\right)(\boldsymbol{q}) = N\frac{b^2}{V} + \frac{b^2}{V}\sum_i \int_V \left[n_i(\boldsymbol{r_{ij}}) - n_0\right]\langle e^{-i\boldsymbol{q}\boldsymbol{r_{ij}}}\rangle dV_i \\ + n_0\frac{b^2}{V}\sum_i \int_V \langle e^{-i\boldsymbol{q}(\boldsymbol{r_i}-\boldsymbol{r_j})}\rangle dV_i\end{aligned} \tag{2.39}$$

This results in two distinct coherent scattering contribution. The first part to equation (2.39) describes the atomic/molecular correlations, whereas the last part accounts for scattering from a homogenous atom density. The separation remains exact as long as there are no correlations between atomic structures and larger-scale structural features. In practice, this condition is generally met in crystal lattices with long-range order and when the characteristic length scale of the larger structure is significantly greater than typical atomic distances. However, even when the difference in length scales between atomic and higher-order structures is small, often such correlations are negligible [64,65].

Taking only the first two terms in equation (2.39), considering isotropy and the spatial average of $\langle e^{-i\boldsymbol{q}\boldsymbol{r}_{ij}} \rangle$ (see equation (2.41) [65]), alongside the introduction of the radial distribution function being $g(r) = n(r)/n_0$, the general expression of the (static) structure factor $S(q)$ is presented as:

$$S(q) = \frac{\left(\frac{\mathrm{d}\Sigma}{d\Omega}\right)(q)}{N}\frac{V}{b^2} = 1 + \frac{4\pi}{q}\int_0^\infty r[g(r) - 1]\sin(qr)\ dr \tag{2.40}$$

$$\langle e^{-i\boldsymbol{q}\boldsymbol{r}} \rangle = \langle e^{i\boldsymbol{q}\boldsymbol{r}} \rangle^* = \frac{1}{4\pi}\int_0^{2\pi}\int_0^{\pi} e^{(-iqrcos\theta)}\sin(\theta) d\theta\, d\phi = \frac{\sin(qr)}{qr} \tag{2.41}$$

Moving forward, a reconsideration of the given problem involves abandoning the idea of an atomistic structure, as the small angle scattering part (SAS) described by the last term of equation (2.39), considers fluctuations in the average density n_0 at a higher hierarchical level and the absence of long-range order. Thus, the summation in the last term of equation (2.39) is replaced by an integral and the scattering length density $\tilde{\rho} = n_0\, {}^{b}/_{V}\, [cm^{-2}]$ (SLD) is introduced [64,65].

$$\left(\frac{\mathrm{d}\Sigma}{d\Omega}\right)_{SAS}(\boldsymbol{q}) = \iint_V \tilde{\rho}(\boldsymbol{r_i})\tilde{\rho}(\boldsymbol{r_j})\langle e^{-i\boldsymbol{q}(\boldsymbol{r_i}-\boldsymbol{r_j})}\rangle dV_i dV_j \tag{2.42}$$

Further, the autocorrelation function $\tau^2(\boldsymbol{r})$ is introduced and equation (2.42) can be rewritten as:

$$\tau^2(\boldsymbol{r}) = \int_V \tilde{\rho}(\boldsymbol{r_i})\tilde{\rho}(\boldsymbol{r}+\boldsymbol{r_i})\,[cm^{-4}]\; with\; \boldsymbol{r} = \boldsymbol{r_j} - \boldsymbol{r_i}$$

$$\left(\frac{\mathrm{d}\Sigma}{d\Omega}\right)_{SAS}(\boldsymbol{q}) = \int_V \tau^2(\boldsymbol{r})\,\langle e^{i\boldsymbol{q}\boldsymbol{r}}\rangle dV \tag{2.43}$$

Again, assuming isotropy and taking the spatial average leads to:

$$\left(\frac{\mathrm{d}\Sigma}{d\Omega}\right)_{SAS}(q) = \int 4\pi r^2\,\tau^2(r)\frac{\sin(qr)}{qr}dr \tag{2.44}$$

For $r = 0$ the auto-correlation function $\tau^2(r)$ equals $\langle\tilde{\rho}^2\rangle$, which is the spatial ensemble average of the squared SLD. At $r = \infty$, $\tau^2(r)$ approaches $\langle\tilde{\rho}\rangle^2$and adds a constant background in the autocorrelation function, which does not contribute to the coherent scattering intensity. Thus, it is convenient to subtract the mean SLD and only consider the scattering length density fluctuations and introducing the correlation function $V\gamma(r) = \tau^2(r) - V\langle\tilde{\rho}\rangle^2$, transforms equation (2.44) to:

$$\left(\frac{\mathrm{d}\Sigma}{d\Omega}\right)_{SAS}(q) = V\int 4\pi r^2\gamma(r)\frac{\sin(qr)}{qr}dr \tag{2.45}$$

The correlation function holds all information about spatial fluctuation of scattering length density of a sample. In the following, the general expression of equation (2.45) is further applied to the special case of a non-particular two-phase system with sharp interfaces, like interconnected pore networks illustrated in Figure 2.17 (a).

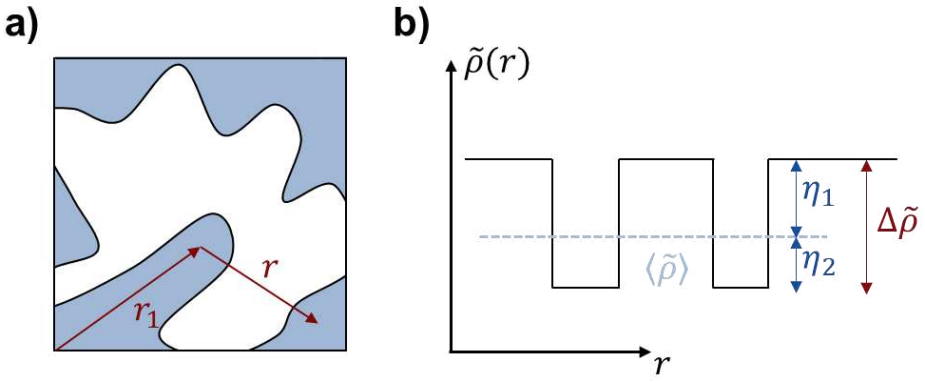

Figure 2.17: a) Schematic representation of a disordered porous two-phase system and b) scattering length density profile of the two-phase system. Adapted from Ref. [69]

For isotropic systems, the correlation function can be rewritten as the spatial average of the scattering length density fluctuation $\eta(r) = \tilde{\rho} - \langle\tilde{\rho}\rangle$ [65]:

$$\gamma(r) = \langle\eta(r_1)\eta(r_1 + r)\rangle = \varphi(1-\varphi)(\Delta\tilde{\rho})^2\gamma_0(r) \tag{2.46}$$

Here, the normalized autocorrelation function $\gamma_0(r)$ was introduced, while V is the irradiated sample volume, φ the volume fraction of one phase (e.g. pores) and $\Delta\tilde{\rho}$ the scattering length density difference (see Figure 2.17 (b)). Inserting equation (2.46) in (2.45) results in:

$$\left(\frac{\mathrm{d}\Sigma}{d\Omega}\right)_{SAS}(q) = V(1-\varphi)\varphi(\Delta\tilde{\rho})^2\int_0^\infty 4\pi r^2\gamma_0(r)\frac{\sin(qr)}{qr}dr \tag{2.47}$$

From equation (2.46) it becomes immediately evident that small-angle scattering arises due to density differences of any kind, thus changing the SLD of one phase, results in changes of the scattering intensity. The discussion of the density fluctuations can be easily extended to a multi-phase system by considering the mean SLD $\langle\tilde{\rho}\rangle$ of the system and the respective volume fractions ϕ_i of the phase, as long as there are no correlations between the phases, and reads [66]:

$$\overline{\eta^2} = \sum_{i=1}^{N}\phi_i\,(\tilde{\rho}_i - \langle\tilde{\rho}\rangle)^2 \; with \; \langle\tilde{\rho}\rangle = \sum_{i=1}^{N}\phi_i\,\tilde{\rho}_i \tag{2.48}$$

A visualization of a multiphase system embedded in a matrix is shown in Figure 2.18. When the SLD of the matrix $\langle\tilde{\rho}\rangle$ and a respective phase is the same, there is no scattering contrast ($(\tilde{\rho}_i - \langle\tilde{\rho}\rangle)^2 = 0$), yet there is still a contrast between the individual phases, which leads to a measurable scattering intensity.

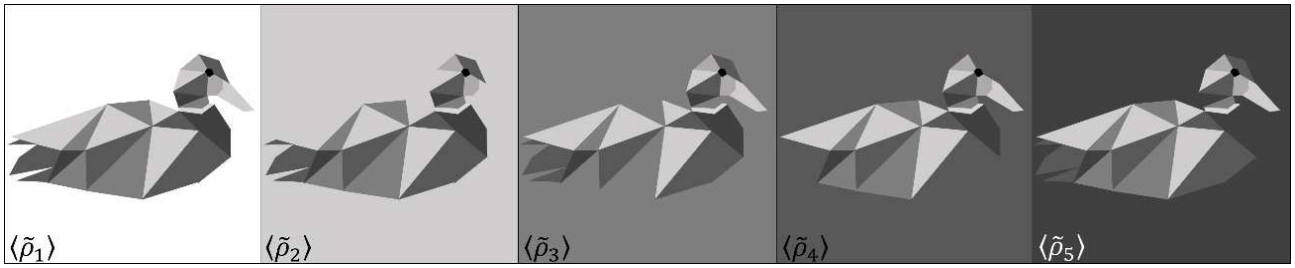

Figure 2.18: Schematic representation of a multiphase system embedded in a matrix. The mean SLD of the matrix is increasing from left to right, showcasing contrast matching scenarios.

With the analysis given by (2.48), a general trend of the density evolution of a system can be achieved, yet the information about underlying structure of the phases is lost.

Continuing the earlier thought, that the correlation function holds all information of the spatial distribution of scattering length density, a special case of a correlation functions is discussed, to which the integral in equation (2.47) yields an analytic expression, the Debye-Anderson-Brumberger (DAB) model [70]. The exponentially decaying correlation function (see equation (2.49) and Figure 2.19 (a)) implies a random pore structure, where the correlation length T is defined as the arithmetic average of the correlation function, e.g. the average chord length of the system. The correlation length T is related to the specific surface $S\ /\ V$ of the pore network, as shown in equation (2.49).

$$\gamma_0(r) = \exp\left(-\frac{r}{T}\right)\ with\ T = \frac{4V\varphi(1-\varphi)}{S} \tag{2.49}$$

The resulting scattering intensity is an analytical function given by [70]:

$$I_{DAB}(q) = \frac{2\pi(\Delta\tilde{\rho})^2 \cdot S}{\left(\frac{1}{T^2} + q^2\right)^2 \cdot V} \tag{2.50}$$

The observant reader may have realized that the macroscopic cross section $\left(\frac{\mathrm{d}\Sigma}{d\Omega}\right)(q)$ was replaced by $I(q)$ in equation (2.50). In literature discussing small angle scattering data often $I(q)$ (in arbitrary units) is used as no calibration to absolute units was performed, whereas $\left(\frac{\mathrm{d}\Sigma}{d\Omega}\right)(q)$ is given in units of cm^{-1}. In the following this notation is kept, such that reader is familiar with the meaning of the respective notation.

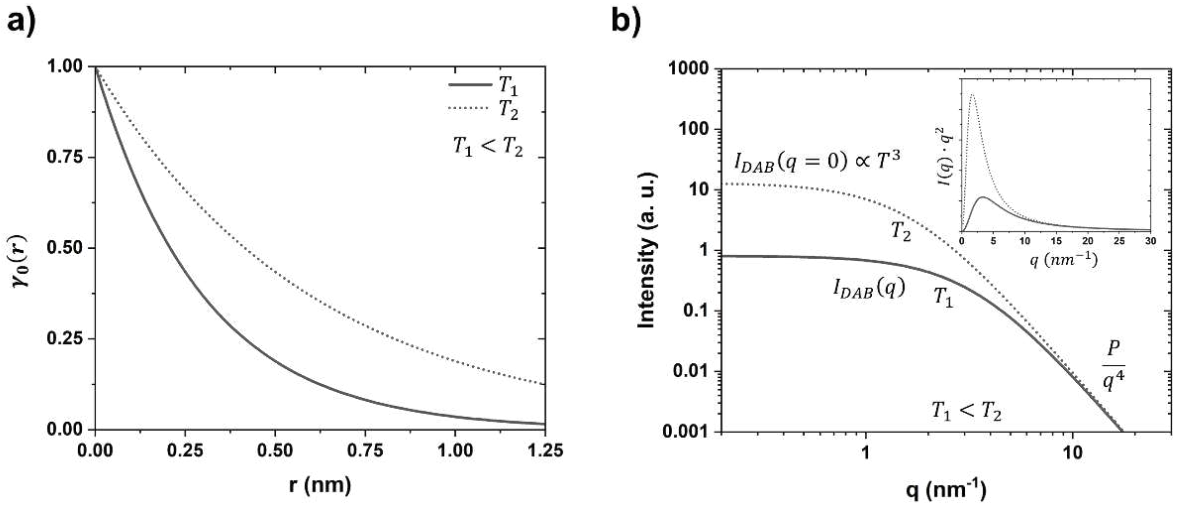

Figure 2.19: a) visualization of the correlation functions $\gamma_0(r)$ resulting from the DAB model and b) scattering intensity of the DAB model. Displayed for two different correlation lengths: $T_1 < T_2$.

Figure 2.19 (b) shows the scattering intensity resulting from the DAB model, which will be further used to derive some *universal* laws of SAS. The following laws are independent of the used correlation function and a only applicable when applied to a two-phase system with sharp interfaces. The scattering intensity in the low-q limit (e.g. $q = 0$) is proportional to the correlation volume T^3:

$$I_{DAB}(q=0) = T^3 8\pi\varphi(1-\varphi)(\Delta\tilde{\rho})^2 \tag{2.51}$$

Changes to the correlation length during scattering experiments, for example as a result of strain, will therefore significantly influence the scattering intensity at low-q.

In the intermediate q-regime, the transition of constant contribution of $I_{DAB}(q=0)$ to a power law decay is seen. Figure 2.19 (b) shows a comparison of two DAB functions with

different correlations lengths, such that $T_1 < T$, thus showing that the inflection point is inverse proportional to the correlation length.

In the large q-regime the scattering intensity decays according to a power-law, which is known as Porod's law [65,71]. For an ideal two-phase system with sharp interfaces, e.g. the assumption in our model, the scattering intensity at $q \to \infty$ takes the form of equation (2.52), where P is the Porod constant.

$$I_{DAB}(q \to \infty) = V\varphi(1-\varphi)(\Delta\rho)^2 \frac{8\pi}{T} \cdot \frac{1}{q^4} = (\Delta\rho)^2 \frac{2\pi}{q^4} \cdot S = \frac{P}{q^4} \tag{2.52}$$

The inset in Figure 2.19 (b), shows the so-called Kratky plot (named after the Austrian physicist Otto Kratky), which plots $I(q) \cdot q^2 dq$ against q. This plot is especially useful to calculate the integrated intensity $\tilde{I}$ (also often referred to as the invariant) takes the form of equation (2.53).

$$\tilde{I} = \int_0^\infty I(q) \cdot q^2 dq = 2\pi^2 V\varphi(1-\varphi)(\Delta\rho)^2 \tag{2.53}$$

The Porod constant P as well as the integrated intensity $\tilde{I}$ can be obtained from the scattering intensity and be further used to calculate the volume specific surface area S/V of the sample, as shown in equation (2.54).

$$\frac{\tilde{I}}{P} = \frac{2\pi^2\varphi(1-\varphi)(\Delta\rho)^2 V}{2\pi(\Delta\rho)^2 S} = \pi\varphi(1-\varphi)\frac{V}{S}$$

$$\frac{S}{V} = \pi\varphi(1-\varphi)\frac{P}{\tilde{I}} \tag{2.54}$$

Further considering the definition of the correlation length in equation (2.49), T can be further derived with:

$$T = \frac{4\tilde{I}}{\pi P} = 4\varphi(1-\varphi)\frac{V}{S} \tag{2.55}$$

The strength of these integral parameters is that there is no need for a calibration to absolute units to derive the S/V and T. For a two-phase system, consisting of pores and a dense (carbon) matrix, the respective chord lengths of pores and the matrix can be calculated using

equation (2.55). The correlation length T (or average chord length) is sometimes also referred to as the Porod length.

$$T = \frac{4\tilde{I}}{\pi P} = (1-\varphi)l_p = \varphi l_c \tag{2.56}$$

2.4.4 Wide angle scattering

Extending the above derivation of the scattering intensity into the wide-angle regime and discussing the scattering of neutron on a crystal, equation (2.38) is put into another perspective. When neutrons interact with a crystal, they scatter elastically at the atomic nuclei. The fundamental equation governing neutron scattering intensity from a crystal is given by the equation (2.63):

$$\left(\frac{\mathrm{d}\Sigma}{d\Omega}\right)(\boldsymbol{q}) = \frac{1}{V}\sum_i \sum_j b_i b_j e^{-i\boldsymbol{q}\boldsymbol{r}_{ij}} \tag{2.57}$$

The summation runs over all atomic positions, accounting for both interatomic and intra-unit cell contributions to the scattering intensity. A crystal is defined by its periodic structure, which can be described as the convolution of a Bravais lattice and a basis. The Bravais lattice defines the translational symmetry of the crystal, while the basis describes the atomic positions within a unit cell [64]. If $\boldsymbol{R_n}$ represents the position of a unit cell and $\boldsymbol{d_m}$ the atomic position inside that cell, the total atomic position is given by $\boldsymbol{r_{ij}} = \boldsymbol{R_n} + \boldsymbol{d_m}$. Substituting this into the scattering equation allows separation of the contributions from the periodic lattice and the atomic arrangement within the unit cell:

$$\left(\frac{\mathrm{d}\Sigma}{d\Omega}\right)(\boldsymbol{q}) = \frac{b^2}{V}\sum_n e^{-i\boldsymbol{q}\boldsymbol{R_n}} \sum_m e^{-i\boldsymbol{q}\boldsymbol{d_m}} \tag{2.58}$$

The second summation term, which accounts for the internal arrangement of atoms in the unit cell, is known as the structure factor:

$$F(\boldsymbol{q}) = \sum_i e^{-i\boldsymbol{q}\boldsymbol{d_m}} \tag{2.59}$$

The first summation term involves the lattice positions $\boldsymbol{R_n}$ and leads to constructive interference only when the scattering vector corresponds to a reciprocal lattice vector.

The concept of the reciprocal lattice is crucial in diffraction analysis, as it provides a mathematical representation of periodic structures in reciprocal space. The reciprocal lattice is constructed such that each point in this lattice corresponds to a set of lattice planes in real space. The reciprocal lattice vectors a_1^*, a_2^*, a_3^* are defined by the relationships:

$$a_1^* = \frac{2\pi}{V}(a_2 \times a_3), a_2^* = \frac{2\pi}{V}(a_3 \times a_1), a_3^* = \frac{2\pi}{V}(a_1 \times a_2) \tag{2.60}$$

Where V is the unit cell volume and a_1, a_2, a_3 are the lattice vectors. Constructive diffraction arises when the Laue condition is fulfilled: $\boldsymbol{q} = \boldsymbol{G}$**.** Here, $\boldsymbol{q}$ is the scattering vector, and $\boldsymbol{G}$ is a reciprocal lattice vector. This formulation connects the physical geometry of the crystal lattice with the mathematical structure of diffraction, allowing for the prediction of diffraction angles and intensities.

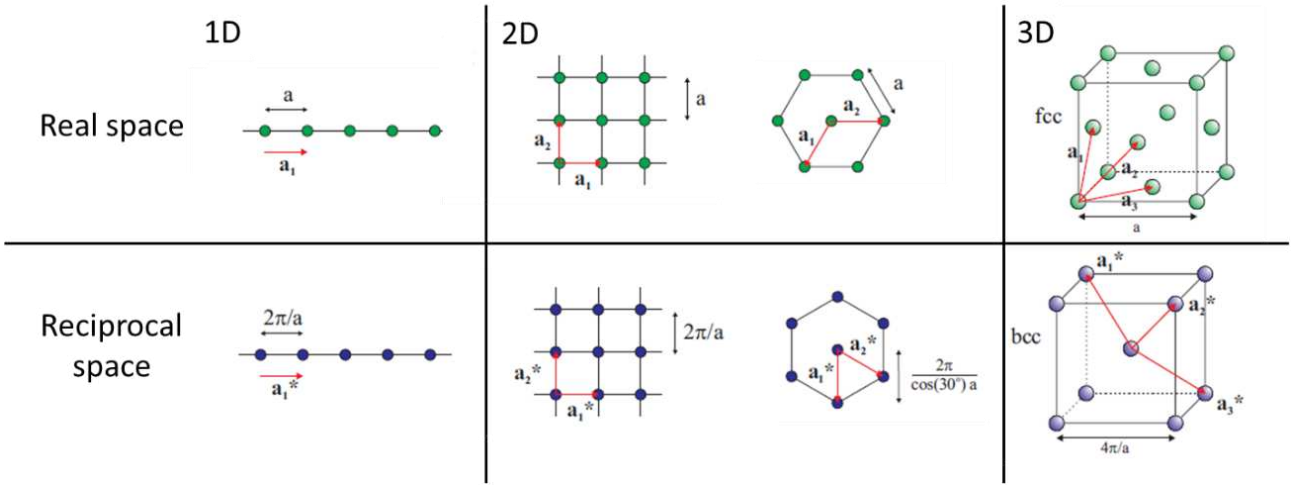

Figure 2.20: Schematic of the construction of the reciprocal lattice from the real space lattice in 1D, 2D and 3D. Adapted from Ref. [64] and with permission from Wiley VCH.

Bragg's Law provides a direct geometric interpretation of diffraction conditions in terms of reflections from atomic planes. If atomic planes are separated by a distance d, constructive

interference of scattered waves occurs when the extra path length traveled by a neutron wave reflecting off adjacent planes is equal to an integer multiple of the neutron wavelength. This condition is written as:

$$2d\ sin\theta = n\lambda \tag{2.61}$$

Here θ is the angle of incidence of the neutron beam with respect to the atomic planes, λ is the neutron wavelength, and n is an integer representing the diffraction order. Bragg's Law is fundamental to neutron diffraction because it determines the angles at which diffraction peaks occur, thereby allowing the determination of interatomic spacings and crystal structures. The orientation and spacing of atomic planes in a crystal are described using Miller indices. These indices define a family of parallel atomic planes and are determined from the reciprocal of the plane's intercepts with the crystallographic axes. The interplanar spacing for a given set of Miller indices in a cubic system is given by:

$$d_{hkl} = \frac{a}{\sqrt{h^2 + k^2 + l^2}} \tag{2.62}$$

Here a is the lattice constant. Since diffraction occurs when the scattering vector corresponds to a reciprocal lattice vector, the magnitude of is related to the interplanar spacing with $|G_{hkl}| = \frac{2\pi}{d_{hkl}}$. Thus, Bragg's Law reads: $2d_{hkl}\ sin\theta = n\lambda$ and is equivalent to the Laue condition.

For a 2D crystal, like graphene (see Figure 2.21 (a)), the lattice parameter as a function of the Miller indices (h, k) is given by $d_{hk} = \frac{a}{\sqrt{h^2+k^2+hk}} = \frac{2\pi}{q_{hk}}$, whereas the interplane distance of stacked graphene sheets in graphite (or turbostratic carbon), as shown in Figure 2.21 (b), is directly related to the peak position with $q_{002} = \frac{2\pi}{d_{002}}$.

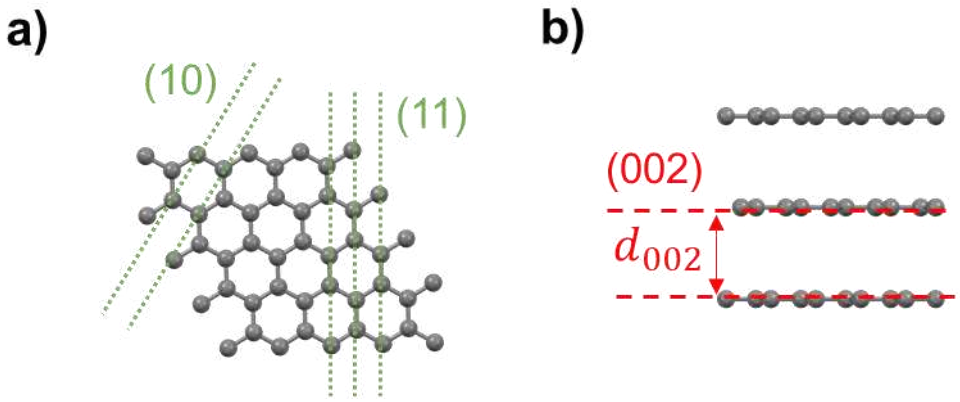

Figure 2.21: a) Representation of a 2D crystal, like graphene, with indication of the (10)- and (11)-planes and b) stacking of graphene sheets found in graphite or turbostratic carbon with indication of the interlayer spacing d_{002} and the (002)-plane.

2.4.5 Neutron and X-ray scattering of nanoporous carbons

"Broadly speaking, the discovery of X-rays has increased the keenness of our vision ten thousand times, and we can now 'see' the individual atoms and molecules."
William Henry Bragg

In the beginning of this chapter, the difference in interaction of neutrons and X-rays with matter was shortly outlined and shall be further discussed. Neutrons interact with the potential of atomic nucleus and thus the scattering length of elements vary randomly across the periodic table. X-rays, being electromagnetic waves, interact with the electron cloud of the atom, thus the scattering length increases with the atomic number Z according to equation (2.63) [63,64]. Here, r_e is the classical radius of the electron, e the elemental charge, ε_0 the dielectric constant of vacuum and m_e the electron mass.

$$b_{coh}(q) = Z\, r_e\, g(q)\; with\; r_e = \frac{e^2}{4\pi\varepsilon_0 m_e c^2} = 2.818\; fm \qquad (2.63)$$

With this, further the atomic formfactor $g(q)$ was introduced, which accounts for the spatial extensions of the electron cloud around the nucleus. X-ray photons scattered by different electrons interfere, resulting in a Gaussian-like distribution of the atomic form factor, as illustrated Figure 2.22. This distribution corresponds to the Fourier transform of the electron

density distribution. A comparison between the atomic formfactor for X-rays and the coherent neutron scattering length of hydrogen and carbon is given in Figure 2.22.

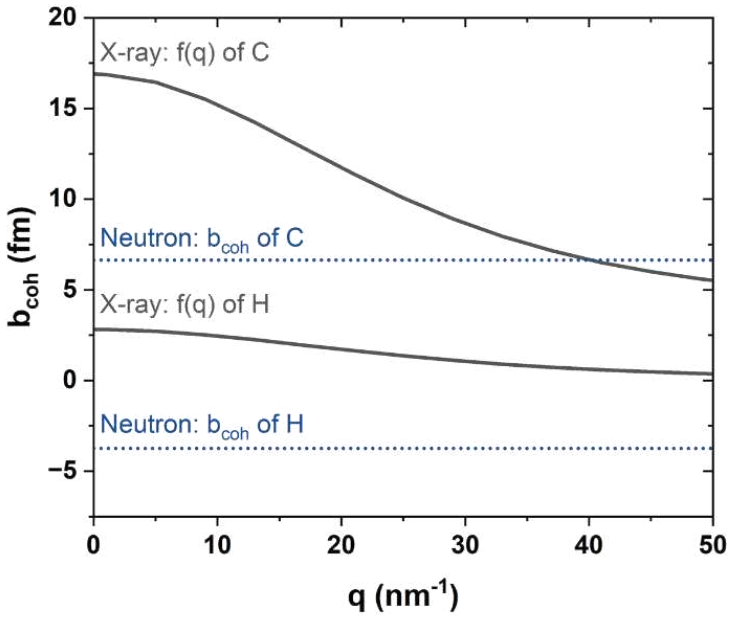

Figure 2.22: Comparison of the atomic formfactor for X-rays and the neutron coherent scattering length of Carbon and Hydrogen.

The distinct interactions of both kinds of waves makes them useful to probe different effects in structures and physical phenomenon. It becomes evident that hydrogen is essentially invisible to X-rays in comparison to the scattering length of carbon, whereas for neutrons hydrogen and carbon have a high scattering length, yet of opposite signs. Thus, studies involving hydrogen benefit highly from the use of neutrons, whereas when the effects of hydrogen adsorption on a structure, like deformation, should be studied, X-rays might be beneficial.

In the following section the scattering signal obtained from nanoporous carbons will be further discussed in more detail and is valid for both neutrons and X-rays used as the probe. Figure 2.23 (a) shows the general set-up of a scattering experiment in transmission mode, where 2θ is the scattering angle. Figure 2.23 (b) showcases neutron scattering pattern in a log-log-scale, of a nanoporous carbon covering a wide range of scattering vectors. For scattering vectors q < 1 nm^{-1}, the scattering pattern shows a power-law decrease $I_{ext}(q)$, which is related to the scattering of larger structures or external surface of individual carbon particles.

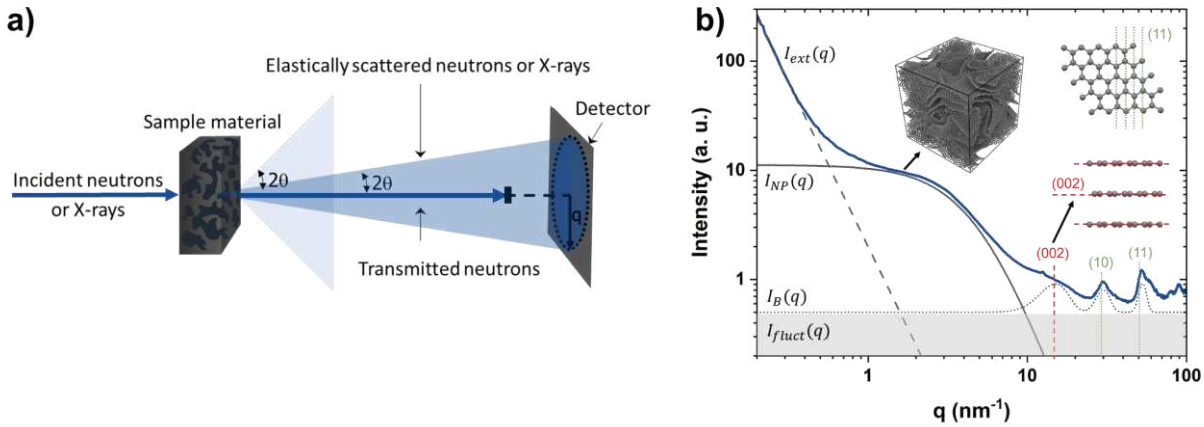

Figure 2.23: a) Schematic representation of elastic scattering experiment and b) Small- and wide-angle neutron scattering profile of nanoporous carbon. The individual contributions from $I_{ext}(q)$ (dashed grey line), $I_{NP}(q)$ (solid grey line), and $I_B(q)$ (dotted grey line) are illustrated schematically. Vertical red dashed lines indicate the (002) stacking peak, while in-plane peaks of the atomic-scale carbon structure (hk) are marked with green dotted lines. The inset presents real-space structural models (reprinted with permission from Ref. [72]) alongside an atomic structure visualization.

For scattering vectors > 1 nm^{-1}, the slope is changing and traversing into almost constant plateau which is related to the nanopore scattering $I_{NP}(q)$, which might be described by the DAB model (see equation (2.50)). As discussed earlier, the DAB function approaches a slope of -4 in the high q-regime (~ 4 nm^{-1}), yet the experimentally observed scattering pattern decays with a slope < -4. This deviation generally could stem from two contributions, a fluctuation term $I_{fluct}(q)$ and a coherent scattering contribution $I_B(q)$, which originates from the structure factor of the carbon atoms (see also equation (2.40)). All coherent contributions to the scattering pattern are summarized in equation (2.64).

$$I_{SAS}(q) = I_{ext}(q) + I_{NP}(q) + I_{fluct}(q) + I_B(q) \tag{2.64}$$

The fluctuation term $I_{fluct}(q)$ considers imperfections of the atomistic carbon structure, thus leading to density fluctuations. Isotropic three-dimensional fluctuations lead to a constant [73], scattering vector independent, scattering contribution, comparable to Laue-scattering in alloys, which might me directly incorporated in $I_B(q)$. One dimensional fluctuation along a crystallographic direction, e.g. the (002)-stacking of graphene sheets (depicted by the inset in Figure 2.23 (b)), would cause an additional coherent contribution that decays with a slope of -2 in the high q-regime [74,75]. In the scattering vector range > 10 nm^{-1}, multiple contributions add to the scattering intensity and deviation of the ideal slope proposed by Porod´s law. In addition to possible fluctuations and scattering from small pores (< 0.5 nm, or rough pore wall), the scattering of the atomistic carbon structure becomes noticeable. The (002)-reflection of stacked graphene sheets are rather broad, which based on the discussion above, hints towards a low degree of ordering along that crystallographic direction. This is also noticeable in the atomistic structure of Figure 2.23 (b), as only a couple of layers are visibly stacked. Further this poses the question whether the separation of $I_{fluct}(q)$ and $I_B(q)$ is necessary, as the discrimination between those contributions is not unambiguous, considering the length scale of the smallest pores and the atomic distances between stacked graphene sheets being in the same order of magnitude (0.5 and 0.3 nm, respectively). Determining whether the deviation from the q^{-4} decay should be attributed to the intrinsic nanopore scattering intensity (characterized by a power-law decay with an exponent smaller than four) or treated as an additional term within the carbon structure factor appears somewhat arbitrary. In general, distinguishing between these contributions is particularly challenging for carbons with very small mean pore sizes (typically < 1 nm in our case). Given this complexity, multiple approaches exist, each of which can be considered equally valid.

2.4.6 Scattering from atomistic models of nanoporous carbons

"In the intervening more than six decades enormous progress has been made in finding approximate solutions of Schrödinger´s wave equation for systems with several electrons, decisively aided by modern electronic computers." Walter Kohn, Nobel Lecture 1998

Atomistic models of structures and molecules built a substantial part of today's materials research, as molecular simulations can be directly compared to experimental findings. Given that an atomistic model was generated by means of DFT, MD or MC, it can be used as input to calculate the scattering signal of the respective structure. In earlier chapters, the development of atomistic models of nanoporous carbons was discussed in more detail and as was promised in the beginning of this chapter, the originally derived equations shall be used in this context. Equation (2.65) is formally equivalent to equation (2.38), yet it already considers the result found by Peter Debye for the spatial averaging of the scattered wave function (Fourier transform) and is thus named, Debye equation.

$$I(q) = \frac{1}{V}\sum_i \sum_j b_i(q) b_j(q) \frac{\sin(qr_{ij})}{qr_{ij}} \tag{2.65}$$

Here the summation runs over all atoms i and j, and considers the respective coherent scattering lengths $b_i(q)$ and $b_j(q)$. This equation computes the scattering intensity as the summation of products of the coherent scattering length with $\frac{\sin(qr_{ij})}{qr_{ij}}$, where r_{ij} is the distance between the respective atoms. The solution given by the Debey equation is exact yet given the high number of atoms in the atomistic models of the nanoporous carbons (~10000 atoms), as shown in Figure 2.9, this method is computationally demanding. To decrease the computation time for such large structures a different approach might be better suited. The reciprocal lattice approach, summarized by Tomšič et. al. [76], is based on the idea to arrange duplicates of the simulation box indefinitely in all three dimensions, next to each other, leading to a 3-D periodic structure. The intensity is calculated by squaring the sum of the scattering amplitudes along specific crystallographic direction, indicated in equation (2.66) by the Miller indices (h, k, l), where $b_j(q_n)$ is the coherent scattering length of the respective pseudo-atom. The respective scattering vectors q_n are calculated by equation (2.67), which

considers the fact that only integers of n lead to constructive interference. The minimal value of the scattering vector (q_{min}) obtained is closely linked to the dimension of the simulation box L and reads: $q_{min} = \frac{2\pi}{L}$.

$$I(q_n) = \left| \sum_{j=1}^{N} b_j(q_n) \exp\left(-\frac{2\pi n}{L} i \cdot \left(hx_j + ky_j + lz_j \right) \right) \right|^2 \tag{2.66}$$

$$q_n = n \cdot \frac{2\pi}{L} \sqrt{h^2 + k^2 + l^2} \tag{2.67}$$

Thus, the computational time depends on the chosen number of lattice directions and their multiplicity as well as the number of atoms. Yet this approach reduces the number of calculations by a factor of at least N compared to the Debey equation, given the same spacing of scattering vectors and number atoms N.

For both computational approaches, a fundamental challenge arises due to the finite size of the simulation box, which contrasts with the effectively infinite sample volume in experimental measurements. In small angle scattering, this finite size leads to spurious signals at low q values, as the abrupt density discontinuity at the simulation box boundaries introduces artificial scattering features. This effect has been widely discussed in the context of molecular simulations, where the simulation box is often only slightly larger than the solute, causing unwanted contributions in the same q-range as the solute's scattering signal. However, in the case of atomistic structures of nanoporous carbons, the impact of this finite size effect is significantly reduced. Since these models contain thousands of atoms and are designed to approximate an extended, disordered network, their simulation boxes are already large compared to typical molecular simulations. As a result, the characteristic length scale of the finite size effect, which manifests at $q_{min} = \frac{2\pi}{L}$, is shifted to much smaller scattering vectors, well below the range of interest for analyzing the internal structure of the material. This ensures that the computed scattering signal primarily reflects the structural features of the nanoporous carbon rather than artifacts introduced by box boundaries, making the reciprocal lattice approach a robust tool for studying such disordered materials. Further consideration on limiting the finite size effect was given by Majumdar et. al. [77], introducing a novel

approach by combining the strengths of the reciprocal lattice approach and the Debey equation.

2.5 Neutron scattering of adsorbed hydrogen – a literature review

"What we observe is not nature itself, but nature exposed to our method of questioning." Werner Heisenberg

In 1949, Scheaffer et. al. made an observation of an isotherm displaying an unusually high helium (He) uptake for the first adsorbed layer on carbon black at 4K [78]. The first phenomenological explanation was given by Steele, assuming a double-layer formation to explain the high observed He capacity [79]. Later studies uncovered significant discrepancies in the surface area determination of Graphon (graphitized soot) using nitrogen adsorption at 77 K and hydrogen adsorption at 20 K. Their analysis suggested an intermolecular distance of 2.95 Å between hydrogen molecules in the adsorbed monolayer, pointing to a density far exceeding the three-dimensional density of solid hydrogen. In the previous chapters the interaction of neutrons with hydrogen was shown to be quite advantageous for studying the physical processes involving the molecule. The negative coherent scattering length of H_2 and the positive one for D_2 allow to study isotope effects in more detail, while the high in incoherent scattering length gives rise to the study the dynamics of the molecule. In the following recent works are discussed in more detail, highlighting how different neutron scattering techniques can contribute to a deeper understanding of some unexpected properties of molecular hydrogen in confinement.

A recent study from 2022 by Balderas-Xicohténcatl, revisited this phenomenon observed by Schaeffer and others, by combining INS and path-integral molecular dynamics simulation [80]. They studied the adsorption of H_2 and D_2 on a mesoporous silica surface, which consist solely of mesopores of size around 10 nm. In relation to the kinetic diameter of the molecule around 0.3 nm, the silica surface was assumed to be basically flat. Figure 2.24 (a) shows the adsorption isotherms measured using Ar, H_2 and D_2 and at their respective boiling points (87.3 K, 20.37 and 23.31, respectively). As stated in section 2.1.2, the BET-theory is applicable for fluids at their respective boiling point, which lead to specific areas of 359, 719 and 664 m^2/g. This observation aligns with earlier ones, and indicates that hydrogen forms a monolayer of much higher density on a silica surface, compared to Ar at its respective boiling point. The lack of microporosity within the mesoporous silica indicates that for all molecules the accessible

surface area is the same, thus the difference in monolayer capacity is attributed to the existence of a super-dense hydrogen monolayer.

Based on the determined monolayer capacity of H_2 and the surface area measured using Ar, a molecular cross-sectional area for adsorbed H_2 of 7.1 Å² was calculated. Assuming a 2D hexagonal arrangement of H_2 molecules, the corresponding intermolecular distance on the surface is 2.9 Å. If this 2D spacing were extended into three dimensions to form a hexagonal close-packed lattice, the resulting 3D density would be 202 kg m^{-3}. This density is nearly three times higher than the bulk densities of liquid hydrogen and more as double as large as the one of solid hydrogen ($\rho_{liq} = 70.9\ kg/m^3$ $\rho_s = 86\ kg/m^3$). For D_2 the same analysis yields a similar high-density monolayer with a cross-sectional area of 7.0 Å².

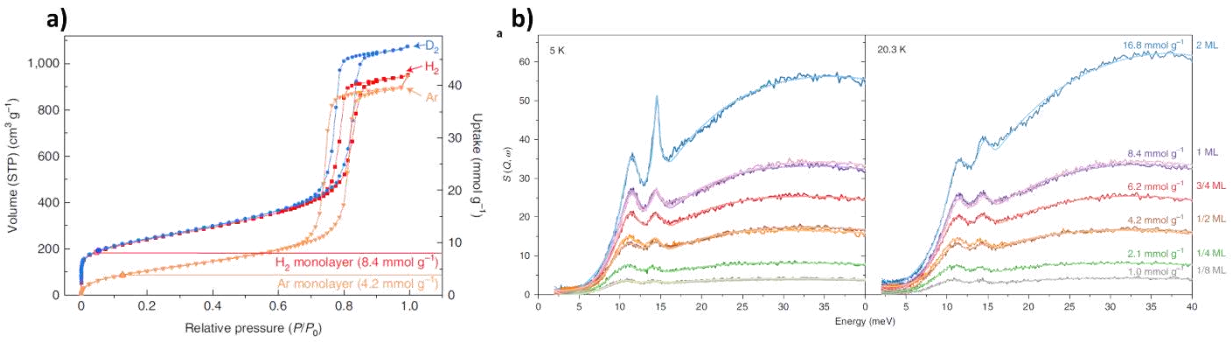

Figure 2.24: a) Adsorption isotherms of H_2, D_2, and Ar in KIT-6 at their respective condensation. All adsorbates exhibit Type IV isotherms (Ar: orange triangles; H_2: red squares; D_2: blue circles). The monolayer capacity for H_2 is twice that of Ar (8.4 mmol/g vs. 4.2 mmol/g), indicating that twice as many H_2 molecules are required to cover the surface compared to Ar atoms. b) Temperature-dependent INS spectra at various H_2 loadings: INS spectra at 5 K (left) and 20.3 K (right) correspond to coverages of 1/8, 1/4, 1/2, 3/4, 1, and 2 monolayers. All spectra feature two low-energy peaks near 11 and 14 meV, associated with hindered transitions of the free-rotor energy (14.6 meV). Reproduced from Ref. [81] and with permission from Springer Nature.

Figure 2.24 (b) shows a comparison between the INS neutron energy loss spectra collected at 5 K (left) and 20.3 K (right) after dosing different amounts of H_2 corresponding to coverages of 1/8-, 1/4-, 1/2-, 3/4-, 1- and 2-times monolayer capacity. For both temperatures the spectra show two low-energy peaks centered at energies around 11 and 14 meV and a very broad maximum at 30 meV. A detailed peak analysis revealed a splitting of the two peaks into three contributions centered around 10.6, 11.6 and 14.2 meV. The peak-splitting has been theoretically shown to result from a hindered rotation due to anisotropic interaction

potentials of the molecule with the surface. For the first adsorbed layer, the rotation is hindered, whereas the second layer behaves as a free-rotor (sharp peak at 14.6 meV) for the spectra collected at 5 K, whereas the free-rotor transition at 20.3 K seems further to be of hindered nature. Thus, the second adsorbed layer is no longer influenced by the adsorbent surface. The theoretical calculations have shown that H_2 can be packed tightly into a hexagonal arrangement with a H_2-H_2 distance of 3.2 Å, which is larger compared to the experimental finding of 2.9 Å. This high density is possible due adsorption energy of the surface exceeding the intermolecular interactions by a factor of 5, whereas the strong compressibility is also achieved by the absence of core electrons.

Similar findings have been reported earlier, observed at higher temperatures and in disordered systems containing mainly micropores (d_{50} = 0.7 nm). Ting et. al. performed INS measurements of adsorbed H_2 at different gas pressures and temperatures, which showed the presence of the rotor line (14.7 meV) at even the lowest H_2 amounts adsorbed [56]. This suggests an accumulation of solid-like H_2, rather than a dense gaseous phase that increases density with increasing pressure. The rotor line remained visible to a temperature of 100 K. Similar experiments using carbon materials exhibiting a larger mean pore size do not show the free rotor line, suggesting the confinement effects, play an influential role in this phenomenon. This was further investigated by Tian et. al. studying the disordered TE7, a single walled carbon nanotube (SWCNT) and a carbide derived carbon sample [54]. The three samples exhibit distinct but different pores sizes and geometries, thus allowing to study the influences on the H_2 densification. The combination of INS with molecular simulations of H_2 adsorption in slit- and cylindrical pores revealed a strong confinement effect for pores below 1 nm in size, whereas the same solid-like behavior was found at lowest amounts present.

The TE7 material has been proven to be a good candidate to study confinement effects, due to its bimodal PSD. The studies presented so far only probed the neutron energy loss spectra, thus the signal originating from para-H_2. Terry et. al. have also collected the neutron energy gain spectra of the TE7 material at 1 bar H_2 loading and different temperatures (see Figure 2.25 (a-d)). This allowed to study the ratio of ortho- and para-H_2 confined in the pore space at different temperatures. As discussed before, the anisotropy of the interaction potential can lead to a splitting of the rotational line. This was also observed clearly for the ortho-species.

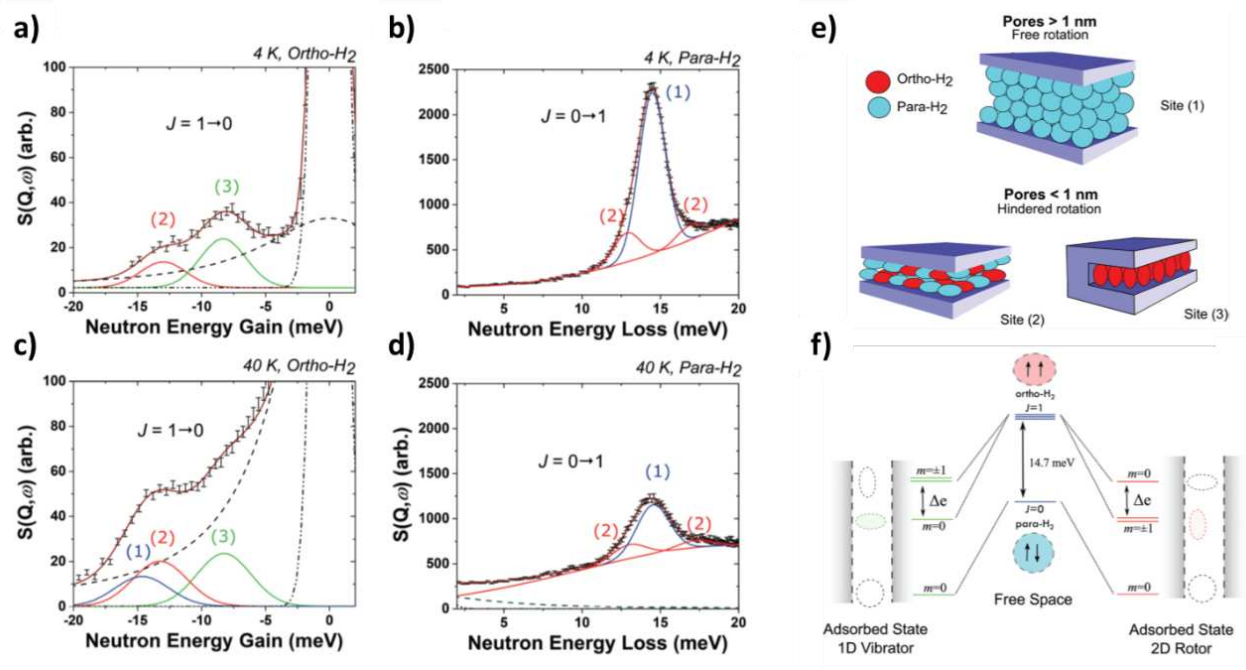

Figure 2.25: Temperature-dependent INS of J = 1→ 0 ortho-to-para and J = 0→ 1 para-to-ortho transitions of 1 bar H_2 confined in highly microporous TE7 at 4 K (a, b) and 40 K (c, d), Q = 3.4 $Å^{-1}$. Solid lines show rotational transitions: freely rotating H_2 in pores >1 nm (1) and hindered H_2 in pores <1 nm (2, 3). Dashed lines indicate elastic scattering. e) Distribution of ortho- and para-H_2 across adsorption sites in TE7 at 4 K, highlighting dominant rotational orientations and f) Quantum rotational energy levels of H_2 in free space versus within a pore with anisotropic potential: Adsorption into the pore lifts the degeneracy of J = 1 and splits the magnetic rotational sub levels. Reproduced from Ref. [38] and with permission from Royal Society of Chemistry

The overlap of the anisotropic potential from the pore walls becomes substantial, hindering the free rotation of H_2 molecules and altering their rotational energy levels. This overlap lifts the degeneracy of the triplet J=1 state, causing a 2:1 splitting of the magnetic rotational sublevels (see Figure 2.25 (f)). As the pore size decreases further, the overlapping anisotropic potential intensifies, increasing the separation of rotational energy levels for each orientation and widening the energy gap (Δe) between the split states.

In TE7, the sub-nanometer pore sizes are sufficiently small to accommodate up to a double layer of H_2, maximizing the influence of the overlapping anisotropic potential on the solid-state H_2 confined within the pores. INS measurements reveal two split peaks in a 2:1 intensity ratio for the J=0→1 excitation, which is indicative of para-H_2 trapped in micropore adsorption sites smaller than 1 nm. These findings suggest three distinct adsorption environments within the carbon structure that influence H_2 behavior: a mesopore-type environment with

diameters greater than 1 nm (site 1), and two distinct micropore environments smaller than 1 nm (sites 2 and 3). The adsorption environments also exhibit differences in molecular ordering and the para-to-ortho H_2 ratio. At 40 K, freely rotating para- and ortho-H_2 in a ratio of 87:13 were observed in the mesopore adsorption site (1). However, at 4 K, only freely rotating para-H_2 is present, indicating a rapid and complete thermodynamic conversion of ortho-H_2 to para-H_2 in pores larger than 1 nm. In contrast, micropore adsorption sites (2 and 3) exhibit a para-to-ortho ratio of 57:43 at 4 K, demonstrating that the thermodynamic conversion in sub-nanometer pores is significantly less efficient compared to larger pores. Notably, at site (3), only J=1→0 transitions were observed at all temperatures, indicating that only ortho-H_2 is adsorbed at this site. These results point to preferential adsorption and potential spin-trapping of ortho-H_2 at site (3), even at low temperatures, highlighting the reduced thermodynamic conversion rate of ortho-H_2 to para-H_2 in smaller pores. Generally, the transition rate was reported to be as slow as 0.4 %/h or as fast as 140 %/h in the presence of paramagnetic sites within the carbon material [38,82,83].

The study by Terry et. al. also included neutron diffraction experiments at different temperatures and high pressures of up to 2000 bar [38]. Figure 2.26 (a, b), shows the neutron diffractograms for a micro- and a mesoporous carbon samples, collected for two different q-ranges. The diffractograms show peaks that can be related to the presence of hexagonally closed packed (HCP) and a face centered cubic (FCC) solid H_2 phase at 10 K and pressures of 200 and 2000 bar. FCC H_2 consists of orientationally-ordered ortho-H_2 and is a metastable phase. It requires an ortho-H_2 concertation of > 60% and is achieved by the alignment of H_2 electric quadrupole moments (see Figure 2.26 (c)). The presence of the FCC phase indicated that the thermodynamic ortho-para conversion was hindered and is primarily found in micropores, as also concluded from the INS data.

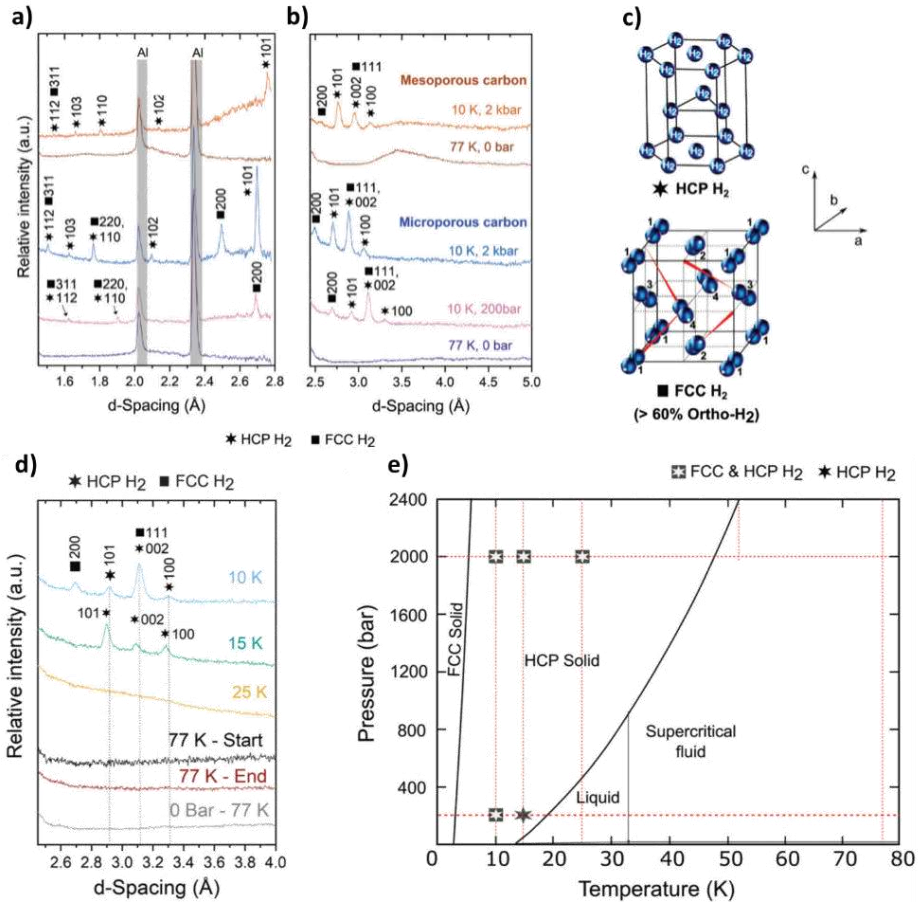

Figure 2.26: Neutron powder diffraction of confined crystalline H_2 at low temperatures: collected in two different scattering vector ranges (a and b) and H_2 pressures, for a microporous and mesoporous carbon, respectively. The Bragg peaks indicate two distinct crystalline H_2 phases: hexagonal close-packed (HCP, ★) and face-centered cubic (FCC, ■). c) Crystal structures of H_2 showing the orientationally disordered HCP lattice and the orientationally ordered FCC lattice. d) Temperature-dependent neutron powder diffraction data of microporous carbon dosed to 200 bar H_2 at 77 K. e) Bulk phase diagram of ortho-H_2 at T = 0 as a function of pressure overlaid with the observed crystalline phases of H_2 in microporous carbon. Reproduced from Ref. [38] with permission from Royal Society of Chemistry.

Figure 2.26 (d) shows the temperature dependency of the diffractogram of the microporous carbon dosed to 200 bar. The ordered FCC and HCP phase are seen at 10 K, while an increase in temperature just reveals the FCC phase. At 20 K the solid ordered phase is completely gone. This indicates that the strong confinement effects of small micropores stabilize the ordered ortho-H_2 phase, at conditions it wouldn´t be expected in the bulk phase, as shown in the phase diagram in Figure 2.26 (e).

In the earlier considerations of the mathematical derivation of the interaction of neutrons with matter, we have established that not only the spatial average can be probed, but also the time average. This gives rise to the dynamics of system and its scatters. In addition to rotational transitions, translation transitions of self-diffusional processes can be probed. From the broadening to the quasi-elastic peak diffusion constants can be calculated and linked to structure and thermodynamic properties of a system. In particular, H_2 due to its high incoherent scattering cross section gives rise to quasi-elastic scattering. Concluding from the studies presented above that hydrogen shows solid-like behavior at temperatures ranging from the melting point up to 100 K. Such a solid-like phase would be characterized by a certain degree of translational immobility. Contescu et. al. performed QENS experiments to study H_2 diffusion within two different carbon materials at temperatures from 7-37 K, thus from below the melting point to above the critical point [84]. They have applied different diffusion models to the observed quasi-elastic broadening and concluded that below 25 K, H_2 is basically immobilized due to strong confinement effects. When the temperature increases the H_2 molecules become mobile and show characteristics of a jump-diffusion-like behavior, rather than a liquid-like diffusion. This study was later continued by Bahadur and Contescu et. al. combining the QENS and INS [85]. For low amounts of H_2 adsorbed they have also found a splitting of the rotational lines due to anisotropy of the adsorption sites, whereas at higher loadings just a single free-rotor line was detected. The immobility of H_2 molecules prevailed up to temperatures of 110 K and 3.35 bar and up to 40 bar at 77 K, where bulk H_2 would be purely in the gas phase. The dynamics of H_2 within nanopore confinement is thus restricted by strong immobilization, due to anisotropic adsorption sites. In comparison, the heavier isotope D_2 exhibits a liquid-like diffusion and is mobilized at temperatures around 13 K, whereas the diffusional constant of D_2 is ~70 times higher compared to H_2 [86]. At the onset of mobility (25 and 13 K), both isotopes exhibit the same thermal de Broglie wavelength, thus getting mobile when the quantum size is getting smaller than the effective pore with (see also equation (2.14)).

The accessible time constants for diffusion are limited by the energy resolution of the used instrument ($\Delta E \Delta t \geq \frac{\hbar}{2}$). A study by Koppel et. al. tried to bridge the energy resolution of two different instruments, in order to get a more comprehensive picture of the dynamics of

confined H_2 [87,88]. They have investigated a well-ordered carbide-derived carbon, with a broad PSD, ranging from ultramicropores to large mesopores. Figure 2.27 (a and b) show the QENS spectra collected at 50 K and loadings of 10 and 31 mmol/g, respectively. Similar measurements at another instrument allowed to use the obtained quasi-elastic broadening as input for the other one, as both time-regimes are in principle convoluted within the spectra. From applying a jump-diffusional model to the observed quasielastic broadening (Figure 2.27 (c and d)) can be related to the energy of certain adsorption sites (see Figure 2.27 (d)). In the monolayer, H_2 shows low activation energy (E_a) due to strong confinement to the pore walls, limiting mobility. In subsequent layers, reduced interactions with the walls lead to higher mobility. At higher concentrations, H_2 in outer layers diffuses freely due to lower densities and minimal intermolecular interactions.

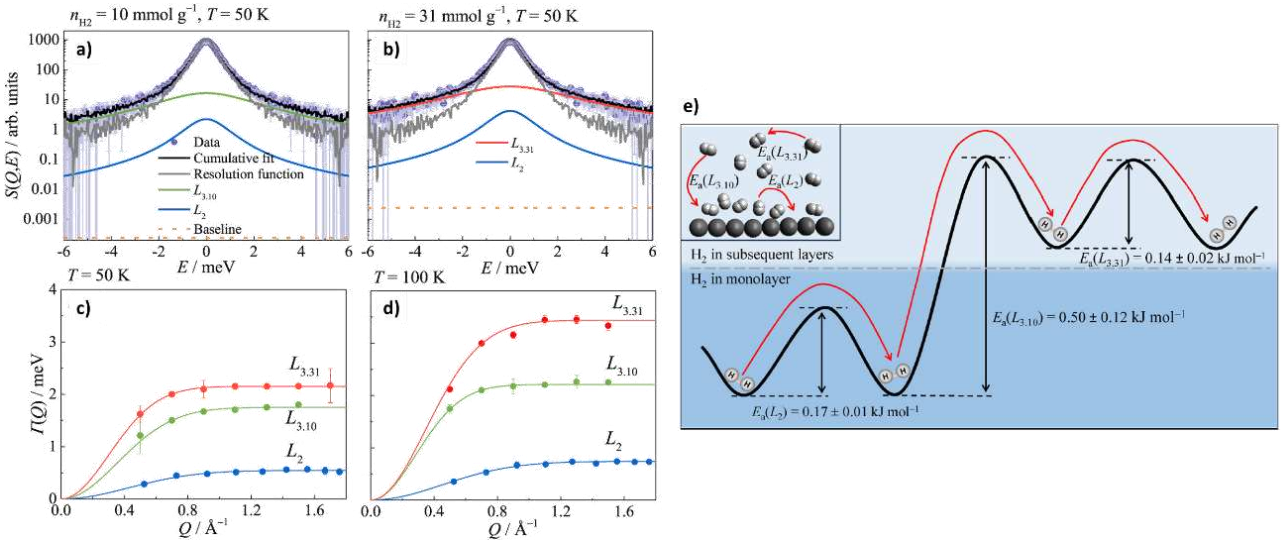

Figure 2.27: $S(Q,E)$ at $Q = 1.3$ Å^{-1} and 50 K for a loading of 10 and 31 mmol/g H_2, in a) and b), respectively. L_2, $L_{3.10}$ and $L_{3.31}$ represent the quasi-elastic components obtained by fitting the spectra (see also equation DYNAMIC). c) and d) display $\Gamma(Q)$ of the quasi-elastic broadening of the three components (blue, green and red points) at 50 and 100 K, respectively. The solid lines depict the fit of the data with the Hall-Ross model for jump-diffusion e) The proposed mechanism for the diffusion of adsorbed H_2 between various adsorption sites within the monolayer and subsequent layers is illustrated. Reproduced from Ref. [88] with permission from Elsevier.

3 Experimental methods

This section introduces the different experimental methods used to characterize the sample materials and probe the hydrogen physisorption in nanoporous carbons. The results presented in this thesis were measured on a multitude of instruments and by different contributing researchers. Table 3.2 summarizes the contributions to the later presented data, as well as giving an overview of which characterization methods have been used for each sample. The following sections describe the general experimental details used for the experiment and are valid for the samples according to Table 3.2. The affiliations of the contributing researchers are listed in Table 3.1 and their contribution to the experimental data is referenced by their initials also found in Table 3.2.

Table 3.1: Names, initials and affiliations of researchers contributing to the data presented in the thesis. The contribution to measurements is referenced in Table 3.2 by their respective initials.

Name	Initials	Affiliation
Sebastian Stock	SS	Chair of Physics, Department Physics, Mechanics and Electrical Engineering, Montanuniversität Leoben, Leoben, Austria
Malina Seyffertitz	MS	
Max Valentin Rauscher	MVR	
Nikolaos Kostoglou	NK	Chair of Functional Materials and Materials Systems, Department of Materials Science, Montanuniversität Leoben, Leoben, Austria
Stefan Zeiler	SZ	
Julian Selinger	JS	Institute of Bioproducts and Paper Technology, Graz University of Technology Department of Bioproducts and Biosystems, Aalto University, Aalto, Finland
Theodore Steriotis	TS	Institute of Nanoscience and Nanotechnology, National Center for Scientific Research "Demokritos", Athens, Greece
Christos Tampaxis	CT	
Bruno Demé	BD	Institut Laue Langevin, Grenoble, France
Viviana Cristiglio	VC	
Volker Presser	VP	INM – Leibniz Institute for New Materials, Saarbrucken, Germany
Nicholas Corrente	NC	Department of Chemical and Biochemical Engineering, Rutgers, The State University of New Jersey, Piscataway, United States

Table 3.2: Experimental techniques used to characterize the nanoporous carbon materials regarding structure, hydrogen uptake performance and samples used for in-situ neutron scattering experiments. The initials in the parentheses reference to contributing researches and the respective affiliations are found in Table 3.1.

Method	Gas sorption analysis Autosorb IQ3		X-ray scattering		Chemical analysis	Hydrogen adsorption			Neutron scattering at the Institute Laue Langevin
Material	N_2	CO_2	SAXS Bruker	XRD Bruker	CHNS-O	Autosorb IQ3	SETARAM	Hiden IMI	SANS D16 (BD, VC)
ACC	✓ (SS, NK)	✓ (SS, NK)	✓ (SS)	✓ (SS)	✓ (VP)	✓ (SS)		✓ (SS, MS)	✓ (SS, MS)
MSC-30	✓ (SZ)	✓ (SZ)	✓ (SS)			✓ (SZ)		✓ (SS, NK)	✓ (SS, NK)
MSP20-X	✓ (SS, NK)	✓ (SS, NK)	✓ (SS)	✓ (SS)		✓ (SS, NK)		✓ (SS, MS)	✓ (SS, MS)
YP80-F	✓ (SS, NK)	✓ (SS, NK)	✓ (SS)	✓ (SS)	✓ (VP)	✓ (SS, NK)		✓ (SS, MS)	✓ (SS, MS)
UTL samples	✓ (SS, NK)		✓ (SS)	✓ (SS)	✓ (JS)	✓ (SS, NK)	✓ (TS, CT)		
OP samples	✓ (SS, NK)		✓ (SS)	✓ (SS)	✓ (JS)	✓ (SS, NK)	✓ (TS, CT)		

3.1 Materials characterization

3.1.1 Materials synthesis

The activated carbon materials studied within the framework of this thesis were synthesized from different precursors and activated using different agents. The activated carbon cloth (ACC) material was synthesized from a viscose rayon cloth, that underwent an impregnation in an aqueous mixture of NH_4Cl and $ZnCl_2$, with a subsequent carbonization at 630°C under nitrogen atmosphere. Subsequently, an activation step under CO_2 atmosphere at 930°C was performed. More details to the synthesis can be found in Ref. [89]. The phenol-based MSP20-X and the petroleum coke-based MSC-30 are commercially available activated carbon powders and are activated using KOH (Kansai Coke and Chemicals Co., Japan). The coconut shell-derived activated carbon YP80-F (Kuraray Chemical Co., Japan) is generally activated using steam.

The other nanoporous carbons outlined in Table 3.2 were synthesized through a two-step process of carbonization and chemical activation, following the method outlined by Gupta et al. [90,91]. Used tea leaves (UTL) and orange peels (OP) were individually washed and dried overnight at 60 °C in a furnace before being ground into fine powders. The pre-carbonization step was performed at 450 °C for 2 hours under a nitrogen atmosphere, with a controlled heating rate of 5 °C/min. The resulting pre-carbonized tea leaves and orange peels, which remained non-activated at this stage, are referred to as UTL0 and OP0, respectively. Subsequently, the powders underwent chemical activation using KOH. For each activation step, 1 g of pre-carbonized tea leaves or orange peels was mixed with KOH in a 1:1 mass ratio. The mixtures were then pyrolyzed in a tube furnace (OTF-1200X-100-HNG, MTI Corporation, USA) at 800 °C for 2 hours under a nitrogen flow of 50 cm^3/h, maintaining a heating rate of 5 °C/min. The process utilized a quartz (SiO_2) tube with alumina (Al_2O_3) sample holders for both pre-carbonization and activation. Following pyrolysis, the activated carbon powders were washed thoroughly with 1 M HCl and deionized water, then dried overnight at 60 °C. The activation procedure was also conducted with higher KOH mass ratios of 1:2 and 1:3, producing additional samples. The final activated carbons derived from UTL0 and OP0 are

designated as UTL1, UTL2, UTL3, and OP1, OP2, OP3, where the numerical suffix represents the KOH-to-carbon ratio. A schematic representation of the synthesis process is provided in

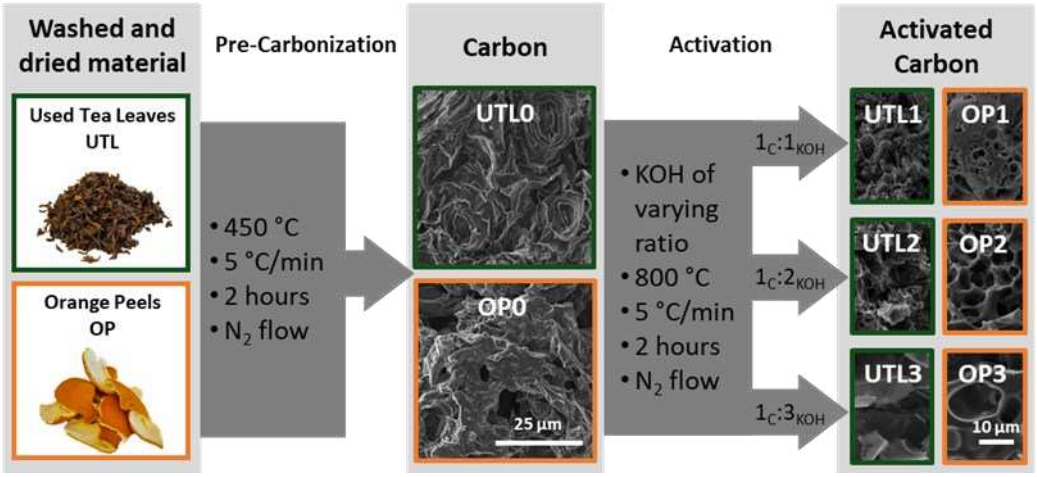

Figure 3.1: Schematic representation of the synthesis process from used tea leaves and orange peels to nanoporous carbons, including SEM images depicting the material's morphology after carbonization and activation.

3.1.2 Gas sorption analysis and hydrogen sorption experiments

The following description of the gas sorption analysis and the hydrogen sorption experiments is valid for all samples studied, according to the methods used as outlined in Table 3.2 for each sample, respectively.

Low-pressure gas sorption experiments were performed with an Autosorb iQ^3 gas sorption analyzer (Anton Paar QuantaTec) using N_2 and CO_2 gases of ultra-high purity (i.e., 99.999% and 99.995%, respectively) as adsorbates. The carbon mass for each measurement was around 40 mg. Before the respective measurements, the sample was outgassed under vacuum (10^{-6} mbar) for 24 h at 250 °C. The dead volume of the sample cell was reduced by inserting non-porous glass filler rods, which were automatically assessed using He (purity 99.999%) gas before each run. N_2 adsorption/desorption isotherms were measured at 77 K using liquid N_2 as cryogen in the relative pressure (P/P_0) range of 10^{-6}-0.99 in 77 steps for adsorption and 36 steps for desorption. CO_2 adsorption/desorption isotherms were collected at 273 K with 48 adsorption points and 20 desorption points in the absolute pressure range of 1.23 - 1060 mbar,

where the temperature was controlled using a circulation bath filled with a mixture of water and anti-freezing liquid.

Both the quenched solid density functional theory (QSDFT) method using the N_2-carbon equilibrium transition kernel at 77 K for slit pores [20] and the multi-point Brunauer-Emmet-Teller (BET) method using the BET consistency criteria (ISO 9277:2022) were used to determine the specific surface area from the N_2 sorption data. Using the QSDFT method, the specific pore volume and pore size distribution (PSD) were also determined. A Grand Canonical Monte Carlo (GCMC) or NLDFT kernel for CO_2 adsorption on carbon materials was used to calculate the PSD between 0.35-1.50 nm [92].

Low-pressure H_2 and D_2 (99.999% purity) adsorption/desorption isotherms were collected with an Autosorb iQ3 gas sorption analyzer (Anton Paar QuantaTec) at 77 K and 87 K using 57 adsorption and 20 desorption points starting from 10^{-3} mbar to 1000 mbar. For the 77 K measurements, a liquid N_2 bath was used, while the same bath was coupled with a CryoSync cryostat (Anton Paar QuantaTec) to reach 87 K.

High pressure H_2 adsorption/desorption isotherms (0 to 100 bar) were recorded using a SETARAM Hy-Energy PCTPro-2000 manometric system and ultra-pure (99.999%) H_2 gas. Excess H_2 adsorption isotherms were measured at 77 K using a liquid nitrogen bath. Each sample, approximately 200 mg, was loaded into a stainless-steel sample holder and subjected to degassing under high vacuum conditions (10^{-6} mbar) at 250 °C for 12 h. Before each measurement, the dead volume was determined through a series of volume calibrations conducted at 303 K using ultra-pure (99.999%) He gas. Consequently, the dead volume at the experimental temperature was determined by a reference volume calibration curve in order to prevent potential calibration errors stemming from He adsorption at 77 K. The reference curve was generated by conducting multiple volume calibrations at 303 K and 77 K using varying quantities of a non-adsorbing material (non-porous glass) within the same sample holder.

3.1.3 X-ray Scattering

Small-angle X-ray scattering (SAXS) measurements were performed using a NanoStar laboratory SAXS setup (Bruker AXS). The system featured an X-ray micro-source operating at 45 kV and 0.65 mA, producing Cu Kα radiation with a wavelength (λ) of 0.1549 nm. A Vantec 2000 area detector was used to measure the SAXS signal. The isotropic 2D scattering patterns were azimuthally averaged to derive the scattered intensity as a function of the scattering vector length ($q = 4\pi \sin\theta\ /\lambda$, 2θ being the scattering angle).

X-ray diffraction (XRD) measurements were carried out using a D8 Advance Eco instrument (Bruker AXS). The setup included an X-ray sealed tube with a Cu anode operating at 40 kV and 25 mA, paired with an energy-sensitive LYNXEYE-XE detector. Data acquisition covered an angular range (2θ) from 10° to 130°, with a step size of 0.01° and an exposure time of 1 second per step, utilizing a zero-background sample holder. To mitigate air scattering effects, measurements were also performed with an empty sample holder under identical conditions, and the resulting background signal was subtracted from the sample data.

3.1.4 Chemical analysis

In the study outlined in section 4.1, regarding the UTL and OP samples, a Thermo Scientific FlashSmart Elemental Analyzer was utilized to analyze the carbon, hydrogen, nitrogen, sulfur and oxygen (CHNS/O) contents of the tea leaves and orange peel-derived samples. Approximately 2.5 mg of sample powder was placed in a tin or silver cup for each measurement, with 8-10 mg of vanadium pentoxide added as a catalyst. BBOT (2,5-Bis(5-tert-butyl-benzoxazol-2-yl)thiophene) served as the standard for all measurements. The samples underwent combustion in an oxygen atmosphere for CHNS analysis, while a He flow was employed for pyrolysis to quantify the oxygen content.

For the study outlined in section 4.1, regarding the ACC and YP80-F, the CHNS-O analysis was conducted on the samples both before and after sulfidation to determine sulfur and oxygen content (measurements were performed by Volker Presser et. al.). The CHNS analysis was performed using a Vario Micro Cube (Elementar). A standard amount of WO_3 was added to each sample during weighing. Samples were placed into tin boats, compressed to remove air,

and directly loaded into the CHNS analyzer's autosampler. Calibration was carried out using sulfanilamide standards provided by the manufacturer, with theoretical values of 16.26 mass% N, 41.85 mass% C, 4.68 mass% H, and 18.62 mass% S. The combustion tube was operated at 1150 °C, and the reduction tube at 850 °C. Oxygen content was analyzed using a rapid OXY cube (Elementar). Samples were weighed into silver boats, compressed to exclude air, and then loaded into the O-analyzer's autosampler. Calibration was performed with benzoic acid standards of varying weights, provided by the manufacturer, with a theoretical oxygen content of 26.2 mass%. The daily calibration factor was determined by measuring approximately 3 mg of benzoic acid five times prior to analysis. The pyrolysis temperature for oxygen measurement was 1450 °C.

3.2 Statistical analysis - Kendall Rank Correlation Coefficient

The statistical analysis and visualization of the correlation matrix were performed by Claus Othmar Wolfgang Trost. Kendall's τ_b [93] is a non-parametric rank correlation coefficient, meaning it does not require any assumptions about the distribution or linearity of the data. It evaluates the relationship between two ranked variables, indicating the direction of the correlation through positive and negative values—where positive values represent a direct association, and negative values indicate an inverse relationship. The absolute value of τ_b reflects the strength of the correlation, with values close to 0 signifying no correlation, while values approaching ±1 indicate a strong association. The correlations in this study were computed using Kendall's τ_b as implemented in SciPy [94]. Kendall's τ_b is mathematically defined as:

$$\tau_b = \frac{P - Q}{\sqrt{(P + Q + T) * (P + Q + U)}} \tag{3.1}$$

where:

- P represents concordant pairs (where both variables increase or decrease together),
- Q represents discordant pairs (where one variable increases while the other decreases),
- T accounts for ties in the first variable (x), and
- U accounts for ties in the second variable (y).

If a tie occurs in both variables within the same pair, it is not included in either T or U. Kendall's τ_b was selected over Spearman's correlation due to its better suitability for small sample sizes. To ensure meaningful p-values, a minimum of 10 samples is recommended [95]. Given the limited dataset, the analysis was extended by incorporating additional parameters from activated carbons reported in references [96] and [57]. Furthermore, Kendall's τ_b has been shown to be less susceptible to Type I errors (incorrect rejection of a true null hypothesis) in cases with small sample sizes [95].

It is important to note that small p-values do not indicate a stronger correlation but rather provide evidence of statistical significance ($p < 0.05$), meaning the observed correlation is unlikely to occur under the assumption of parameter independence [95].

3.3 Grand-canonical Monte Carlo simulations

Grand-Canonical Monte Carlo (GCMC) simulations were performed by Nicholas Corrente using the open-source RASPA2 software [97]. Forcefield parameters for the adsorbate and adsorbent molecules are detailed in Table 6.7 of the Supplementary Information. H_2 and D_2 molecules were modeled as Lennard-Jones (LJ) spheres with Feynman-Hibbs (equations (2.15) and (2.16)) corrections to account for quantum effects. N_2 and structural carbon were modeled as LJ spheres. GCMC simulations were performed on each carbon model using 50000 MC cycles, with the latter 25000 cycles used for statistical averaging.

3.4 In-situ small angle neutron scattering at the D16 instrument

Small-angle neutron scattering (SANS) experiments were conducted at the small momentum transfer diffractometer D16 at the Institute Laue-Langevin (Grenoble, France) using a wavelength of λ = 0.447 nm. The neutron beam dimension at the sample position was shaped by slits of (25×3) mm^2 (see Figure 3.3 (c)) and centered on the cylindrical aluminum sample holder (EN AW-7049A) of an inner diameter of 6 mm, wall thickness of 0.5 mm and length of 66 mm (see Figure 3.4 (a)). The neutron beam intentionally under-illuminated the sample cell to avoid edge scattering effects of the cell and for proper sample transmission measurements. For the experiments associated with proposal number 1-04-218 (http://doi.ill.fr/10.5291/ILL-DATA.1-04-218) and 1-04-235 (http://doi.ill.fr/10.5291/ILL-DATA.1-04-235), the of scattering vector range ($q = 4\pi \sin\theta\,/\lambda$, 2θ being the scattering angle) of 0.4-20 nm^{-1}, was achieved using 5 detector positions (see also Figure 3.3 (c)). for each SANS data set the data acquisition time was 1 min for transmission measurements using an attenuator of the direct beam, 5 min each for the first two, and 10 min each for the remaining three detector positions leading to a total measurement time of roughly 45 min (including detector- and beam stop movement and data saving). The SANS data were corrected for detector pixel efficiency and solid angle, sample transmission, then radially averaged using and the empty aluminum cell scattering was subtracted using the ILL's LAMP package [98]. For correction to absolute units, the incoherent scattering of a Vanadium standard of the same thickness as the sample holder was measured at the same conditions. Since the measured intensity from the Vanadium sample displayed small-angle scattering at low q, and a slight increase of the intensity also for q > 10 nm^{-1}, as seen in Figure 3.2, the mean scattering intensity $\overline{I_{meas,V}}$ was calculated in the interval 3 < q < 10 nm^{-1}. The macroscopic differential scattering cross section of the sample was then calculated by $\left(\frac{d\sigma}{d\Omega}\right)_{sample} = \frac{I_{meas,sample}}{\overline{I_{meas,V}}} \cdot \left(\frac{d\sigma}{d\Omega}\right)_V$, with the differential scattering cross section of vanadium $\left(\frac{d\sigma}{d\Omega}\right)_V = 0.029\ cm^{-1}$.

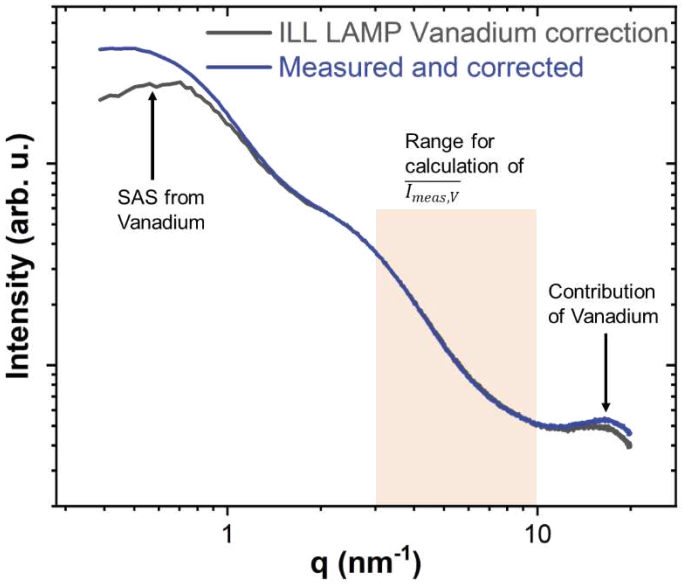

Figure 3.2: Comparison of the SANS signal from ACC as measured at D16 (blue) and the Vanadium corrected signal, which shows a contribution for low scattering vectors. Thus the correction procedure outline in the text was applied, whereas the orange box indicates the range for the calculation of $\overline{I_{meas,V}}$.

For the dataset associated with proposal number 1-04-242 (http://doi.ill.fr/10.5291/ILL-DATA.1-04-242), the upgraded detector set-up at the D16 instrument was used (see Figure 3.3 (d)). This allowed to cover a q-range from 0.4-25 nm^{-1} using three detector positions. The data correction for transmission and merging was performed in the Mantid software package [99], whereas the absolute units calibration was performed using a vanadium calibration standard.

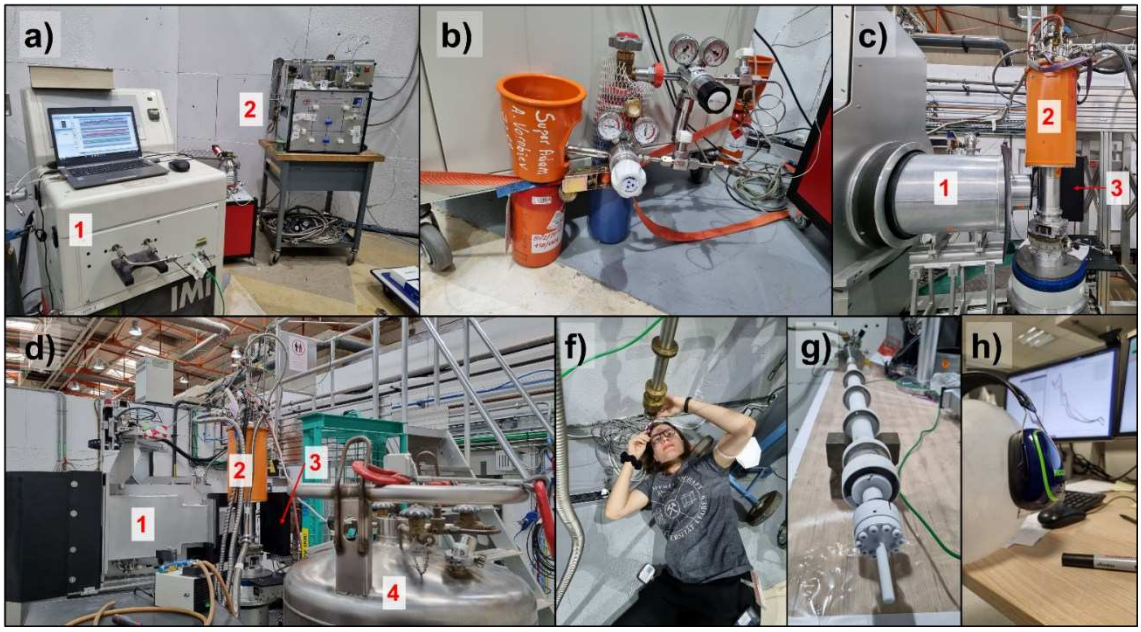

Figure 3.3: a) 1: Hidden Isochema IMI Sievert-apparatus equipped with low -pressure sensor, ranging from 0-1 bar with an accuracy of 0.2% of maximum pressure, 2: gas mixing station to achieve a zero scattering length density gas mixture of H_2 and D_2. b) H_2 and D_2 gas containers with connection to the Hidden Isochema IMI Sievert-apparatus. c) 1: neutron detector of the D16 instrument before the upgrade in 2022, 2: Orange cryo-furnace (1.5-500 K) for cooling the sample to the temperature of interest. The accuracy of the temperature regulation during the SANS data acquisition time was ΔT= ±0.03 K. 3: slit-collimation and neutron beam entry. d) 1: neutron detector of the D16 instrument after the upgrade, 2: Orange cryo-furnace, 3: slit-collimation and neutron beam entry, 4: liquid nitrogen tank to refill the outer cooling layer of the orange cryostat. f) PhD-student attempting a sample change on the sample stick (printed with permission from Malina Seyffertitz). g) sample stick with mounted sample cell after removing from the cryostat. h) work safety instructor (Moldex) showcasing use of personal protection equipment, while discussing SANS spectra measured at D16.

For the in-situ measurements, a Hidden Isochema IMI Sievert-apparatus equipped with low -pressure sensor, ranging from 0-1 bar (with an accuracy of 0.2 % of maximum pressure), was used to dose H_2 and D_2 (99.999 %) into the system We used an Orange cryo-furnace (1.5-500 K) for cooling the sample to the temperature of interest, as shown in Figure 3.3 (c). The accuracy of the temperature regulation during the SANS data acquisition time was ΔT= ±0.03 K. Before transferring to the aluminum sample cell to the cryostat, the samples were degassed for more than 24 h at 250 °C under a vacuum of 10^{-3} mbar. After transfer, the sample void volume was calibrated using 30 bar of He at room temperature, followed by a subsequent vacuuming step for at least 1 h and cooling to analysis temperature. A measurement sequence consisted of placing the powder sample into the cryo-furnace and vacuuming until the analysis

temperature was reached (at least 1 h) and subsequent collection of the scattering signal of the empty carbon sample. Subsequently, hydrogen was dosed in multiple steps to reach the first desired pressure point, and an equilibration time of 15 min was waited to reach equilibrium before starting the SANS measurement. This cycle continued until a pressure of about 1000 mbar was reached, and the sample was placed under a vacuum for 1 h before starting the next measurement sequence.

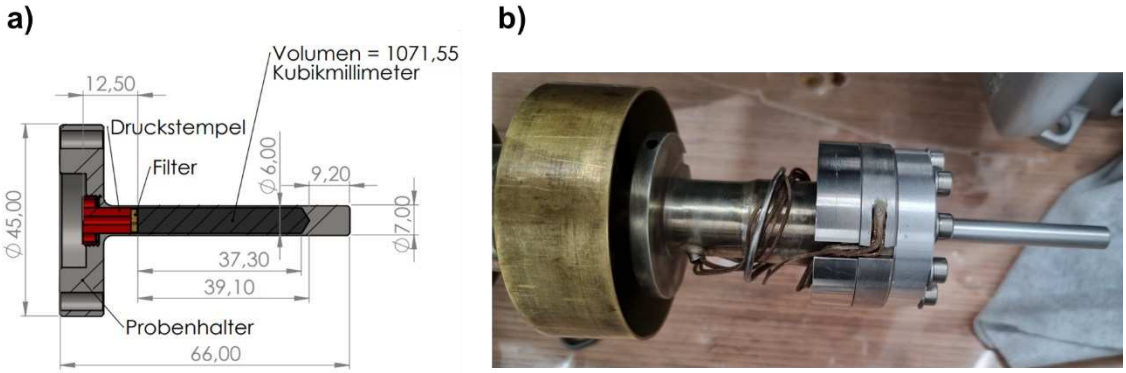

Figure 3.4: a) Adapted powder sample holder (original ILL SANE) to ensure stable powder pouring density throughout the experiments. The sample holder includes a screw-in plunger (red) to compact the sample. b) sample holder mounted on the sample stick and connected to the cold-head. The wires are the Pt-elements for accurate temperature reading of the sample cell and thus the powder.

“There are two possible outcomes: if the result confirms the hypothesis, then you've made a measurement. If the result is contrary to the hypothesis, then you've made a discovery.”

-Enrico Fermi-

Results and Discussion

The postulate by Enrico Fermi shall guide the following presentation and discussion of the results of the experiments and simulations performed within the framework of this thesis and the last 4 years. In the previous section the experimental methods and the samples investigated were outlined. Based on these methods, the following chapters introduce first the basic characterization of nanoporous carbons and further introduces the results obtained by scattering techniques. Furthermore, the influences on supercritical hydrogen adsorption in selected carbon materials is discussed. In the last chapter the several aspects of the results obtained by neutron scattering measurements performed at the small momentum transfer diffractometer D16 are discussed.

4 Characterization of nanoporous carbons

In the earlier chapters the complexity of nanoporous carbons has been highlighted and several characterization methods have been established within this scientific community. To understand the hydrogen storage performance, it is important to have an in depth understanding of the pore structure and chemical composition of the carbon materials.

4.1 Chemical composition

The chemical composition of nanoporous carbons, regarding carbon content and heteroatom concentration varies significantly based on the used pre-cursor and activation method. The chemical composition of the samples was determined by means of elemental combustion analysis, which is limited to the detection of carbon, oxygen, nitrogen, hydrogen and sulfur. Other techniques, like X-ray photoelectron spectroscopy (XPS), lack the ability to detect light elements, like hydrogen, yet reveal the presence of heavier elements, like metals, which might originate from the activation process. Nevertheless, the discussion within this thesis is based on the aforementioned elements, as especially in neutron scattering the prevalent hydrogen content is of importance.

The ACC material was synthesized from a viscose rayon cloth, which basic building block, viscose rayon ($C_{18}H_{32}O_{16}$), contains around 50 and 6 mass% of O and H, respectively, which is

also reflected in the chemical composition of the carbon sample. The phenol-based MSP20-X and the petroleum coke-based MSC-30 show a much lower O and H content [100]. The coconut shell-derived activated carbon YP80-F has a comparable composition as the other commercially available samples.

Table 4.1: Chemical composition of the nanoporous carbon samples based on the elemental combustion analysis.

Element	Carbon (mass%)	Oxygen (mass%)	Nitrogen (mass%)	Hydrogen (mass%)	Sulfur (mass%)	Reference
ACC	70.2	26.3	1.6	1.9	n.d.	[57]
MSC-30	95.0	3.99	0.3	0.55	-	[100]
MSP20-X	95.5	3.37	0.11	0.25	-	[100]
YP80-F	94.6	1.5	0.2	0.4	n.d.	(VP)
UTL0	81.8	12.7	4.5	0.9	0.1	
UTL1	91.3	5.1	1.0	2.6	n.d.	
UTL2	92.4	4.6	0.3	2.7	n.d.	
UTL3	91.3	5.3	0.3	3.0	n.d.	
OP0	83.9	12.9	2.3	0.9	0.1	
OP1	91.6	5.5	0.2	2.7	n.d.	
OP2	91.8	5.2	0.0	2.9	n.d.	
OP3	91.9	4.4	0.4	2.9	0.4	

Orange peels are primarily composed of polysaccharides such as cellulose, lignin, and hemicellulose, with a protein content of 3–6 mass% (wet basis) and a water content of around 50 mass% [101,102]. Fresh tea leaves share a similar composition but contain a higher protein content, reaching up to 15 mass% in dried tea leaves [103]. This difference is reflected in the nitrogen content of the pre-carbonized samples, with UTL0 containing 4.1 mass% nitrogen compared to 2.1 mass% in OP0 (see Table 4.1). After the initial pyrolysis step at 800°C with a

C:KOH ratio of 1:1, the carbon content increases from 74.2 to 89.1 mass% in UTL1 and from 77.9 to 89.9 mass% in OP1. Concurrently, the oxygen content—primarily derived from the polysaccharide backbone—decreases by approximately 50% in both precursor materials due to reactions with carbon. This shift is attributed to more complete carbonization and the removal of oxygen-rich volatile compounds (e.g., water vapor, carbon dioxide, methane, acetic acid, and methanol) at high temperatures. As the KOH ratio increases, nitrogen content systematically declines, dropping from 4.1 mass% in UTL0 to 0.3 mass% in UTL2 and UTL3, and from 2.1 mass% in OP0 to undetectable levels in OP2. This decrease likely results from enhanced interactions between KOH and nitrogen-containing carbon structures, leading to the release of nitrogenous gases such as N_2, HCN, and NH_3 [104,105].

Hydrogen content follows an increasing trend with rising KOH ratios, from 0.8 mass% in UTL0 to 2.7 mass% in UTL3, and from 0.8 mass% in OP0 to 2.8 mass% in OP3. This trend is attributed to hydrogen gas formation during KOH activation, primarily driven by the water-gas shift reaction ($CO + H_2O \rightarrow CO_2 + H_2$) and the water-gas reaction ($C + H_2O \rightarrow CO + H_2$) [106]. As KOH interacts with carbon, the released hydrogen gas may adsorb onto the carbon surface, leading to the formation of hydroxyl (-OH) and other hydrogen-containing functional groups.

Sulfur is either absent or present in trace amounts, with a slight increase to 0.4 mass% detected in OP3. The residual mass after combustion analysis, representing inorganic elements and ash content, is measured at 9.2% and 11.0% for UTL0 and UTL3, and 7.1% and 11.6% for OP0 and OP2, respectively. These residues are likely associated with naturally occurring inorganic mineral deposits, such as cystoliths ($CaCO_3$), in the raw plant material or residual minerals from the KOH activation process that were not entirely removed by washing with 1M HCl. Due to the small quantity of remaining material, further chemical characterization of these combustion residues was not performed.

4.2 Nanopore structure – Gas sorption analysis

The pore structure characteristics can be evaluated from gas sorption analysis, as outlined in section 2.1, where different adsorbates and analysis methods provide a comprehensive understanding of the materials' porosity. The CO_2 adsorption isotherms, shown in Figure 4.1 (a), and the corresponding pore size distributions (PSDs) derived using the GCMC slit-pore kernel on CO_2 adsorption data [92], presented in Figure 4.1 (c), allow for the characterization of ultramicropores. Meanwhile, the N_2 adsorption isotherms at 77 K, depicted in Figure 4.1 (b), along with their respective PSDs obtained using the N_2-carbon QSDFT slit-pore kernel [20] in Figure 4.1 (d), provide insight into the presence of larger micropores and small mesopores. Table 4.2 summarizes the structural parameters derived from the CO_2 and N_2 isotherms, including specific surface area, total specific pore volume, specific volumes of the three pore classes, and mean pore width. Micropores, comprising both super- and ultramicropores, are crucial in defining the adsorption properties of the materials.

For ACC, the CO_2 adsorption isotherm reveals a well-developed microporous structure, with a dominant ultramicropore size of approximately 0.7 nm. The PSD derived from GCMC analysis confirms two distinct peaks, reflecting a significant presence of micropores, particularly in the ultramicropore range. The N_2 adsorption isotherm, classified as Type I(b) according to IUPAC [13], exhibits a steep uptake at low pressures ($P/P_o < 0.1$), indicative of strong gas-solid interactions in narrow micropores. The QSDFT-derived PSD confirms that the majority of the pore volume is attributed to micropores, with only a minor fraction of small mesopores (~2.5 nm). ACC has the lowest overall surface area among the studied materials.

MSC-30, in contrast, displays a broader pore size distribution, with a slightly larger average micropore size (~0.85 nm) and higher micropore volume compared to ACC. The CO_2 adsorption confirms the presence of both ultramicropores and supermicropores, with the latter being more dominant than in ACC. The N_2 adsorption isotherm follows a Type I(b) profile, confirming a primarily microporous structure with minor mesoporosity. The QSDFT-derived PSD presents a bi-modal distribution, with peaks in both the micropore and small mesopore ranges, supporting an increased mesopore volume that enhances gas accessibility at higher pressures.

MSP20-X exhibits the highest CO_2 surface area, indicating an exceptionally well-developed microporous network. The CO_2 adsorption isotherm suggests a dominant ultramicropore size of 0.71 nm, with a significantly larger fraction of ultramicropores (~0.6 nm) compared to MSC-30. The N_2 adsorption isotherm follows a Type I(b) classification, with a steep uptake at low pressures and a plateau at higher relative pressures, confirming its predominantly microporous nature. The QSDFT-derived PSD further reinforces this observation, showing that nearly all pore volume is confined to micropores, with minimal mesoporosity.

YP80-F, in contrast, has the lowest CO_2 uptake among all samples, indicating the smallest ultramicropore surface area and total micropore volume. The CO_2-derived mean pore size (~0.79 nm) suggests a slightly broader micropore distribution than MSP20-X but still within the ultramicropore range. The N_2 adsorption isotherm follows a Type I(b) classification, but the more gradual pore filling mechanism suggests a wider micropore size distribution. Additionally, YP80-F displays a small H4 hysteresis loop with a closure point at P/P_o ~0.4, likely due to cavitation-induced evaporation from mesopores. Unlike the other materials, YP80-F does not exhibit a clear saturation plateau at high pressures, suggesting the presence of macropores (>50 nm) and/or adsorption on external surfaces. The QSDFT-derived PSD confirms higher mesopore surface area and total pore volume compared to MSP20-X, with a larger mean pore size (~1.16 nm). Overall, the analysis of the adsorption isotherms and PSDs highlights substantial differences in pore structures among the materials. While ACC and MSP20-X predominantly feature microporous architectures, MSC-30 and YP80-F exhibits a broader pore size distribution that extends into the mesoporous regime.

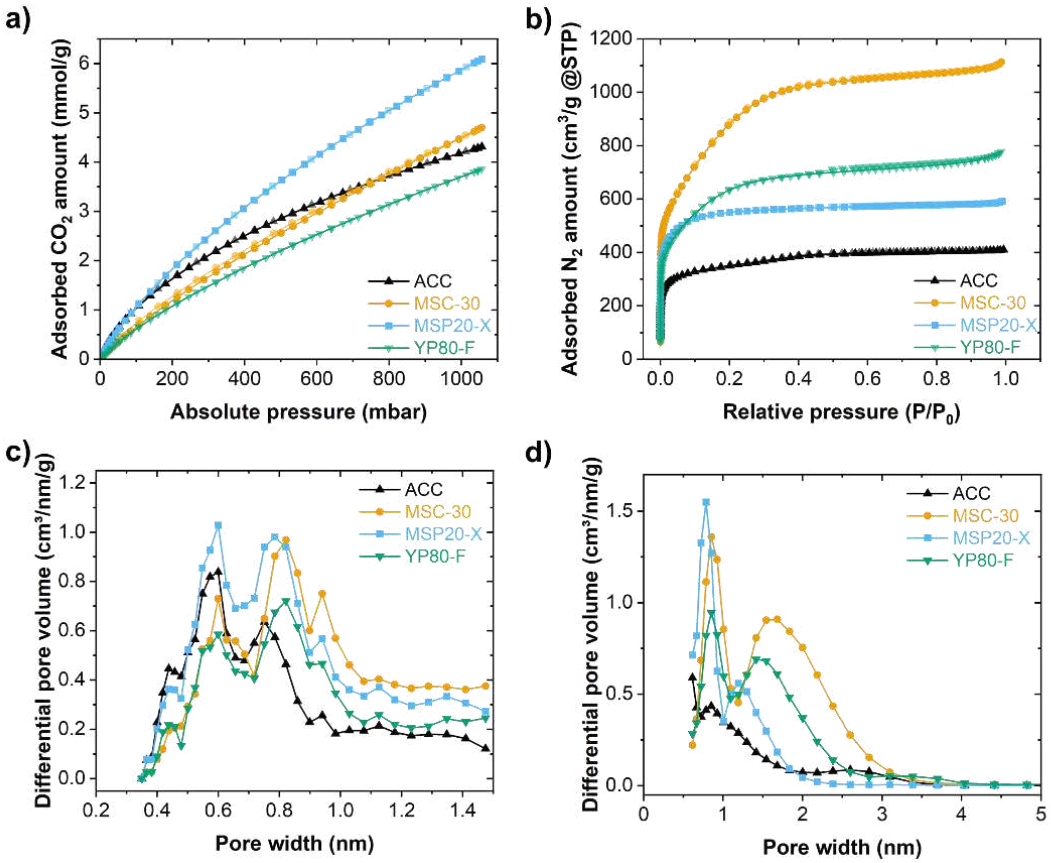

Figure 4.1: Gas sorption measurements of the ACC, MSC-30, MSP20-X and YP80-F activated carbon powders: a) CO_2 adsorption isotherms collected at 273 K, b) N_2 adsorption isotherms collected at 77 K, c) PSD obtained from the CO_2 adsorption isotherms using the GCMC slit-pore kernel and d) PSD obtained from the N_2 adsorption isotherms using the QSDFT slit-pore kernel.

Figure 4.2 (a) and (c) display the N_2 adsorption isotherms recorded at 77 K for the UTL and OP samples, respectively. The non-activated samples, UTL0 and OP0, show minimal N_2 uptake, indicating the absence of open porosity. In contrast, activated samples exhibit a significant increase in N_2 uptake with higher amounts of activation agent, reflecting the development of nanoporous structures. All samples show Type I isotherms, classified as I(a) for most samples and I(b) for UTL3 and OP3, according to the International Union of Pure and Applied Chemistry (IUPAC) standards for microporous materials (<2 nm pore width) [13]. Some samples also exhibit small Type H4 hysteresis loops, particularly UTL1, UTL2, and OP1, indicating the presence of ink-bottle-shaped pores with neck sizes smaller than 4–5 nm. The hysteresis closure point around $P/P_0 \approx 0.45$ suggests cavitation-induced N_2 evaporation [13]. A slight

increase in N_2 uptake near P/P_0 = 1 corresponds to adsorption on the external surface or condensation in macropores.

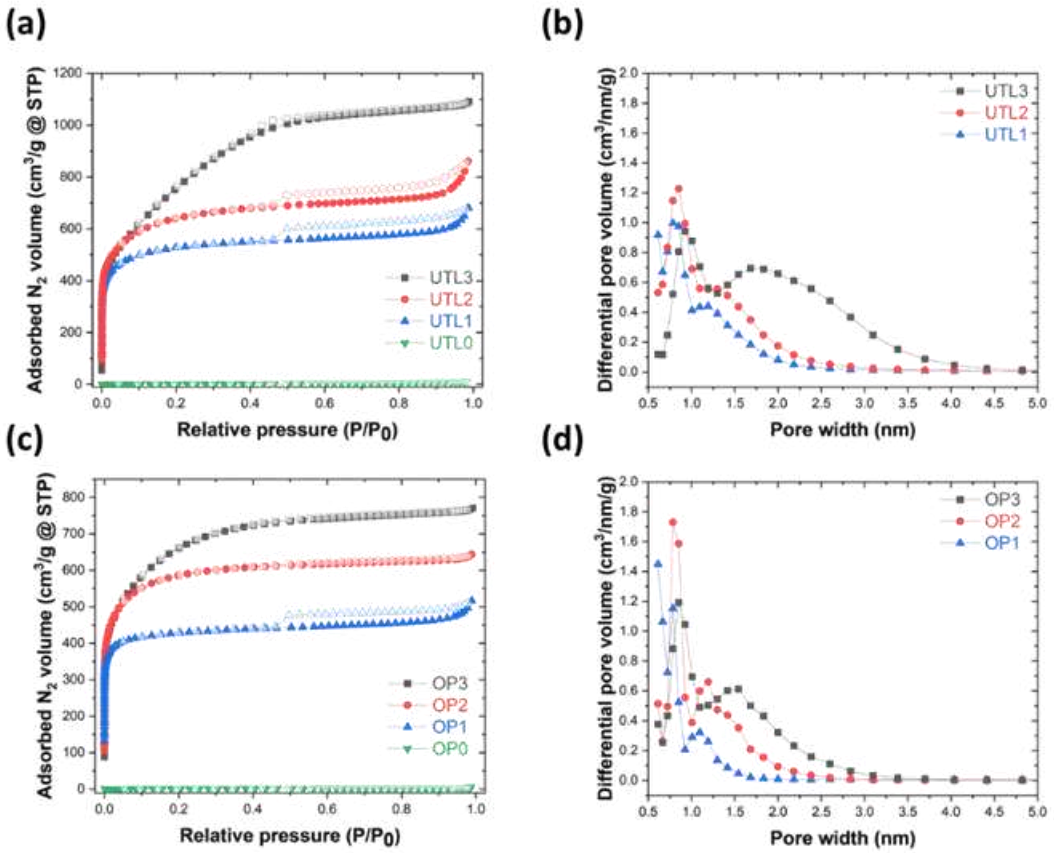

Figure 4.2: Gas sorption measurements of the UTL and OP samples. a) and c): N_2 adsorption and desorption isotherms collected at 77 K. b) and d) respective PSD obtained from the N_2 adsorption isotherms using the QSDFT slit-pore kernel. Reproduced from accepted manuscript [107]: International Journal of Hydrogen Energy, Elsevier.

UTL3 shows the highest N_2 uptake among all samples and displays a distinctive sloped I(b) isotherm, differing from the isotherms of UTL1 and UTL2. The Quenched Solid Density Functional Theory (QSDFT) slit-pore kernels applied to the adsorption branches enabled the calculation of the pore size distribution (PSD), as shown in Figure 4.2 and Figure 4.2. With increasing KOH content during activation, the PSD shifts toward larger pore sizes. For UTL samples, the mean pore size (d_{50}) increases from 0.86 to 1.75 nm, while for OP samples, it increases from 0.67 to 1.17 nm.

The specific surface area and micropore volume initially increase with higher activation agent levels, but further activation leads to a decline in microporosity due to the growth of small

mesopores, as observed in UTL samples. For OP samples, the micropore surface area follows a similar trend, but the micropore volume remains constant. Parameters derived from the gas sorption analysis are summarized in Table 4.3 providing detailed insights into the structural evolution of the materials with increasing activation levels.

Table 4.2: Pore structure characteristics of the ACC, MSC-30, MSP20-X and YP80-F material obtained from the CO_2 and N_2 adsorption isotherm using the GCMC and QSDFT slit-pore kernel, respectively.

Material	$S_{GCMC,CO2}$ [(a)]	$V_{GCMC,CO2}$ [(b)]	$d_{A,CO2}$ [(c)]	S_{BET} [(d)]	$S_{QSDFT,N2}$ [(e)]	S_M [(f)]	S_μ [(g)]	$S_{u\mu}$ [(h)]	V_{QSDFT} [(i)]	V_M [(j)]	V_μ [(k)]	$V_{u\mu}$ [(l)]	$d_{A,N2}$ [(m)]	d_{50} $(d_{25} - d_{75})$ [(n)]
	(m^2/g)	(cm^3/g)	(nm)	(m^2/g)	(m^2/g)	(m^2/g)	(m^2/g)	(m^2/g)	(cm^3/g)	(cm^3/g)	(cm^3/g)	(cm^3/g)	(nm)	(nm)
ACC	1070	0.38	0.71	1318	1389	67	492	912	0.59	0.09	0.27	0.25	0.84	0.89 (< 0.6 - 1.4)
MSC-30	1242	0.53	0.85	3259	2497	284	1686	705	1.59	0.37	1.07	0.22	1.27	1.48 (0.9-1.9)
MSP20-X	1455	0.56	0.77	2134	1978	11	1042	1179	0.83	0.02	0.54	0.37	0.84	0.82 (0.67-1.18)
YP80-F	957	0.38	0.79	2482	1921	125	1239	694	1.12	0.20	0.77	0.21	1.16	1.38 (0.86-1.77)

(a) Specific surface area (SSA), (b) specific pore volume (SPV) and (c) average pore width of slit pores calculated with $2\frac{V_{GCMC,CO2}}{S_{GCMC,CO2}}$ as obtained from CO_2 adsorption using the GCMC slit-pore kernel. (d) SSA obtained by the multi-point BET methods using the N_2 adsorption branch. (e) SSA obtained from the N_2 adsorption isotherm using the QSDFT slit-pore kernel. (f)-(h): SSA of meso-, micro- and ultramicropores, respectively. (i) SPV obtained from the N_2 adsorption isotherm using the QSDFT slit-pore kernel. (j)-(l): SPV of meso-, micro- and ultramicropores, respectively. (m) average pore width of slit pores as obtained from N_2 adsorption using the QSDFT slit-pore kernel and (n) volume-weighted median of the pore size (d50) and the corresponding 25th and 75th percentile (d25 and d75, respectively) derived from the cumulative pore volume distributions based on the QSDFT method.

Table 4.3: Pore structure characteristics of the UTL and OP samples obtained from the N_2 adsorption isotherm using the QSDFT slit-pore kernel.

Material	S_{BET} (d)	$S_{QSDFT,N2}$ (e)	S_M (f)	S_μ (g)	$S_{u\mu}$ (h)	V_{QSDFT} (i)	V_M (j)	V_μ (k)	$V_{u\mu}$ (l)	$d_{A,N2}$ (m)	d_{50} $(d_{25} - d_{75})$ (n)
	(m^2/g)	(m^2/g)	(m^2/g)	(m^2/g)	(m^2/g)	(cm^3/g)	(cm^3/g)	(cm^3/g)	(cm^3/g)	(nm)	(nm)
UTL0	5	-	-	-	-	-	-	-	-	-	-
UTL1	2008	2045	44	853	1148	0.91	0.13	0.46	0.32	0.89	0.86 (na-1.39)
UTL2	2378	2201	77	1211	914	1.13	0.20	0.68	0.25	1.03	1.06 (0.75-1.64)
UTL3	2814	2135	448	1336	350	1.57	0.62	0.86	0.09	1.47	1.75 (1.10-2.38)
OP0	3	-		-		-			-		-
OP1	1700	1926	17	477	1433	0.70	0.06	0.23	0.63	0.72	0.67 (na -0.93)
OP2	2218	2145	27	1108	1011	0.91	0.04	0.59	0.87	0.85	0.87 (0.66-1.26)
OP3	2417	2121	117	1242	762	1.10	0.15	0.74	0.95	1.04	1.17 (0.80-1.67)

* Same legend applies as outlined in the table above

4.3 Atomic and nanostructure – SAXS and XRD

The pore structure of nanoporous carbons might be idealistically described by an accumulation of slit-shaped pores as assumed in the PSD models used in gas sorption analysis. Another method to distinguish intricate differences of the pore structure, regarding size and shape, of different samples is possible by the utilization of SAXS. In earlier chapters it was outlined that a clear discrimination between the smallest pore sizes and the scattering (diffraction) from atomistic structures is not unambiguous. For this reason, in addition to the SAXS measurements also XRD measurements help to identify those differences between the samples. Figure 4.3 8a) shows the SAXS pattern obtained from the first set of samples, namely ACC, MSC-30, MSP20-X and YP80-F. All samples show a power law behavior in the low-q regime, originating from the carbon particle surface. For the ACC material the slope traverses into a constant plateau and further shows an infliction point 0.7 nm^{-1}, which is characteristic for a scattering contribution of pores. The same can be observed for the MSP20-X material, yet at much higher q-values, whereas for the MSC-30 and YP80-F material no clear constant plateau is observed. Given the crude approximation $D = \pi/q$, the size of the pores contributing to the scattering gives ~ 4 nm for the ACC material, which is in the mesopore range also reflected in the PSD. The absence of a clear plateau can be related to the presence of mesopores of similar size. At higher scattering vector the ACC material shows another infliction point 3 nm^{-1}, which is associated with the scattering from micropores of size ~1 nm. It becomes evident that the inflection point for ACC, MSC-30 and MSP20-X is roughly at the same q-position, yet the size of the pores contributing in this regime is quite different. In order to evaluate the mean pore size from SAXS the correlation length T was calculated according to equation (2.56). The Porod constant P was evaluated from a linear fit of the $I(q) \cdot q^4 \; vs. \; q^4$ in the q-range of 7 < q < 8.2 nm^{-1}, whereas the integrated intensity $\tilde{I}$ was calculated from the respective Kratky-plot and extrapolation to infinity. Using the pore volumes obtained from the QSDFT slit pore kernel, the volume fraction of pores was calculated with $\varphi = \frac{V_{QSDFT}}{V_{QSDFT}+1/\rho_{skel}}$, assuming a skeletal density ρ_{skel} of 1.9 g/cm^3 for all samples. The calculated pore chord lengths l_p as well as the correlation lengths are summarized in Table 4.4. The MSP20-X material has the lowest l_p, which is in the same range as the average pore size obtained by

the QSDFT analysis. For the ACC, MSC-30 and YP80-F samples, l_p is larger than the respective $d_{A,N2}$ value, which might be related to an underestimation of the pore size due to the idealistic assumption of slit-shaped pores in the QSDFT analysis.

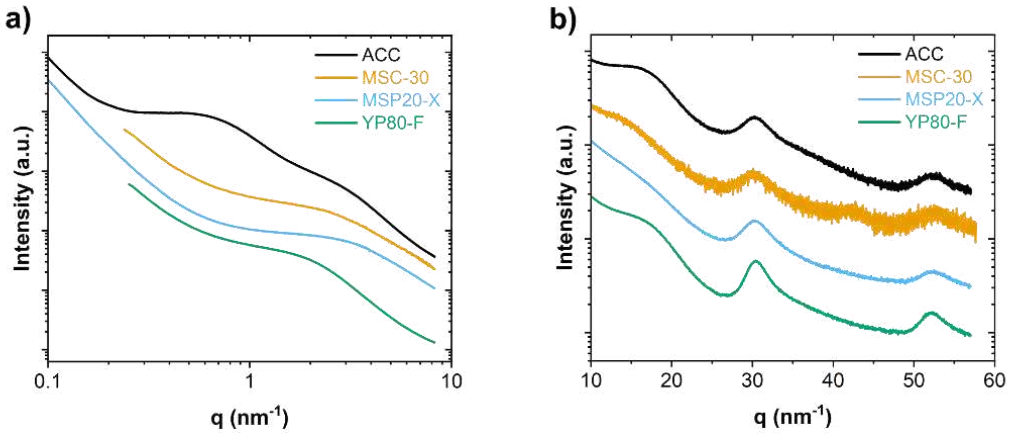

Figure 4.3: a) SAXS and b) XRD patterns measured for the ACC, MSC-30, MSP20-X and YP80-F material.

The XRD patterns in Figure 4.3 (b) show three distinct peaks. The first peak, the (002)-stacking reflection at ~17 nm^{-1}, originates from the stacking of small graphene-like carbon sheets. The broadness of this peak indicates the degree of order perpendicular to the graphene sheets. For the ACC and YP80-F material this reflection is more pronounced than for the MSC-30 and MSP20-X material. The second and third peaks, attributed to the (10)- and (11)- in-plane reflections, appear at ~30 nm^{-1} and ~52 nm^{-1}, respectively. These peaks are sharper and more pronounced than the (002) reflection, indicating a higher degree of in-plane ordering. To derive the lattice parameters of the underlying atomistic structures, the (002) stacking and (10) in-plane diffraction peaks were fitted using a Gaussian and pseudo-Voigt function, respectively. The interlayer spacing and the in-plane lattice parameter were calculated from the peak positions using $d_{(002)} = \frac{2\pi}{q_{(002)}}$ and $a = \frac{4\pi}{\sqrt{3} \cdot q_{(10)}}$, respectively. The out-of-plane (L_c) and in-plane (L_a) correlation lengths were determined using the Scherrer equation $L_{c,a} = K_{c,a} \cdot \frac{2\pi}{\Gamma_{(002),(01)}}$ [108,109], where $K_c = 1$, $K_a = 1.84$ and $\Gamma_{(002),(01)}$ is the respective full width at half maximum of the fitted peak . From L_c and the lattice parameter $d_{(002)}$, the average number of stacked carbon sheets N_c was estimated [110]. A summary of the structural parameters derived from the XRD data is provided in Table 4.4. The in-plane lattice parameters of all samples are around 0.24 nm, which is in good agreement with the lattice parameter of

graphite being 0.246 nm. The interlayer spacing of the MSC-30 samples is the highest, which is related to the broadness of the (002)-reflection.

The scattering patterns of the second set of samples are shown in Figure 4.4. The SAXS patterns for the samples displayed in Figure 4.4 (c) and (d), show a In the, a characteristic power-law decrease in the low-q region, which is again attributed to the rough external surface of individual carbon particles [73,111]. For the non-activated samples, a subtle hump around $q \approx 3\ nm^{-1}$ is visible, suggesting electron density inhomogeneities on a length scale of approximately $\pi/q \approx 1\ nm$. This feature is tentatively linked to micropores, although it could also arise from nanoscale structures related to the original plant material that survived the 450°C pre-carbonization process. Since N_2 adsorption measurements show no evidence of porosity in these samples (see Figure 4.4 (b) and (d), any nanoporosity must stem from closed micropores [112,113].

The intensity for $q > 1\ nm^{-1}$ in the non-activated samples is considerably lower than in the activated samples, suggesting a minimal presence of (closed) nanoporosity prior to activation. In contrast, the activated samples exhibit a significant increase in intensity, which aligns qualitatively with the rise in pore volumes observed in the N_2 adsorption isotherms (Figure 4.4 (c) and (d)). The hump around $q \approx 3\ nm^{-1}$ becomes more pronounced after activation but remains at the same q-position, indicating that these features arise from similar nanometer-scale structures. Significant changes in the scattering patterns are observed at higher activation ratios, particularly for UTL3, OP2, and OP3. These samples show a strong intensity increase in the mid-q region ($q \approx 1\ nm^{-1}$), with UTL3 exhibiting an additional hump. This feature likely corresponds to mesopores, aligning well with the pore size distribution (PSD) obtained from N_2 adsorption studies.

To quantify the characteristic pore length scales, the mean chord length (T) was calculated as described previously. Using the porosity of each sample, the mean chord lengths for the pores (l_p) and the carbon phase (l_c) were derived and are summarized in Table 4.4. The values of l_p increase with higher activation levels, consistent with the PSD trends from N_2 adsorption (Figure 4.2 and Table 4.3). However, the absolute l_p values are smaller than the pore widths obtained from gas sorption for several reasons. First, ultramicropores (<0.7 nm) are not

effectively captured by N_2 sorption at 77 K [114], and these pores are likely present in significant amounts in these bio-derived carbons, explaining the smaller mean pore sizes from SAXS. Second, the mean chord length is influenced by pore shape and cannot be directly equated to pore widths derived from sorption analysis, which typically assumes slit-like pores [111]. Lastly, a fraction of closed pores, as indicated by the SAXS data for the non-activated samples, could contribute to discrepancies between SAXS and sorption results.

Unlike l_p, the chord length of the carbon phase (l_c) decreases with increasing activation, reflecting the progressive "burn-off" of carbon, which leads to thinner pore walls on average. This trend is consistent with the structural evolution of the carbon matrix during activation.

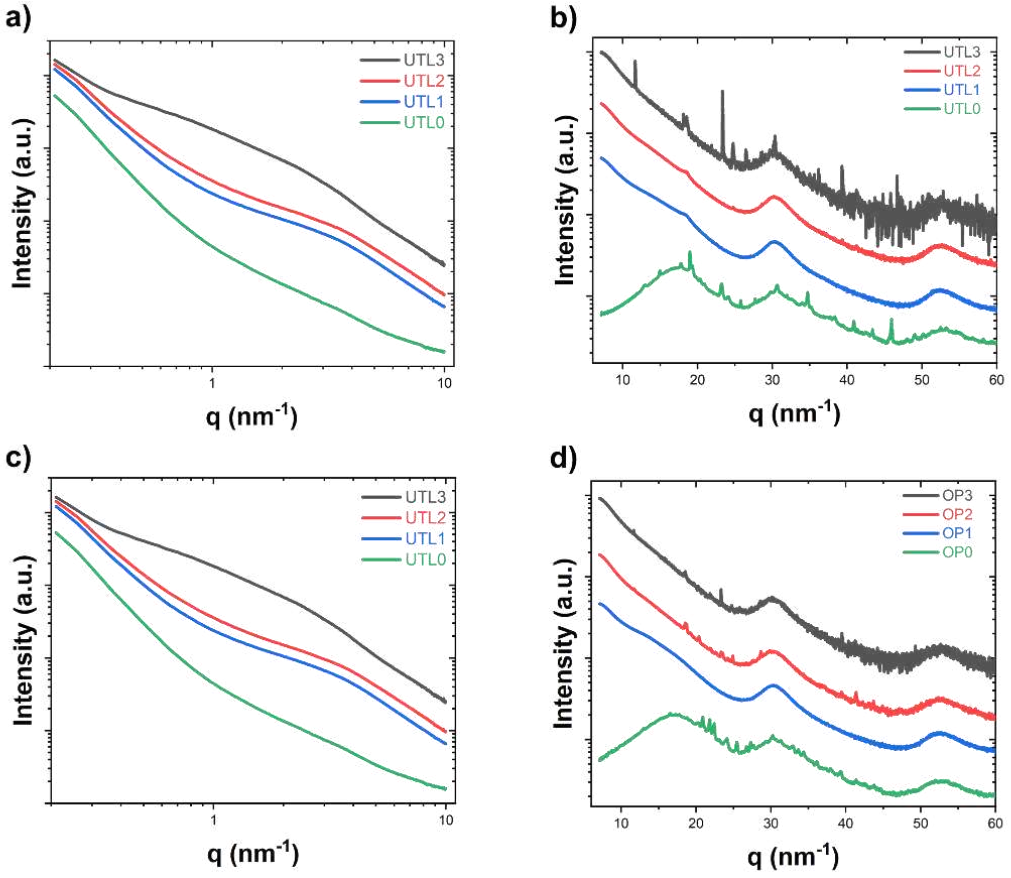

Figure 4.4: a) and c) SAXS and b) and d) XRD patterns measured for the UTL and OP samples, respectively. Reproduced from accepted manuscript [107]: International Journal of Hydrogen Energy, Elsevier.

Figure 4.4 (b) and (d) present the X-ray diffractograms, highlighting three broad diffraction features alongside a few sharp reflections, likely originating from residual mineral particles in the biomass [90,91] or remnants of the activation procedure. The (002) stacking reflection at

~17 nm^{-1} corresponds to the stacking of small graphene-like carbon sheets. The significant broadening of this peak indicates a highly disordered structure with only a few stacked layers on average. Two additional broad peaks, at ~30 nm^{-1} and ~52 nm^{-1}, are attributed to the (10)- and (11)- in-plane reflections of sp^2 carbon, respectively [108,110]. These peaks, although more pronounced than the (002) reflection, are also broad, reflecting limited in-plane ordering. The absence of mixed (hkl) index reflections suggests turbostratic ordering, characteristic of a structure lacking true 3D crystallinity. The XRD results, along with structural parameters derived from SAXS, are summarized in Table 4.4. The distinct reflections observed in the non-activated samples, as well as in OP2 and UTL3, indicate the presence of residual inorganic components. These may originate from heterogeneously distributed mineral phases, such as cystoliths ($CaCO_3$), naturally occurring in the original biomass. This suggests that the washing process may have been insufficient and that a more rigorous chemical treatment, potentially using a higher molarity HCl solution, could improve the removal of residual mineral species. that were not fully eliminated during the chemical treatment. A definitive identification of the crystalline structures was not possible. However, the detected peaks show some correlation with KOH, K_2CO_3, KO_2, SiO_2, $CaCO_3$, $Ca(OH)_2$, and $CaCl_2$.

Table 4.4: Structural parameters derived from XRD and SAXS, for all samples investigated.

Material	a_{10} [a] (nm)	$L_{a,XRD}$ [b] (nm)	$d_{(002)}$ [c] (nm)	L_c [d] (nm)	N_c [e] (-)	φ [f] (-)	T [g] (nm)	l_p [h] (nm)	l_c [i] (nm)
ACC	0.24	1.76	0.39	1.09	2.8	0.53	0.53	1.11	0.99
MSC-30	0.24	1.43	0.45	1.25	2.79	0.75	0.35	1.41	0.47
MSP20-X	0.24	1.42	0.40	0.44	1.10	0.61	0.35	0.89	0.57
YP80-F	0.24	1.92	0.39	0.91	2.37	0.68	0.52	1.62	0.76
UTL0	0.22	0.97	0.36	0.42	1.15	-	0.38	-	-
UTL1	0.23	1.49	0.38	0.82	2.15	0.63	0.34	0.92	0.53
UTL2	0.23	1.48	0.40	0.69	1.74	0.68	0.33	1.02	0.48
UTL3	0.23	1.17	0.43	0.48	1.13	0.75	0.37	1.46	0.49
OP0	0.18	0.76	0.36	0.35	0.96	-	0.29	-	-
OP1	0.23	1.38	0.39	0.78	1.99	0.57	0.34	0.79	0.59
OP2	0.23	1.38	0.39	0.71	1.82	0.63	0.32	0.86	0.50
OP3	0.23	1.41	0.40	0.85	2.13	0.68	0.33	1.04	0.49

(a) in-plane lattice parameter, (b) in-plane correlation length, (c) interlayer spacing, (d) out of-plane correlation length, (e) number of stacked graphene sheets, (f) volume fraction of pores, (g) correlation length obtained from SAXS, (h) average chord length of the pores and (i) average chord length of the carbon matrix.

5 Influences on the hydrogen storage performance

5.1 Structure and chemical composition

Figure 5.1 (a) and (b) present the fully reversible low-pressure (0–1 bar) H_2 isotherms at 77 K. All activated samples achieve H_2 uptake exceeding 2 wt.% under these conditions, while non-activated samples show negligible uptake due to the absence of open porosity. Within both sample series, the materials with the highest KOH ratio exhibit the lowest H_2 uptake. The isotherms lack a clear sorption plateau and exhibit fully reversible behavior upon desorption. UTL3 displays notably lower low-pressure H_2 uptake compared to UTL1 and UTL2. As indicated by the PSD analysis from N_2 adsorption (Fig. 2b), the smallest micropores (<1 nm) slightly enlarge with increasing KOH ratios. Additionally, SAXS-derived pore chord-length (l_p) is smaller for UTL2 than for UTL3. A similar trend is observed for OP samples, suggesting that the smallest micropores primarily govern low-pressure H_2 uptake due to the overlapping potential fields of opposing pore walls.

Figure 5.1 (c) and (d) illustrate the fully reversible high-pressure (0–100 bar) H_2 isotherms. In this regime, the trend reverses, with materials having higher KOH activation ratios showing greater H_2 uptake, peaking at approximately 30–40 bar. This outcome aligns with expectations, as larger pores provide additional space for accommodating H_2 molecules, which becomes critical at pressures exceeding atmospheric levels. The decline in adsorbed H_2 after reaching the uptake maximum is attributed to bulk gas compression effects [115]. Samples with significant amounts of larger pores, such as UTL3 and OP3, exhibit a lower decrease in adsorbed H_2 compared to samples with fewer large pores, such as OP1 and OP2.

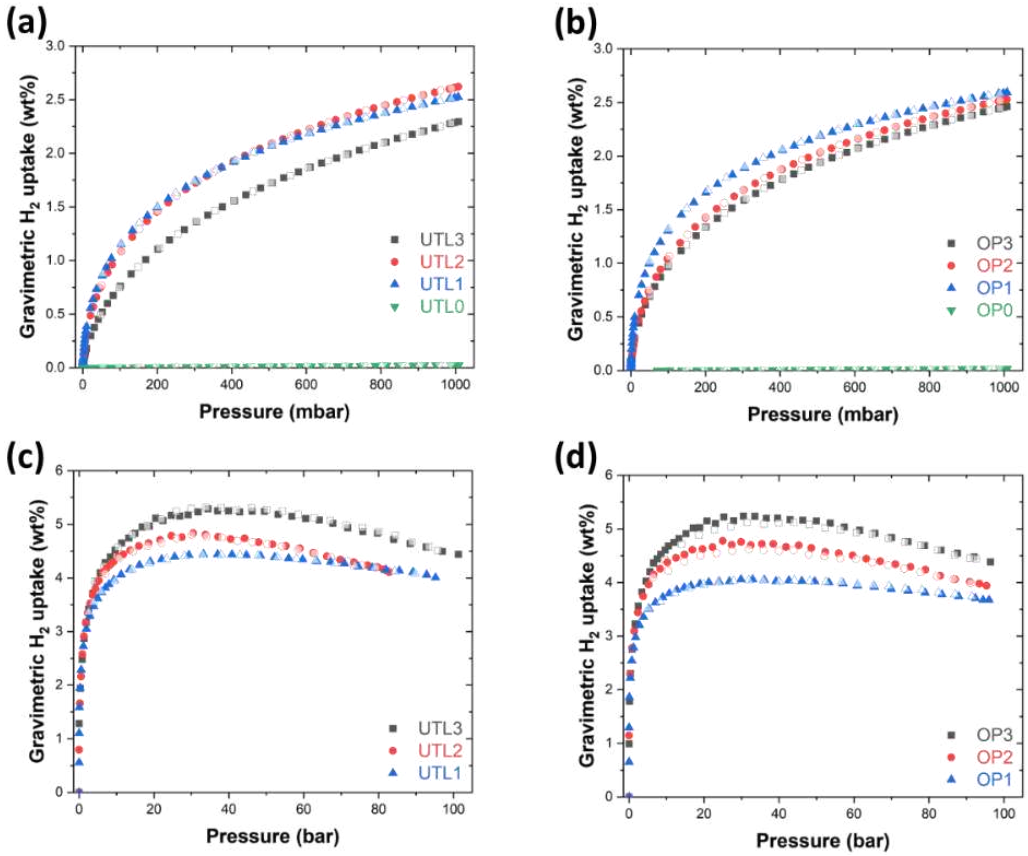

Figure 5.1: (a) and (b) Gravimetric H_2 uptake versus pressure up to 1 bar measured at 77 K for the UTL and OP samples, respectively. Full symbols represent the adsorption isotherms, and open symbols the desorption isotherms. (c) and (d) Excess H_2 uptake at 77 K up to 100 bar. Reproduced from accepted manuscript [107]: International Journal of Hydrogen Energy, Elsevier.

Gravimetric capacities at both low and high pressures are summarized in Table 5.1. The highest H_2 uptakes, 5.24 wt.% and 5.29 wt.%, were recorded at around 30 bar for OP3 and UTL3, respectively. These values represent some of the highest reported uptakes for biomass-derived activated carbons, particularly those derived from orange peel and used tea leaves [10,116]. Comparable H_2 uptakes ranging from 4.6–5.9 wt.% have been reported for other biomass-derived activated carbons, such as those from coffee waste and glucose, as shown in Table 5.2 [96,117].

Table 5.1: Maximum excess H_2 uptakes at different pressures and 77 K for the UTL and OP samples. Reproduced from accepted manuscript [107]: International Journal of Hydrogen Energy, Elsevier.

Material	Excess H_2 uptake at 77 K (wt.%)	
	1 bar	Max. uptake
UTL0	0.14	-
UTL1	2.51	4.44 (33 bar)
UTL2	2.71	4.83 (30 bar)
UTL3	2.61	5.29 (34 bar)
OP0	0.00	-
OP1	2.57	4.06 (33 bar)
OP2	2.80	4.78 (25 bar)
OP3	2.78	5.24 (30 bar)

To further investigate the influence of structural and chemical parameters on hydrogen adsorption across different pressure ranges, a comparative statistical analysis was conducted Kendall's rank correlation coefficients (Figure 5.2), as outlined in section 3.2, were used to construct a correlation matrix, identifying interdependencies between the measured parameters. The dataset was comprised of eleven samples, with eight presented being the ULT and OP samples, one the ACC sample and two additional samples investigated in a previous study (Master´s thesis) [57,89,96]. The corresponding pore characteristics and H_2 uptakes are summarized in Table 5.2.

Table 5.2: Comparison of the pore structure characteristics and maximum excess gravimetric H_2 storage capacities (C_g) at 77 K and pressures from 1-140 bar of selected activated carbon materials reported in literature. Reproduced from accepted manuscript [107]: International Journal of Hydrogen Energy, Elsevier.

Precursor	T [K]	P [bar]	S_{BET} (m^2/g)	V_{tot} (cm^3/g)	C_g [wt.%]	Ref.
Bamboo	77	1	1220-2150	0.4-0.5	2.0-2.3	[118]
Glucose derived	77	100	2140-2550	1.1-2.0	4.6-5.0	[117]
Orange peel	77	10	1000-1400	0.3-0.4	2.3-3-3	[10]
Tangerine peel	77	30	< 1250	-	0.9-1.7	[116]
Coconut shell	77	1/47	2482	1.1	2.2/4.52	[11]
Coffee Waste*	77	1/35	2990-3330	1.2-1.6	2.7-2.8/5.4-5.9	[96]
ACC(a),*	77	1/72	1318	0.6	1.6/3.1	[57,89]
Orange peel*	77	1/25-33	1700-2400	0.6-1	2.6-2.8/4.1-5.2	This work
Tea leaves*	77	1/30-34	2000-2800	0.1-1.6	2.5-2-6/4.4-5.3	This work

(a): Activated carbon cloth (ACC) based on viscose rayon. The low- and high pressure H_2 isotherm, as well as the chemical analysis were taken from Ref. [57,89]. *Activated carbon materials used as input to calculate Kendall´s ranked coefficient matrix.

In Figure 5.2, the chemical composition has been normalized to the heteroatom-to-carbon ratio to account for variations in carbon content across samples. The statistical analysis included parameters derived from gas sorption analysis, specifically median pore width (d_{50}), as well as surface areas and pore volumes associated with ultramicropores (<0.7 nm), supermicropores (0.7–2 nm), and mesopores (>2 nm), following IUPAC recommendations [13]. Hydrogen uptake values at 250, 500, 750, and 1000 mbar, as well as 5 and 10 bar, were used as input data, alongside the maximum recorded uptake. In Figure 5.2, positive correlations (shaded in red) indicate that an increase in a given parameter enhances H_2 uptake at a specific pressure, whereas negative correlations (shaded in blue) suggest that an increase in the parameter results in lower H_2 uptake.

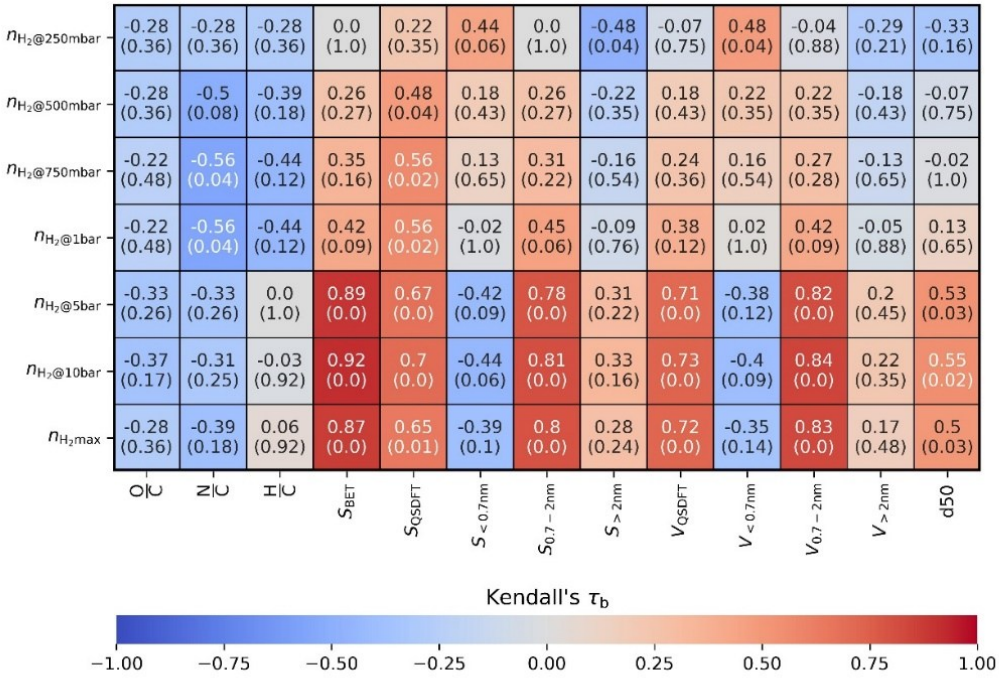

Figure 5.2: Kendall's rank correlation coefficients matrix based on the surface chemistry and pore structure parameters obtained for the activated samples and their influence on the cryogenic (77 K) H_2 uptake at different pressures. The dataset consists of 11 samples, of which 9 include chemical analysis (O/C, N/C, H/C). The size of the correlation is indicated via the upper value in each box, the corresponding p-value is placed in brackets below, all values are rounded to two decimal places. All p-values ≤ 0.05 represent statistically significant correlations. Reproduced from accepted manuscript [107]: International Journal of Hydrogen Energy, Elsevier.

Based on Kendall's rank correlation coefficients, our analysis confirms that micropore volume ($V_{0.7-2\,nm}$) and total surface area (S_{BET}) are the most significant predictors of hydrogen uptake, particularly at higher pressures. The strongest positive correlations appear between H_2 uptake at 5–100 bar and micropore surface area ($S_{0.7-2\,nm}$), highlighting that pores in the range of 0.7–2 nm serve as the primary adsorption sites. Additionally, the total pore volume (V_{QSDFT}) exhibits a positive correlation, indicating that as pressure increases, an expanded cumulative pore volume enhances hydrogen storage capacity.

At low pressures (≤1 bar), ultramicropores (<0.7 nm) demonstrate a moderate to strong correlation with H_2 uptake, consistent with the potential overlap of opposing pore walls, which promotes gas densification [57,58]. However, as pressure increases, ultramicropores become less effective, and their correlation with H_2 uptake diminishes significantly. This suggests that

while ultramicropores dominate adsorption at low pressures, their storage capacity saturates quickly, requiring additional adsorption in larger micropores and small mesopores at higher pressures. The negative or weak correlation between H_2 uptake at high pressure and ultramicropore surface area ($S_{<0.7\,nm}$) supports this interpretation. Previous studies by Davoodi et al. found that mesopores play a secondary role in H_2 uptake, becoming relevant only at very high pressures [119]. However, this trend is not statistically significant in Figure 5.2, as mesopore volume ($S_{>2\,nm}$) shows a slightly negative correlation with low-pressure hydrogen uptake. The correlation analysis further shows that S_{BET} is strongly linked to H_2 uptake across all pressures, though its influence varies depending on pressure. At low pressures, the correlation is weak and not statistically significant, reinforcing the notion that surface area alone is not sufficient to predict uptake in the ultramicropore regime. However, at higher pressures, the correlation becomes statistically significant and highly positive, demonstrating that larger surface areas, particularly those composed of microporous networks, are crucial for maximizing hydrogen adsorption at elevated pressures. These findings align with those of Nguyen et al. [120], [who identified S_{BET} and $S_{0.7-2\,nm}$ as the strongest predictors of H_2 uptake using Pearson correlation analysis.

Beyond textural properties, the elemental composition of porous carbons plays an essential role in adsorption behavior. Our analysis finds no statistically significant correlation between oxygen content (O/C ratio) and hydrogen uptake, contradicting the results of Kusdhany et al. [121], who reported a positive correlation between oxygen content (8–12 wt.%) and H_2 uptake based on SHAP analysis (SHapley Additive exPlanations) [122] in machine learning models, suggesting that moderate oxygen functionalization enhances storage capacity. However, Davoodi et al. [119] observed a weaker correlation, aligning with the idea that oxygen's role in H_2 storage may be highly dependent on pore size and/or pressure. The analysis also identifies a statistically significant negative correlation between nitrogen content (N/C ratio) and hydrogen uptake, particularly at 750–1000 mbar, suggesting that nitrogen incorporation does not enhance physisorption despite previous studies proposing N-doping as a strategy for improving adsorption in nanoporous carbons [123]. However, due to the small sample size and limited variation in chemical composition, our ability to resolve subtle heteroatom doping effects may be constrained. Theoretical studies have suggested that N- and O-doping can

enhance H_2 uptake by introducing additional binding sites and modifying the electronic environment of the adsorbent [123,124].

Regarding hydrogen content (H/C ratio), our analysis finds no statistically significant correlation with H_2 uptake, suggesting that hydrogen functionalities in the carbon matrix do not significantly influence adsorption performance. This result aligns with Kusdhany et al. [121], who reported only a weak interaction between H-content and adsorption capacity, reinforcing the idea that textural parameters outweigh chemical composition in determining H_2 storage efficiency.

These findings reinforce the widely accepted understanding that microporosity (0.7–2 nm) and total surface area are the dominant factors governing H_2 uptake, while heteroatom doping does not exhibit a strong direct correlation with adsorption performance. However, due to the limited dataset size and relatively small variations in chemical composition, further controlled doping experiments are required to systematically explore the influence of nitrogen and oxygen functionalities. To address these uncertainties, future studies should incorporate precisely controlled heteroatom doping experiments, systematically varying O and N contents while maintaining constant pore structures. This approach would allow for a clearer distinction between direct electronic effects and indirect structural modifications, leading to a more detailed understanding of heteroatom-induced effects on H_2 adsorption.

5.2 Isotope specific adsorption

Apart from the influences of structural and chemical properties of nanoporous carbons, the intricate properties of the adsorbate influences the achievable adsorption capacity. Thus, in the following the isotope specific adsorption of H_2 and D_2 will be discussed. Figure 5.3 (a) and (b) presents the fully reversible H_2 adsorption isotherms measured at 77 K using two different manometric gas sorption analyzers. Both setups yielded consistent hydrogen uptake results as a function of pressure for the ACC and MSC-30 sample, despite differences in experimental conditions. The neutron scattering setup with the Hidden Isochema instrument (Figure 5.3 (b)) involved a larger sample cell volume and a temperature gradient from room to cryogenic temperatures, while the laboratory Quantachrome instrument (Figure 5.3 (b)) offered a more optimized setup. For the MSP20-X and the YP80-F sample the uptakes using the in-situ set-up over- and underestimate the H_2 uptake compared to the laboratory instrument, respectively. This might be attributed to insufficient equilibration time in the one case and an overestimated sample mass in the other case. The sample mass of YP80-F in the cold volume of the sample stick might have changed, due to powder elutriation during the prior performed vacuuming and the absence of the stamp depicted in Figure 3.4. Thus, the quantitative analysis presented in the following of those two samples shall be taken with a grain of salt. Nevertheless, a comparison to the isotherm collected with D_2 between the samples is possible as both are accompanied by the same source of error. The isotherms exhibit a monotonic increase with pressure, with D_2 showing slightly higher molar uptake than H_2. The average D_2/H_2 uptake ratio for ACC is 1.16 at 77 K. While isotope-dependent uptake has been reported previously, the ratios observed here at 77 K are higher than those in prior studies (1.082 in [125] and 1.063 in [126]). This discrepancy may arise from differences in micropore volume, as the ACC material has a micropore volume of 0.5 cm^3/g compared to 0.2 cm^3/g in Ref. [125].

Quantum effects are likely to contribute to these differences in uptake. When the thermal de Broglie wavelength approaches the difference between the pore diameter and the molecular kinetic diameter [59,125,127], the zero-point energy variations between isotopes, due to their mass difference, play a significant role. Estimated D_2/H_2 uptake ratio for a pore diameter of 0.64 nm—the approximate average size of ultramicropores in the ACC sample—is 1.18 at 77

K (see equation (2.17) in chapter 2.3.2), which aligns closely with the observed ratio of 1.16. For the MSC-30 sample the uptake ratio is close to unity at all collected pressure points, whereas the MSP20-X sample shows a preferred uptake of D_2 at the lowest pressure and a decreasing ratio at higher pressures (2.03-1.04 compared to 1.44-1.09 for the ACC). This might be attributed to the considerably larger ultramicropore volume of the MSP20-X sample compared to the ACC. The respective average ratios for the MSC-30, MSP20-X and YP80-F samples are 0.99, 1.31 and 1.07. These discrepancies suggests additional factors at play, potentially involving the selective occupation of the smallest pores by different para:ortho forms of H_2 and D_2 and their distinct temperature-dependent behaviors as outlined by the studies presented in section 2.5.

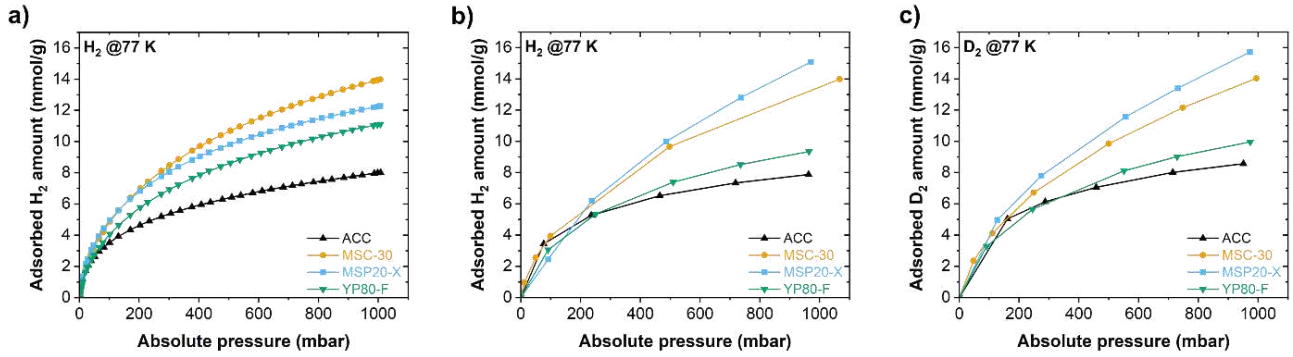

Figure 5.3: H_2 adsorption isotherm measured at 77 K using the Autosorb IQ3 instrument, b) H_2 and c) D_2 adsorption isotherm measured at 77 K using the Hiden IMI Sievert apparatus in the in-situ set-up at D16.

6 Neutron scattering of hydrogen adsorbed in nanopores

In the previous chapters the structural characterization of nanoporous carbons, as well as the structure-performance relationships were discussed in detail. The following chapter evolves around the results obtained from neutron scattering experiments, performed at the D16 instrument of the ILL, to further elucidate the spatial arrangement and densification of hydrogen in nanopore confinement and shed a light on isotope effects.

6.1 Evaluating the difference between SAXS and SANS

The difference between the interaction of X-rays and neutrons with matter allow to gain a comprehensive understanding of the structure of the nanoporous carbons. As outlined in section 2.4.5, hydrogen is practically invisible to X-rays (in respect to carbon), whereas for neutrons the negative coherent scattering length gives rise to measurable scattering intensity. The elemental analysis, shown in Table 4.1, revealed high concentrations of H, O and N within the samples. The atomic form factor for X-rays, the coherent and incoherent scattering lengths are summarized in Table 6.1.

Table 6.1: Atomic form factor for X-rays and coherent and incoherent neutron scattering length of carbon, oxygen, nitrogen and hydrogen.

Element	Carbon	Oxygen	Nitrogen	Hydrogen
f_{SAXS}[(a)] (fm)	16.91	22.54	19.73	2.82
b_{SANS}[(b)] (fm)	6.65	5.80	9.36	-3.74
b_{inc}[(c)] (fm)	0.00	0.00	0.00	25.27

As these elements are somewhere located within the carbon matrix or on the carbon surface in the form of functional groups, it is expected that the SAS signals obtained by X-rays and neutrons might reveal some differences. Figure 6.1 (a-d) show the respective scattering signals from X-ray and neutron scattering experiments. For the X-ray measurements no calibration to absolute units was performed, thus the neutron scattering signals were adjusted to overlap with the intensity obtained by X-ray scattering in the low q-range, where an influence on the

scattering signal of a possible spatial arrangement of heteroatoms at the nanopore surface is not expected. The data in the plots are shown as measured and no background subtractions were performed. Starting with the ACC sample having the highest concentration of H and O, the difference between SAXS and SANS becomes immediately evident. In the high q-regime the incoherent scattering contribution of H can be seen, whereas also a difference in the q-position of the second inflection point is observed. Following the previous discussion, the correlation length observed with SAXS T_{SAXS} is larger compared to the one obtained by SANS T_{SANS}. The quantitative analysis was carried out in the same way as discussed in section 4.3 and the respective results are summarized in Table 6.2. The scattering patterns from MSC-30 sample show a similar slope in the high q-regime below 10 nm^{-1}, whereas the incoherent signal from the somewhat elevated H content becomes visible above 10 nm^{-1}.

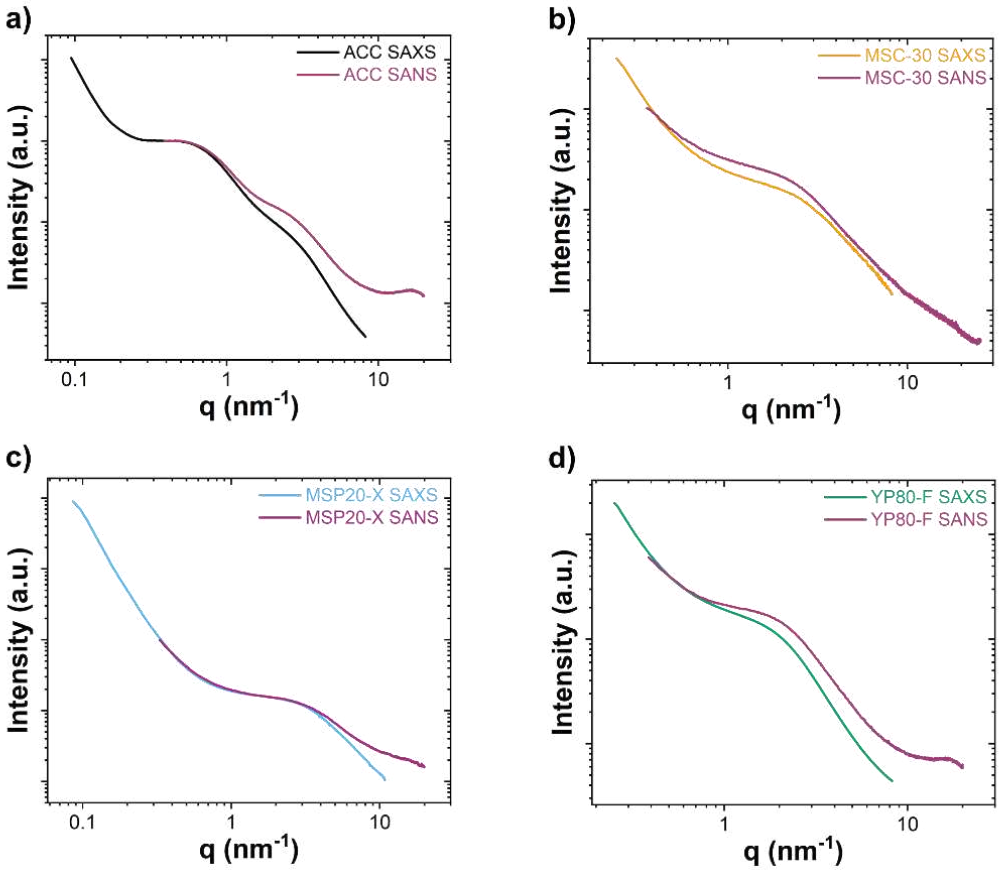

Figure 6.1: SAXS and SANS pattern of the different samples: a) ACC, b) MSC-30, c) MSP20-X and d) YP80-F

The same trend is observed for the MSP20-X sample which has a slightly lower H content. The YP80-F sample shows the same trend as the ACC sample, where a clear shift in the inflection

point is observed. Considering the same pore volume, the average chord length for both X-rays $l_{p,SAXS}$ and neutrons $l_{p,SANS}$ can be calculated (results are summarized in Table 6.2). For the MSC-30 and the MSP20-X sample, both calculated pore chord lengths are comparable and differ 0.7% and 5.6%, respectively, and further considering measurement and fitting errors, both values are practically similar. For the ACC and YP80-F samples, the obtained pore chord lengths differ substantially, which is also reflected in the scattering patterns. The difference between the two sets of samples can be attributed to a different distribution and spatial arrangement of heteroatoms, given that MSC-30 has an even higher O and H content compared to YP80-F. From this simple analysis, the hypothesis that functional groups are located at the surface of the pores, thus reducing the effective pore size for neutrons, can be drawn. For the other two samples it seems reasonable to assume that the heteroatoms are located within the atomistic carbon structure, replacing individual carbon atoms.

Table 6.2: Correlations lengths and average chord lengths of pores obtained from SAXS and SANS.

Material	T_{SAXS} (nm)	T_{SANS}	$l_{p,SAXS}$ (nm)	$l_{p,SANS}$ (nm)
ACC	0.53	0.47	1.12	1.00
MSC-30	0.35	0.35	1.40	1.39
MSP20-X	0.35	0.33	0.89	0.84
YP80-F	0.52	0.44	1.62	1.38

6.2 Neutron scattering of H_2 and D_2 adsorption

The introduction of H_2 and D_2 into the pore space leads to distinct changes in the SANS signal, reflecting variations in adsorption behavior and density distribution. Contrast differences between the gas phase and the carbon matrix provide insight into how hydrogen interacts with the pore structure. In the following a general interpretation of the changes to the SANS signal upon hydrogen adsorption is given, which is valid for all the samples discussed.

Figure 6.2 (a-d) and Figure 6.3 (a-d) display the SANS curves of the different samples collected at 77 K for H_2 and D_2 sorption at various gas pressures, respectively. These curves were corrected for instrument background and normalized to transmission, without subtracting the incoherent background at this stage. Across the entire scattering vector range, significant intensity changes are observed, differing notably between H_2 and D_2 adsorption within the pores. At the largest q-values, a correlation peak around 17 nm^{-1} is evident, attributed to the carbon structure factor of the empty sample. This peak primarily arises from the graphene stacking in the disordered turbostratic carbon [108]. With increasing pressure, the D_2 data (Figure 6.3 (a-d)) show an intensity increase and a shift in this peak. Since significant changes in the carbon structure factor due to gas adsorption are unlikely, this shift is attributed to intermolecular correlations within a dense (liquid- or solid-like) D_2 phase forming in some of the pores. Similar intermolecular correlation effects would be expected for H_2. However, for H_2, these effects are masked by a much larger overall intensity increase caused by its high incoherent scattering cross-section compared to D_2, likely hiding the intermolecular correlation signal in the scattering data.

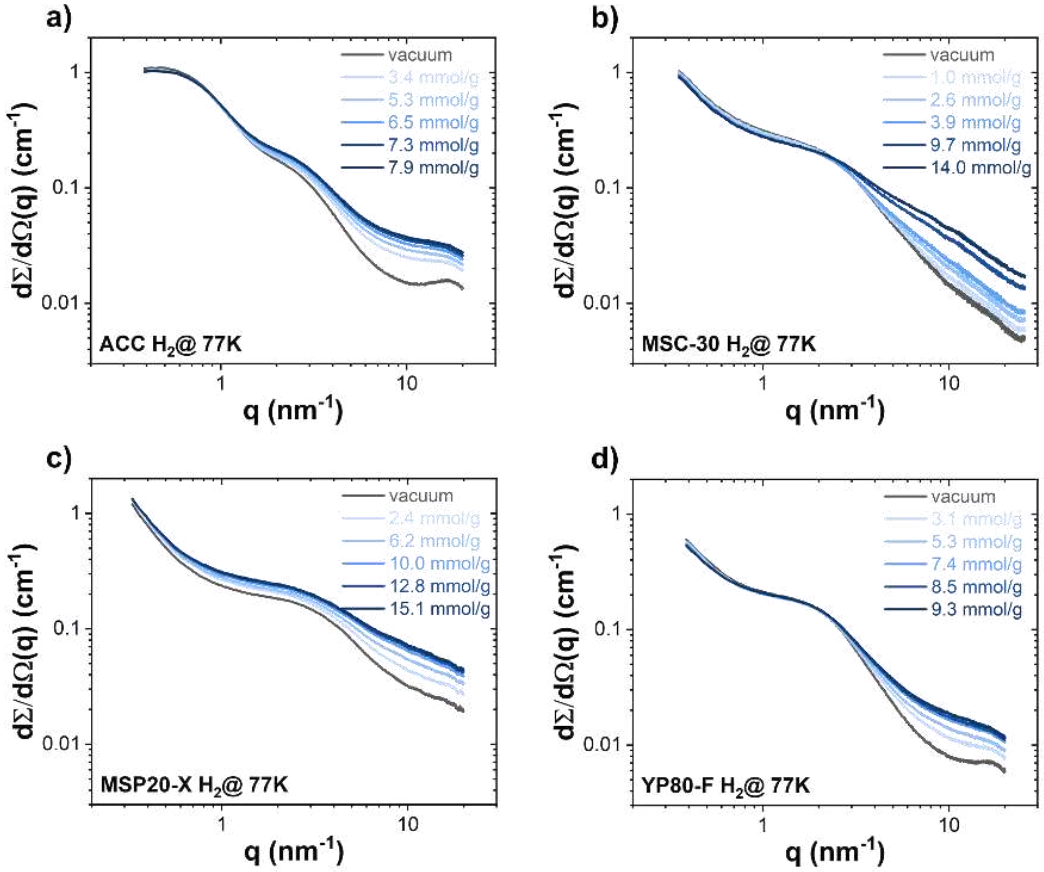

Figure 6.2: Neutron scattering signals measured at different H_2 loadings at 77 K for the different samples: a) ACC, b) MSC-30, c) MSP20-X and d) YP80-F

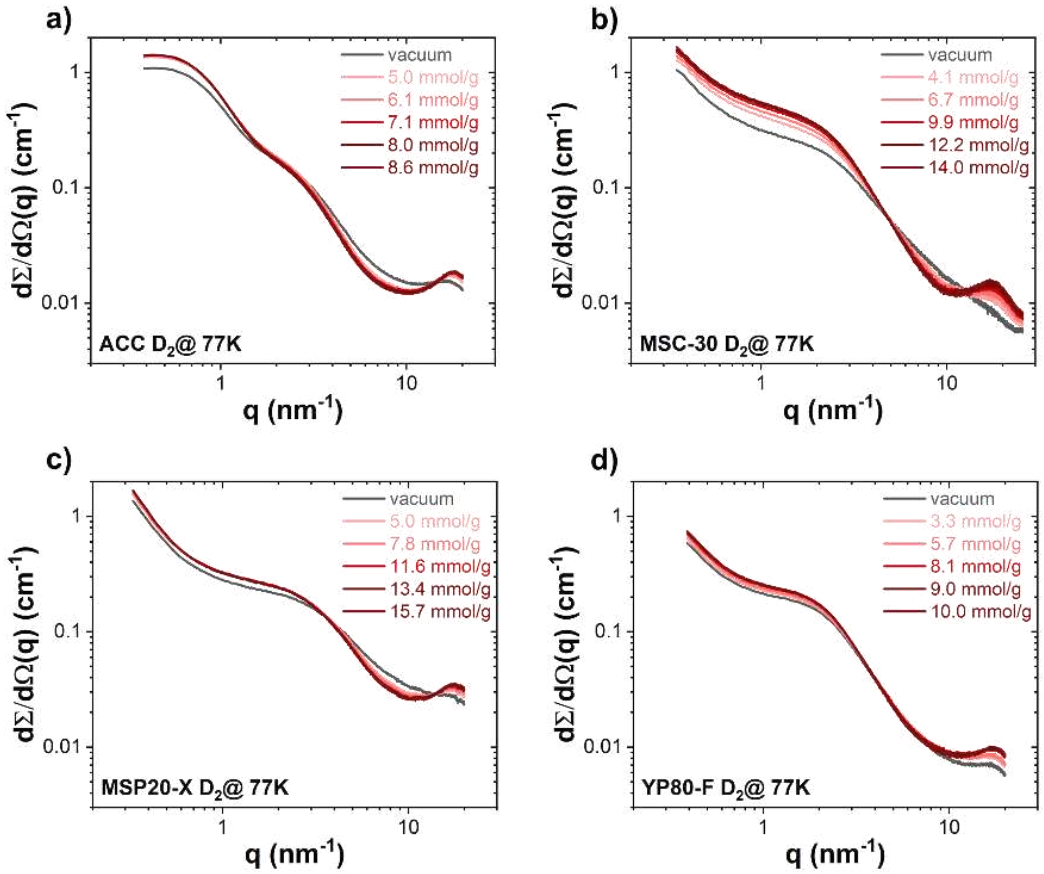

Figure 6.3: Neutron scattering signals measured at different H_2 loadings at 77 K for the different samples: a) ACC, b) MSC-30, c) MSP20-X and d) YP80-F

At smaller q-values (q < 10 nm^{-1}), intensity changes correspond to gas densification within the pores. This alters the coherent scattering length density (SLD) difference $\Delta\tilde{\rho}(p)^2$ between the carbon phase $\langle\tilde{p}_C\rangle$ and the adsorbate phase in the pore space $\langle\tilde{p}_{Ads}\rangle$. In a simple two-phase model, assuming all pores are uniformly filled with an adsorbate phase of constant average density, the scattering intensity is directly proportional to the scattering contrast:

$$\Delta\tilde{\rho}(p)^2 = (\langle\tilde{p}_C\rangle - \langle\tilde{p}_{Ads}\rangle)^2 \; ; \; \tilde{\rho} = N_A \sum_i \frac{w_i b_i}{M_i}\rho \tag{6.1}$$

The scattering length density ($\tilde{\rho}$) of each phase is directly proportional to the mass density (ρ) of the respective phase at a given gas pressure p, where b_i represents the coherent scattering lengths, M_i the molar masses, w_i the fractions of atoms/molecules in the homogeneous phase, and N_A the Avogadro constant.

According to equation (6.1), the SANS curve shape should remain unchanged upon gas adsorption, with only a shift in the logarithmic intensity scale. However, this behavior is not observed in Figure 6.2 and Figure 6.3. For H_2, the intensity increases significantly at intermediate q-values (2–10 nm^{-1}) as gas pressure rises, whereas for D_2, the intensity decreases within the same q-range. This isotope-dependent behavior is expected because hydrogen has a negative coherent scattering length, while both carbon and deuterium have positive values (Table 6.3). As a result, the scattering contrast from equation (6.1) increases for H_2 and decreases for D_2 with gas uptake, indicating a rise in adsorbate mass density in the pores for both cases. At smaller q-values (<1–2 nm^{-1}), the trend reverses: intensity decreases for H_2 and increases for D_2 with successive gas uptake. This behavior cannot be explained by assuming a uniform gas density throughout the pore space. Instead, it suggests that gas density varies within the pores, consistent with previous findings by Gallego and He et al. [128,129], which reported increasing hydrogen density with decreasing pore size at a given external pressure.

Table 6.3: Summary of coherent and incoherent scattering lengths of elements present in the sample material and scattering length densities of the carbon sample, H_2 and D_2. Reproduced with from Ref. [57] and with permission from Elsevier.

Element	Carbon	Nitrogen	Hydrogen	Oxygen	H_2	D_2
b_{coh} (10^{-13} cm)	6.65	9.36	-3.74	5.80	-7.4812	13.34
b_{inc} (10^{-13} cm)	-	-	25.27	-	50.55	8.08
SLD (10^{-10} cm^{-2})	3.98±0.44[(a)]	-	-	-	-1.75 (-1.94)[(b)]	3.24 (3.92)[(c)]

(a) Carbon SLD calculated according to the chemical composition shown Table 4.1 using equation (6.1), (b) and (c): SLD of H_2 and D_2 calculated with equation (6.1) for the liquid bulk density (and solid bulk density), respectively.

When the pressure is increased beyond 1 bar, the intensity in the low q-regime is increasing for H_2 adsorption, as displayed in Figure 6.4 (a) and (b). Considering the simple two-phase model of equation (6.1), it leads to the conclusion that a substantial gas densification in the respective pore size regime occurs.

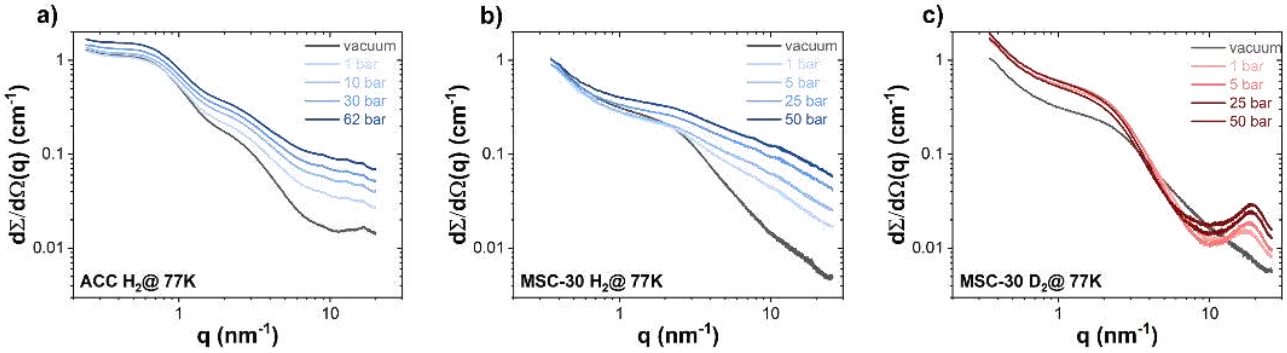

Figure 6.4: Neutron scattering signals measured at elevated H_2 and D_2 pressures: a) ACC and H_2 at 77K, b) and c) MSC-30 and H_2 and D_2 adsorption at 77 K, respectively.

When the applied D_2 pressure is increased, the intensity in the low q-regime is also decreasing, as the contrast scenario compared to H_2 is now reversed. Furthermore, a shift in the inflection point to lower scattering vectors can be observed in Figure 6.4 (c). This shift can be attributed to a contrast matching scenario, such that the adsorbate in the smallest pores has reached the SLD of the surrounding carbon matrix ($\langle\tilde{p}_C\rangle = \langle\tilde{p}_{Ads}\rangle$). This in return leads to the practical absence of these pores contributing to the scattering intensity and thus to an increase in observed chord length of pores. This is further supported by the fact that a notable increase in intensity around 10 nm^{-1}, which might be attributed to the increasing incoherent scattering contribution of D_2. Nevertheless, as discussed in section 2.4.5, the separation of the individual contributions to the intensity at $q \geq 10$ nm^{-1}, is not straightforward and needs some assumptions, which will be further discussed in section 6.3. In the discussion above, as well as in the following sections, an assumption is made that it might be worth to be further verified. It is assumed that the pore space is rigid and not subject to adsorption-induced deformation, which are typically $\varepsilon < 1\%$ [130].

Theoretically it is possible to measure changes to the carbon framework due to the adsorption of hydrogen, when making use of the different coherent scattering lengths of H_2 and D_2, by preparing a 0-SLD gas mixture. To do so, the gases must be mixed prior to adsorption in the pore structure and a molar ratio of 0.64 mol% H_2 and 36 mol% D_2, according to equation

(6.2).

$$(\rho^*_{H2}+\rho^*_{D2})^2 = \left(\frac{p_{tot}}{kT}\right)^2 \cdot [b_{H2} \cdot x_{H2} + b_{D2} \cdot (1 - x_{H2})]^2$$

$$x_{H2} = -\frac{b_{D_2}}{b_{H_2} - b_{D_2}} = 0.64 \qquad (6.2)$$

Such an ideal gas mixture, when evenly distributed and densified within the pore space would not contribute to the measured scattering intensity. The scattering patterns of such an experiment as well as the respective collected isotherms are shown in Figure 6.5.

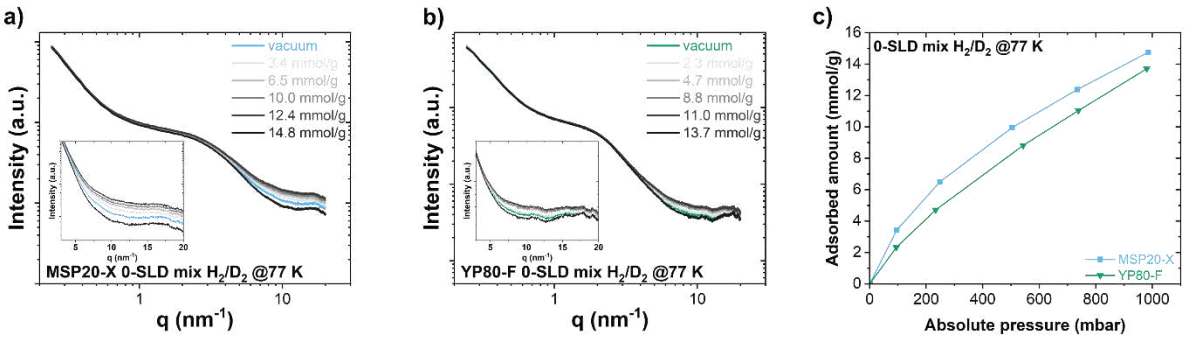

Figure 6.5: Neutron scattering signals measured at 77 K and different pressures of a 0-SLD gas mixture: a) MSP20-X and b) YP80-F. c) Respective adsorption isotherms collected using the IMI sievert apparatus in the in-situ set-up at D16.

From the previous discussion about the isotope specific adsorption, it is evident that nature is opposing this theoretical concept, as H_2 and D_2 are adsorbed and most likely densify differently. Nevertheless, it seems that around the respective inflection points the intensity is not changing, at least not to the extent expected for single fluid adsorption. In the high q-regime at first an increase of in the intensity can be seen (insets in Figure 6.5 (a) and (b)), which is attributed to the incoherent scattering of mainly H_2. Surprisingly, at the highest gas

loading the incoherent scattering contribution is not detectable and the scattering intensity is even below the value measured for the samples under vacuum.

Remembering the statement from Enrico Fermi at the beginning of the chapter, this phenomenon could either be a further discovery or based on a failed experiment. As mentioned, for those experiments, the sample cell was not closed, such that powder could escape the irradiated volume, due to powder elutriation when gas is dosed into the system. This would result in a shift of the whole scattering signal down the log-scale, which is not observed (see small q-values). Thus, it seems that the measurement was indeed correct, and the observed phenomenon has physical explanation. The collection time of one SANS pattern was in the order of 45 min, thus the total residence time for the molecules that were adsorbed first within the pores was around 3.5 h. The thermodynamic ortho-para transition rate of H_2 was reported to range from a 0.4% to 140% in the presence of paramagnetic sites within the carbon material [38,82,83]. Assuming that D_2 is adsorbed first in the smallest pores, thus essentially decreasing the scattering contrast for $q \geq 10$ nm^{-1} and that H_2 unrestrictedly transitions to the para-state (which has no incoherent scattering contribution), it might be possible that both effects combined lead to the observed phenomena. This hypothesis may be further investigated with additional neutron scattering experiments. As stated before the separation of the individual contributions is not unambiguous, yet considering the simpler case of single fluid adsorption, the densification of hydrogen studied by neutron scattering will be discussed in more detail in the following section.

6.3 Fitting of the SANS data

The goal of the following section is to quantitatively determine the average absolute adsorbate density within three distinct pore-size classes. This is achieved by fitting the SANS data using a hierarchical pore model [57]. The SANS signal from the pure ACC material (Figure 6.2 (a), grey line) exhibits a distinct carbon structure factor peak at approximately 17 nm^{-1}, along with two prominent "humps" at ~0.7 nm^{-1} and ~3 nm^{-1}. These features correspond to nanopores, with their positions inversely related to typical length scales associated with pore widths, approximated by π/q. As indicated by the pore size distribution (Figure 4.1 (c) and (d)), the ACC sample contains a significant fraction of ultramicropores with a mean size of around 0.6 nm. However, no distinct shoulder is observed in the SANS data near 5–6 nm^{-1}, which would directly correspond to this pore class. This absence is expected, as the (decreasing) SANS signal from ultramicropores overlaps with the (increasing) carbon structure factor in this q-range (see discussion in chapter 2.4.6).

At non-zero pressures, the data around 10 nm^{-1} could not be adequately described using only two pore-size classes, as suggested by the two visible shoulders in the SANS curves. To account for this, a simplified analytical model was developed to fit the SANS curves, incorporating contributions from three independent pore classes: mesopores (pore class I), supermicropores (class II), and ultramicropores (class III). Additional incoherent and coherent scattering contributions from both the carbon and adsorbate phases were also included to accurately capture the measured data.

Each of the three SANS contributions is modeled using a simple two-phase approach, assuming that within each pore class, the adsorbate density remains constant for a given gas pressure (as described in equation (6.1)). Furthermore, the geometry of the pore space is assumed to remain largely unchanged during adsorption, neglecting any adsorption-induced deformation [130,131]. Under these assumptions, the individual SANS contributions can be separated into a q-dependent scattering function $I_{SANS,i}(q,p)$, which encapsulates the structural information of the respective pore space (i=I, II, III), and a pressure-dependent scaling factor $S_i(p)$ (see equation (6.4), which quantifies the adsorbate density in that pore space. This relationship is expressed as:

$$\frac{d\Sigma}{d\Omega}(q,p) = I_{SANS,I}(q,p) + I_{SANS,II}(q,p) + I_{SANS,III}(q,p) + I_{B,C}(q) + I_{B,Ads}(q,p) \quad (6.3)$$

A major challenge in the quantitative analysis of the SANS data is the complexity and disordered nature of the pore structure, combined with the large pore space volume fraction. One of the earliest models to describe small-angle scattering from uncorrelated, randomly shaped scattering objects was the Debye-Anderson-Brumberger (DAB) model, which uses an exponentially decaying correlation function [70]. Later extensions improved on this approach by incorporating correlations between scattering objects, introducing damped oscillatory terms into the correlation function [73,111,132,133].

A model developed by Fratzl et al. [134,135], originally used to describe short-range correlated mineral platelets in bone with a two-phase system, is applied to describe $I_{SANS,i}(q,p)$ in equation (6.4). This "stack-of-cards" model provides an analytical solution for 1D correlations of plate-like scattering entities, where *T* is the mean chord-length of the two-phase system, and *a* and *b* are reduced lengths related to the damping part and the oscillatory part of the correlation function, respectively.

$$I_{SANS,i}(q) = S_i(p) \cdot \frac{T_i^2}{q^2}\left[\frac{(qT_i)^2+(a_i-1)\cdot(a_i^2+b_i^2)}{\left((qT_i)^2+a_i^2-b_i^2\right)^2+4a_i^2b_i^2}\right] \quad (6.4)$$

$$S_i(p) \cdot \frac{T^2}{q^2} = 8\pi^3 V_{tot}\varphi_1\varphi_2(\Delta\tilde{\rho})^2 \quad (6.5)$$

The scaling factors $S_i(p)$, also known as integrated intensities, are directly related to the volume fractions of the two phases and their scattering contrast ($\Delta\tilde{\rho}(p)^2$), and can thus be used to determine the adsorbate density as a function of pressure within the pores Here $\varphi_1$and φ_1 are the volume fractions of the two phases, and V_{tot} is the sample volume. The volume fractions for the respective pore classes were estimated according to the IUPAC recommendation [13] of mesopores (> 2 nm), supermicropores (0.7-2 nm), and ultramicropores (<0,7 nm) from the corresponding specific pore volumes V given in Table 4.2, with the skeletal density of the carbon material ρ_{skel} = (1.9 ± 0.2) g/cm^3 as determined by He pycnometry. For activated carbons, micropores are often approximated as slit-like pores formed between relatively flat (but multilayered) graphene sheets, akin to a "stack-of-cards"

model. This approach is considered a reasonable approximation for the ACC sample's micropores. Although mesopores are less likely to exhibit perfectly slit-like geometries, the stack-of-cards model is also applied to pore class I for simplicity, aligning with the QSDFT slit-pore model used to calculate the pore size distribution from the N_2 adsorption isotherms (Figure 4.1 (d)). In addition to the coherent SANS contributions, simple empirical expressions were used to describe the background terms $I_{B,C}(q)$ and $I_{B,Ads}(q,p)$ in equation (6.3) to account for interatomic/intermolecular interactions in the scattering curves at large q. These expressions for the SANS signal account for the correlation peaks at q>10 nm^{-1} (Figure 6.2 (a) and Figure 6.3 (a)) and consider that the coherent intermolecular structure factor approaches a constant value proportional to the coherent scattering cross-section as q→0. For both, the carbon stacking reflection and the intermolecular peak, a Gaussian function was used to empirically describe the correlation peak around 17-19 nm^{-1}.

$$I_{B,C}(q) = C_C + A \cdot exp\left(-\frac{1}{2}\left(\frac{q-q_m}{W_G}\right)^2\right) \tag{6.6}$$

$$I_{B,Ads}(q,p) = C_{Ads}(p) + A_{ads}(p) \cdot exp\left(-\frac{1}{2}\left(\frac{q-q_{D_2-D_2}}{W_{D_2-D_2}}\right)^2\right) \tag{6.7}$$

With A being the Amplitude, q_m the position and W_G the width (standard deviation) of the Gaussian. The absolute values of the constants C_C and C_{Ads} in equation (6.6) and (6.7) depend not only on the coherent scattering cross-section but also on the q-independent spin-incoherent scattering cross-section, which is particularly large for H_2 and is sensitive to the para/ortho ratio of the adsorbate. Including spin-incoherent scattering contribution in the model is crucial, as even the empty sample contains significant hydrogen content within the carbon matrix (see Table 4.1). Explicit calculations for the pre-factors C_C and $C_{Ads}(p)$ are given below in equation (6.8) and (6.9).

$$\begin{aligned} C_C = \left(\frac{d\Sigma}{d\Omega}\right)_{carbon} &= \frac{\rho_{pouring}}{\rho_{apparent}} \cdot \left(\frac{N}{V}\right)_i \left(\frac{d\sigma}{d\Omega}\right) = \frac{\rho_{pouring}}{\rho_{apparent}} \cdot \frac{m_c \cdot N_A}{V_{sample}} \cdot \sum_i \frac{w_i}{M_i} \cdot \left(\left(b_{inc,i}\right)^2 + \left(b_{coh,i}\right)^2\right) \\ &= \frac{\rho_{pouring}{}^2}{\rho_{apparent}} \cdot N_A \cdot \sum_i \frac{w_i}{M_i}\left(\left(b_{inc,i}\right)^2 + \left(b_{coh,i}\right)^2\right) \end{aligned} \tag{6.8}$$

$$C_{Ads} = \left(\frac{d\Sigma}{d\Omega}\right)_{ads,coh} + \left(\frac{d\Sigma}{d\Omega}\right)_{ads,inc} = \frac{\rho_{pouring}}{\rho_{apparent}} \cdot \left(\frac{N_{H_2/D_2}}{V_{sample}}\right)_{Mol} \left(\left(\frac{d\sigma}{d\Omega}\right)_{ads,coh} + \left(\frac{d\sigma}{d\Omega}\right)_{ads,inc}\right)$$

$$C_{Ads} = \frac{\rho_{pouring}}{\rho_{apparent}} \cdot \frac{\eta_{ex} \cdot m_c \cdot N_A}{V_{sample}} \cdot \left(\left(\frac{d\sigma}{d\Omega}\right)_{ads,coh} + \left(\frac{d\sigma}{d\Omega}\right)_{ads,inc}\right)$$

$$= \frac{{\rho_{pouring}}^2}{\rho_{apparent}} \cdot \eta_{ex} \cdot N_A \left(\left(b_{coh,^{H_2}/_{D_2}}\right)^2 + f_{op} \cdot \left(b_{inc,^{H_2}/_{D_2}}\right)^2\right) = K_{H_2/D_2} \cdot \eta_{ex} \qquad (6.9)$$

Here, m_C is the carbon sample mass, V_{sample} the irradiated sample volume, w_i the mass fraction, b_i the scattering length, and M_i the molar mass of the respective element i according to the chemical composition. The pouring density of the carbon powder within the sample holder $\rho_{pouring}$ was set to 0.3 g/cm³, whereas the apparent density is calculated by $\rho_{apparent} = \frac{1}{\frac{1}{\rho_{skel}} + V_{tot}}$. The constant C_{Ads} for $I_{B,Ads}(q,p)$ was determined entirely by the known adsorbate uptake η_{ex} (Figure 5.3 (b) and (c)). The spin-incoherent scattering length density of the molecule is not simply twice the one of the atoms but depends on the ratio of para- (p) to ortho-hydrogen (o). At room temperature, the corresponding factors in equation (6.9) are $f_{op,H2} = \frac{3}{4}$ and $f_{op,D2} = \frac{1}{3}$ for H_2 and D_2, respectively [39], while they are $f_{op,H2} = \frac{5}{9}$ and $f_{op,D2} = \frac{5}{16}$ for 87 K and $f_{op,H2} = \frac{1}{2}$ and $f_{op,D2} = \frac{1}{3}$ for 77 K. “Normal” H_2/D_2 corresponding to the equilibrium ratio at room temperature was dosed, but the equilibrium values at 87 K or 77 K may not have been reached. Hence, this factor comes with quite some uncertainty in the determination of the incoherent contribution. Since the calculation of C_{Ads} in equation (6.9) is additionally based on several other parameters of limited known accuracy, the error bands were calculated based on multiple fitting runs, where the parameters were varied within meaningful limits given in Table 6.4.

Table 6.4: Values used to calculate C_C (equation (6.8)) and C_{Ads} (equation (6.9)) and the respective upper and lower limits. Permutations of those values allow us to estimate the mean, minimal and maximal values of C_C as well as the increase in q-independent signal due to adsorption C_{Ads}. Reproduced from Ref. [57] and with permission from Elsevier.

Value	Mean	Min	Max
$\rho_{skel}\ (g/cm^3)$	1.9	1.7	2.1
$\rho_{pouring}\ (g/cm^3)$	0.2947	0.2653	0.3242
$\rho_{\text{apparent}}\ (g/cm^3)$	0.8945	0.6824	1.1069
$f_{op}(H2/D2)(g/cm^3)$	0.75/0.33	0.55/0.29	1/0.67
$C_C\ (cm^{-1})$	0.0076	0.0045	0.0134
$K_{H_2}\ (cm^{-1}\frac{g}{mol})$	1.1531	0.5593	2.4218
$K_{D_2}\ (cm^{-1}\frac{g}{mol})$	0.1167	0.0755	0.2057

The resulting fitting-function was obtained by combining equation (6.3) to (6.9) and was initially used to fit the SANS curve of the empty ACC sample (p=0, $I_{B,Ads}(q,p)$ =0), with the constant C_C for $I_{B,C}(q)$ determined entirely by the known sample composition (see Table 4.1). The fitting results are shown exemplarily for the highest loading of H_2 and D_2 in Figure 6.6, with fitting parameters for the three SANS contributions summarized in Table 6.5 and the rest can be Ref. [57]. The parameter $D_{\text{pore-pore}}$, representing the average distance between pores within the same size regime, aligns qualitatively with the pore size ranges for ultra- and supermicropores. However, for pore class I, the value is higher than expected, likely because the assumption of slit-like pores does not accurately represent the mesopores in the sample.

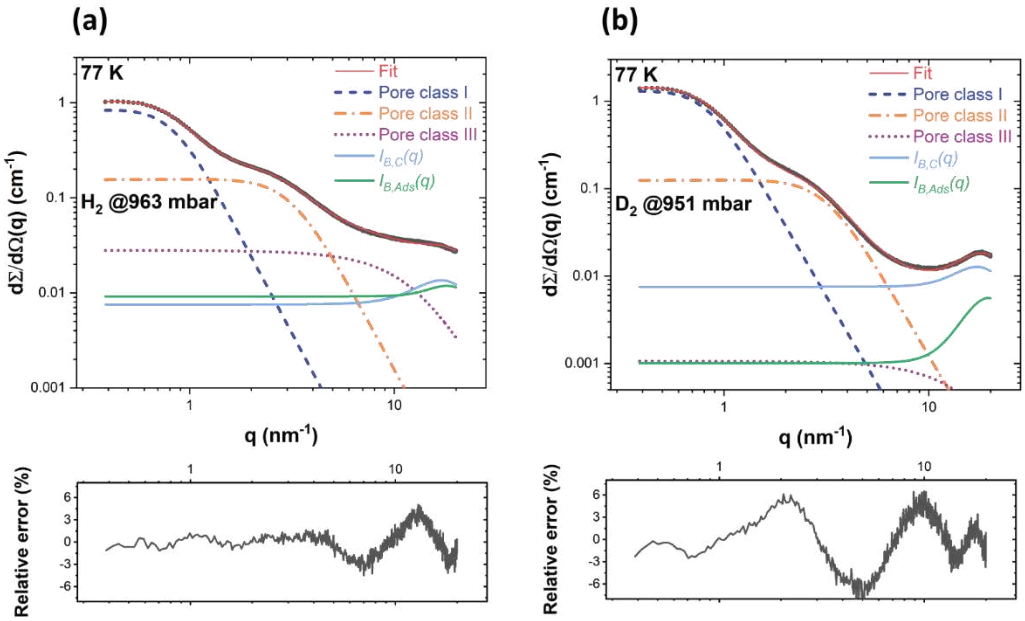

Figure 6.6: Fitting results of the SANS curves for the highest investigated gas pressure for (a) H_2 (963 mbar) and (b) D_2 (951 mbar) at 77 K. Reproduced from Ref. [57] and with permission from Elsevier.

For p≠0, the structural parameters from the empty sample, including the respective pore scattering contributions equation (6.4) and $I_{B,C}(q)$ equation (6.6), were fixed. The integrated intensities $S_i(p)$ and the adsorbate contribution $I_{B,Ads}(q,p)$ were then fitted to the pressure-dependent H_2/D_2 SANS data. Using this approach, all SANS curves for both H_2 and D_2 at all pressures were fitted accurately (Figure 6.6). The pre-factors $S_i(p)$ provide the scattering contrast $\Delta\tilde{\rho}(p)^2$, which is directly related to the density of adsorbed H_2/D_2 in each pore size regime as a function of pressure.

Two key factors affecting the reliability of the adsorbate density calculations are highlighted here. First, for H_2, the large incoherent scattering cross-section ($b_{inc,H_2}/b_{inc,D_2} \approx 40$) results in a high $C_{Ads}(p)$ (equation (6.9)) at pressures near 1 bar (Figure 6.6 (a)). This notably impacts the fit for pore class III, where the incoherent scattering contribution (solid line) is comparable to the coherent scattering from class III (dotted line). Second, for D_2, a different challenge arises at higher pressures. As D_2 densifies, its scattering length density approaches that of the carbon phase, reducing the scattering contrast (equation (6.1)). If the contrast vanishes, the SANS signal from pore class III becomes very small and comparable to $I_{B,Ads}(q,p)$.

Table 6.5: Parameters obtained from the fitting procedure of the empty carbon sample under vacuum at 77 K and 87 K. The order displays the sequence in which the SANS measurements were performed. For each new run, the SANS signal of the empty carbon sample was newly determined and used for the fitting procedure of the subsequent data set. The parameter $D_{pore-pore}$ is associated with the average distance between pores of the same size regime calculated by $D_{pore-pore} = 2\pi T/b$ [134,135]. Reproduced from Ref. [57] and with permission from Elsevier.

	H_2 @77 K				H_2 @87 K				D_2 @77 K				D_2 @87 K			
Pore regime	T (nm)	a (-)	b (-)	$D_{pore-pore}$ (nm)	T (nm)	a (-)	b (-)	$D_{pore-pore}$ (nm)	T (nm)	a (-)	b (-)	$D_{pore-pore}$ (nm)	T (nm)	a (-)	b (-)	$D_{pore-pore}$ (nm)
Pore class I	1.95	1	1.26	9.73	1.95	1	1.26	9.73	1.93	1	1.24	9.77	1.94	1	1.25	9.78
Pore class II	0.47	1	1.11	2.68	0.47	1	1.11	2.68	0.49	1	1.13	2.70	0.48	1	1.11	2.69
Pore class III	0.09	1	0.59	0.93	0.09	1	0.59	0.93	0.06	1	0.60	0.67	0.07	1	0.59	0.77

6.3.1 Pore-size dependent adsorbate densification – A hierarchical contrast model

When hydrogen enters the pore space, the scattering length density (SLD) for each pore size regime changes based on the average density of the adsorbed phase in that regime. Consequently, during the fitting procedure, only the pore size-dependent scaling factors $S_i(p)$ and the baseline $C_{Ads}(p)$ are allowed to vary with pressure. A hierarchical pore model was introduced to determine the adsorbate density within the distinct pore size classes (Figure 6.7).

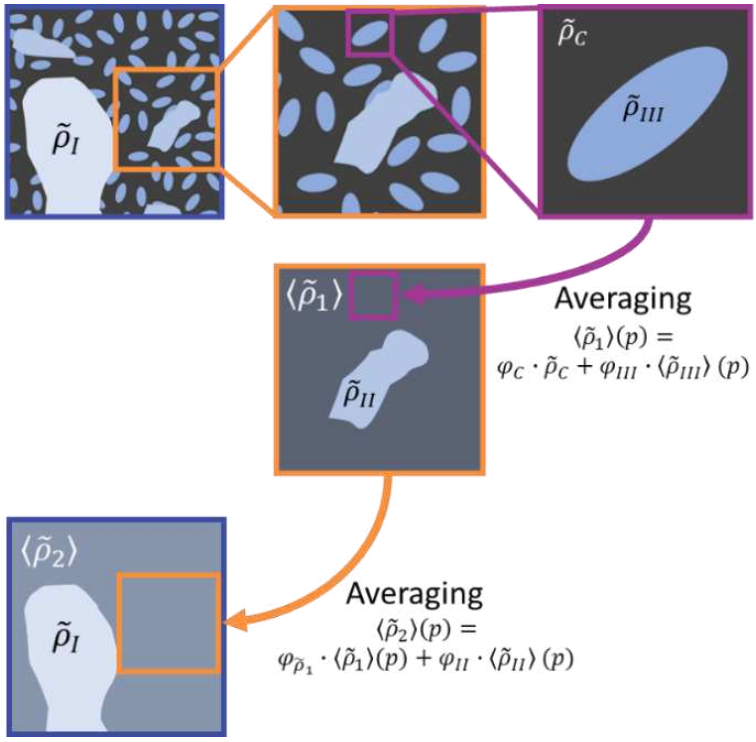

Figure 6.7: Schematic depiction of the hierarchical pore model used to calculate the pore size-dependent adsorbate density from SANS. Reproduced from Ref. [57] and with permission from Elsevier.

This model begins with the smallest pore size. For ultramicropores (class III), the scaling factor $S_{III}(p)$ represents a two-phase system of adsorbate-filled ultramicropores surrounded by the solid carbon matrix. At the next hierarchy level, supermicropores (class II) are embedded in a "matrix" that includes both the solid carbon phase and the already adsorbate-filled ultramicropores (class III). Similarly, for mesopores (class I), the matrix consists of the carbon phase and the adsorbate-filled ultramicropores and supermicropores, each with different

adsorbate densities. The respective scaling factors for each pore class in the filled and empty state are shown in equations (6.10)-(6.12):

$$S_{III}(p) = 8\pi^3 V \varphi_{III} \cdot \varphi_c \cdot (\langle\tilde{\rho}_C\rangle - \langle\tilde{\rho}_{III}(p)\rangle)^2$$
$$S_{III}(0) = 8\pi^3 V \varphi_{III} \cdot \varphi_c \cdot \langle\tilde{\rho}_C\rangle^2 \quad (6.10)$$

$$S_{II}(p) = 8\pi^3 V \varphi_{II} \cdot (\varphi_c + \varphi_{III}) \cdot (\{\langle\tilde{\rho}_C\rangle(p) \cdot \varphi_c + \langle\tilde{\rho}_{III}\rangle(p) \cdot \varphi_{III}\} - \langle\tilde{\rho}_{II}(p)\rangle)^2$$
$$S_{II}(0) = 8\pi^3 V \varphi_{II} \cdot (\varphi_c + \varphi_{III}) \cdot (\langle\tilde{\rho}_C\rangle \cdot \varphi_c)^2 \quad (6.11)$$

$$S_I(p) = 8\pi^3 V \varphi_I \cdot (\varphi_c + \varphi_{III} + \varphi_{II}) \cdot \left(\{\langle\tilde{\rho}_C\rangle \cdot \varphi_c + \langle\tilde{\rho}_{III}\rangle(p) \cdot \varphi_{III} + \langle\tilde{\rho}_{II}\rangle(p) \cdot \varphi_I\} - \langle\tilde{\rho}_I\rangle(p)\right)^2$$
$$S_I(0) = 8\pi^3 V \varphi_I \cdot (\varphi_c + \varphi_{III} + \varphi_{II}) \cdot (\langle\tilde{\rho}_C\rangle \cdot \varphi_c)^2 \quad (6.12)$$

$$\langle\tilde{\rho}_c\rangle = \sum_i \varphi_i \, \tilde{\rho}_i = \sum_i \frac{V_i}{V_{skel}} \frac{\rho_i \, b_i \, N_A}{M_i} = \sum_i \frac{V_i}{V_{skel}} \frac{m_i \, b_i \, N_A}{M_i \, V_i} = \sum_i \frac{V_i}{m_{skel}} \frac{m_i \, b_i \, N_A \, \rho_{skel}}{M_i \, V_i}$$
$$= \rho_{skel} \, N_A \sum_i \frac{b_i \, w_i}{M_i} \quad (6.13)$$

In these equations, V denotes the sample volume, and $\varphi_{III}, \varphi_{II}, \varphi_I$ are the volume fractions of ultramicropores, supermicropores, and mesopores, respectively. The carbon phase volume fraction is $\varphi_C = 1 - \varphi_{III} + \varphi_I + \varphi_I$. The SLDs of the adsorbate phase in the respective pore classes are denoted as $\tilde{\rho}_{III}(p), \tilde{\rho}_{II}(p), \tilde{\rho}_I(p)$. Importantly, the "carbon phase" in these equations is not pure carbon but includes non-negligible amounts of oxygen, nitrogen, and hydrogen. Since the specific locations of functional groups are unknown, the average SLD of the carbon matrix ($\langle\tilde{\rho}_C\rangle$) was calculated using equation (6.13) and is based on the composition of the empty sample (Table 4.1). The small amount of zinc in the sample was excluded due to its low concentration, negligible incoherent scattering cross-section, and similar coherent scattering cross-section to that of carbon [136].

To calculate the absolute mass density of the adsorbed phase in each pore size class, the scaling factor at a given pressure (equations (6.10)-(6.12)) is normalized by the corresponding factor in the empty state, where $\langle\tilde{\rho}_{III}\rangle(p) = \langle\tilde{\rho}_{II}\rangle(p) = \langle\tilde{\rho}_I\rangle(p) = 0$. Starting with ultramicropores (equation (6.14)), the mean SLD of the adsorbed phase is determined, which is then used to calculate the SLD for supermicropores (equation (6.15)) and finally for mesopores (equation (6.16)). The mass density of the adsorbate in each pore regime as a

function of pressure is derived from the relationship between SLD and mass density (equation (6.17)).

$$\langle\tilde{\rho}_{III}\rangle(p) = \langle\tilde{\rho}_C\rangle - \langle\tilde{\rho}_C\rangle \cdot \sqrt{\frac{S_{III}(p)}{S_{III}(0)}} \tag{6.14}$$

$$\langle\tilde{\rho}_{II}\rangle(p) = -\left(\langle\tilde{\rho}_C\rangle \cdot \varphi_C \cdot \sqrt{\frac{S_{II}(p)}{S_{II(0)}}} - \langle\tilde{\rho}_C\rangle \cdot \varphi_C - \langle\tilde{\rho}_{III}\rangle(p) \cdot \varphi_{III}\right) \tag{6.15}$$

$$\langle\tilde{\rho}_I\rangle(p) = -\left(\langle\tilde{\rho}_C\rangle \cdot \varphi_C \cdot \sqrt{\frac{S_I(p)}{S_I(0)}} - \langle\tilde{\rho}_C\rangle \cdot \varphi_C - \langle\tilde{\rho}_{III}\rangle(p) \cdot \varphi_{III} - \langle\tilde{\rho}_{II}\rangle(p) \cdot \varphi_{II}\right) \tag{6.16}$$

$$\rho_i(p) = \frac{M_{H_2/D_2} \cdot \langle\tilde{\rho}_i\rangle(p)}{b_{H_2/D_2} \cdot N_A} \tag{6.17}$$

The evolution of the pore-size-dependent adsorbate density for the three size regimes is illustrated in Figure 6.8. The shaded error bands reflect uncertainties in skeletal density, chemical composition, volume fractions, pouring density, and the estimation of the para-to-ortho ratio, while fitting errors were not considered (see Table 6.4). At 77 K (Figure 6.8 (a) and (c)), the adsorbate densities for pore classes I and II are relatively similar and remain well below the liquid density of bulk hydrogen. In contrast, pore class III shows a much stronger increase in adsorbate density with rising pressure. For H_2, the density surpasses the bulk liquid density of 0.072 g/cm³ at approximately 500 mbar and even slightly exceeds the bulk solid density of 0.087 g/cm³ at higher pressures. This finding is consistent with earlier experimental and simulation studies reporting the formation of solid-like hydrogen in micropores under supercritical conditions [54,56,123,128,129].

The D_2 density evolution (Figure 6.8 (c)) demonstrates weaker densification compared to H_2, with the mass densities in pore class III being of a similar order to those for H_2 but corresponding to approximately half the molar density. This discrepancy between H_2 and D_2 is unexpected, as adsorption isotherms (Figure 5.3 (b) and (c)) suggest a slightly higher molar D_2 density than H_2 density. However, for D_2, the scattering contrast decreases significantly as the density approaches the bulk solid density, eventually reaching a matching point where the scattering contrast for the carbon phase becomes negligible (Table 6.3). This diminishing

contrast reduces the sensitivity of density measurements for D_2, making the absolute values less reliable than those for H_2, particularly in pore class III at higher pressures.

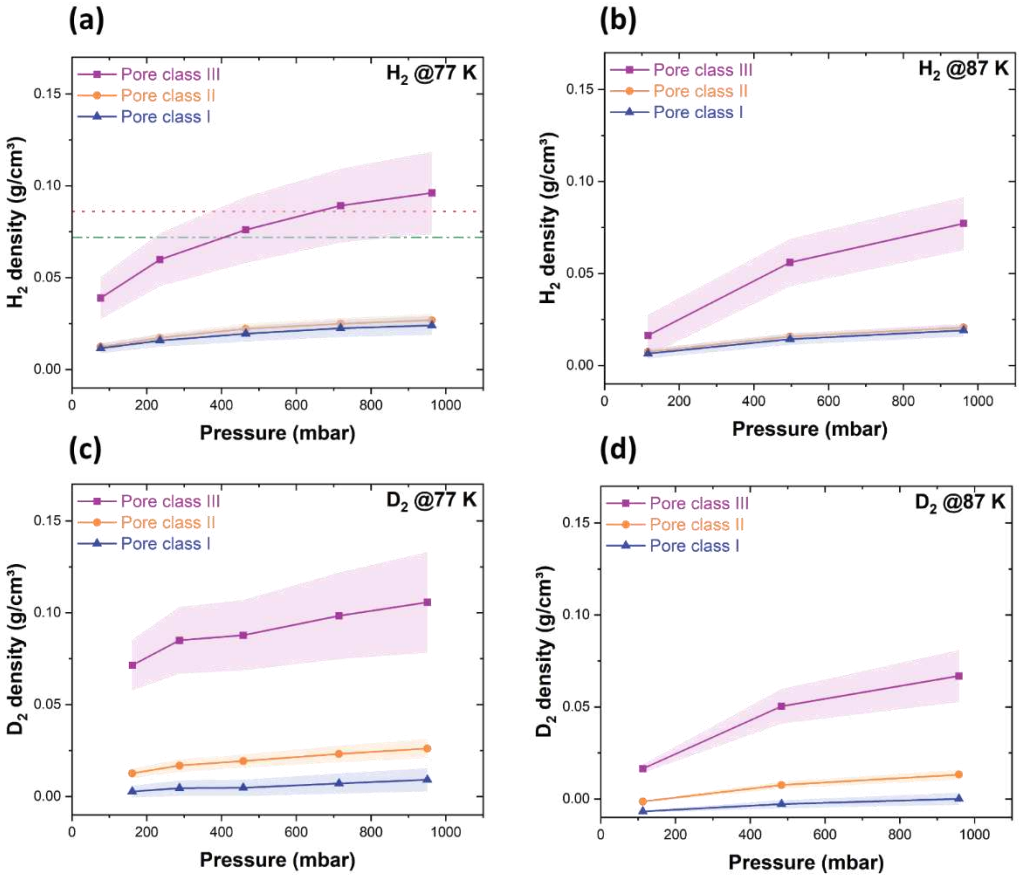

Figure 6.8: Pore-size-dependent density evolution as a function of pressure and temperature. H_2 at 77 K (a) and 87 K (b); D_2 at 77 K (c) and 87 K (d). The dashed-dotted horizontal lines in Figure 8a depict the liquid H_2 density, whereas the horizontal dotted lines depict the corresponding solid density. Reproduced from Ref. [57] and with permission from Elsevier.

Further evidence supporting the notion that the D_2 molar density in the smallest pores approaches similar values to H_2 comes from the D_2-D_2 correlation peak at ~18 nm^{-1} in Figure 6.3 (a). The peak intensity increases with the adsorbed amount, and the peak maximum (q_{max}) shifts to higher q-values. The quantity $d_{D_2-D_2} = 2\pi/q_{max}$, representing the mean intermolecular distance, is plotted as a function of molar uptake in Figure 6.9 (a). Assuming a hexagonally-close-packed (hcp) molecular arrangement, as proposed by Balderas-Xicohténcatl et al. [80], the density of the molecules responsible for this correlation peak can be estimated.

Figure 6.9 shows that the mass density of D_2 derived from this estimate aligns with the bulk liquid density at low adsorbed amounts at 87 K and exceeds the solid density at the highest adsorbed amounts at 77 K. While the correlation peak cannot be definitively assigned to a specific pore size class, this observation supports the hypothesis that the molar densities of D_2 and H_2 in pore class III are similarly high, both exceeding the bulk solid density due to the effects of strong confinement. For H_2-H_2 correlations, a similar peak is expected. However, due to the much lower coherent scattering cross-section of H_2 (approximately 1/4 that of D_2) and the high incoherent scattering contribution of H_2, the detailed evolution of this peak could not be evaluated.

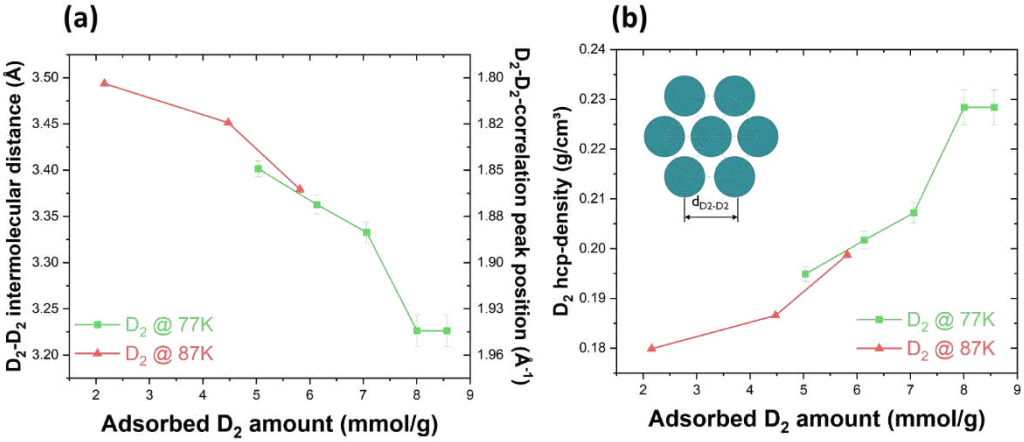

Figure 6.9: a) Evolution of the D_2-D_2-intermolecular distance as a function of the adsorbed amount and b) the evolution of D_2 density calculated from the D_2-D_2-intermolecular distance assuming hexagonal packing of the molecules [81]. Reproduced from Ref. [57] and with permission from Elsevier.

A further explanation for the discrepancy in D_2 density calculation arises from the subtle effect of hydrogen exchange within the carbon matrix. The empty sample contains a considerable amount of chemically bound hydrogen. If these hydrogen atoms are accessible to the adsorbate, a hydrogen-deuterium (H-D) exchange may occur during D_2 adsorption, leaving some chemically bound deuterium (D) in the carbon matrix and forming HD or H_2 in the physically adsorbed phase. Indeed, up to 25% of the hydrogen was observed to be replaced by deuterium, as evidenced by changes in both the sample transmission and the SANS signal of the empty sample before and after a D_2 adsorption/desorption cycle.

Figure 6.10 (a) displays the SANS curves of the empty carbon sample collected before each of the four adsorption runs, performed sequentially as H_2 at 77 K, H_2 at 87 K, D_2 at 77 K, and D_2 at 87 K. After each adsorption/desorption cycle, the sample was evacuated, and SANS measurements were repeated for this nominally empty state. The curves are nearly identical, except for noticeable differences around 10 nm^{-1}. The initial measurement (black curve) represents the fully outgassed sample before any adsorption. After the first H_2 adsorption/desorption cycle at 77 K (red curve), the high-q intensity increases slightly, while the low-q intensity decreases, suggesting residual H_2 remained in the sample after evacuation. Following the second H_2 cycle at 87 K (blue curve), the SANS curve aligns perfectly with the original (black curve), indicating that the sample returned to its initial state. However, after the first D_2 adsorption/desorption cycle (green curve), the high-q intensity drops below the initial value, strongly suggesting that chemically bound hydrogen atoms in the sample exchanged with deuterium. This exchange reduces the dominant incoherent scattering contribution in the 10 nm^{-1} region.

This conclusion is further supported by changes in the sample transmission (T). Since neutron absorption is negligible for the elements in the sample, 1-T is directly proportional to the total scattering cross section (incoherent + coherent) of atoms in the neutron beam. As shown in Figure 6.10 (b), 1-T remains consistent at ~0.16 for the empty sample after the two H_2 adsorption cycles. However, after the first D_2 adsorption/desorption cycle, 1-T drops significantly to ~0.145, further confirming the exchange of H with D. Given the substantial hydrogen content in the activated carbon cloth and hydrogen's high incoherent scattering cross section, this decrease strongly indicates that H-containing functional groups were replaced by D, reducing the total scattering cross section. Stronger evidence for H-D exchange emerges during D_2 adsorption. Initially, 1-T increases with D_2 uptake but begins to decrease at higher D_2 uptake levels. In contrast, during H_2 adsorption at both 77 K and 87 K, a reversible linear relationship is observed between 1-T and the adsorbed amount, as expected. A decreasing total scattering cross section with increasing D_2 uptake can only be explained by H-D exchange, where the resulting HD or H_2 molecules escape into the gas phase outside the neutron beam. Using equation (6.8), it is estimated that approximately 25% of all H atoms in the sample are replaced by D during the process.

This exchange process would lead to an increase in the carbon matrix's coherent scattering length density (see equation (6.13)), resulting in an underestimation of the absolute scattering intensity and, consequently, the adsorbate density. Due to the lack of information on the time scale of this exchange and the specific locations of the functional groups involved, no quantitative analysis was undertaken. Therefore, the D_2 density evolution, particularly for pore class III (Figure 6.8), should be interpreted with caution.

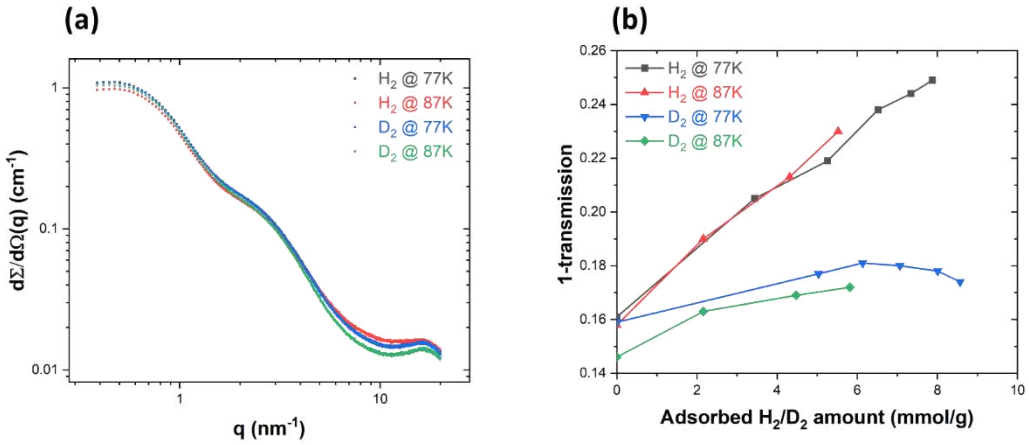

Figure 6.10: (a) SANS curves of the evacuated (empty) carbon sample before each subsequent adsorption run. (b) Relative changes of the total scattering cross section as a function of the H_2/D_2 uptake, measured via the sample transmission before each SANS run. The legend shows the order in which the measurements where conducted. Reproduced from Ref. [57] and with permission from Elsevier.

6.3.2 Model limitations and conclusion

The SANS model developed in this study provides consistent quantitative results for the pore size-dependent densification of supercritical H_2 at low gas pressures. However, for D_2, the derived densities appear underestimated, likely due to H-D exchange within the sample during adsorption, which could not be accounted for quantitatively. The fitting procedure was carefully designed to address non-uniqueness in parameters, especially for pore class III, where the SANS region (dominated by scattering contrast) overlaps with the structure factor region (dominated by the squared SLD of the adsorbate). Multiple fitting runs were conducted, constraining key parameters to physically meaningful limits, including the carbon matrix composition, skeleton density, and pore class volume fractions. An essential consistency check was that the total gas uptake could be calculated in absolute units from $C_{Ads}(p)$ (equation

(6.9)), aligning closely with the adsorption isotherms. While these efforts validate the error bands shown in Figure 6.8, some fundamental limitations of the SANS analysis using the hierarchical contrast model warrant critical discussion.

Figure 6.8 shows that adsorbate densification in pore classes I and II is similar across all temperatures and pressures, whereas pore class III exhibits significantly different behavior. Given the comparable mean pore sizes of classes II and III, the assumption that class II pores are exclusively surrounded by smaller class III pores may oversimplify the system. The hierarchical model also neglects inter-pore scattering contributions, such as the influence of class II pores on those in class III. Additionally, the pore volumes used in the analysis were derived from QSDFT data based on N_2 adsorption, which may not accurately represent the pore space accessible to hydrogen, especially in ultramicropores. Another oversimplification is the assumption that heteroatoms like oxygen, nitrogen, and hydrogen are uniformly distributed throughout the carbon matrix. In reality, these elements are likely localized within surface functional groups, leading to variations in the SLD of the carbon matrix depending on the pore size.

This work also highlights the need to extend experimental measurements to larger scattering vectors. Distinguishing phenomena in the smallest pores from atomistic adsorbate/adsorbent structures remains challenging with the current data. Capturing the full intermolecular correlation peak (Figure 6.3 (a)) would allow for a more detailed and quantitative analysis of its shift with pressure, providing complementary insights into adsorbate density. Future experiments would benefit from neutron scattering instruments capable of covering a broader scattering vector range, such as 0.3 nm^{-1} to >50 nm^{-1}, to further enhance understanding of adsorbate behavior in nanoporous materials [137,138]. Isotope effects and the preferential adsorption of para- and ortho-H_2/D_2 may contribute to the observed differences in adsorption behavior and the temperature- and isotope-dependent density evolution.

6.4 Comparing atomistic simulations with experiments

The hierarchical contrast model previously developed allowed for the separation of pore size categories, demonstrating that densification is strongest in ultramicropores (~0.7 nm). However, its analytical approach, based on slit-shaped pores and homogeneous adsorbate density, may not fully capture molecular interactions and quantum effects in highly confining pore structures. To address these limitations, in-silico neutron scattering simulations of H_2 and D_2 adsorption in analogous nanoporous carbons were performed. By incorporating isotope-specific quantum corrections, these simulations provide a refined understanding of confinement-dependent densification and enable a direct comparison with experimental neutron scattering data.

6.4.1 Nanoporous carbon models

Nanoporous carbon (NPC) structures were selected from atomistic models generated through annealed molecular dynamics simulations, based on the work of de Tomas et al. [35]. These structures were chosen to closely resemble MSC-30 (NPC1 and NPC2) and ACC (NPC3 and NPC4) in terms of their pore structural characteristics, as shown in Figure 6.11(a,b) and Figure 6.11(g,h), respectively. To evaluate their pore structure characteristics, nitrogen (N_2) adsorption simulations were performed, following the methodology outlined in Ref. [139]. While an exact match between the model structures and the experimental materials was not achieved, the pore characteristics were sufficiently similar to justify using NPC1 and NPC2 as "digital twins" for MSC-30, and NPC3 and NPC4 as corresponding models for ACC.

A clear influence of annealing temperature on the NPC structures is apparent from Figure 6.11, despite achieving comparable porosities. Lower annealing temperatures (NPC1 and NPC3) result in highly fragmented surfaces with numerous local defects, whereas higher annealing temperatures (NPC2 and NPC4) produce smoother structures with fewer defects [35,140]. However, despite these visible differences, both annealing conditions yield similar adsorption isotherms, leading to comparable pore size distributions (PSDs) for N_2 at 77 K, as shown in Figure 6.11 (d) and Figure 6.11 (f).

Beyond gas sorption analysis, measured neutron scattering profiles of MSC-30 and ACC were compared with simulated scattering curves of the NPC structures, calculated using a reciprocal lattice approach (see section 2.4.6). The agreement between MSC-30 and NPC1/NPC2 is relatively strong (Figure 6.11 (c)), whereas for ACC and NPC3/NPC4, the match is more qualitative rather than quantitative (Figure 6.11 (e)). Several factors may contribute to these discrepancies:

i) The simplified model carbons may not fully capture the complexity of the experimental materials, particularly in the mesopore regime.

ii) The NPC models consist solely of carbon, whereas ACC contains a non-negligible amount of surface functional groups, primarily hydrogen- and oxygen-based species.

iii) The small simulation box size (<10 nm) introduces statistical noise in the calculated scattering curves, limiting statistical averaging.

Consistent with the gas adsorption results, the simulated scattering curves for high- and low-temperature annealed structures exhibit remarkable similarity below q ≈ 25 nm^{-1}. However, the discrepancies, particularly visible in Figure 6.11 (e), are likely due to finite simulation box effects. The two peaks observed at q ≈ 30 nm^{-1} and q ≈ 55 nm^{-1} correspond to the in-plane 2D lattice of curved graphene sheets [108]. Additionally, the increased structural distortion at lower annealing temperatures (Figure 6.11 (a), (g)) results in broader peaks and lower peak intensity, in contrast to the higher annealing temperatures (Figure 6.11 (b), (h)), which yield more well-defined local ordering.

To compare the simulated nanoporous carbon (NPC) structures with the experimental carbon samples, pore structure characteristics derived from N_2 adsorption and the correlation length obtained from SANS are summarized in Table 6.6. For the MSC-30 sample and the NPC1/NPC2 structures, a good quantitative agreement is observed between the mean pore size $d_{A,N2}$ obtained from gas sorption and the correlation length l_c derived from SANS. However, as previously noted, the NPC models lack the mesoporous contribution present in MSC-30, as seen in the pore size distribution for pores larger than 2 nm (Figure 6.11 (d)).

In the case of the ACC sample, the discrepancies between the experimental and simulated structural parameters are more pronounced. These differences likely stem from the presence

of heteroatoms in the experimental carbon material, which are absent in the simulated models. Despite this limitation, NPC3 and NPC4 were identified as the best-matching structures among those reported by de Tomas et al. [35], offering the closest approximation to the porosity characteristics of ACC.

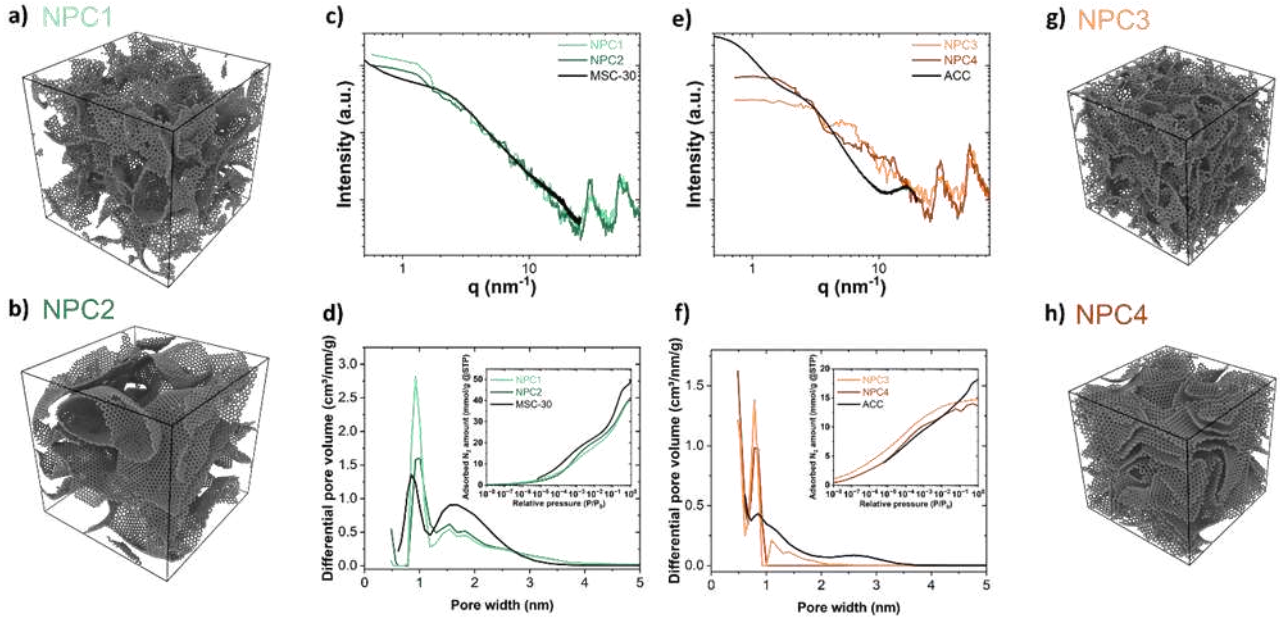

Figure 6.11: Molecular dynamics-generated nanoporous carbon (NPC) structures. (a) NPC1: porosity ϕ = 0.65, annealing temperature T = 2000 K; (b) NPC2: ϕ = 0.65, T = 4000 K; (g) NPC3: ϕ = 0.48, T = 2000 K; (h) NPC4: ϕ = 0.48, T = 4000 K. The cubic simulation box measures 10.85 nm for NPC1 and NPC2, and 8.61 nm for NPC3 and NPC4. (c, e) Simulated neutron scattering patterns for NPC1 and NPC2 (turquoise) and NPC3 and NPC4 (orange), obtained using the method described in Section S1.1. The signals were smoothed for clarity, with the corrected and scaled SANS signals from MSC-30 and ACC shown in black. (d, f) Differential pore volume distributions derived from the QSDFT slit-pore model applied to simulated N_2 isotherms of NPC1 and NPC2, and NPC3 and NPC4, respectively. The PSDs of MSC-30 and ACC are included for comparison (black curves). Insets in (d) and (f) display the simulated adsorption branches of the isotherms on a semi-logarithmic scale alongside experimental isotherms. Reproduced from submitted manuscript [141]: Carbon, Elsevier.

Table 6.6: Comparison of the pore structure characteristics from gas sorption using N_2 at 77 K and from SANS.

Sample	$S_{QSDFT,N2}$ (a)	$V_{QSDFT,N2}$ (b)	$d_{A,N2}$ (c)	φ (d)	l_c (e)
	(m^2/g)	(cm^3/g)	(nm)	(-)	(nm)
MSC-30	**2497**	**1.59**	**1.27**	**0.73**	**0.7**
NPC1	1946	1.31	1.35	0.66	0.74
NPC2	2003	1.33	1.33	0.65	0.71
ACC	**1389**	**0.59**	**0.84**	**0.53**	**0.79**
NPC3	1624	0.48	0.59	0.48	0.59
NPC4	1381	0.48	0.70	0.48	0.66

(a) specific surface area calculated using the Quenched Solid Density Functional Theory (QSDFT) method, (b) total specific pore volume derived by the QSDFT method covering the range of pore sizes from 0.6 to 35 nm, (c) average pore width d_A calculated for slit pores using $2 \cdot V_{QSDFT} / S_{QSDFT}$, (d) porosity of the carbon structure. For the carbon samples the porosity φ, where ρ_{skel} was chosen to be 1.9 g/cm³ for both samples, (e) correlation length obtained by using equation (2.56). Reproduced from submitted manuscript [141]: Carbon, Elsevier.

6.4.2 Monte Carlo simulations of H_2 and D_2 adsorption

The simulated adsorption isotherms for H_2 and D_2 in the NPC structures are presented in Figure 6.12(a) and Figure 6.12(b), respectively (see section 2.3.2 and for more detail). The LJ-parameters used in equation (2.14) and (2.15) are summarized in Table 6.7). The higher H_2 and D_2 uptake in NPC3 at ≈1000 mbar can be attributed to its greater specific surface area, resulting from a smaller average pore size at an equivalent pore volume, compared to NPC4 (Table 6.6).

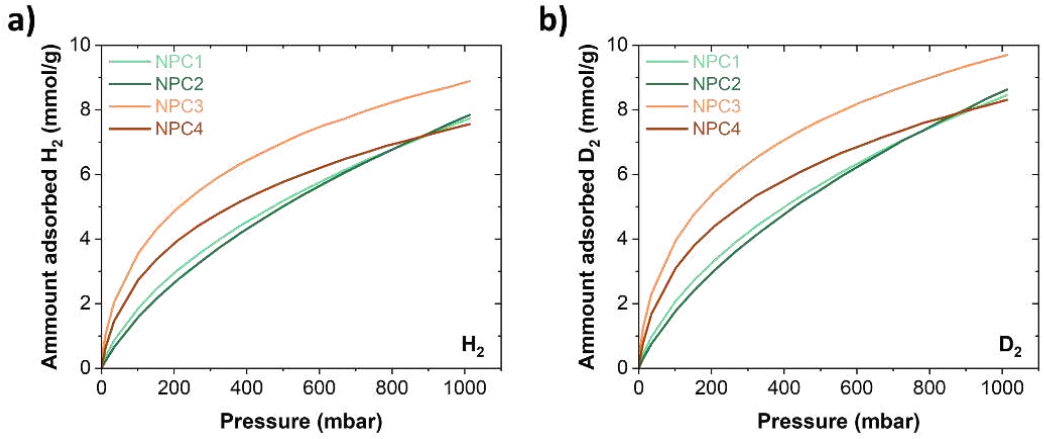

Figure 6.12: (a,b) low-pressure H_2 and D_2 adsorption isotherms at 77 K of the two carbon materials and the NPC models, respectively. The parameters for the interaction potential can be found in Table 6.7. Reproduced from submitted manuscript [141]: Carbon, Elsevier.

A slightly higher D_2 uptake compared to H_2 is observed for all four NPC structures, which can be explained by the deeper Lennard-Jones (LJ) potential well for D_2, a consequence of its higher mass and the Feynman-Hibbs quantum correction term (equation (2.14) and (2.15), see also Figure 6.15(a), inset). This trend is in good agreement with experimental findings, which also show a marginally higher D_2 uptake relative to H_2.

When comparing the experimental adsorption isotherms (Figure 5.3(a) and Figure 5.3(b)) with the simulated data (Figure 6.12 (a) and Figure 6.12 (b)), a strong correlation is observed between ACC and NPC3/NPC4. However, for MSC-30, the agreement with NPC1/NPC2 is poor, particularly at high pressures (~1000 mbar). In the experiments, MSC-30 reaches uptake values close to 14 mmol/g, whereas the simulated structures exhibit a lower uptake of approximately 8 mmol/g. This discrepancy arises from the significantly higher specific pore volume and surface area (Table 6.6), which is largely due to the presence of mesopores, a feature not captured in the simulated NPC models.

Table 6.7: Parameters used to model the interaction potential of different adsorbates according to equation (2.14) and (2.15). Reproduced from submitted manuscript [141]: Carbon, Elsevier.

Adsorbate	σ_{ij} (Å)	ε_{ij}/k_b (K)	m_r (g/mol)	Reference
N_2	3.615	101.5	-	[142]
C	3.4	28.0	-	[143]
H_2	2.958	36.7	1.00784	
D_2	2.958	36.7	2.01410	

6.4.3 Influence of the atomistic structure – Degree of confinement

A more detailed investigation of the influence of atomic-scale carbon structure, particularly pore size and shape, on H_2/D_2 uptake can be achieved by introducing a parameter that quantifies the local geometry of the carbon framework around an adsorbed molecule. This is captured by the Degree of Confinement (DoC), a concept introduced by van Meel et al. [144] as a parameter-free nearest-neighbor algorithm. Initially developed to study ion confinement in nanoporous carbon models [145,146], the DoC has since been adapted to investigate molecular adsorption in confined environments.

The DoC is defined by the total solid angle formed between an adsorbed molecule and its neighboring carbon atoms within a predefined cut-off radius [146], as visualized in Figure 6.13 (a). Since carbon atoms in graphene-like structures predominantly arrange in hexagonal rings, the maximum solid angle is determined by the hexagonal lattice geometry. The reference value for a perfect six-membered carbon ring is $A_{carbon_6} = 0.6046$ represents the fractional surface area occupied by a hexagonal carbon arrangement. This value changes for pentagonal $A_{carbon_6} = 0.9132$and heptagonal $A_{carbon_6} = 0.5811A$(structures, which appear in Stone-Wales defects that induce curvature in graphene layers).

The solid angle contribution ($\alpha_{i,j}$) of each carbon atom j surrounding a molecule i within a given cut-off radius R_C can be calculated using equation (6.18). There where $d_{i,j}$ is the distance between the molecule and the carbon atom, and R_j is the radius assigned to each carbon site, which is set to half of the C–C bond length in a perfect hexagonal carbon lattice

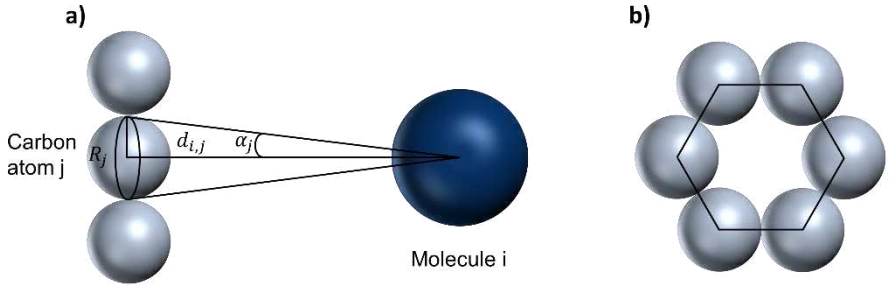

Figure 6.13: (a) Schematic representation of the distances used to calculate the Degree of Confinement (DoC) based on equations (6.18) and (6.19). (b) Idealized arrangement of carbon atoms contributing to the DoC. Reproduced from submitted manuscript [141]: Carbon, Elsevier.

$$\alpha_{i,j} = 2\pi\left(1 - \frac{d_{i,j}}{\sqrt{d_{i,j}^2 + R_j^2}}\right) \text{ with } R_j = \frac{d_{c-c}}{2} = 0.715 \text{ Å} \tag{6.18}$$

$$DoC = \frac{\sum_{j=1}^{N_{carbon}} \alpha_{i,j}}{4\pi \cdot A_{carbon}} \cdot 100 \text{ with } A_{carbon_6} = 0.6046 \tag{6.19}$$

The cut-off radius R_C, which defines the maximum distance at which carbon atoms contribute to confinement effects, is strongly influenced by the nature of molecular interactions. In previous studies, Prehal et al. [147] selected a fixed cut-off radius of 13.9 Å when modeling argon adsorption in non-atomistic carbon structures. In contrast, Merlet et al. [146] proposed a more adaptive approach for ion-electrosorption in atomistic models of disordered carbons, where R_C was defined as the first minimum of the radial distribution function (RDF) $g(r)$. Following this methodology, the present study determined R_C by analyzing the RDFs of carbon, H_2, and D_2, as illustrated in Figure 6.14 (a)–(c). The first minimum of $g(r)$ was identified at approximately 5 Å for both H_2 and D_2, establishing it as the relevant cut-off radius for confinement analysis in this system.

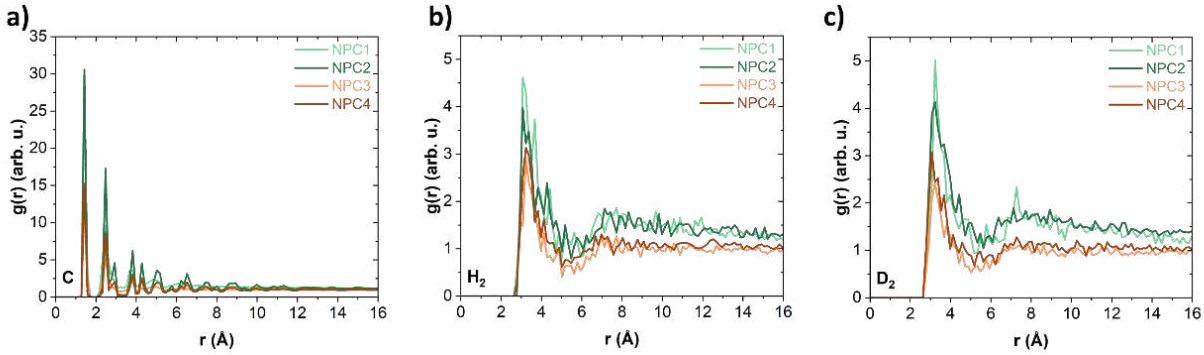

Figure 6.14: Radial distribution function g(r) for carbon calculated from (a) the NPC models and from the final spatial arrangement of adsorbed (b) H_2 and (c) D_2 molecules within the NPCs at a pressure of 1000 mbar, respectively. Reproduced from submitted manuscript [141]: Carbon, Elsevier.

The radial distribution function (RDF) of carbon (Figure 6.14 (a)) exhibits distinct peaks at 1.43 Å, 2.48 Å, and 3.83 Å, corresponding to the C–C bond length, the lattice vector length, and the approximate separation between graphene sheets, respectively. Additionally, the shortest H_2–H_2 distance observed is around 3.26 Å, which aligns well with the minimum of the interaction potential calculated using equation (2.14) (as illustrated in the inset of Figure 6.15 (a)).

The Degree of Confinement (DoC) was computed individually for each molecule within the NPC structures, allowing for tracking of the respective values. This enabled the construction of DoC histograms for various adsorption loadings, which are presented in Figure 6.15 (b) and (c). From these histograms, the mean DoC was determined, and its evolution as a function of loading is depicted in Figure 6.15 (a). A higher DoC value indicates that the molecule is closer to the surrounding carbon atoms and is more tightly enclosed by the pore walls, reflecting stronger adsorption interactions. As a result, the DoC provides insight into the local pore geometry, effectively linking pore structure to adsorption strength. A visual representation of this concept is provided in the top row of Figure 6.15.

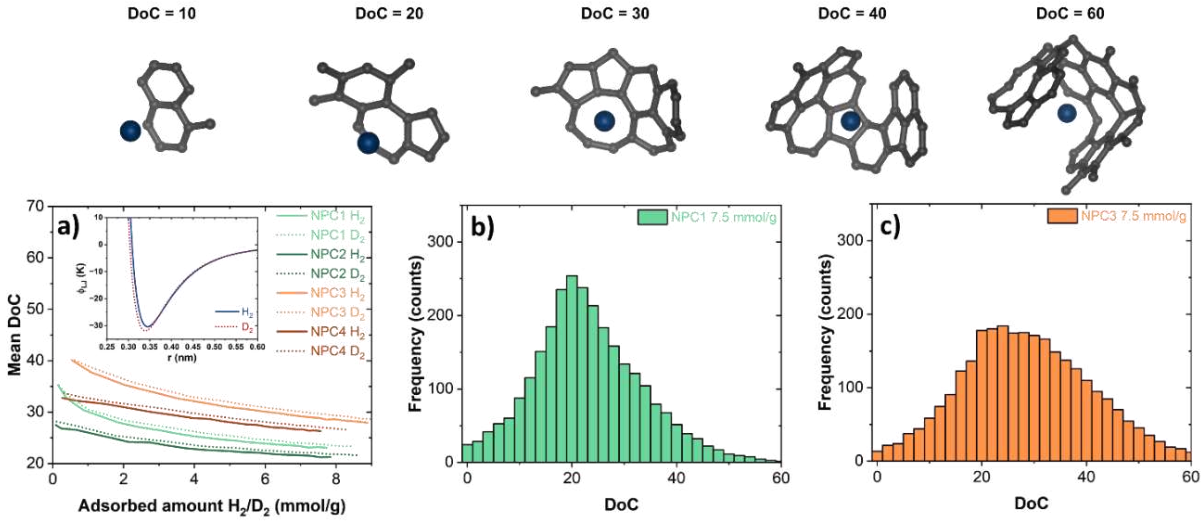

Figure 6.15: (a) Mean Degree of Confinement (DoC) as a function of H_2/D_2 loading for the four NPC structures. Solid lines represent H_2 adsorption, while dashed lines correspond to D_2 adsorption. The inset displays the Lennard-Jones fluid molecule interaction potential, calculated using equation (2.14) and (2.15) with parameters from Table 6.7. (b) DoC histogram for the NPC1 structure at an H_2 loading of 7.5 mmol/g, and (c) the corresponding DoC histogram for NPC3. The top row illustrates visualizations of various carbon substructures associated with different DoC values. Reproduced from submitted manuscript [141]: Carbon, Elsevier.

Figure 6.15 (a) illustrates the evolution of the mean Degree of Confinement (DoC) as a function of the H_2/D_2 adsorbed amount. At low filling fractions, the mean DoC is at its highest, which aligns with the expectation that adsorption sites with the strongest confinement potential—those with high DoC values—are occupied first. This trend highlights the preference of hydrogen molecules for strongly confining adsorption sites at low loadings.

The DoC distributions for NPC1 and NPC3 at a simulated H_2 uptake of 7.5 mmol/g are shown in Figure 6.15 (b) and Figure 6.15 (c), respectively. The mean DoC for NPC1 is approximately 20, with values extending up to 60, though these higher values correspond to only a few adsorption sites. In contrast, NPC3 exhibits a higher median DoC at the same loading, reflecting its smaller mean pore size, as confirmed by Figure 6.11 (f) and Table 6.6. The highest DoC values occur in pores where adsorbed molecules are almost entirely surrounded by carbon, as visualized in the top right of Figure 6.15. The mean DoC decreases with increasing pore filling, with median DoC values at low uptake being approximately 25% higher than at high uptake, although the overall distribution broadens as loading increases. Additionally, structural porosity plays a key role in confinement, as seen in Figure 6.15 (a), where NPC3 and

NPC4, which have a lower overall pore volume fraction, consistently exhibit higher mean DoC values.

6.4.4 Comparison of simulated and experimental neutron scattering

The simulated and experimental H_2/D_2 adsorption isotherms provide a global measure of isotope-specific interactions within nanoporous carbon structures. While the Degree of Confinement (DoC) offers insight into the distribution of adsorbed molecules as a function of loading, additional experimental data is required to validate whether the local molecular arrangement is accurately reproduced by simulations. Thus, in-situ Small-Angle Neutron Scattering (SANS) measurements shall be compared to their in-silico counterpart. The global changes in scattering intensity upon adsorption were previously discussed in section 6.2.

Figure 6.16 and Figure 6.17 compare the relative scattering intensity profiles (I(q,n)/I(q,n=0)) obtained experimentally with those derived from in-silico adsorption simulations using the reciprocal lattice approach (section 2.4.6). These curves were normalized to the scattering intensity of the empty carbon structure, ensuring that changes in intensity directly reflect the impact of H_2/D_2 adsorption. To improve statistical accuracy, the simulated adsorption configurations were averaged over six equilibrium Monte Carlo (MC) structures for each filling fraction, while NPC1 and NPC2 were treated as model carbons for MSC-30, and NPC3 and NPC4 represented ACC. Experimental data corresponding to these simulations are shown in Figure 6.16 (e), (f) for MSC-30 and Figure 6.17 (e), (f) for ACC. The spin-incoherent scattering—particularly significant for H_2—was subtracted from the SANS data (as described in section 6.3), ensuring that the relative scattering curves displayed in Figure 6.16 and Figure 6.17 contain only coherent contributions.

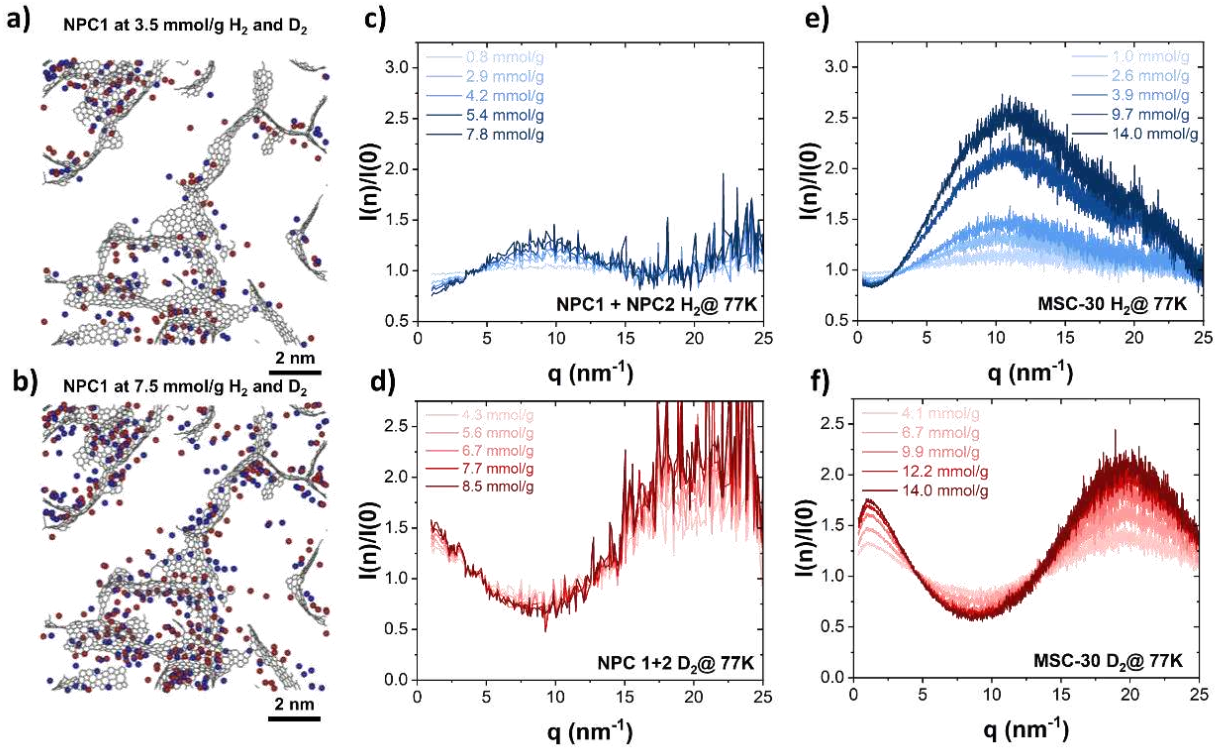

Figure 6.16: Snapshots of the MC simulation within the NPC1 structure at loadings of 3.5 and 7.5 mmol/g for H_2 (blue) and D_2 (red) are shown in (a) and (b), respectively. (c, d) Display the ratio of the SANS intensity at different loadings compared to the zero-loading sample, averaged for NPC1 and NPC2 structures for H_2 and D_2, respectively. (e, f) Show the experimentally obtained intensity ratios for the MSC-30 material. Reproduced from submitted manuscript [141]: Carbon, Elsevier.

A key observation is the good agreement between the simulated and experimental data for D_2 adsorption across both MSC-30 and ACC samples (Figure 6.16 (d), (f) and Figure 6.17 (d), (f)). The relative intensity decreases at intermediate q-values, reaching a minimum around q ≈ 8 nm^{-1}, which corresponds to the contrast reduction between the adsorbed D_2 and the carbon matrix due to their similar scattering length densities. This effect is reversed at low q-values, where the overall intensity increases upon D_2 adsorption, as expected from the total scattering length density increase of the system. At high q-values (>10 nm^{-1}), short-range correlations such as D_2-D_2 and D_2-C interactions become relevant, leading to a strong correlation peak at q ≈ 20 nm^{-1}. The quantitative agreement between NPC1/NPC2 and MSC-30 confirms that the simulated models effectively capture the experimental scattering trends. Similarly, the correspondence between NPC3/NPC4 and ACC is also reasonable, though the minimum in the experimental curve appears slightly shifted toward q ≈ 10 nm^{-1} and the

intensity ratio is somewhat smaller at equivalent loadings. For the ACC sample, experimental data extends only up to q ≈ 20 nm^{-1}, and the strong statistical fluctuations in the simulated data limit a definitive comparison.

In contrast, the simulated results for H_2 exhibit significant deviations from experimental data (Figure 6.16 (c) and Figure 6.17 (c)). The expected minimum at q ≈ 15–20 nm^{-1} in the simulated data—arising from H_2-C interactions—is not observed experimentally. Instead, a secondary peak appears in the experimental curve around q ≈ 20 nm^{-1}, which is absent in the simulation results. This discrepancy suggests that H_2 adsorption does not strictly follow the expected two-phase adsorption model (i.e., a homogeneous H_2 layer inside a uniform carbon matrix). Instead, the observed scattering trends imply a more complex local arrangement of adsorbed H_2 molecules, possibly involving H_2 clustering effects.

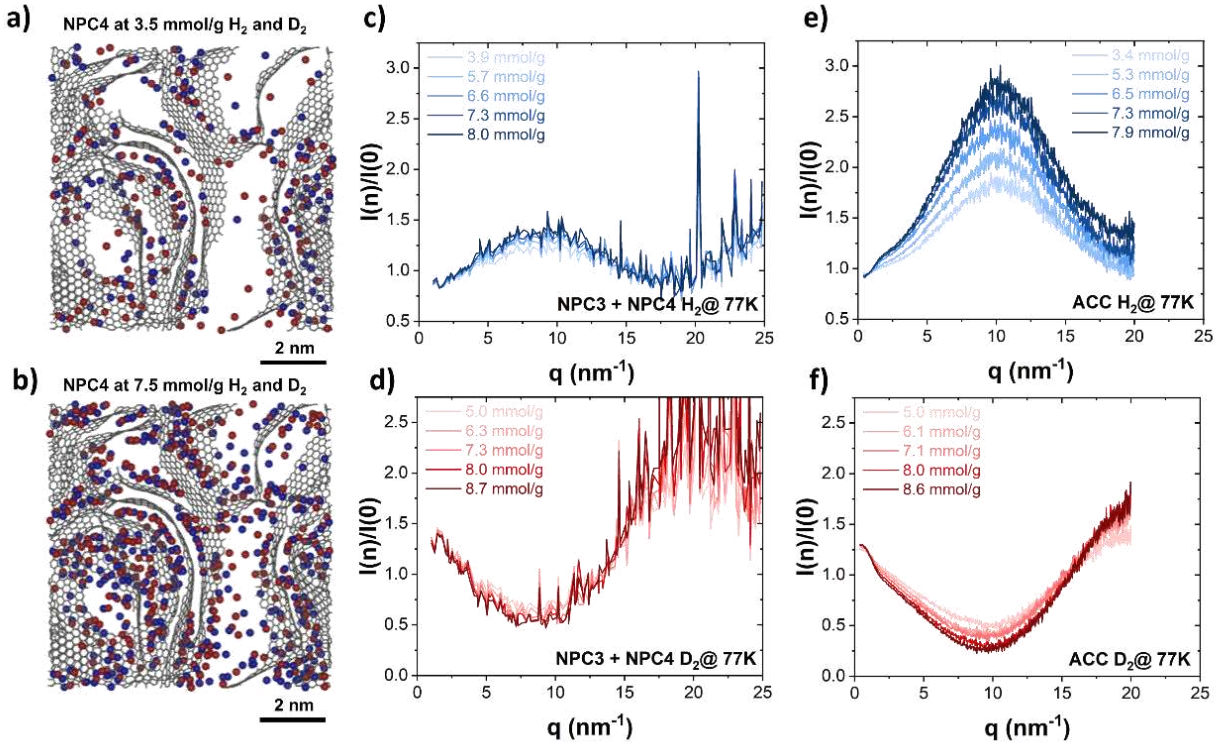

Figure 6.17: Snapshots of the MC simulation within the NPC4 structure at loadings of 3.5 and 7.5 mmol/g for H_2 (blue) and D_2 (red) are shown in (a) and (b), respectively. (c, d) Present the ratio of the SANS intensity at different loadings compared to the zero-loading sample, averaged for NPC1 and NPC2 structures for H_2 and D_2, respectively. (e, f) Show the experimentally obtained intensity ratios for the ACC material. Reproduced from submitted manuscript [141]: Carbon, Elsevier.

The apparent lack of a minimum in the experimental H_2 scattering data at q ≈ 15–20 nm^{-1} suggests that H_2-H_2 correlations dominate over H_2-C correlations, which is the opposite of the D_2 adsorption case. This could indicate the formation of locally dense H_2 clusters, which differs from the expected uniform adsorption behavior. A similar observation is made for the ACC sample (Figure 6.17 (e)), where the relative scattering intensity increases more significantly than in simulations, suggesting a higher-than-expected H_2 density in confinement.

Furthermore, the experimental H_2 scattering intensity increase at q ≈ 10 nm^{-1} is nearly threefold for ACC, whereas the simulated counterpart exhibits only a 1.4-fold increase. This quantitative mismatch strongly suggests additional local interactions or structural effects in the experimental system that are not captured by the simulations. Notably, the ACC sample contains a higher concentration of surface functional groups, particularly O-H species (see Table 4.1), which may contribute to unexpected H_2-H interactions. In contrast, MSC-30 has a lower inherent hydrogen content, reducing the likelihood of such interactions and reinforcing the interpretation that the discrepancies arise from adsorbate-specific effects rather than sample impurities.

For MSC-30 and ACC at their highest loadings (14 and 8 mmol/g, respectively), the experimental intensity ratio at q ≈ 10 nm^{-1} for ACC exceeds that of MSC-30, despite MSC-30 having 1.75 times more adsorbed molecules. This suggests that the scattering intensity does not solely depend on the absolute adsorbed amount but is also influenced by hydrogen densification and local interactions. Given the similar pore size distributions (<1.5 nm) for both materials (Figure 6.11), the differences in scattering behavior appear to be dictated by surface chemistry rather than pore size effects. The stronger D_2 densification in ACC, as observed in Figure 6.17 (f), further reinforces the role of oxygen-rich carbons in enhancing adsorption. Previous studies [123,124,148] have shown that oxygen-functionalized carbons enhance hydrogen uptake and densification, an effect that may partially explain the observed discrepancies.

6.4.5 Further considerations – A heuristic modelling approach

The comparison between simulated and experimental neutron scattering data reveals significant differences in the physisorption behavior of H_2 and D_2 in nanoporous carbons at supercritical temperatures, warranting further discussion. While the simulations align well with the experimental results for D_2 adsorption, a clear discrepancy arises for H_2, suggesting that the local molecular configurations of the two isotopes differ considerably in confinement. The findings indicate that D_2 exhibits strong interactions with the carbon framework, leading to pronounced D_2-C correlations, whereas H_2 appears to favor a cluster-like arrangement, deviating from the expected gas densification model [149–152].

Previous inelastic neutron scattering (INS) studies support this interpretation, demonstrating a solid-like behavior of H_2 molecules at 77 K in sub-nanometer pores (~0.7 nm) [56]. The presence of a free-rotor line in the INS spectra suggests that H_2 accumulates in clusters rather than undergoing uniform densification with increasing pressure [54,56]. Moreover, isotope-specific and temperature-dependent confinement effects further influence adsorption dynamics. Due to its greater mass, D_2 exhibits a smaller thermal de Broglie wavelength than H_2 at the same temperature, resulting in distinct mobility characteristics. D_2 becomes mobile at ~13 K when heated from the solid state, whereas H_2 remains immobilized until ~25 K [84,86]. Even at low pressures (<5 bar) and elevated temperatures (up to 110 K), restricted dynamics resembling a solid-like state of confined H_2 have been observed [85]. While similar studies for D_2 are lacking, its significantly higher diffusivity (~70 times that of H_2 at 77 K) may explain some of the observed differences in scattering behavior between the two isotopes (Figure 6.16 and Figure 6.17). Beyond mass effects, the spin isomer distribution of hydrogen isotopes, particularly the ortho-to-para conversion, also plays a crucial role in adsorption. Ortho-H_2, which possesses a quadrupole moment, exhibits an ordered phase under strong confinement, arising from anisotropic interactions with the carbon surface [149]. This anisotropy causes a splitting of the free-rotor line, which in turn hinders the ortho-to-para transition in highly confining pores [38]. In the SANS experiments, variations in spin-incoherent scattering contributions—particularly at scattering vectors above 10 nm^{-1} (Figure 6.2 (a,b) and Figure 6.3 (a,b))—suggest a potential link between ortho-H_2 clustering and deviations in the H_2 scattering intensity. Since the incoherent scattering is generally q-independent, it was subtracted from

the data as outlined in section 6.3, thereby excluding its influence. Nevertheless, a localized clustering of ortho-H_2 could introduce additional coherent scattering contributions, complicating the interpretation of the results.

To further investigate the local configurations of adsorbed H_2 molecules, heuristic Monte Carlo simulations were performed, utilizing the Degree of Confinement (DoC) as a measure of interaction strength. The heuristic approach allowed for direct manipulation of C-H_2 and H_2-H_2 equilibrium distances, as well as the preferential placement of molecules in high- or low-DoC regions. The first set of simulations examined the influence of H_2-H_2 distance on the scattering signal, systematically varying the intermolecular separation between 0.75 and 3 Å, while maintaining a DoC threshold of 45 as a placement criterion. The Monte Carlo algorithm selected two random positions within the pore structure and computed the respective DoC values. If either site had DoC > 45, the molecule was placed immediately. If both DoC values were below 45, placement probability was determined by a weighted function based on the mean DoC and the predefined threshold value. The results are summarized in Figure 6.18, where the radial distribution functions (RDFs) for various H_2-H_2 separations at 7.8 mmol/g loading are shown in Figure 6.18 (a), while the scattering intensity ratios for H_2 and D_2 are displayed in Figure 6.18 (b) and Figure 6.18 (c), respectively. Additional heuristic simulations explored the effect of adsorption site preference, comparing scenarios in which molecules were selectively placed in high-DoC regions (DoC > 45) versus low-DoC regions (DoC < 30) (Figure 6.18 (d) and Figure 6.18 (e)). Finally, the intensity ratio for clustered molecular arrangements was examined, where H_2 molecules were arranged in close-packed clusters of ~4.4 Å and randomly distributed within the pore structure (Figure 6.18 (f)).

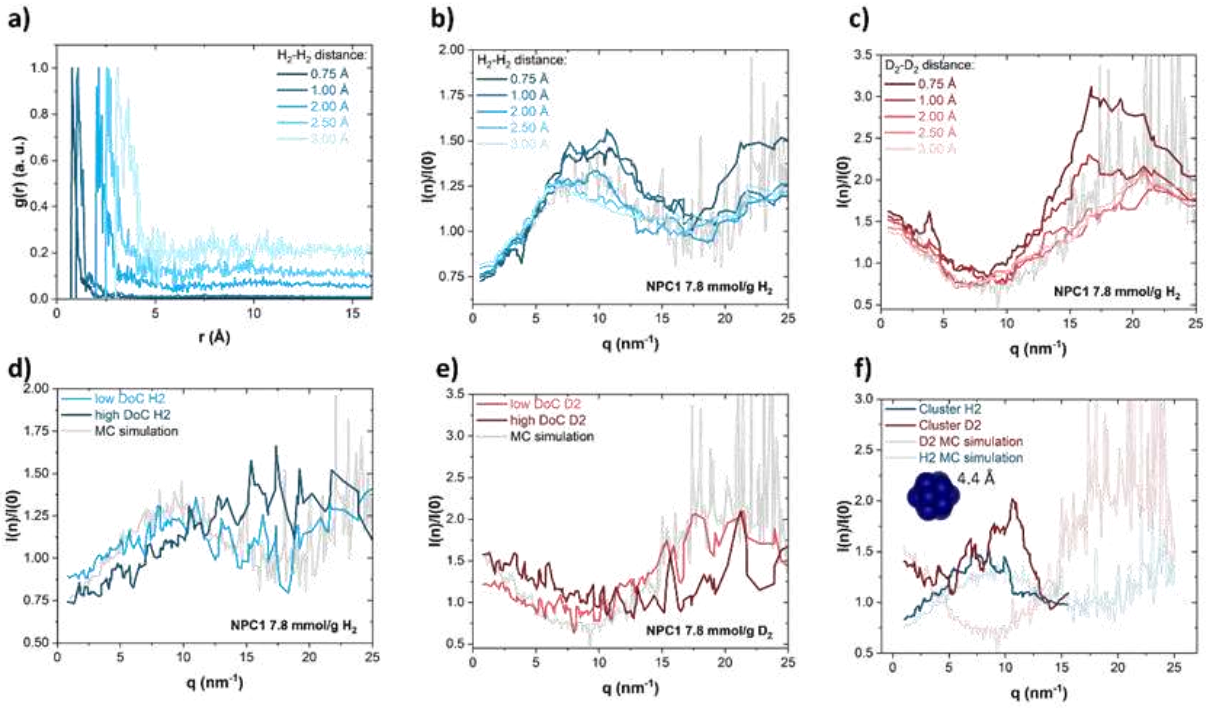

Figure 6.18: Heuristic simulations of various H_2 and D_2 placements within the NPC1 structure. (a) Radial distribution function g(r) of H_2 for different H_2-H_2 distances, considering a placement threshold DoC of 45. (b, c) Intensity ratio I(n)/I(0) for varying molecule-molecule distances for H_2 and D_2, respectively, with the light black curve representing the MC simulation at the same loading. (d, e) I(n)/I(0) for preferential placement at low and high DoC regions (DoC < 30 and DoC > 45, respectively) for H_2 and D_2. (f) I(n)/I(0) for H_2 and D_2 molecules arranged in an icosahedral geometry with a molecule-molecule distance of 2.3 Å. The data in (b)-(f) was smoothed to minimize noise, as it originates from a single simulation run, while the light-colored curves in the plots represent the average of multiple runs. Reproduced from submitted manuscript [141]: Carbon, Elsevier.

Despite yielding qualitative trends consistent with experimental observations, none of the heuristic simulation configurations fully reproduced the experimental scattering curves. Interestingly, the simulated scattering signal for H_2 clusters arranged in an icosahedral pattern (~4.4 Å separation) qualitatively matched the experimental results (Figure 6.18 (f)), whereas D_2 clusters resulted in a distinctly different scattering intensity profile. This supports the hypothesis that H_2 clustering plays a significant role in its adsorption behavior, whereas D_2 adsorption follows a more uniform distribution within the pore space—a trend also predicted by equilibrium Monte Carlo simulations.

However, the heuristic approach is inherently limited by the large parameter space required to fully explore all possible configurations. While the C-H_2 and H_2-H_2 distances and DoC-based

placement strategies were adjustable, additional nuclear interactions may need to be incorporated to accurately capture the clustering tendencies of confined H_2 molecules. Future atomistic simulations must integrate more sophisticated interaction potentials that account for subtle quantum effects, spin isomer distributions, and polarization interactions. Additionally, developing more realistic nanoporous carbon models with explicit surface functionalization may provide further insights into the subtle differences in H_2 and D_2 adsorption mechanisms under confinement.

7 Summary and conclusion

The transition to a hydrogen-based energy economy continues to be a global priority, as nations seek to decarbonize key industries and transportation sectors. Hydrogen storage remains one of the greatest challenges in this transition, particularly for mobile applications requiring high energy density and compact storage solutions. Among the different storage approaches, physisorption in nanoporous materials has emerged as a promising candidate, offering high storage capacities under cryogenic conditions without requiring extreme pressures. However, a fundamental understanding of how pore structure, chemical composition, and quantum effects influence hydrogen adsorption behavior is necessary to optimize material performance. This thesis addresses these challenges by combining material synthesis, neutron scattering techniques, and molecular modeling to provide new insights into hydrogen densification in nanoporous carbons.

The synthesis of bio-derived activated carbons from orange peels and used tea leaves, demonstrates that sustainable precursor materials can be effectively transformed into highly porous carbon frameworks suitable for hydrogen storage. Using a simple chemical activation process, these biomass-derived carbons achieve surface areas exceeding 2100 m^2/g and pore volumes greater than 1.5 cm^3/g, both of which are critical parameters for optimizing hydrogen uptake. Through a systematic investigation of pore structure and chemical composition, the study reveals that ultramicropores (<0.7 nm) dominate hydrogen adsorption at low pressures, while supermicropores (0.7–2 nm) and mesopores (>2 nm) become increasingly relevant at higher pressures. However, despite extensive characterization, the role of heteroatom functionalization—particularly oxygen- and hydrogen-containing surface groups—in hydrogen adsorption remains insufficiently understood. While statistical correlation analysis confirms that micropore volume and total surface area are the strongest predictors of storage performance, the influence of heteroatom concentration and spatial distribution requires further investigation to fully elucidate their role in hydrogen-carbon interactions.

To further explore the impact of heteroatom-functionalized carbons, a comparison of small-angle X-ray scattering (SAXS) and small-angle neutron scattering (SANS) data provides additional insights into how heteroatoms influence pore accessibility and effective pore size.

The differences observed between SAXS and SANS measurements suggest that functional groups may reduce neutron-accessible pore volume, depending on their location within the carbon structure. In samples like MSC-30 and MSP20-X, the pore chord lengths obtained from X-ray and neutron scattering are nearly identical, indicating a homogeneous carbon structure with heteroatoms incorporated within the atomic lattice. However, in ACC and YP80-F, significant discrepancies between SAXS and SANS results suggest that hydrogen and oxygen functional groups are predominantly located at the pore surfaces, thereby reducing the effective pore size accessible to neutrons. This finding supports the hypothesis that heteroatoms play a crucial role in determining hydrogen adsorption efficiency, highlighting the need for a more detailed understanding of functional group distribution and its influence on adsorption dynamics.

Building upon this structural analysis, the use of in-situ small-angle neutron scattering (SANS) at cryogenic temperatures to directly probes the spatial distribution of hydrogen within nanoporous carbons. The results reveal a pore-size-dependent densification, where hydrogen confined within the smallest ultramicropores (<0.7 nm) approaches or even exceeds its bulk solid density. The development of a hierarchical contrast model allows for quantitative description of the density evolution across different pore classes, providing experimental evidence that strong confinement in ultramicropores leads to extreme densification. Additionally, the neutron scattering data confirm a significant exchange of D_2 with pre-existing hydrogen in the carbon structure, further emphasizing the need for a deeper understanding of isotope substitution effects. Despite these advances, the local molecular arrangement of confined hydrogen remains poorly understood, necessitating further investigation through atomistic simulations. Extending to higher pressures, SANS reveilles a gas densification in mesopores, yet to a much lower degree compared to the ultramicropores. One major obstacle when interpreting elastic scattering signals is the separation of the coherent and incoherent scattering contribution. As only ortho-hydrogen is contributing to the strong incoherent signal and that the ratio of para-orthro hydrogen is subject to thermodynamic equilibration and catalytic transformation, further studies would benefit from an experiment just observing the scattering at high scattering vectors to track the evolution of the incoherent signal. Such experiments, and the combination of INS can help to further unravel the time-dependency of

the ortho-para transition as a function of pore size distribution and heteroatom concentration. Further experiments using single spin-isomer adsorption could help to elucidate spin-trapping effects.

The last part of this thesis integrates molecular simulations to complement experimental elastic neutron scattering observations, providing insight into the confinement-dependent adsorption mechanisms. By employing realistic atomistic models of nanoporous carbons, the study identifies preferred adsorption sites, demonstrating that highly defective regions enhance local hydrogen density. A comparison of simulated and experimental scattering data reveals that while deuterium (D_2) follows the predicted adsorption trends, hydrogen (H_2) exhibits unexpected clustering effects, likely due to spin-isomer interactions not fully accounted for in the existing interaction potentials. In particular, ortho-H_2, which possesses a permanent quadrupole moment, may undergo anisotropic interactions with the carbon surface, leading to ordered phase formation and clustering within narrow pores. These findings suggest that current adsorption models, based on classical physisorption assumptions, fail to fully capture the complex quantum effects governing H_2 adsorption in confinement.

To further investigate these discrepancies, heuristic Monte Carlo simulations were performed, manipulating H_2-H_2 and H_2-C distances within the nanoporous carbon models. While these simulations successfully reproduced certain trends observed in the neutron scattering data, no configuration led to a fully satisfactory agreement with experiment. Interestingly, when H_2 molecules were arranged into icosahedral clusters, the simulated scattering profiles qualitatively resembled the experimental data, further supporting the hypothesis that H_2 may form localized clusters rather than homogeneously filling the pore space. This phenomenon is not captured in standard adsorption models, emphasizing the need for more refined atomistic potentials that incorporate quantum effects, nuclear spin states, and complex fluid-fluid interactions.

The findings of this thesis contribute to a deeper understanding of hydrogen adsorption in nanoporous carbons, demonstrating the crucial role of pore structure, surface chemistry, and isotope-specific interactions in governing storage performance. The results highlight the importance of ultramicroporosity for achieving high storage densities, while also revealing

unresolved complexities in heteroatom interactions and quantum effects that require further study. Future research should focus on:

- Developing more accurate atomistic models that account for functional groups and surface heterogeneity
- Refining interaction potentials to include quantum nuclear effects and spin-isomer transitions
- Combining elastic neutron scattering with inelastic and quasi-elastic techniques within a sample series of similar pore characteristics, yet of different chemical composition, to further probe the influences on molecular mobility and local structure in combination with molecular simulations

By bridging the gap between experiment and simulation, this work lays the foundation for a more comprehensive understanding of nanoporous carbon-based hydrogen storage systems. The insights gained not only enhance our knowledge of hydrogen-carbon interactions but also provide a roadmap for the rational design of next-generation hydrogen storage materials, supporting the broader transition toward a sustainable hydrogen economy.

8 Declaration of the use of AI-based tools

The purpose of this section is to outline the areas within this thesis where AI-based tools have been utilized to comply with the "*Richtlinie des Vizerektors für Lehre und Internationales sowie des Studiendekans für den Einsatz KI-basierter generativer Werkzeuge*" as published in "Mitteilungsblatt 108" on April 4, 2024.

I would like to point out that the percentages indicated in the following table represent an estimate of the extent of AI-assisted work. The respective prompts used, and the outputs are summarized in an additional document. No AI support was utilized for creating diagrams, figures, schematic drawings, tables, or any other type of illustration.

Table A: *AI contribution to different subjects of this thesis*

Subject	AI contribution	Tool/Version	Comments
Summarize research papers	4-5% (based on the 6-8 publications summarized out of the 145 cited)	LM Notebook	Research papers discussed in section 2.5 as input to summarize their main conclusions
Enhancement of language clarity and paraphrasing	35% of the words written in this thesis may originate as a result from AI. Yet, the text within this thesis may have been altered from the response from ChatGPT summarized in the provided additional document.	ChatGPT/4o	ChatGPT was used for enhancement of language clarity and paraphrasing independently written experimental details for publications, figure captions, summaries from LM Notebook and writing of combined paragraphs from publications. Common prompts include: • Paraphrase this • Summarize this • Combine paragraphs
Conceptualization	2%	ChatGPT/4o	Conceptualization of paragraphs

9 References

[1] International Energy Agency, Global Hydrogen Review 2024, 2024. https://www.iea.org/reports/global-hydrogen-review-2024.

[2] European Commission, A hydrogen strategy for a climate-neutral Europe, Brussels, 2020. https://eur-lex.europa.eu/legal-content/EN/TXT/?uri=CELEX:52020DC0301.

[3] J. Sreńscek-Nazzal, A. Kamińska, J. Serafin, B. Michalkiewicz, Chemical Activation of Banana Peel Waste-Derived Biochar Using KOH and Urea for CO2 Capture, Materials (Basel). 17 (2024). https://doi.org/10.3390/ma17040872.

[4] T.T. Nadew, M. Keana, T. Sisay, B. Getye, Synthesis of activated carbon from banana peels for dye removal of an aqueous solution in textile industries: optimization, kinetics, and isotherm aspects, Water Pract. Technol. 18 (2023) 947–966. https://doi.org/10.2166/wpt.2023.042.

[5] S. Gadipelli, C.A. Howard, J. Guo, N.T. Skipper, H. Zhang, P.R. Shearing, D.J.L. Brett, Superior Multifunctional Activity of Nanoporous Carbons with Widely Tunable Porosity: Enhanced Storage Capacities for Carbon-Dioxide, Hydrogen, Water, and Electric Charge, Adv. Energy Mater. 10 (2020). https://doi.org/10.1002/aenm.201903649.

[6] M.H. Park, Y.S. Yun, S.Y. Cho, N.R. Kim, H.J. Jin, Waste coffee grounds-derived nanoporous carbon nanosheets for supercapacitors, Carbon Lett. 19 (2016) 66–71. https://doi.org/10.5714/CL.2016.19.066.

[7] D.M. Godinez-Adame, J.A. Diaz-Hernandez, L.E. Alvarez-Jacinto, L.I.C. Ortiz-Garcia, E.G. Cahum-Chan, S.M. Canul-Petul, C.B. Santiago-Martinez, L.J. Solis-Uc, J. Borbolla-Vazquez, Activated Carbon Obtained from Coffee and Orange Wastes, J. Sustain. Dev. 12 (2019) 140–146. https://doi.org/10.5539/jsd.v12n4p140.

[8] T. Ratnaji, L.J. Kennedy, Hierarchical porous carbon derived from tea waste for energy storage applications: Waste to worth, Diam. Relat. Mater. 110 (2020) 1–12. https://doi.org/10.1016/j.diamond.2020.108100.

[9] S. Ha, S.G. Jeong, S. Myeong, C. Lim, Y.S. Lee, High-performance CO2 adsorption of jellyfish-based activated carbon with many micropores and various heteroatoms, J. CO2 Util. 76 (2023) 1–11. https://doi.org/10.1016/j.jcou.2023.102589.

[10] J.M. Juárez, B.C. Ledesma, A.R. Beltramone, M.B. Gómez Costa, Orange peel as a biosource for the synthesis of activated carbon and its application in hydrogen storage, J. Chem. Technol. Biotechnol. 99 (2023) 2488–2495. https://doi.org/10.1002/jctb.7568.

[11] N. Kostoglou, C. Koczwara, S. Stock, C. Tampaxis, G. Charalambopoulou, T. Steriotis, O. Paris, C. Rebholz, C. Mitterer, Nanoporous polymer-derived activated carbon for hydrogen adsorption and electrochemical energy storage, Chem. Eng. J. 427 (2022) 131730. https://doi.org/10.1016/j.cej.2021.131730.

[12] L.A.M. Mahmoud, J.L. Rowlandson, V.P.T. De, S. Nayak, D.J. Fermin, Porous carbons : a class of nanomaterials for efficient adsorption-based hydrogen storage, RSC Appl. Interfaces. 2 (2025) 25–55. https://doi.org/10.1039/D4LF00215F.

[13] M. Thommes, K. Kaneko, A. V. Neimark, J.P. Olivier, F. Rodriguez-Reinoso, J. Rouquerol, K.S.W. Sing, Physisorption of gases, with special reference to the evaluation of surface area and pore size distribution (IUPAC Technical Report), Pure Appl. Chem. 87 (2015) 1051–1069. https://doi.org/10.1515/pac-2014-1117.

[14] A. Züttel, Materials for hydrogen storage, Mater. Today. 6 (2003) 24–33. https://doi.org/10.1016/S1369-7021(03)00922-2.

[15] S.M. Stock, The potential of biomass-derived activated carbons for hydrogen storage, Montanuniversität Leoben, 2021. https://pure.unileoben.ac.at/de/publications/the-potential-of-biomass-derived-activated-carbons-for-hydrogen-s.

[16] M. Thommes, Characterization of Nanoporous Materials, Chemie Ing. Tech. Tech. 82 (2010) 1059–1073. https://doi.org/10.1002/cite.201000064.

[17] R. Balderas-Xicohténcatl, High-Density Hydrogen Monolayer Formation and Isotope Diffusion in Porous Media, Universität Stuttgart, 2019. https://elib.uni-stuttgart.de/items/23192aa7-ba02-42cb-b342-490b0da00d51.

[18] S. Brunauer, P.H. Emmet, E. Teller, Gases in Multimolecular Layers, J. Am. Chem. Soc. 60 (1938) 309–319. https://doi.org/10.1021/ja01269a023.

[19] S. Lowell, J.E. Shields, M.A. Thomas, M. Thommes, Characterization of Porous Solids and Powders: Surface Area, Pore Size and Density, Springer Netherlands, Dordrecht, 2004. https://doi.org/10.1007/978-1-4020-2303-3.

[20] G.Y. Gor, M. Thommes, K.A. Cychosz, A. V. Neimark, Quenched solid density functional theory method for characterization of mesoporous carbons by nitrogen adsorption, Carbon N. Y. 50 (2012) 1583–1590. https://doi.org/10.1016/j.carbon.2011.11.037.

[21] J. Landers, G.Y. Gor, A. V. Neimark, Density functional theory methods for characterization of porous materials, Colloids Surfaces A Physicochem. Eng. Asp. 437 (2013) 3–32. https://doi.org/10.1016/j.colsurfa.2013.01.007.

[22] F. Vallejos-Burgos, C. de Tomas, N.J. Corrente, K. Urita, S. Wang, C. Urita, I. Moriguchi, I. Suarez-Martinez, N. Marks, M.H. Krohn, R. Kukobat, A. V. Neimark, Y. Gogotsi, K. Kaneko, 3D nanostructure prediction of porous carbons via gas adsorption, 2023. https://doi.org/10.1016/j.carbon.2023.118431.

[23] D. Pasaribu, K. Lahiri-Dutt, Coal reliance, human development, and gender equality: At what scale should we look for a relationship?, Energy Res. Soc. Sci. 90 (2022) 102612. https://doi.org/10.1016/j.erss.2022.102612.

[24] N.A. Hassan, Z. Hashim, J.H. Hashim, Impact of Climate Change on Air Quality and Public Health in Urban Areas, Asia-Pacific J. Public Heal. 28 (2014) 38S-48S. https://doi.org/10.1177/1010539515592951.

[25] J.J. West, S.J. Smith, R.A. Silva, V. Naik, Y. Zhang, Z. Adelman, M.M. Fry, S. Anenberg, L.W. Horowitz, J.F. Lamarque, Co-benefits of mitigating global greenhouse gas emissions for future air quality and human health, Nat. Clim. Chang. 3 (2013) 885–889. https://doi.org/10.1038/nclimate2009.

[26] M. Schulte, S. Balasubramanian, C.M. Paris, Blood diamonds and ethical consumerism: An empirical investigation, Sustain. 13 (2021) 1–18. https://doi.org/10.3390/su13084558.

[27] K.S. Novoselov, A.K. Geim, S. V Morozov, D. Jiang, Y. Zhang, S. V Dubonos, I. V Grigorieva, A.A. Firsov, Electric Field Effect in Atomically Thin Carbon Films, Science (80-.). 306 (2004) 666–669. https://doi.org/10.1126/science.1102896.

[28] J. Bernholc, D. Brenner, M.B. Nardelli, V. Meunier, C. Roland, Mechanical and electrical properties of nanotubes, Annu. Rev. Mater. Res. 32 (2002) 347–375. https://doi.org/10.1146/annurev.matsci.32.112601.134925.

[29] S.E. Cami, Jan; Bernard-Salas, Jeronimo; Malek, Detection of C60 and C70 in a Young Planetary Nebula, Science (80-.). 329 (2010) 1180–1182. https://doi.org/10.1126/science.1192035.

[30] M. Arndt, O. Nairz, J. Vos-Andreae, C. Keller, G. Van Der Zouw, A. Zeillinger, Wave-particle duality of C60 molecules, Nature. 401 (1999) 680–682. https://doi.org/10.1038/44348.

[31] J. Zhang, C. Duan, X. Huang, M. Meng, Y. Li, H. Huang, H. Wang, M. Yan, X. Tang, A review on research progress and prospects of agricultural waste-based activated carbon: preparation, application, and source of raw materials, J. Mater. Sci. 59 (2024) 5271–5292. https://doi.org/10.1007/s10853-024-09526-3.

[32] A.K. Mohanty, S. Vivekanandhan, O. Das, L.M. Romero Millán, N.B. Klinghoffer, A. Nzihou, M. Misra, Biocarbon materials, Nat. Rev. Methods Prim. 4 (2024). https://doi.org/10.1038/s43586-024-00297-4.

[33] P. González-García, Activated carbon from lignocellulosics precursors: A review of the synthesis methods, characterization techniques and applications, Renew. Sustain. Energy Rev. 82 (2018) 1393–1414. https://doi.org/10.1016/j.rser.2017.04.117.

[34] Z. Heidarinejad, M.H. Dehghani, M. Heidari, G. Javedan, I. Ali, M. Sillanpää, Methods for preparation and activation of activated carbon: a review, Environ. Chem. Lett. 18 (2020) 393–415. https://doi.org/10.1007/s10311-019-00955-0.

[35] C. De Tomas, I. Suarez-Martinez, N.A. Marks, Carbide-derived carbons for dense and tunable 3D graphene networks, Appl. Phys. Lett. 112 (2018). https://doi.org/10.1063/1.5030136.

[36] I.F. Silvera, R. Dias, Phases of the hydrogen isotopes under pressure : metallic hydrogen, Adv. Phys. X. 6 (2021). https://doi.org/10.1080/23746149.2021.1961607.

[37] L. Zhang, M.D. Allendorf, R. Balderas-Xicohténcatl, D.P. Broom, G.S. Fanourgakis, G.E. Froudakis, T. Gennett, K.E. Hurst, S. Ling, C. Milanese, P.A. Parilla, D. Pontiroli, M. Riccò, S. Shulda, V. Stavila, T.A. Steriotis, C.J. Webb, M. Witman, M. Hirscher, Fundamentals of hydrogen storage in nanoporous materials, Prog. Energy. 4 (2022). https://doi.org/10.1088/2516-1083/ac8d44.

[38] L.R. Terry, S. Rols, M. Tian, I. da Silva, S.J. Bending, V.P. Ting, Manipulation of the crystalline phase diagram of hydrogen through nanoscale confinement effects in porous carbons, Nanoscale. 14 (2022) 7250–7261. https://doi.org/10.1039/d2nr00587e.

[39] R. Frauenfelder, F. Heinrich, J.B. Olin, Das Ortho-Para-Gleichgewicht Von H_2, D_2 Und T_2, Helv. Phys. Acta. 38 (1965) 279. https://doi.org/10.5169/seals-113596.

[40] US Department of Engery, DOE Technical Targets for Onboard Hydrogen Storage for Light-Duty Vehicles, (2021). https://www.energy.gov/eere/fuelcells/doe-technical-targets-onboard-hydrogen-storage-light-duty-vehicles (accessed November 25, 2021).

[41] J.O. Abe, A.P.I. Popoola, E. Ajenifuja, O.M. Popoola, Hydrogen energy, economy and storage: Review and recommendation, Int. J. Hydrogen Energy. 44 (2019) 15072–15086. https://doi.org/10.1016/j.ijhydene.2019.04.068.

[42] U. Eberle, M. Felderhoff, F. Schüth, Chemical and physical solutions for hydrogen storage, Angew. Chemie - Int. Ed. 48 (2009) 6608–6630. https://doi.org/10.1002/anie.200806293.

[43] European Commission, A European Green Deal, Eur. Green Deal. (2019). https://ec.europa.eu/info/sites/default/files/european-green-deal-communication_en.pdf (accessed December 14, 2021).

[44] R. Moradi, K.M. Groth, Hydrogen storage and delivery: Review of the state of the art technologies and risk and reliability analysis, Int. J. Hydrogen Energy. 44 (2019) 12254–12269. https://doi.org/10.1016/j.ijhydene.2019.03.041.

[45] E. Boateng, A. Chen, Recent advances in nanomaterial-based solid-state hydrogen storage, Mater. Today Adv. 6 (2020). https://doi.org/10.1016/j.mtadv.2019.100022.

[46] R.K. Ahluwalia, J.K. Peng, Automotive hydrogen storage system using cryo-adsorption on activated carbon, Int. J. Hydrogen Energy. 34 (2009) 5476–5487. https://doi.org/10.1016/j.ijhydene.2009.05.023.

[47] A. Beaudet, F. Larouche, K. Amouzegar, P. Bouchard, K. Zaghib, Key challenges and opportunities for recycling electric vehicle battery materials, Sustain. 12 (2020) 1–12. https://doi.org/10.3390/su12145837.

[48] J.L. Popien, J. Husmann, A. Barke, C. Thies, F. Cerdas, C. Herrmann, T.S. Spengler, Comparison of lithium-ion battery supply chains - a life cycle sustainability assessment, Procedia CIRP. 116 (2023) 131–136. https://doi.org/10.1016/j.procir.2023.02.023.

[49] V. Rizos, P. Urban, Barriers and policy challenges in developing circularity approaches in the EU battery sector: An assessment, Resour. Conserv. Recycl. 209 (2024) 107800. https://doi.org/10.1016/j.resconrec.2024.107800.

[50] H. Nazir, C. Louis, S. Jose, J. Prakash, N. Muthuswamy, M.E.M. Buan, C. Flox, S. Chavan, X. Shi, P. Kauranen, T. Kallio, G. Maia, K. Tammeveski, N. Lymperopoulos, E. Carcadea, E. Veziroglu, A. Iranzo, A.M. Kannan, Is the H_2 economy realizable in the foreseeable future? Part I: H_2 production methods, Int. J. Hydrogen Energy. 45 (2020) 13777–13788. https://doi.org/10.1016/j.ijhydene.2020.03.092.

[51] D.P. Broom, D. Book, Hydrogen storage in nanoporous materials, in: Adv. Hydrog. Prod. Storage Distrib., Elsevier Inc., 2014: pp. 410–450. https://doi.org/10.1533/9780857097736.3.410.

[52] M. Hirscher, L. Zhang, H. Oh, Nanoporous adsorbents for hydrogen storage, Appl. Phys. A Mater. Sci. Process. 129 (2023) 1–10. https://doi.org/10.1007/s00339-023-06397-4.

[53] D.P. Broom, C.J. Webb, K.E. Hurst, P.A. Parilla, T. Gennett, C.M. Brown, R. Zacharia, E. Tylianakis, E. Klontzas, G.E. Froudakis, T.A. Steriotis, P.N. Trikalitis, D.L. Anton, B. Hardy, D. Tamburello, C. Corgnale, B.A. van Hassel, D. Cossement, R. Chahine, M. Hirscher, Outlook and challenges for hydrogen storage in nanoporous materials, Appl. Phys. A Mater. Sci. Process. 122 (2016) 1–21. https://doi.org/10.1007/s00339-016-9651-4.

[54] M. Tian, M.J. Lennox, A.J. O'Malley, A.J. Porter, B. Krüner, S. Rudić, T.J. Mays, T. Düren, V. Presser, L.R. Terry, S. Rols, Y. Fang, Z. Dong, S. Rochat, V.P. Ting, Effect of pore geometry on ultra-densified hydrogen in microporous carbons, Carbon N. Y. 173 (2021) 968–979. https://doi.org/10.1016/j.carbon.2020.11.063.

[55] I. Cabria, Comparison of theoretical methods of the hydrogen storage capacities of nanoporous carbons, Int. J. Hydrogen Energy. 46 (2021) 12192–12205. https://doi.org/10.1016/j.ijhydene.2020.04.212.

[56] V.P. Ting, A.J. Ramirez-Cuesta, N. Bimbo, J.E. Sharpe, A. Noguera-Diaz, V. Presser, S. Rudic, T.J. Mays, Direct Evidence for Solid-like Hydrogen in a Nanoporous Carbon Hydrogen Storage Material at Supercritical Temperatures, ACS Nano. 9 (2015) 8249–8254. https://doi.org/10.1021/acsnano.5b02623.

[57] S. Stock, M. Seyffertitz, N. Kostoglou, M.V. Rauscher, V. Presser, B. Demé, V. Cristiglio, M. Kratzer, S. Rols, C. Mitterer, O. Paris, Hydrogen densification in carbon nanopore confinement: Insights from small-angle neutron scattering using a hierarchical contrast model, Carbon N. Y. 221 (2024). https://doi.org/10.1016/j.carbon.2024.118911.

[58] I. Cabria, M.J. López, J.A. Alonso, The optimum average nanopore size for hydrogen storage in carbon nanoporous materials, Carbon N. Y. 45 (2007) 2649–2658. https://doi.org/10.1016/j.carbon.2007.08.003.

[59] J.J.M. Beenakker, V.D. Borman, S.Y. Krylov, Molecular transport in subnanometer pores: zero-point energy, reduced dimensionality and quantum sieving, Chem. Phys. Lett. 232 (1995) 379–382. https://doi.org/10.1016/0009-2614(94)01372-3.

[60] J. Chadwick, Possible existence of a Neutron, Nature. 129 (1932) 312. https://doi.org/https://doi.org/10.1038/129312a0.

[61] B. Schwaighofer, Experimental and Computational Studies of Oxide Ion Conductors, 2023. http://etheses.dur.ac.uk/14999/.

[62] G.L. Squires, Introduction to the Theory of Thermal Neutron Scattering, University of Cambridge, 2012. https://doi.org/https://doi.org/10.1017/CBO9781139107808.

[63] Sivia, Elementary scattering theory, Oxford University Press, 2010. https://doi.org/10.1017/cbo9780511616471.014.

[64] J. Als-Nielsen, Elements of Modern X-ray of Modern X-ray Physics, Wiley-VCH Verlag, 2011.

[65] O. Glatter, Scattering methods and their application in colloid and interface science, Elsevier, 2018.

[66] Y.B. Melnichenko, Small-angle scattering from confined and interfacial fluids: Applications to energy storage and environmental science, 2015. https://doi.org/10.1007/978-3-319-01104-2.

[67] M.R. Spiegel, Schaum's outline of Theory and Problems of Laplace Transforms, McGraw-Hill, 1965. https://baixardoc.com/preview/transformadas-de-laplace-murray-spieguel-serie-schaum-5c35084eb6fd3.

[68] C.S. Tsao, Y. Liu, M. Li, Y. Zhang, J.B. Leao, H.W. Chang, M.S. Yu, S.H. Chen, Neutron scattering methodology for absolute measurement of room-temperature hydrogen storage capacity and evidence for spillover effect in a pt-doped activated carbon, J. Phys. Chem. Lett. 1 (2010) 1569–1573. https://doi.org/10.1021/jz1004472.

[69] C. Prehal, Ion electrosorption in nanoporous carbons, Montanuniverität Leoben, 2017. https://pure.unileoben.ac.at/files/1909877/AC14493873n01.pdf.

[70] P. Debye, H.R. Anderson, H. Brumberger, Scattering by an inhomogeneous solid. II. the correlation function and its application, J. Appl. Phys. 28 (1957) 679–683. https://doi.org/10.1063/1.1722830.

[71] S. Ciccariello, J. Goodisman, H. Brumberger, On the Porod Law, J. Appl. Cryst. 21 (1988) 117–128. https://doi.org/https://doi.org/10.1107/S0021889887010409.

[72] C. de Tomas, A. Aghajamali, J.L. Jones, D.J. Lim, M.J. López, I. Suarez-Martinez, N.A. Marks, Transferability in interatomic potentials for carbon, Carbon N. Y. 155 (2019) 624–634. https://doi.org/10.1016/j.carbon.2019.07.074.

[73] C. Prehal, C. Koczwara, N. Jäckel, H. Amenitsch, V. Presser, O. Paris, A carbon nanopore model to quantify structure and kinetics of ion electrosorption with in situ small-angle X-ray scattering, Phys. Chem. Chem. Phys. 19 (2017) 15549–15561. https://doi.org/10.1039/c7cp00736a.

[74] W. Ruland, Fourier Transform Methods for Random-Layer Line Profiles, Acta Cryst. 22 (1967) 615. https://doi.org/https://doi.org/10.1107/S0365110X67001252.

[75] C.J. Jafta, A. Petzold, S. Risse, D. Clemens, D. Wallacher, G. Goerigk, M. Ballauff, Correlating pore size and shape to local disorder in microporous carbon: A combined small angle neutron and X-ray scattering study, Carbon N. Y. 123 (2017) 440–447. https://doi.org/10.1016/j.carbon.2017.07.046.

[76] M. Tomšič, G. Fritz-Popovski, L. Vlček, A. Jamnik, Calculating small-angle X-ray scattering intensities from Monte Carlo results: Exploring different approaches on the example of primary alcohols, Acta Chim. Slov. 54 (2007) 484–491.

[77] A. Majumdar, M. Müller, S. Busch, Computation of X-ray and Neutron Scattering Patterns to Benchmark Atomistic Simulations against Experiments, Int. J. Mol. Sci. 25 (2024). https://doi.org/10.3390/ijms25031547.

[78] W.D. Schaeffer, W.R. Smith, C.B. Wendell, The Adsorption of Helium on Carbon Black at Liquid Helium Temperatures, J. Am. Chem. Soc. 71 (1949) 4165. https://doi.org/10.1021/ja01180a620.

[79] W.A. Steele, Concerning a theory of multilayer adsorption, with particular reference to adsorbed helium, J. Chem. Phys. 25 (1956) 819–823. https://doi.org/10.1063/1.1743130.

[80] R. Balderas-Xicohténcatl, H.-H. Lin, C. Lurz, L. Daemen, Y. Cheng, K. Cychosz Struckhoff, R. Guillet-Nicolas, G. Schütz, T. Heine, A.J. Ramirez-Cuesta, M. Thommes, M. Hirscher, Formation of a super-dense hydrogen monolayer on mesoporous silica, Nat. Chem. (2022). https://doi.org/10.1038/s41557-022-01019-7.

[81] R. Balderas-Xicohténcatl, H.-H. Lin, C. Lurz, L. Daemen, Y. Cheng, K. Cychosz Struckhoff, R. Guillet-Nicolas, G. Schütz, T. Heine, A.J. Ramirez-Cuesta, M. Thommes, M. Hirscher, Formation of a super-dense hydrogen monolayer on mesoporous silica, Nat. Chem. 14 (2022) 1319–1324. https://doi.org/10.1038/s41557-022-01019-7.

[82] C.A. Swenson, The Catalysis of the Ortho-Para Conversion in Liquid Hydrogen, J. Chem. Phys. 18 (1950) 520–522. https://doi.org/10.1063/1.1747674.

[83] P.R. Kubik, W.N. Hardy, H. Glattli, Orientational ordering of hydrogen molecules adsorbed on graphite, (1984).

[84] C.I. Contescu, D. Saha, N.C. Gallego, E. Mamontov, A.I. Kolesnikov, V. V. Bhat, Restricted dynamics of molecular hydrogen confined in activated carbon nanopores, Carbon N. Y. 50 (2012) 1071–1082. https://doi.org/10.1016/j.carbon.2011.10.016.

[85] J. Bahadur, C.I. Contescu, A.J. Ramirez-Cuesta, E. Mamontov, N.C. Gallego, Y. Cheng, L.L. Daemen, Y.B. Melnichenko, Properties of immobile hydrogen confined in microporous carbon, Carbon N. Y. 117 (2017) 383–392. https://doi.org/10.1016/j.carbon.2017.03.007.

[86] C.I. Contescu, H. Zhang, R.J. Olsen, E. Mamontov, J.R. Morris, N.C. Gallego, Isotope effect on adsorbed quantum phases: Diffusion of H_2 and D_2 in nanoporous carbon, Phys. Rev. Lett. 110 (2013) 1–5. https://doi.org/10.1103/PhysRevLett.110.236102.

[87] M. Koppel, R. Palm, R. Härmas, M. Russina, V. Grzimek, J. Jagiello, M. Paalo, H. Kurig, M. Månsson, O. Oll, E. Lust, Pore Wall Corrugation Effect on the Two Timescaled Diffusion of Adsorbed H_2 Studied by Quasi-Elastic Neutron Scattering, SSRN Electron. J. 197 (2022) 359–367. https://doi.org/10.2139/ssrn.4092449.

[88] M. Koppel, R. Palm, R. Härmas, M. Telling, M.D. Le, T. Guidi, K. Tuul, M. Paalo, L. Kalder, J. Jagiello, T. Romann, J. Aruväli, M. Månsson, E. Lust, Disentangling the self-diffusional dynamics of H_2 adsorbed in micro- and mesoporous carbide-derived carbon by wide temporal range quasi-elastic neutron scattering, Carbon N. Y. 219 (2024). https://doi.org/10.1016/j.carbon.2024.118799.

[89] N. Kostoglou, C. Koczwara, C. Prehal, V. Terziyska, B. Babic, B. Matovic, G. Constantinides, C. Tampaxis, G. Charalambopoulou, T. Steriotis, S. Hinder, M. Baker, K. Polychronopoulou, C. Doumanidis, O. Paris, C. Mitterer, C. Rebholz, Nanoporous activated carbon cloth as a versatile material for hydrogen adsorption, selective gas separation and electrochemical energy storage, Nano Energy. 40 (2017) 49–64. https://doi.org/10.1016/j.nanoen.2017.07.056.

[90] C.K. Ranaweera, P.K. Kahol, M. Ghimire, S.R. Mishra, R.K. Gupta, Orange-Peel-Derived Carbon: Designing Sustainable and High-Performance Supercapacitor Electrodes, C — J. Carbon Res. 3 (2017) 25. https://doi.org/10.3390/c3030025.

[91] S. Bhoyate, C.K. Ranaweera, C. Zhang, T. Morey, M. Hyatt, P.K. Kahol, M. Ghimire, S.R. Mishra, R.K. Gupta, Eco-Friendly and High Performance Supercapacitors for Elevated Temperature Applications Using Recycled Tea Leaves, Glob. Challenges. 1 (2017) 1700063. https://doi.org/10.1002/gch2.201700063.

[92] P.I. Ravikovitch, A. Vishnyakov, R. Russo, A. V. Neimark, Unified approach to pore size characterization of microporous carbonaceous materials from N_2, Ar, and CO2 adsorption isotherms, Langmuir. 16 (2000) 2311–2320. https://doi.org/10.1021/la991011c.

[93] M.G. Kendall, A New Measure of Rank Correlation, Biometrika Trust. 30 (1938) 81–93. http://www.jstor.org/stable/2332226.

[94] P. Virtanen, R. Gommers, T.E. Oliphant, M. Haberland, T. Reddy, D. Cournapeau, E. Burovski, P. Peterson, W. Weckesser, J. Bright, S.J. van der Walt, M. Brett, J. Wilson, K.J. Millman, N. Mayorov, A.R.J. Nelson, E. Jones, R. Kern, E. Larson, C.J. Carey, İ. Polat, Y. Feng, E.W. Moore, J. VanderPlas, D. Laxalde, J. Perktold, R. Cimrman, I. Henriksen, E.A. Quintero, C.R. Harris, A.M. Archibald, A.H. Ribeiro, F. Pedregosa, P. van Mulbregt, A. Vijaykumar, A. Pietro Bardelli, A. Rothberg, A. Hilboll, A. Kloeckner, A. Scopatz, A. Lee, A. Rokem, C.N. Woods, C. Fulton, C. Masson, C. Häggström, C. Fitzgerald, D.A. Nicholson, D.R. Hagen, D. V. Pasechnik, E. Olivetti, E. Martin, E. Wieser, F. Silva, F. Lenders, F. Wilhelm, G. Young, G.A. Price, G.L. Ingold, G.E. Allen, G.R. Lee, H. Audren, I. Probst, J.P. Dietrich, J. Silterra, J.T. Webber, J. Slavič, J. Nothman, J. Buchner, J. Kulick, J.L. Schönberger, J.V. de Miranda Cardoso, J. Reimer, J. Harrington, J.L.C. Rodríguez, J. Nunez-Iglesias, J. Kuczynski, K. Tritz, M. Thoma, M. Newville, M. Kümmerer, M. Bolingbroke, M. Tartre, M. Pak, N.J. Smith, N. Nowaczyk, N. Shebanov, O. Pavlyk, P.A. Brodtkorb, P. Lee, R.T. McGibbon, R. Feldbauer, S. Lewis, S. Tygier, S. Sievert, S. Vigna, S. Peterson, S. More, T. Pudlik, T. Oshima, T.J. Pingel, T.P. Robitaille, T. Spura, T.R. Jones, T. Cera, T. Leslie, T. Zito, T. Krauss, U. Upadhyay, Y.O. Halchenko, Y. Vázquez-Baeza, SciPy 1.0: fundamental algorithms for scientific computing in Python, Nat. Methods. 17 (2020) 261–272. https://doi.org/10.1038/s41592-019-0686-2.

[95] S. Arndt, C. Turvey, N.C. Andreasen, Correlating and predicting psychiatric symptom ratings: Spearman's v versus Kendall's tau correlation, J. Psychiatr. Res. 33 (1999) 97–104. https://doi.org/10.1016/S0022-3956(98)90046-2.

[96] S. Stock, N. Kostoglou, J. Selinger, S. Spirk, C. Tampaxis, G. Charalambopoulou, T. Steriotis, C. Rebholz, C. Mitterer, O. Paris, Coffee Waste-Derived Nanoporous Carbons for Hydrogen Storage, ACS Appl. Energy Mater. 5 (2022) 10915–10926. https://doi.org/10.1021/acsaem.2c01573.

[97] D. Dubbeldam, S. Calero, D.E. Ellis, R.Q. Snurr, RASPA: Molecular simulation software for adsorption and diffusion in flexible nanoporous materials, Mol. Simul. 42 (2016) 81–101. https://doi.org/10.1080/08927022.2015.1010082.

[98] D. Richard, M. Ferrand, G.J. Kearley, Analysis and visualisation of neutron-scattering data, J. Neutron Res. 4 (1996) 33–39. https://doi.org/10.1080/10238169608200065.

[99] O. Arnold, J.C. Bilheux, J.M. Borreguero, A. Buts, S.I. Campbell, L. Chapon, M. Doucet, N. Draper, R. Ferraz Leal, M.A. Gigg, V.E. Lynch, A. Markvardsen, D.J. Mikkelson, R.L. Mikkelson, R. Miller, K. Palmen, P. Parker, G. Passos, T.G. Perring, P.F. Peterson, S. Ren, M.A. Reuter, A.T. Savici, J.W. Taylor, R.J. Taylor, R. Tolchenov, W. Zhou, J. Zikovsky, Mantid - Data analysis and visualization package for neutron scattering and μ SR experiments, Nucl. Instruments Methods Phys. Res. Sect. A Accel. Spectrometers, Detect. Assoc. Equip. 764 (2014) 156–166. https://doi.org/10.1016/j.nima.2014.07.029.

[100] R.L.S. Canevesi, S. Schaefer, M.T. Izquierdo, A. Celzard, V. Fierro, Roles of Surface Chemistry and Texture of Nanoporous Activated Carbons in CO2 Capture, ACS Appl. Nano Mater. 5 (2022) 3843–3854. https://doi.org/10.1021/acsanm.1c04474.

[101] C.A.S. and D.G.M. Jose R. Ayala , Gisela Montero , Marcos A. Coronado , Conrado Garcia , Mario A. Curiel-Alvarez, Jose A. León, Obtain Reducing Sugars, Molecules. 26 (2021) 1–14. https://doi.org/10.3390/ molecules26051348.

[102] F. Ahmadi, M.J. Zamiri, M. Khorvash, Z. Banihashemi, A.R. Bayat, Chemical composition and protein enrichment of orange peels and sugar beet pulp after fermentation by two Trichoderma species, Iran. J. Vet. Res. 16 (2015) 25–30.

[103] H.N. Graham, Green tea composition, consumption, and polyphenol chemistry, Prev. Med. (Baltim). 21 (1992) 334–350. https://doi.org/10.1016/0091-7435(92)90041-F.

[104] J. Selinger, S. Stock, W. Schlemmer, M. Hobisch, N. Kostoglou, Q. Abbas, O. Paris, C. Mitterer, M. Hummel, S. Spirk, Nanoporous carbon electrodes derived from coffee side streams for supercapacitors in aqueous electrolytes, Nanomaterials. 12 (2022) 2647. https://doi.org/https://doi.org/10.3390/nano12152647.

[105] S.G. Wabo, O. Klepel, Nitrogen release and pore formation through KOH activation of nitrogen-doped carbon materials: an evaluation of the literature, Carbon Lett. 31 (2021) 581–592. https://doi.org/10.1007/s42823-021-00252-3.

[106] P. Thomas, C.W. Lai, M.R. Bin Johan, Recent developments in biomass-derived carbon as a potential sustainable material for super-capacitor-based energy storage and environmental applications, J. Anal. Appl. Pyrolysis. 140 (2019) 54–85. https://doi.org/10.1016/j.jaap.2019.03.021.

[107] S. Stock, C.O.W. Trost, M. Seyffertitz, J. Selinger, R.K. Gupta, C. Tampaxis, T.A. Steriotis, C. Rebholz, C. Mitterer, O. Paris, N. Kostoglou, Transforming breakfast bio-waste into hydrogen storage materials, Accept. by Int. J. Hydrog. Energy. (2025).

[108] G.A. Zickler, B. Smarsly, N. Gierlinger, H. Peterlik, O. Paris, A reconsideration of the relationship between the crystallite size La of carbons determined by X-ray diffraction and Raman spectroscopy, Carbon N. Y. 44 (2006) 3239–3246. https://doi.org/10.1016/j.carbon.2006.06.029.

[109] C. Koczwara, S. Rumswinkel, L. Hammerschmidt, M. Salihovic, M.S. Elsaesser, H. Amenitsch, O. Paris, N. Huesing, Nanofibers versus Nanopores: A Comparison of the Electrochemical Performance of Hierarchically Ordered Porous Carbons, ACS Appl. Energy Mater. 2 (2019) 5279–5291. https://doi.org/10.1021/acsaem.9b01035.

[110] K.J. Putman, M.R. Rowles, N.A. Marks, C. de Tomas, J.W. Martin, I. Suarez-Martinez, Defining graphenic crystallites in disordered carbon: Moving beyond the platelet model, Carbon N. Y. 209 (2023) 117965. https://doi.org/10.1016/j.carbon.2023.03.040.

[111] C.J. Gommes, Stochastic models of disordered mesoporous materials for small-angle scattering analysis and more, Microporous Mesoporous Mater. 257 (2018) 62–78. https://doi.org/10.1016/j.micromeso.2017.08.009.

[112] J. Bahadur, C.R. Medina, L. He, Y.B. Melnichenko, J.A. Rupp, T.P. Blach, D.F.R. Mildner, Determination of closed porosity in rocks by small-angle neutron scattering, J. Appl. Crystallogr. 49 (2016) 2021–2030. https://doi.org/10.1107/S1600576716014904.

[113] L. Zhang, Z. Deng, M. Sun, J. Lin, C.F. Ukaomah, Q. Hu, B. Yu, J. Zhang, X. Liang, G. Wang, J. Shu, Characterization of Closed Pores in Longmaxi Shale by Synchrotron Small-Angle X-ray Scattering, Energy and Fuels. 35 (2021) 6738–6754. https://doi.org/10.1021/acs.energyfuels.1c00190.

[114] A.M. Puziy, O.I. Poddubnaya, B. Gawdzik, M. Sobiesiak, Comparison of heterogeneous pore models QSDFT and 2D-NLDFT and computer programs ASiQwin and SAIEUS for calculation of pore size distribution, Adsorption. 22 (2016) 459–464. https://doi.org/10.1007/s10450-015-9704-6.

[115] N. Bimbo, W. Xu, J.E. Sharpe, V.P. Ting, T.J. Mays, High-pressure adsorptive storage of hydrogen in MIL-101 (Cr) and AX-21 for mobile applications: Cryocharging and cryokinetics, Mater. Des. 89 (2016) 1086–1094. https://doi.org/10.1016/j.matdes.2015.10.069.

[116] M. Doğan, P. Sabaz, Z. Bicil, B. Koçer Kizilduman, Y. Turhan, Activated carbon synthesis from tangerine peel and its use in hydrogen storage, J. Energy Inst. 93 (2020) 2176–2185. https://doi.org/10.1016/j.joei.2020.05.011.

[117] F.G. Tseng, D. Bhalothia, K.H. Lo, C.H. Syu, Y.C. Chen, A. Sihag, C.W. Wang, H.Y.T. Chen, T.Y. Chen, Glucose-based highly-porous activated carbon nanospheres (g-ACNSs) for high capacity hydrogen storage, Energy Adv. 3 (2024) 1283–1292. https://doi.org/10.1039/d4ya00126e.

[118] A.R. Selvaraj, N. Kostoglou, R. Rajendiran, I. Cho, C. Rebholz, N.D. Chakravarthi, K. Prabakar, Scalable synthesis of biomass-derived three-dimensional hierarchical porous activated carbons for electrochemical energy storage and hydrogen physisorption, J. Energy Storage. 92 (2024) 112085. https://doi.org/10.1016/j.est.2024.112085.

[119] S. Davoodi, H. Vo Thanh, D.A. Wood, M. Mehrad, M. Al-Shargabi, V.S. Rukavishnikov, Machine-learning models to predict hydrogen uptake of porous carbon materials from influential variables, Sep. Purif. Technol. 316 (2023) 123807. https://doi.org/10.1016/j.seppur.2023.123807.

[120] T.X. Nguyen, N. Cohaut, J.S. Bae, S.K. Bhatia, New method for atomistic modeling of the microstructure of activated carbons using hybrid reverse Monte Carlo simulation, Langmuir. 24 (2008) 7912–7922. https://doi.org/10.1021/la800351d.

[121] M.I. Maulana Kusdhany, S.M. Lyth, New insights into hydrogen uptake on porous carbon materials via explainable machine learning, Carbon N. Y. 179 (2021) 190–201. https://doi.org/10.1016/j.carbon.2021.04.036.

[122] S.M. Lundberg, S.I. Lee, A unified approach to interpreting model predictions, Adv. Neural Inf. Process. Syst. 2017-Decem (2017) 4766–4775. https://dl.acm.org/doi/10.5555/3295222.3295230.

[123] S. Anuchitsakol, W. Dilokekunakul, N. Khongtor, S. Chaemchuen, N. Klomkliang, Combined experimental and simulation study on H_2 storage in oxygen and nitrogen co-doped activated carbon derived from biomass waste: superior pore size and surface chemistry development, RSC Adv. 13 (2023) 36009–36022. https://doi.org/10.1039/d3ra06720c.

[124] T.S. Blankenship, N. Balahmar, R. Mokaya, Oxygen-rich microporous carbons with exceptional hydrogen storage capacity, Nat. Commun. 8 (2017) 1–12. https://doi.org/10.1038/s41467-017-01633-x.

[125] I. Krkljus, T. Steriotis, G. Charalambopoulou, A. Gotzias, M. Hirscher, H_2/D_2 adsorption and desorption studies on carbon molecular sieves with different pore structures, Carbon N. Y. 57 (2013) 239–247. https://doi.org/10.1016/j.carbon.2013.01.069.

[126] X. Zhao, S. Villar-Rodil, A.J. Fletcher, K.M. Thomas, Kinetic isotope effect for H_2 and D_2 quantum molecular sieving in adsorption/desorption on porous carbon materials, J. Phys. Chem. B. 110 (2006) 9947–9955. https://doi.org/10.1021/jp060748p.

[127] J.Y. Kim, H. Oh, H.R. Moon, Hydrogen Isotope Separation in Confined Nanospaces: Carbons, Zeolites, Metal–Organic Frameworks, and Covalent Organic Frameworks, Adv. Mater. 31 (2019) 1–23. https://doi.org/10.1002/adma.201805293.

[128] N.C. Gallego, L. He, D. Saha, C.I. Contescu, Y.B. Melnichenko, Hydrogen confinement in carbon nanopores: Extreme densification at ambient temperature, J. Am. Chem. Soc. 133 (2011) 13794–13797. https://doi.org/10.1021/ja202432x.

[129] L. He, Y.B. Melnichenko, N.C. Gallego, C.I. Contescu, J. Guo, J. Bahadur, Investigation of morphology and hydrogen adsorption capacity of disordered carbons, Carbon N. Y. 80 (2014) 82–90. https://doi.org/10.1016/j.carbon.2014.08.041.

[130] L. Ludescher, R. Morak, C. Balzer, A.M. Waag, S. Braxmeier, F. Putz, S. Busch, G.Y. Gor, A. V. Neimark, N. Hüsing, G. Reichenauer, O. Paris, In Situ Small-Angle Neutron Scattering Investigation of Adsorption-Induced Deformation in Silica with Hierarchical Porosity, Langmuir. 35 (2019) 11590–11600. https://doi.org/10.1021/acs.langmuir.9b01375.

[131] L. Ludescher, R. Morak, S. Braxmeier, F. Putz, N. Hüsing, G. Reichenauer, O. Paris, Hierarchically organized materials with ordered mesopores: adsorption isotherm and adsorption-induced deformation from small-angle scattering, Phys. Chem. Chem. Phys. 22 (2020) 12713–12723. https://doi.org/10.1039/d0cp01026j.

[132] M. Teubner, R. Strey, Origin of the scattering peak in microemulsions, J. Chem. Phys. 87 (1987) 3195–3200. https://doi.org/10.1063/1.453006.

[133] D. Saurel, J. Segalini, M. Jauregui, A. Pendashteh, B. Daffos, P. Simon, M. Casas-Cabanas, A SAXS outlook on disordered carbonaceous materials for electrochemical energy storage, Energy Storage Mater. 21 (2019) 162–173. https://doi.org/10.1016/j.ensm.2019.05.007.

[134] P. Fratzl, H.S. Gupta, O. Paris, A. Valenta, P. Roschger, K. Klaushofer, Diffracting “stacks of cards” - Some thoughts about small-angle scattering from bone, Prog. Colloid Polym. Sci. 130 (2005) 33–39. https://doi.org/10.1007/b107343.

[135] A. Gourrier, C. Li, S. Siegel, O. Paris, P. Roschger, K. Klaushofer, P. Fratzl, Scanning small-angle X-ray scattering analysis of the size and organization of the mineral nanoparticles in fluorotic bone using a stack of cards model, J. Appl. Crystallogr. 43 (2010) 1385–1392. https://doi.org/10.1107/S0021889810035090.

[136] N. Kostoglou, C. Koczwara, C. Prehal, V. Terziyska, B. Babic, B. Matovic, G. Constantinides, C. Tampaxis, G. Charalambopoulou, T. Steriotis, S. Hinder, M. Baker, K. Polychronopoulou, C. Doumanidis, O. Paris, C. Mitterer, Nano Energy Nanoporous activated carbon cloth as a versatile material for hydrogen adsorption , selective gas separation and electrochemical energy storage, 40 (2017) 49–64. https://doi.org/10.1016/j.nanoen.2017.07.056.

[137] K.L. Stefanopoulos, E.P. Favvas, G.N. Karanikolos, W. Alameri, V.C. Kelessidis, T.G.A. Youngs, D.T. Bowron, Monitoring the CO2 enhanced oil recovery process at the nanoscale: an in situ neutron scattering study, Energy Adv. 1 (2022) 67–75. https://doi.org/10.1039/d1ya00058f.

[138] A. Maity, S. Singh, S. Mehta, T.G.A. Youngs, J. Bahadur, V. Polshettiwar, Insights into the CO2 Capture Characteristics within the Hierarchical Pores of Carbon Nanospheres Using Small-Angle Neutron Scattering, Langmuir. 39 (2023) 4382–4393. https://doi.org/10.1021/acs.langmuir.2c03474.

[139] N.J. Corrente, E.L. Hinks, A. Kasera, R. Gough, P.I. Ravikovitch, A. V. Neimark, Modeling adsorption of simple fluids and hydrocarbons on nanoporous carbons, Carbon N. Y. 197 (2022) 526–533. https://doi.org/10.1016/j.carbon.2022.06.071.

[140] C. de Tomas, I. Suarez-Martinez, N.A. Marks, Graphitization of amorphous carbons: A comparative study of interatomic potentials, Carbon N. Y. 109 (2016) 681–693. https://doi.org/10.1016/j.carbon.2016.08.024.

[141] S. Stock, N.J. Corrente, M. Seyffertitz, M.V. Rauscher, S. Zeiler, N. Kostoglou, B. Demé, N.A. Marks, A. V. Neimark, O. Paris, On the supercritical adsorption of molecular hydrogen and deuterium in microporous carbons, Submitt. to Carbon. (2025).

[142] P.I. Ravikovitch, A. Vishnyakov, A. V. Neimark, Density functional theories and molecular simulations of adsorption and phase transitions in nanopores, Phys. Rev. E - Stat. Physics, Plasmas, Fluids, Relat. Interdiscip. Top. 64 (2001) 20. https://doi.org/10.1103/PhysRevE.64.011602.

[143] P. Kowalczyk, R. Hołyst, M. Terrones, H. Terrones, Hydrogen storage in nanoporous carbon materials: Myth and facts, Phys. Chem. Chem. Phys. 9 (2007) 1786–1792. https://doi.org/10.1039/b618747a.

[144] J.A. Van Meel, L. Filion, C. Valeriani, D. Frenkel, A parameter-free, solid-angle based, nearest-neighbor algorithm, J. Chem. Phys. 136 (2012). https://doi.org/10.1063/1.4729313.

[145] C. Prehal, C. Koczwara, N. Jäckel, A. Schreiber, M. Burian, H. Amenitsch, M.A. Hartmann, V. Presser, O. Paris, Quantification of ion confinement and desolvation in nanoporous carbon supercapacitors with modelling and in situ X-ray scattering, Nat. Energy. 2 (2017) 1–8. https://doi.org/10.1038/nenergy.2016.215.

[146] C. Merlet, C. Péan, B. Rotenberg, P.A. Madden, B. Daffos, P.L. Taberna, P. Simon, M. Salanne, Highly confined ions store charge more efficiently in supercapacitors, Nat. Commun. 4 (2013) 1–6. https://doi.org/10.1038/ncomms3701.

[147] C. Prehal, S. Grätz, B. Krüner, M. Thommes, L. Borchardt, V. Presser, O. Paris, Comparing pore structure models of nanoporous carbons obtained from small angle X-ray scattering and gas adsorption, Carbon N. Y. 152 (2019) 416–423. https://doi.org/10.1016/j.carbon.2019.06.008.

[148] A. Gotzias, E. Tylianakis, G. Froudakis, T. Steriotis, Theoretical study of hydrogen adsorption in oxygen functionalized carbon slit pores, Microporous Mesoporous Mater. 154 (2012) 38–44. https://doi.org/10.1016/j.micromeso.2011.10.011.

[149] R.J. Olsen, A.K. Gillespie, C.I. Contescu, J.W. Taylor, P. Pfeifer, J.R. Morris, Phase Transition of H_2 in Subnanometer Pores Observed at 75 K, ACS Nano. 11 (2017) 11617–11631. https://doi.org/10.1021/acsnano.7b06640.

[150] M. Carmichael, K. Chenoweth, C.E. Dykstra, Hydrogen Molecule Clusters, J. Phys. Chem. A. 108 (2004) 3143–3152. https://doi.org/10.1021/jp037209u.

[151] A. Choudhary, T.A. Ho, Confinement-induced clustering of H_2 and CO_2 gas molecules in hydrated nanopores, Phys. Chem. Chem. Phys. 26 (2024) 10506–10514. https://doi.org/10.1039/d3cp06024a.

[152] J.I. Martínez, M. Isla, J.A. Alonso, Theoretical study of molecular hydrogen clusters : Growth models and magic numbers, in: Eur. Phys. J. D, 2007: pp. 61–64. https://doi.org/10.1140/epjd/e2007-00095-7.

10 List of Publications

The manuscripts published and/or submitted within the framework of this thesis are: (7), (9) and (10)

(1) Kostoglou, N.; Koczwara, C.; **Stock, S.**; Tampaxis, C.; Charalambopoulou, G.; Steriotis, T.; Paris, O.; Rebholz, C.; Mitterer, C. Nanoporous Polymer-Derived Activated Carbon for Hydrogen Adsorption and Electrochemical Energy Storage. Chem. Eng. J. 2022, 427, 131730. https://doi.org/10.1016/j.cej.2021.131730.

(2) Selinger, J.; **Stock, S.**; Schlemmer, W.; Hobisch, M.; Kostoglou, N.; Abbas, Q.; Paris, O.; Mitterer, C.; Hummel, M.; Spirk, S. Nanoporous Carbon Electrodes Derived from Coffee Side Streams for Supercapacitors in Aqueous Electrolytes. Nanomaterials 2022, 12, 2647. https://doi.org/https://doi.org/10.3390/nano12152647.

(3) Christopoulou, M. A.; Koutsovitis, P.; Kostoglou, N.; Paraskevopoulou, C.; Sideridis, A.; Petrounias, P.; Rogkala, A.; **Stock, S.**; Koukouzas, N. Evaluation of the CO_2 Storage Capacity in Sandstone Formations from the Southeast Mesohellenic Trough (Greece). 2022.

(4) **Stock, S.**; Kostoglou, N.; Selinger, J.; Spirk, S.; Tampaxis, C.; Charalambopoulou, G.; Steriotis, T.; Rebholz, C.; Mitterer, C.; Paris, O. Coffee Waste-Derived Nanoporous Carbons for Hydrogen Storage. ACS Appl. Energy Mater. 2022, 5, 10915–10926. https://doi.org/10.1021/acsaem.2c01573.

(5) Rauscher, M. V.; Seyffertitz, M.; Kohns, R.; **Stock, S.**; Amenitsch, H.; Huesing, N.; Paris, O. Optimizing Surfactant Removal from a Soft-Templated Ordered Mesoporous Carbon Precursor: An in Situ SAXS Study . J. Appl. Crystallogr. 2023, 56 (3), 801–809. https://doi.org/10.1107/s1600576723003886.

(6) Seyffertitz, M.; **Stock, S.**; Rauscher, M. V.; Prehal, C.; Haas, S.; Porcar, L.; Paris, O. Are SAXS and SANS Suitable to Extract Information on the Role of Water for Electric-Double-Layer Formation at the Carbon-Aqueous-Electrolyte Interface? Faraday Discuss. 2023, 249, 363–380. https://doi.org/10.1039/d3fd00124e.

(7) **Stock, S.**; Seyffertitz, M.; Kostoglou, N.; Rauscher, M. V.; Presser, V.; Demé, B.; Cristiglio, V.; Kratzer, M.; Rols, S.; Mitterer, C.; Paris, O. Hydrogen Densification in Carbon Nanopore Confinement: Insights from Small-Angle Neutron Scattering Using a Hierarchical Contrast Model. Carbon N. Y. 2024, 221 (118911). https://doi.org/10.1016/j.carbon.2024.118911.

(8) Kostoglou, N.; **Stock, S.**; Solomi, A.; Holzapfel, D. M.; Hinder, S.; Baker, M.; Constantinides, G.; Ryzhkov, V.; Maletaskic, J.; Matovic, B.; Schneider, J. M.; Rebholz, C.; Mitterer, C. The Roles of Impurities and Surface Area on Thermal Stability and Oxidation Resistance of BN Nanoplatelets. Nanomaterials 2024, 14 (7). https://doi.org/10.3390/nano14070601.

(9) **Stock, S.**; Trost, C. O. W.; Seyffertitz, M.; Selinger, J.; Gupta, R. K.; Tampaxis, C.; Steriotis, T. A.; Rebholz, C.; Mitterer, C.; Paris, O.; Kostoglou, N. Transforming Breakfast Bio-Waste into Hydrogen Storage Materials. Accept. by Int. J. Hydrog. Energy 2025.

(10) **Stock, S**.; Corrente, N. J.; Seyffertitz, M.; Rauscher, M. V.; Zeiler, S.; Kostoglou, N.; Demé, B.; Marks, N. A.; Neimark, A. V.; Paris, O. On the Supercritical Adsorption of Molecular Hydrogen and Deuterium in Microporous Carbons. Submitt. to Carbon 2025.